Jesús Cerdá Calatayud

Computations on non–covalent assemblies:

Supramolecular organization and transport properties

PhD Thesis

Doctorate program in:

Theoretical Chemistry and Computational Modelling

Supervised by

Dr. Juan Aragó March and Prof. Enrique Ortí Guillén

MolMatTC Group

Theoretical Chemistry Research Unit

Institute of Molecular Science

Valencia, January 2022

Instituto de ciencia molecular
Departamento de química física

D. Enrique Ortí Guillén y **D. Juan Aragó March,** Catedrático del Departamento de Química Física e Investigador Ramón y Cajal en el Instituto de Ciencia Molecular (ICMol), respectivamente, CERTIFICAN que la memoria presentada por **Jesús Cerdá Calatayud** con el título "*Computations on non–covalent assemblies: Supramolecular organization and transport properties*" corresponde a su Tesis Doctoral y ha sido realizada bajo su dirección dentro del Programa de Doctorado **3156 Química Teórica y Modelización Computacional**, autorizando mediante este escrito la presentación de la misma.

En Valencia, a 24 de enero de 2022.

Director:
Prof. Enrique Ortí Guillén

Director y tutor:
Dr. Juan Aragó March

Agradecimientos

Con estas líneas pretendo agradecer de alguna manera a toda la gente que me ha acompañado en todos estos años, tanto si han contribuido activamente en que alguno de los estudios de esta tesis llegara a buen puerto o simplemente han ayudado a que no pierda la cabeza en el intento.

En primer lugar, me gustaría agradecer a la gente que compone la unidad de química teórica, con los que paso la mayor parte del tiempo que estoy despierto. Gracias por todos los cafés, discusiones y en general por ayudar a que el trabajo suponga menos esfuerzo. En especial, quisiera dar las gracias a mis directores de Tesis: Enrique, quien me permitió unirme al grupo de investigación, a pesar de conocer bastante bien los muchos defectos que tengo y que siempre ha dejado la puerta abierta para todo. Juan, a ti debo agradecerte muchas cosas, por un lado, todo lo que me has aportado desde el punto de vista científico, sobre todo esas ideas y proyectos que generas. Pero por encima de eso, gracias por tu carácter y por ser más un amigo que un jefe.

También quiero agradecer a todas las personas que han contribuido como colaboradores en los distintos proyectos y que claramente son responsables directos del éxito de esta Tesis.

El último grupo de personas que han contribuido científicamente son los amigos que hice en el Master (Enrique, Xabi, Guille y Elena) quienes además de todo lo que me han enseñado son una gran fuente de anécdotas y una de las mayores motivaciones para ir a congresos.

Me gustaría agradecer también a la gente que me ha ayudado a evadirme y encontrar vías de escape cuando lo he necesitado. Los amigos de la infancia (Tuso, Sula, Chema y Josep), los compañeros de la carrera (Carles, Carlos, Néstor y Raúl) y esa gente a la que siempre quiero ver cerca del mar (Manu, María, Isa y Alexis). Todos vosotros habéis conseguido que disfrute de la vida y habéis conseguido sacarme una sonrisa cada vez que nos hemos visto. Me gustaría agradecer también a dos personas que de una manera muy particular me han ayudado muchísimo a coger perspectiva en muchas situaciones: Ana, una de las primeras personas que conocí cuando entre a la universidad y una compañera increíble hasta este año que los dos hemos acabado la tesis; y Paula, a ti simplemente gracias por estar siempre ahí.

Por último, y son los últimos porque lo mejor siempre va al final, tengo que dar las gracias a mis padres. Ellos son quien siempre han procurado darme los medios para que llegara a donde quisiera llegar y también quienes más me han aguantado. Papá, Mamá, gracias por todo.

Contents

Chapter 1. Introduction

Non-covalent interactions, which are one of the most important kind of interactions in chemistry, are the attractive forces that emerge between either atoms or molecular entities at distances larger than the typical covalent bonds. These forces generally determine the macroscopic properties like the states of matter at a defined temperature (solid, liquid or gas). Non-covalent interactions are also responsible for the molecular conformations since they are the main interaction acting between non-bonded fragments within a molecular system. Actually, the great importance of non-covalent interactions has been widely demonstrated in biological systems, where their final 3D structures (and, consequently, its functionality) are determined by these kind of interactions. As examples, enzymes lose their catalytic activity when the environment conditions (*e.g.*, pH or temperature) are enough to alter or break the non-covalent interactions that stabilize their functional structure. Another good example is the cellulose fibers, whose extraordinary mechanical resistance comes from the interaction by means of non-covalent H-bonds between the different molecular chains.

Chemists, in particular material chemists, have found in biological systems a source of inspiration for the design of novel supramolecular systems with desired properties for potential applications. Thus, the use of non-covalent interactions, mimicking the biological systems, and the synthesis of new materials with new functionalities is one the main topics of material chemistry, and different kinds of materials based on non-covalent assemblies can be found. For instance, molecular crystals are ordered structures made by small-medium size molecules and they hold together only by non-covalent

interactions. Actually, non-covalent interactions are of high relevance not only in solid state but also in solution, supramolecular polymers or even just dimers can be found in solution where a compromise between molecule-molecule interactions and solvent-solute interactions must be fulfilled to obtain a stable assembly.

In this Thesis, a theoretical study on the structural and electronic properties of non-covalent assemblies is performed. First, the structural organization of supramolecular polymers is studied (Chapter 4). The main goal is to understand and deepen in how non-covalent interactions determine the properties of different supramolecular polymers. Second, intermolecular charge and energy transport processes in several non-covalent assemblies (molecular crystals, donor–acceptor dimers and supramolecular polymers) formed by different of organic semiconducting building blocks are investigated in Chapters 5 and 6.

1.1 Supramolecular polymers

Polymers are macromolecular systems with a high molecular weight and composed of repeating units (monomers) of low molecular mass.[1] Nowadays, chemistry is able to build a great diversity of polymers with a wide variety of physical and chemical properties. Polymers can be usually classified according to their chemical composition, structure or polymerization mechanism. An alternative criterion is the nature of the interactions between the monomers.

Although polymers are traditionally bonded through covalent bonds, the monomers constituting the polymer can be also held together by non-covalent

interactions giving rise to supramolecular polymers (Figure 1).[2] The weak nature of these non-covalent interactions compared with covalent bonds leads to reversible assemblies that may be controlled through external stimuli as: temperature, pH or interaction with light.[3,4] Nevertheless, highly stable supramolecular polymers can be also achieved owing to the contribution of a great number of non-covalent interactions. An excellent example of a stable supramolecular assembly governed by non-covalent interactions in Nature is the DNA double helix, which is stabilized by H-bonds and π-stacking between the nucleobases.[5]

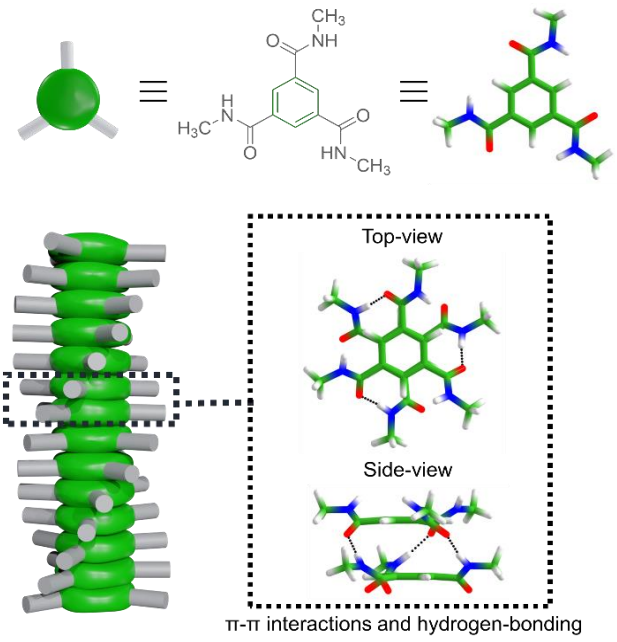

Figure 1. Schematic representation of a helical columnar supramolecular polymer based on a benzene-1,3,5-tricarboxamide (BTA) derivative. The BTA core is shown in green and the three arms in grey sticks.

The building up of supramolecular polymers is driven by a molecular self-assembly process in an efficient and controlled way.[6] Molecular self-assembly is indeed a powerful tool in materials science to construct functional architectures by a smart design of the constituting building blocks. The molecules are chemically and structurally conceived to promote specific intermolecular interactions in order to obtain a desired supramolecular growth.[7,8] The appealing properties shown by supramolecular polymers make them very attractive as recyclable, degradable, stimulus responsive and self-healing materials for many applications.

An example of soft self-healing materials are the supramolecular gels.[9,10] Gels present a density similar to liquids but with a solid-like structure. They have been widely used in cosmetics, alimentary or petrol industry. Another important kind of supramolecular materials with direct application for the electronic industry is the liquid crystals, which are essential for (liquid crystal display) screens.[11–14] LCDs are formed by two polarizing filters oriented perpendicularly with a layer of a liquid crystal between them. The light striking the first filter does not pass through the second filter unless the liquid crystal rotates the polarized light, which is achieved by the orientation of the liquid crystal, typically in a columnar disposition, controlled by an electrical field. Therefore, the on-off switching of the electrical field is the external stimulus used to provoke a reversible change in the liquid crystal structure leading to its functionality.

A special type of liquid crystals is the discotic liquid crystals; whose molecular monomers incorporate a planar π-conjugated core that reminds a disc-like shape. In general, π-conjugated discotic-based liquid crystals can behave as

semiconductors. This has motivated an intensive investigation of the charge and energy transport properties in these systems, as a function of the molecular building blocks, because the electronic structure of the discotic molecules can be easily tuned by chemical design.[15,16]

A key point in the self-assembly process of supramolecular polymers is the mechanism. The supramolecular polymerization mechanism can be understood as the sequential addition of a monomer to the pre-existing polymeric chain.[17] Generally, two different mechanisms,[18] isodesmic and cooperative (Figure 2), are proposed for the polymerization process. In the isodesmic mechanism, the addition of each new molecule occurs with the same binding or equilibrium constant. This mechanism usually leads to polymers with a high polydispersity and short-length chains.[19–21] In the cooperative mechanism, the self-assembly process starts with the formation of a short supramolecular oligomer (nucleation) and continues with a thermodynamically more favorable supramolecular growth (elongation). The cooperative polymerization therefore encompasses two regimes, nucleation and elongation, with the corresponding binding constants K_{nuc} and K_{elo}, and leads to longer chains and lower polydisperse polymers.[22] The experimental way to characterize the supramolecular polymerization mechanism is to plot a property inherent to the aggregate (*e.g.*, the optical absorbance or the circular dichroic signal recorded at a specific wavelength) as a function of concentration or temperature. If the resulting plot presents a sigmoidal shape the mechanism is assigned to be isodesmic, whereas if it looks like a hyperbola that finally saturates then corresponds to a cooperative mechanism (Figure 2). A third mechanism, known as anti-cooperative, can also be found. In that mechanism, the initial step of the polymerization (nucleation) is

thermodynamically favored compared to the elongation. The anti-cooperative mechanism is quite uncommon because the small oligomers initially formed (in many cases dimers) must be more stable than the long aggregates. Metastable phases showing an anti-cooperative supramolecular behavior have been reported in the literature.[23,24] In principle, all the mechanisms mentioned above follow the same thermodynamic balances, the main difference between them is the thermodynamic stability of the initial and final states or, in other words, the binding constants of the nucleation and elongation steps (Figure 2).

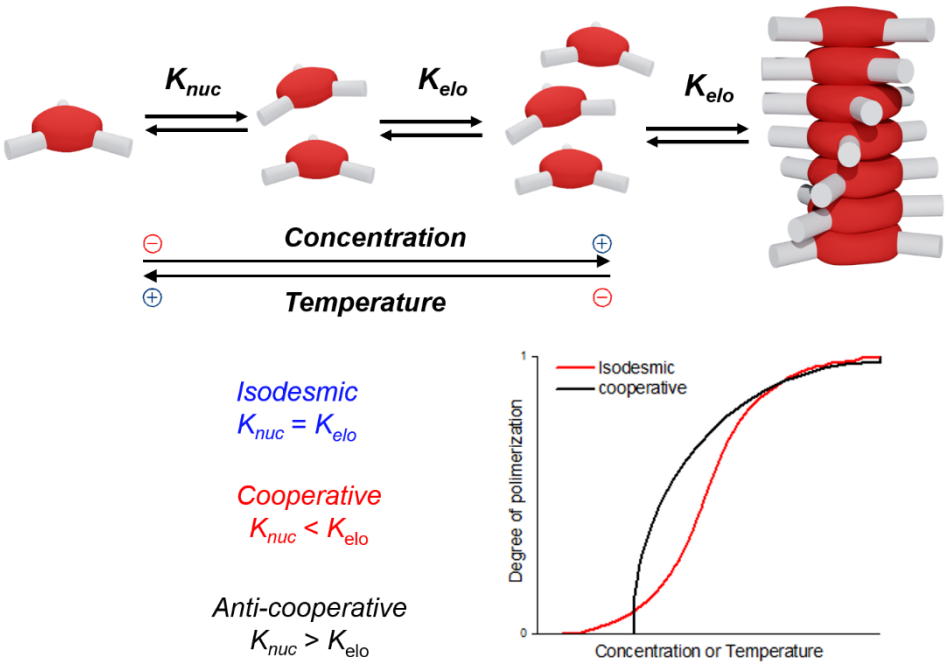

Figure 2. Scheme of the supramolecular polymerization mechanisms characterized by the relative values of the nucleation (K_{nuc}) and elongation (K_{elo}) binding constants and its evolution with concentration or temperature. A representative plot of the degree of polymerization as function of concentration

or temperature for isodesmic and cooperative mechanisms is provided as an example.

An important property that can emerge spontaneously in supramolecular polymers is the phenomenon of chirality. Many supramolecular polymers may present chiral shapes even though the constituting monomers are completely achiral. Chirality is a property that determines the biological activity of many macromolecules. For instance, only *L*-aminoacids are used to build up proteins, enzymes present a different metabolic activity depending on the enantiomeric character of the substrates and the DNA chain is organized in a double-helix pattern inherently chiral. In nature, chirality goes beyond the molecular scale (Figure 3). Many plants and animals, as the patterns of the seashells, and human building elements, as columns of emblematic buildings, are chiral structures, and even our galaxy presents a chiral spiral shape.

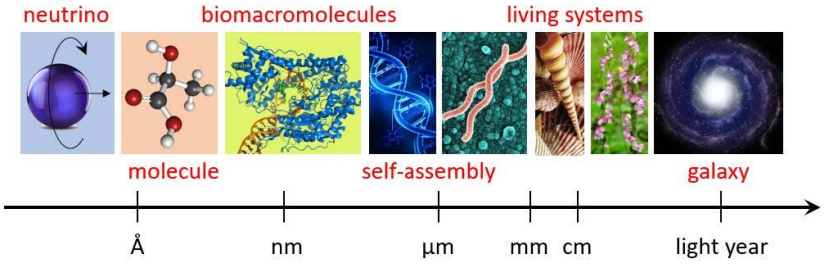

Figure 3. Representation of different chiral structures at different scale sizes, from atomic to astronomic scales.

As mentioned, even achiral molecules may promote chiral patterns at the supramolecular level (*e.g.*, supramolecular helices), but these assemblies give rise to racemic mixtures since both *P*- and *M*-type supramolecular helices are isoenergetic (Figure 4). However, if the monomers hold a chiral center,

although the chiral center does not participate in the main interactions that stabilize the polymer, a specific polymeric enantiomer is energetically favored. Thus, the monomer transfers its chirality to the polymer and produces an enantiomeric disequilibrium.[25] Over the last years, an increasing research effort has been dedicated to the understanding of the phenomena of chirality transfer and chirality amplification in supramolecular polymers. Experiments in which a small fraction of chiral molecules mixed with a majority of achiral molecules induces a clear chirality (sergeants and soldiers (SaS) experiments) or mixing unequal amounts of two enantioenriched samples (majority rules (MRs) experiments) leads to chiral amplification are routinely performed (Figure 4). These experiments allow to obtain the thermodynamic parameters that are used to evaluate the chirality transfer and amplification capabilities of the self-assembling system. The SaS and MRs experiments are usually conducted by recording circular dichroism spectroscopy data for mixtures of different composition. For chiral systems, circular dichroism provides an optical response of opposite sign for the different enantiomers.

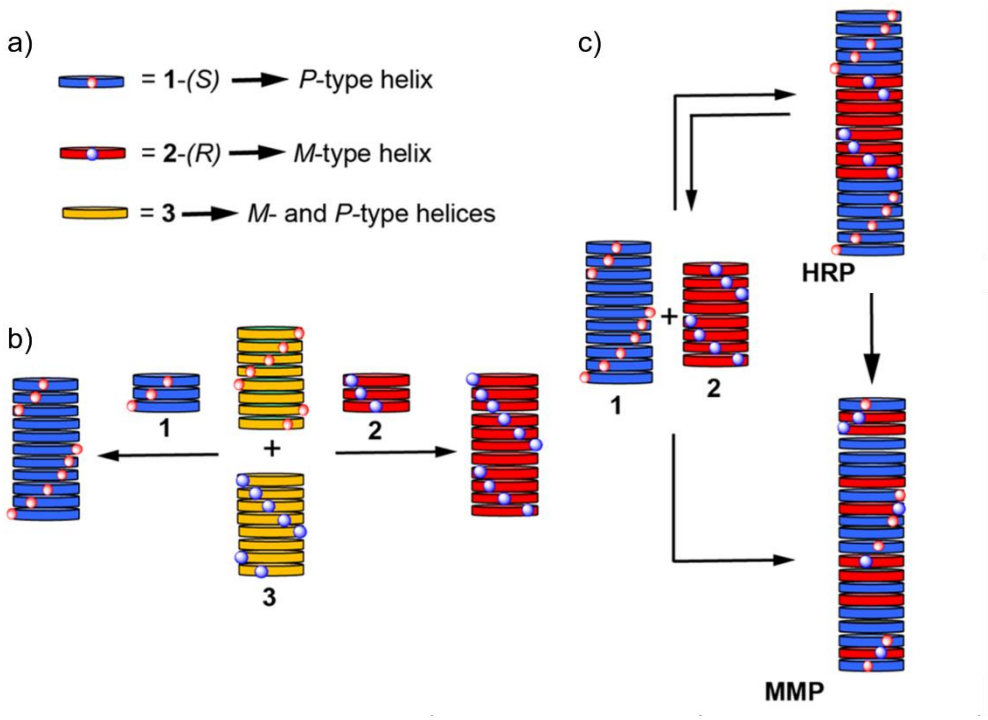

Figure 4. a) Schematic representation of the three point-chirality possibilities in a monomer and its preferred helical outcome. b) Sergeants-and-soldiers (SaS) experiments between chiral and achiral molecules. c) Majority rules (MRs) experiments for mixtures of different chirality molecules.

1.2 Organic semiconductors

Nowadays, electronic devices play a primary role in our life, supporting us in a wide range of applications of our daily routine, from basic needs as lightning or communication to the entertainment. Among the materials used for electronic purposes, semiconductors are likely to be the most important components for an optimal performance. Inorganic semiconductors such as

silicon, germanium or gallium arsenide dominate our current electronics industry and can be found in computer processors, integrated electronic circuits or photovoltaic cells. Nonetheless, the inherent properties of these inorganic semiconductors are also a restriction in terms of their processability and manufacturing costs, because, in general, high processing temperatures are needed.

A new class of materials, known as organic semiconductors, has emerged and become very popular in the last decades due to their potential for optoelectronic applications.[26–30] In contrast to crystalline inorganic materials, organic semiconductors are mainly composed by carbon-based molecules and present low cost and easy processability, since they can be processed from vapor or solution,[31–33] without the need of high temperatures. In addition to the processing advantages, the main features of organic semiconductors are their excellent mechanical properties. Unlike the rigidity and brittleness of inorganic materials, the flexibility of organic semiconductors allows to build alternative devices that can bend or stretch easily.[34–38] Although electronic devices based on organic semiconductors do not necessarily surpass the device efficiencies obtained by traditional inorganic semiconductors, organic-based (opto)electronic devices open the door for novel architectures and applications due to their unique mechanical properties. At molecular and supramolecular level, organic semiconducting systems also hold an attractive feature: its tuneability; *i.e.*, the structural, electronic and optical properties of organic semiconductors can be modulated by chemical design (organic synthesis). This has resulted, by rational design, in a great variety of improved organic semiconducting systems according to the target application.[39]

The most suitable chemical family of compounds to be used in the field of organic electronics applications is the π-conjugated compounds. The extended π-conjugation in these organic compounds is key to obtain the desired electronic and optical properties. For instance, π-conjugated compounds generally exhibit light absorption and emission in the visible range of the electromagnetic spectra. In addition, the energy levels and energy gaps associated to the frontier molecular orbitals are in the same energy window as in the traditional inorganic semiconductors, which is essential for obtaining high electrical conductivities and charge injection from metallic electrodes. Figure 5 displays the chemical structure of several well-known organic semiconductors all sharing, as a common feature, the π-conjugated skeleton.

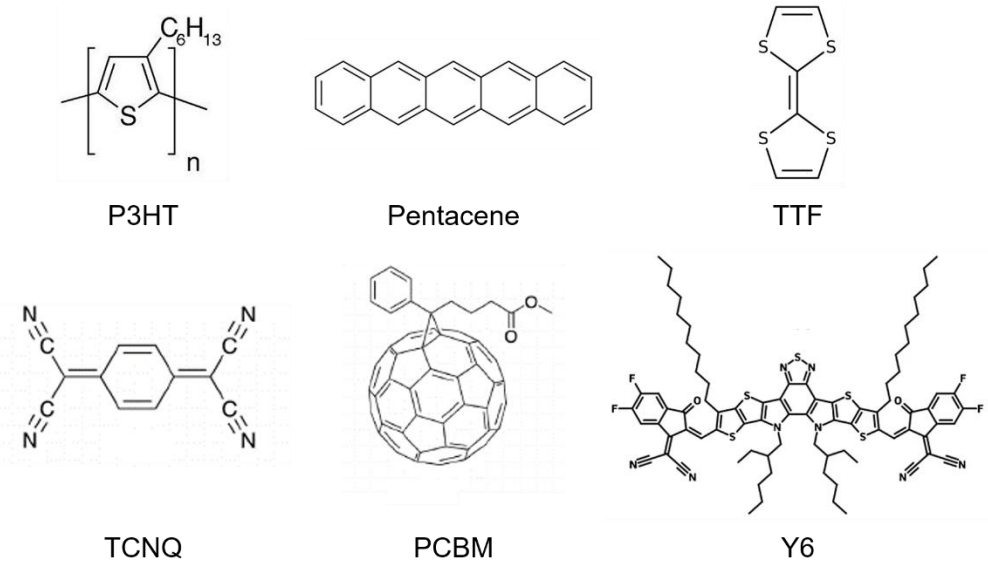

Figure 5. Chemical structure of relevant organic π-conjugated semiconductors.

Among the possible applications of organic π-conjugated semiconductors, their use in optoelectronic devices such as organic light-emitting diodes (OLEDs),[40–42] organic field-effect transistors (OFETs),[26,43–46] and organic photovoltaics (OPV) should be stressed.[39,47–54] OLEDs are electroluminescent devices in which the charges are injected from the electrodes and transported to the active layer where they recombine forming an exciton that decays to the ground state *via* radiative processes (light emission by fluorescence or phosphorescence). In OFETs, the working mechanism is based on the charge transport through the active organic semiconducting layer deposited between two electrodes polarizing the direction of the charge motion across the material due to a potential bias. Finally, OPV devices are designed to convert light into electrical current, where a sequence of several fundamental processes (*e.g.*, exciton diffusion, exciton dissociation and charge transport) should take place in an efficient manner. All optoelectronic devices based on organic semiconductors have in common that efficient electronic transport processes should occur for optimal performances. Among them, OPV devices show the best architecture to understand the relevance of the electronic transport phenomena. The simplest OPV architecture is the bilayer donor–acceptor solar cell shown in Figure 6, whose working mechanism can be summarized in the following steps:

1. Light absorption generating an exciton (a Coulombically-bound electron-hole pair) or, in other words, an excited state of one or several molecules. This process usually takes place at the donor layer.
2. Exciton diffusion or exciton transport from the bulk of the donor layer to the interface between the donor and the acceptor.

3. Exciton dissociation at the donor–acceptor interface, where the hole and the electron are generated.
4. Charge (holes and electrons) migration from the interface to the electrodes.
5. Charge extraction at the respective electrodes.

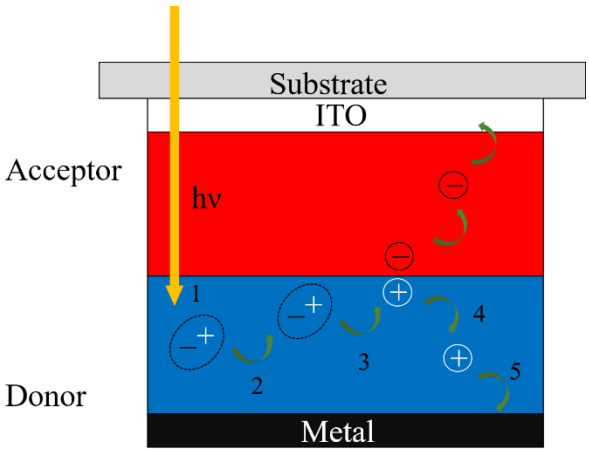

Figure 6. Scheme of the working mechanism of a bilayer donor–acceptor organic solar cell: light absorption in the donor (1), exciton diffusion (2) exciton dissociation (3), charge-carrier migration (4) and charge-carrier extraction (5).

All the five steps of the mechanism should be optimized to achieve high efficiencies in the OPV devices. Light absorption is the first step, and its efficiency critically depends on the absorption properties of the donor component. To maximize the light absorption in the UV-vis and near IR range, special types of π-conjugated dyes can be added to the device.[55,56] Tandem solar cells allow to absorb a wider region of the spectrum by building two or

more solar cells, made of different materials, sequentially (Figure 7a).[57–62] An alternative strategy is the ternary solar cells, in which, to get a wider absorption region, two donors that absorb at different wavelengths are mixed (Figure 7c).[62–68]

The second step is the exciton diffusion in the bulk of the donor. This process generally consists in an energy transfer between the donor molecules *via* a random walk mechanism.[69] Excitons can be seen as neutral electron-hole quasi-particles and they are not therefore affected by the electrical field generated between the electrodes. An efficient exciton/energy transport is highly required to achieve good OPV performances. Unfortunately, most organic π-conjugated semiconductors present relatively poor exciton transport properties. In general, they exhibit small exciton diffusion lengths (magnitude measuring the distance that the exciton moves during its lifetime) of a few tenths of nanometers. Note that the thickness of the donor layer in an OPV device (usually between 80 to 200 nm)[39,70] is generally much higher than the typical exciton diffusion lengths. Therefore, in bilayer OPV architectures, only the excitons generated close to the interface may reach the heterojunction for the proper exciton dissociation (also known as charge separation). To mitigate the shortcomings derived from the low exciton diffusion lengths in organic semiconductors, a novel and practical device architecture was developed and known as bulk-heterojunction solar cells. In these cells, instead of clearly having two well-delimited layers, the donor and the acceptor materials are mixed in only one layer (Figure 7b), where the distance between the donor bulk and the donor–acceptor interface has significantly diminished.[50,52,71,72] Nevertheless, bulk-heterojunction solar cells also require continuous donor and

acceptor domains in contact with the electrodes to allow the charge migration and extraction processes (steps 4 and 5 in Figure 6).[73–77]

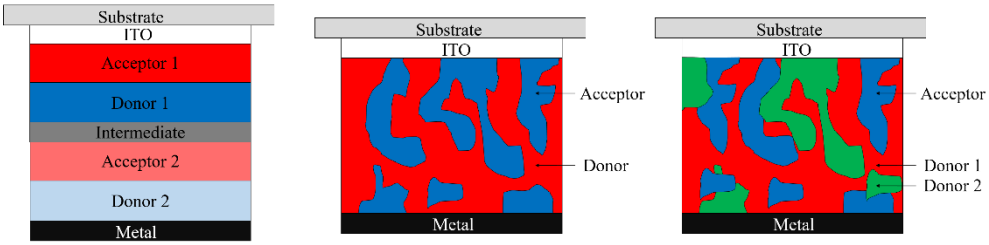

Figure 7. Schemes showing the basic architectures of tandem (a), bulk heterojunction (b), and ternary bulk heterojunction (c) solar cells

As already mentioned, exciton dissociation (step 3) takes places at the donor–acceptor (D–A) interface. The heterojuntion is necessary in OPVs because the typical exciton binding energy (the attractive Coulombic potential between the hole and electron) in donor molecules is higher than the thermal energy and, therefore, the charge separation between identical molecules in the bulk does not occur spontaneously. At the D–A interface, the exciton binding energy is energetically compensated by the electron transfer from the lowest unoccupied molecular orbital (LUMO) of the donor to the LUMO of the acceptor, which is lower in energy.[51,52] That electron transfer gives rise to a more stable charge-separated D^+–A^- state (compared to a D^+–D^- state). Bulk-heterojunction solar cells improve the exciton dissociation since they present a large D–A contact surface, thus increasing the probability for the charge separation event.

The fourth step is the charge carrier migration towards the electrodes; *i.e.*, the transport of holes and electrons, once the exciton dissociation takes place, within the donor and acceptor domains, respectively. The charge motion is not

random as in the exciton transport since holes and electrons are electrically charged particles and are therefore affected by the electrical field generated by the difference on the work function of the electrodes. Nevertheless, the most important factor that determines the charge migration in the donor/acceptor material is the supramolecular organization of the molecules governed by weakly intermolecular interactions. A wide range of charge carrier mobilities in organic semiconductors is usually found going from 10^{-6} cm^2 V^{-1} s^{-1} in amorphous organic materials to ~1.0 cm^2 V^{-1} s^{-1} in highly-ordered organic molecular crystals.[78] High mobilities are required to avoid the detrimental charge recombination process that reduces the efficiency of the OPV devices.

The last process involved in solar cells devices is the charge extraction, in which the holes and electrons are transferred from the donor and acceptor domains to the electrodes. The efficiency of these processes is mainly governed by the work function of the electrodes.

Exciton diffusion (also known as energy transport), exciton dissociation and charge migration (or charge transport) are processes in which this Thesis has been focused. In all of these processes, in which either charge or energy is transferred from a molecular fragment or unit to another, the relative spatial disposition (supramolecular arrangement) of the two moieties determines the efficiency of the process.

Several theoretical models for charge and exciton transport in molecular assemblies have been proposed. Band theory, which is the dominant theory in describing charge transport in inorganic semiconductors, does not seem to fit properly to explain the behavior of the electronic transport phenomena in organic semiconductors. This is because molecules in organic crystals are

weakly bound by non-covalent interactions, making the transport along the crystal more sensitive to molecular vibrations promoting the localization of the charge/exciton carriers.[79] The band model therefore leads to unphysical results and incorrect temperature dependences in organic semiconductors.[80] Thus, the localized charge/exciton carrier models (hopping models) are usually more appropriate for the transport description in organic semiconductors.[81–83] However, certain organic semiconductors present broad densities of states (typical for band-like transport) but, at the same time, electronic localization (characteristic for a hopping process). That situation leads to an intermediate regime known as transient localization scenario.[84,85] In this regime, the bands are localized in a few molecular sites during a short period of time similar to that found for molecular vibrations.

Independently of the transport regime, the most important experimental observable used to characterize the charge transport in organic semiconductors is the charge-carrier mobility (μ), which is the property that relates the velocity of the charge carrier and the electric field that accelerates it. On the other hand, the most common observables for the exciton (energy) transport in molecular systems are the exciton diffusion coefficient and the exciton diffusion lengths. In Chapters 5 and 6, the charge and energy transport properties of some organic π-conjugated materials are characterized using theoretical and computational tools.

Chapter 2. Objectives

The aim of the current Thesis is to rationalize, from a theoretical perspective, the structural, electronic, optical and transport properties of different electroactive supramolecular systems of special relevance in the field of organic electronics. The ultimate goal is to establish valuable supramolecular structure-property relationships. In particular, this Thesis focuses on three types of systems: hole-transporting materials, donor–acceptor supramolecular complexes and supramolecular polymers. For each system, the spotlight has been put on different relevant electronic processes. For the family of hole-transporting materials, the charge transport is thoroughly studied and compared with the experimental observables (mobilities) in thin-film transistors. For donor–acceptor supramolecular complexes, the photoinduced electron transfer, which is a crucial electronic process for light-to-electrical conversions, is investigated for a donor–acceptor supramolecular complex model. Finally, the optical and energy/exciton transport properties of some supramolecular polymers are studied with implications for photonic applications.

The specific goals pursued in the Thesis are detailed as follows:

1) Chapter 4. Supramolecular polymers. This chapter is divided into three subsections where three types of supramolecular polymers with different properties are theoretically investigated.
   i) *Discotic-like benzene-triscarboxamide supramolecular polymers*. In this subsection (Section 4.2.1), the main goal is to establish the relationship between the supramolecular organization and the

phenomena of transfer and amplification of chirality observed experimentally in a family of discotic-like benzene-triscarboxamide derivatives. The study also explores the role of the number of chiral side chains and the size of the discotic core on the chirooptical properties.

ii) *The T3C$_4$ host–guest complex*. The main aim in this subsection (Section 4.2.2) is to provide insights, at atomistic resolution, into the hierarchical self-assembly process of a 1:3 host-guest supramolecular complex formed by a tris(triazolyl)triazine derivative and 3,4,5-(4-alkoxybenzyloxy) benzoic acids. The study also offers some clues to rationalize why the 1:3 host-guest complex is able to form a liquid crystal whereas the isolated host is unable.

iii) *A squaramide-based macrocycle*. Here, the supramolecular polymerization of a bisquaramide-based macrocycle is theoretically investigated with the aim of understanding the pathway complexity and the unusual optical properties of the final supramolecular aggregates characterized experimentally.

2) Chapter 5. Charge transport. This chapter focuses on the charge transport or charge transfer processes in two different electroactive systems with potential applications in optoelectronic devices. The particular aims are:

i) To unveil the effect that H-bonding has on the transport properties of a family of fused polyaromatic compounds incorporating 7-azaindole units in the π-conjugated skeleton (Section 5.2.1).

ii) To shed light onto the kinetics (Section 5.2.2) of the nonradiative photoinduced processes (charge-separation and charge-recombination) experimented in solution by a supramolecular complex formed by an

electron-donating bowl-shaped truxene-tetrathiafulvalene (truxTTF) derivative and an electron-accepting fullerene fragment (hemifullerene, $C_{30}H_{12}$).

3) Chapter 6. Energy transport. This chapter tackles issues related to the theoretical description of the energy (exciton) transport in molecular aggregates, which is of great relevance for optoelectronic devices. The chapter has a two-fold objective:
   i) To analyze the performance of different popular approximations to estimate excitonic couplings when Frenkel and charge-transfer excited states are energetically close and delocalization effects are present.
   ii) To identify the mechanism that makes the energy transport in *N*-heterotriangulene-based supramolecular polymers so efficient.

Chapter 3. Methodology: computational chemistry

Over the last decades, the fast speed up of processing capabilities of modern computers, together with the advance in the first principles computational methods and algorithms, has given rise to an enormous advance in the computational chemistry discipline. These advances have led to more accurate calculations and simulations of large systems, reaching chemical systems and processes of unaffordable size and complexity a few years ago. Currently, the computational techniques have acquired a reasonable predictive character allowing the scientific community to enter in the era of the *in silico* design of materials.[86]

First-principles methodologies are generally limited to relatively simple chemical structures of small–medium molecular size. Nowadays, first-principles methodologies, in particular density functional theory (DFT), allow to get accurate results for systems up to systems consisting of hundreds of atoms. The use of computationally cheaper methodologies as semiempirical methods or force-field based calculations is still a common approach to address the modelling of large chemical systems involving many molecules such as supramolecular polymers or molecular crystals. To deal with these systems, it is convenient to use a bottom-up approach in which the building-block molecule or even a small oligomer are theoretically characterized through first-principles calculations and some derived structural or electronic parameters are used for the validation of the simulation of larger systems employing cheaper

methodologies. This bottom-up approach consequently implies the use of combined hierarchical computational protocols.

In this chapter, all the computational approaches used in this Thesis are briefly explained. Most of the calculations were carried out by using DFT or computationally cheaper methodologies for large systems by means of commercial or distributed-for-academia software packages such as: Gaussian,[87] MOPAC,[88] Grimme's xTB,[89] TINKER[90] and QUANTICS.[91] Home-made programs have been also developed to implement some methodological approximations that are incorporated in commercial programs. The particular approaches used in this Thesis to calculate the Huang–Rhys factors and the electronic/excitonic couplings are explained in detail in Sections 3.2.5 and 3.2.6.

3.1 Standard computational chemistry methods

3.1.1 General Background

The primary aim of all computational methods is the computation of physical observables or properties. Among all possible observables, energy (E) is likely to be the most important since it rules all the thermodynamic and even kinetic properties of any physical system. From a quantum physics perspective, the energy of a system in a stationary state can be obtained, in most of the cases, by solving the non-relativistic time-independent Schrödinger equation (Eq. 1).

$$\hat{H}\Psi = E\Psi \tag{1}$$

In this equation, $\hat{H}$ is the Hamiltonian operator, E the energy and Ψ the wavefunction that contains all the information of the system. Unfortunately, Ψ is usually unknown and it is necessary to develop methods able to simultaneously estimate Ψ and E. The Hamiltonian operator is described as the sum of two operators associated to the kinetic ($\hat{T}$) and potential ($\hat{V}$) energies. For a molecular electrostatic system, which can be visualized as a system comprised of light negative charges (electrons) and heavy positive charges (nuclei), $\hat{H}$ is expressed as follows (Eq. 2)

$$\hat{H} = \hat{T}_{\mathrm{e}} + \hat{T}_{\mathrm{N}} + \hat{V}_{\mathrm{eN}} + \hat{V}_{\mathrm{ee}} + \hat{V}_{\mathrm{NN}}, \tag{2}$$

where e and N represent electrons and nuclei, respectively. Thus, $\hat{T}_{\mathrm{e}}$ and $\hat{T}_{\mathrm{N}}$ refers to the electronic and nuclear kinetic energies (Eqs. 3 and 4), respectively, $\hat{V}_{\mathrm{eN}}$ is the attractive electron–nucleus potential energy (Eq. 5), and $\hat{V}_{\mathrm{ee}}$ and $\hat{V}_{\mathrm{NN}}$ represent the repulsive electron–electron (Eq. 6) and nucleus–nucleus potential energies (Eq. 7), respectively.

$$\hat{T}_{\mathrm{e}} = -\sum_{i} \frac{1}{2} \nabla_i^2 \tag{3}$$

$$\hat{T}_{\mathrm{N}} = -\sum_{A} \frac{1}{2M_A} \nabla_A^2 \tag{4}$$

$$\hat{V}_{\mathrm{eN}} = -\sum_{i} \sum_{A} \frac{Z_A}{r_{iA}} \tag{5}$$

$$\hat{V}_{\mathrm{ee}} = \sum_{i} \sum_{j>i} \frac{1}{r_{ij}} \tag{6}$$

$$\hat{V}_{\mathrm{NN}} = \sum_{A} \sum_{B>A} \frac{Z_A Z_B}{r_{AB}} \tag{7}$$

Capital letters (*A, B*) denote the nuclei and lowercase letters (*i, j*) the electrons. Therefore, M_A is the nuclear mass, Z_A the atomic number of atom *A*, r_{iA} the distance between electron *i* and nucleus *A*, r_{ij} the distance between electrons *i* and *j*, r_{AB} the distance between nuclei *A* and *B*, and the Laplacian operator $\left(\nabla^2\right)$ implies the sum of second derivatives with respect to the Cartesian coordinates of electrons and nuclei. Eqs. 3–7 are written in atomic units (a.u.).

From the expression of the Hamiltonian, it can be inferred that the wavefunction must contain information about all the electron and nuclear coordinates leading to a very complex expression. To alleviate the complexity of the wavefunction and to be able to solve the Schrödinger equation in molecular systems, the Born–Oppenheimer (BO) approach, also called adiabatic approximation, is generally used. This approximation relies on the separation of the nuclear and electronic wavefunctions (Eq. 8) as a product of independent functions due to the timescale difference of the nuclear and electronic motions; that is, the nuclear and electronic motions are treated separately since electrons are much faster than nuclei and, therefore, it is reasonable to assume that the electrons are moving in an electrostatic potential of fixed nuclei.

$$\Psi(r_i, R_A) = \Psi_{\mathrm{nuc}}(R_A)\Psi_{\mathrm{el}}(r_i) \tag{8}$$

The BO approach neglects the nuclear kinetic energy of the Schrödinger equation and the equation can be solved using only the Hamiltonian terms that

imply electrons ($\hat{H}_{\text{el}} = \hat{T}_{\text{e}} + \hat{V}_{\text{eN}} + \hat{V}_{\text{ee}}$) and the electronic wavefunction (Ψ_{el}), obtaining the electronic energy E_{el} (Eq. 9). Finally, the repulsion potential energy between nuclei is added to the electronic energy in order to obtain the total energy at a fixed position of the nuclei (Eq. 10).

$$\hat{H}_{\text{el}}\Psi_{\text{el}} = E_{\text{el}}\Psi_{\text{el}} \tag{9}$$

$$E_{\text{BO}} = E_{\text{el}} + V_{\text{NN}} \tag{10}$$

3.1.2 Hartree–Fock Method

The Hartree–Fock (HF) method[92,93] is likely to be the simplest approach that allows to approximately solve the electronic Schrödinger equation for an *N*-electrons system. The first approach assumed by the HF method is that the wavefunction can be written as a Slater determinant, which is defined as an antisymmetrized product of monoelectronic wavefunctions called spin-orbitals (ψ_i). The second approximation consists in estimating the electron-electron potential energy as the interaction of one electron with an average electron distribution created by the rest *N*-1 electrons. That approximation makes the HF method a feasible approach for the treatment of many-electron systems transforming the complex Schrödinger equation in a set of pseudo-eigenvalue monoelectronic equations (Eq. 11), in which the Hamiltonian is replaced by a one-electron operator known as Fock operator (Eq. 12).

$$\hat{f}(i)\psi_i = \varepsilon_i\psi_i \tag{11}$$

$$\hat{f}_i = h_i + \sum_j (\hat{J}_{ij} - \hat{K}_{ij}) \tag{12}$$

In Eq. 11, $\hat{f}(i)$ denotes the Fock operator acting on electron *i* and ε_i is the one-electron energy of the spin-orbital ψ_i. Eq. 12 decomposes $\hat{f}(i)$ in other operators. h_i is the core Hamiltonian (Eq. 13) that includes the electronic kinetic energy and the electron–nucleus potential energy. $\hat{J}_{ij}$ and $\hat{K}_{ij}$ correspond to the Coulomb and exchange operators (Eq. 14 and 15), respectively. The latter emerges as consequence of the antisymmetric character of the electronic wavefunction with no classical homologue.

$$\hat{h}_i = -\frac{1}{2}\nabla_i^2 - \sum_A \frac{Z_A}{r_{iA}} \tag{13}$$

$$\hat{J}_{ij}\psi_i = \left[\int \psi_j^*(r_2)\frac{1}{r_{12}}\psi_j(r_2)dr_2\right]\psi_i(r_1) \tag{14}$$

$$\hat{K}_{ij}\psi_i = \left[\int \psi_j^*(r_2)\frac{1}{r_{12}}\psi_i(r_2)dr_2\right]\psi_j(r_1) \tag{15}$$

The main problem of the HF method is to find the spin-orbitals that minimize the energy of the *N*-electrons system according to the variational principle. Therefore, the total HF energy is the sum of the spin-orbital energies but without double-counting the electron–electron interactions (Eq, 16).

$$E_{\mathrm{HF}} = \sum_i h_i + \frac{1}{2}\sum_i\sum_j (J_{ij} - K_{ij}) = \sum_i \varepsilon_i - \frac{1}{2}\sum_i\sum_j (J_{ij} - K_{ij}) \tag{16}$$

In practice, the spin-orbitals ψ_i are built as a linear combination of atomic orbitals (ϕ_μ) (Eq. 17), which are usually represented by a basis set of known functions.

$$\psi_i = \sum_\mu c_{\mu i}\phi_\mu \tag{17}$$

The introduction of a set of known basis functions allows the HF equations to be written in a matrix representation (Eq. 18), which is easily to solve it. In Eq. 18, **F** is the matrix representation of the Fock operator, **C** is the eigenvectors matrix that contains the linear combination coefficients $c_{\mu i}$, **ε** is the eigenvalues matrix that includes the orbital energies and **S** is the overlap matrix whose elements are defined as $S_{ij} = \int \psi_i^*(r_1)\psi_j(r_1)dr_1$. Eq. 18 is known as the Roothaan–Hall equation giving rise to the restricted (spin-orbitals of different spin share the same spatial function) formalism of the HF method. The HF method is solved iteratively (Figure 8) and the procedure is known as the self-consistent field (SCF) process. The HF method can be generalized, splitting both spins, in the unrestricted formalism by using the coupled Pople–Nesbet equations[94] (Eq. 19 and Eq. 20).

$$\mathbf{FC} = \mathbf{SC\varepsilon} \tag{18}$$

$$\mathbf{F}^\alpha\mathbf{C}^\alpha = \mathbf{SC}^\alpha\boldsymbol{\varepsilon}^\alpha \tag{19}$$

$$\mathbf{F}^\beta\mathbf{C}^\beta = \mathbf{SC}^\beta\boldsymbol{\varepsilon}^\beta \tag{20}$$

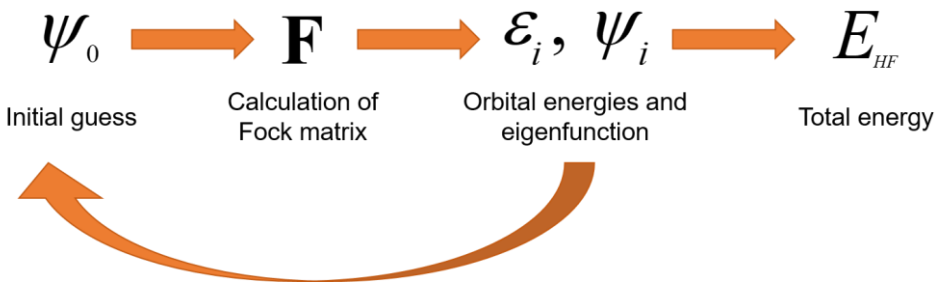

Figure 8. Scheme of the iterative SCF process used to solve the HF equations.

The main limitation of the HF method is the lack of information about the instantaneous electron–electron repulsion (known as electronic correlation). The computational cost of the HF method scales with the fourth power of the number of electrons (N^4) and can be reduced to $N^{2.5}$ by numerical simplifications. The HF approach is not generally used to compute the ground state energy by itself since other approaches as the density functional theory exhibit the same computational scaling but, at the same time, includes electronic correlation (see Section 3.1.3). Notwithstanding, the HF method is a good starting point for more advanced methods (*e.g.*, post-HF methods). The concepts already exposed for the HF approach indeed facilitate the understanding of other methodological approaches that will be explained along this Thesis.

3.1.3 Density Functional Theory

Quantum chemical methods based on solving the Schrödinger equation are based on obtaining the wavefunction that contains all the information about the system and, therefore, can be used to calculate any physical observable. For

instance, the expectation value of the energy, calculated as the expectation value of the respective operator (Eq. 21).

$$\langle E \rangle = \langle \Psi | \hat{H} | \Psi \rangle = \int \Psi^* \hat{H} \Psi dr_1 dr_2 ... dr_N \tag{21}$$

An alternative approach to the wavefunction-based methods is the Density Functional Theory (DFT) approach based on the two Hohenberg–Kohn theorems that can be stated as follows:

1. *The external potential, and hence the total energy, is a unique functional of the electron density ($\rho(r)$).*
2. *The ground state energy can be obtained variationally: the density that minimizes the total energy is the exact ground state density.*

Both theorems present important implications. The most important is that the energy can be obtained from the electronic density (Eq. 22); *i.e.*, the energy and the density are related through a unique and universal functional. However, the Hohenberg–Kohn theorems do not provide the mathematical expression for the universal energy functional. As a last corollary, once the energy functional is known, the density of the ground state can be obtained using the variational principle by minimizing the energy.

$$\langle E \rangle = E[\rho] \tag{22}$$

The first ideas for building up the electronic density functional were based on its separation in functionals associated to different energy terms (Eq. 23), as the kinetic energy (E_T), the nucleus–electron potential energy (E_V), the classical Couloumbic electron–electron repulsion (E_J), the electron–electron exchange energy (E_K) and the correlation energy (E_C), which tries to take into account all the quantum effects missed in the previous terms. Although the

expressions for the E_V and E_J functionals can be derived from classical electrostatics (Eq. 24 and 25), no analytic expressions were available for the E_T, E_K and E_C functionals.

$$E[\rho] = E_T[\rho] + E_V[\rho] + E_J[\rho] + E_K[\rho] + E_C[\rho] \tag{23}$$

$$E_V[\rho] = -\sum_A Z_A \int \frac{\rho(\mathbf{r})}{|R_A - r|} d\mathbf{r} \tag{24}$$

$$E_J[\rho] = \frac{1}{2} \iint \frac{\rho(\mathbf{r}_i)\rho(\mathbf{r}_j)}{|\mathbf{r}_i - \mathbf{r}_j|} d\mathbf{r}_i d\mathbf{r}_j \tag{25}$$

Up to now, density functionals based on the uniform non-interacting electron gas[95] have shown to be quite inaccurate for most of quantum chemistry problems. Even though the approach provided good energy estimations in some cases,[96] it presents fundamental errors, for instance, atoms do not bind to form molecules.[97]

The first practical approach to compute molecular properties in the DFT framework came with the approximation developed by Kohn and Sham. The Kohn–Sham (KS) method consists in building one-electron molecular orbitals as a linear combination of atomic orbitals (similar to the HF method) and computing the exact kinetic energy as it does the HF method. The KS approach leads to an equation analogous to the HF equations (Eq. 11 and 12), with the difference that the KS equation (Eq. 26) presents an extra term that corresponds to the combined exchange–correlation functional (E_{XC}). The E_{XC} functional is computed from the one-electron KS orbitals according to Eq. 27, where n_i is the orbital occupation number.

$$\left[-\frac{1}{2}\nabla_i^2 + \sum_A \frac{Z_A}{\left|\mathbf{R_A} - \mathbf{r}\right|} + \sum_j \int \frac{\left|\psi_j\left(\mathbf{r_j}\right)\right|^2}{\left|\mathbf{r_i} - \mathbf{r_j}\right|} d\mathbf{r_j} + \frac{\delta E_{XC}\left[\rho\right]}{\delta\rho} \right] \psi_i(\mathbf{r_i}) = \varepsilon_i \psi_i(\mathbf{r_i}) \quad (26)$$

$$\rho(r) = \sum_i n_i \left|\psi_i(r)\right|^2 \quad (27)$$

The KS method is widely used in quantum chemistry for practical purposes. As it is based on the HF machinery, it presents a similar computational scaling, and can take advantage of the same numerical approximations to alleviate the computational cost. Additionally, the use of orbitals allows to compute the orbital-dependent observables in the same way as in HF or post-HF methods. However, it still holds one relevant shortcoming: the exchange–correlation functional remains undefined. Over the last two decades, the specialized scientific community has focused on the design of different exchange–correlation functionals.

3.1.3.1 Hierarchy rung of functionals

As mentioned above, a current challenge in DFT is the development of exchange–correlation functionals with a good performance. The first approach was that developed by Thomas and Fermi for the uniform gas of electrons in which the E_{XC} functional only depends on the local density at each point of the space ($E_{XC}[\rho(r)]$). An improvement was the general gradient approximation (GGA), in which the E_{XC} functional depends not only on the local density but

also on its gradient ($E_{XC}[\rho(r),\nabla\rho(r)]$). Among GGA-based density functionals, the Perdew–Burke–Ernzerhof (PBE) functional[98] is one of the most representative. The next level in sophistication of E_{XC} improvements was to add a dependence with the non-interacting kinetic energy density to the GGA formalism leading to the meta-GGA functionals.[99]

A further correction to the GGA and meta-GGA functionals is the incorporation of an exact portion of exchange (taken from the HF theory) to the density functional expression, giving rise to the popular and widely used hydrid density functionals. The most popular hybrid GGA functional is the B3LYP functional that combines the Becke's three-parameters exchange functional (B3),[100] with the Lee–Yang–Parr (LYP) correlation functional.[101] Another popular hybrid functional is that known as PBE0, which derives from the GGA PBE functional with a 25% of exact exchange.[102] Some representative examples of hybrid meta-GGA functionals are the Minnesota functionals such as M06[103], M06-2X[104] and MO6-HF.[105]

In the last years, new series of functionals focusing on specific purposes and applications have emerged, among which the long-range corrected (LC) or range-separated functionals are especially relevant. The LC correction is needed because at long distances the electron correlation is less important than the HF exchange.[106,107] The correction was initially proposed by Hirao for GGA functionals,[108,109] and consists in using the pure DFT exchange at short distances and switching gradually, from a certain distance $1/\omega$, to a pure HF exchange by employing the standard error function (erf) (Eq. 28). Representative examples of LC density functionals are the ωB97X[110] and LC-ωPBE functionals.[111]

$$\frac{1}{r} = \frac{1-\mathrm{erf}(\omega r)}{r} + \frac{\mathrm{erf}(\omega r)}{r} \tag{28}$$

The LC functionals introduces a new parameter (ω) whose value is in principle undefined. Standard values of ω, which proved to give good estimates for ground state properties[112,113] or even for excited states, are found to be in the 0.3–0.5 Bohr^{-1} range.[114] Nevertheless, the most desirable use of the LC correction is with an optimal tuning of the ω parameter.[115–119] The optimal procedure for ω is system-dependent and evaluated in such a way that the HOMO energy matches the ionization potential for the neutral and anion species (Eq. 29 and 30)[120,121] by minimizing either the error function J_1 (Eq. 31)[112,113] or the error function J_2 (Eq. 32).[120,121]

$$T_1(\omega) = \varepsilon^{\omega}_{HOMO}(N) + E^{\omega}(N-1) - E^{\omega}(N) \tag{29}$$

$$T_2(\omega) = \varepsilon^{\omega}_{HOMO}(N+1) + E^{\omega}(N) - E^{\omega}(N+1) \tag{30}$$

$$J_1(\omega) = \sqrt{T_1^2(\omega) + T_2^2(\omega)} \tag{31}$$

$$J_2(\omega) = \left|T_1(\omega)\right| + \left|T_2(\omega)\right| \tag{32}$$

This correction was generalized for hybrid functionals[122] (Eq. 33) by introducing two additional parameters α and β, where α can be set as the exact exchange contribution in the non-corrected hybrid functional, keeping $\beta = 1-\alpha$ to guarantee that the full Fock exchange exhibits an asymptotically correct behavior.[123]

$$\frac{1}{r} = \frac{1-[\alpha + \beta erf(\omega r)]}{r} + \frac{\alpha + \beta erf(\omega r)}{r} \tag{33}$$

Figure 9 displays the popular Perdew–Jacob's ladder showing the hierarchical density functional rungs. In the top of the ladder, double-hybrid density functionals are found. These functionals are built in a similar way to hybrid functionals with an extra correlation energy term that introduces information about the virtual orbitals from a second-order perturbation (PT2) theory.

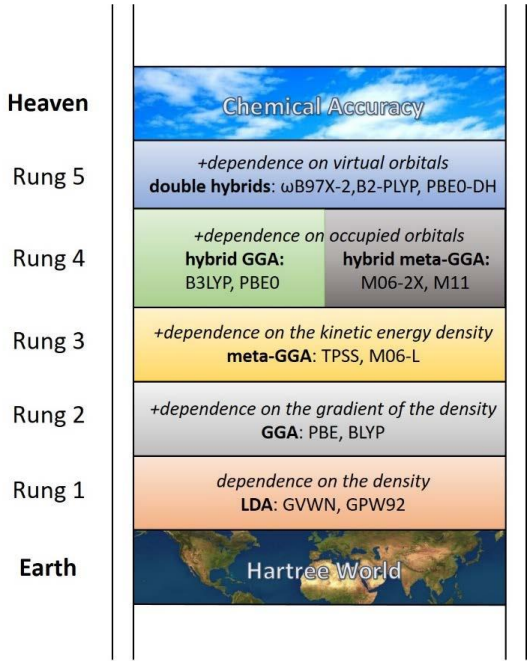

Figure 9. Perdew–Jacob's ladder of density functionals.[124] Figure extracted from Ref. 125.

3.1.3.2 Dispersion-corrected approximations for DFT

Dispersion forces are fundamental to describe the intermolecular interactions, especially when the interaction involves non-polar fragments as is the case for π–π stacking or C–H···π interactions. These forces originate from long-range

instantaneous and correlated fluctuations of the electron density and have a non-local character. However, most of the density functionals present a local or semi-local dependence on the electronic density, and fail in describing correctly non-covalent interactions. Only a minority of meta-GGA functionals (M06 or similar Minnesota functionals) include into the functional expression a treatment for dispersion forces.[103–105] To amend this situation, different approximations added to standard DFT functionals to capture van-der-Waals interactions have been proposed over the last years.[126–129] Among them, the most popular approach to include dispersion forces in most functionals is the Grimme's dispersion correction (D2, D3 or D4),[130,131] which consists in an atom-pairwise stabilizing energy (Eq. 34 for the D3 correction) that is added *a posteriori* to the KS energy.

$$E_{disp} = -\sum_{n=6,8} s_n \sum_{i=1}^{N_{At}-1} \sum_{j>i}^{N_{At}} \frac{C_{n,AB}}{(r_{AB})^n} f_{damp}(r_{ij}) \tag{34}$$

In Eq. 34, s_n are parameters fitted for each density functional, $C_{n,AB}$ is the *n*th order dispersion coefficient for the AB atom pair, r_{AB} is the distance between atoms A and B and $f_{damp}(r_{ij})$ is a damping function that depends on the distance and attenuates the correction at short distances.[131]

3.1.4 Excited states

3.1.4.1 Configuration interaction singles (CIS)

The first approach to compute excited-state energies arises from the post-HF philosophy known as configuration interaction (CI). CI is based on the expansion of the wavefunction into a linear combination of the HF determinant

together with Slater excited determinants (Eq. 35), which can be singly excited (Φ_i^a), doubly excited (Φ_{ij}^{ab})and so on. In Eq. 35, *i* and *j* denote occupied orbitals according to the HF wavefunction whereas *a* and *b* are virtual orbitals. c_0, c_i^a and c_{ij}^{ab} are the expansion coefficients of the CI wavefunction.

$$\Psi_{CI} = c_0\Phi_{HF} + \sum_{i}^{occ}\sum_{a}^{virt} c_i^a\Phi_i^a + \sum_{i,j}^{occ}\sum_{a,b}^{virt} c_{ij}^{ab}\Phi_{ij}^{ab} + \ldots \quad (35)$$

Unfortunately, infinite determinants cannot be included in the expansion and, thus, truncation at some degree is required for practical purposes, leading to the family of truncated CI methods (CIS, CID, CISD, CISDT, etc.) according to the type of excitations that are taken into account (singles (S), doubles (D), triples (T), …). Although CI methods were conceived in its origin as a correction for the ground state, excited states can also be obtained as higher roots and eigenvectors of the CI Hamiltonian.

Among the different CI approximations, the CIS method (Eq. 36) is the first and more basic practical approach to describe excited states. Since single excitations do not couple with the HF Slater determinant, a CIS excited-state wavefunction can be formulated as

$$\Psi_{CIS} = \sum_{i}^{occ}\sum_{a}^{virt} c_i^a\Phi_i^a \quad (36)$$

The most intuitive way to build the CI Hamiltonian matrix is the use of the Slater–Condon rules,[132] which provide the expressions of the operator matrix elements for a multi-determinant expansion. Then a further diagonalization of the Hamiltonian matrix is performed to obtain the energies of the excited states

and the c_i^a coefficients, generally employing the Davidson-based diagonalization algorithm.[133,134]

3.1.4.2 Time-dependent density functional theory

Similar to CIS, which is the most popular method based on monoexcitations of the HF wavefunction, the most widely used approximation to compute excited states within the DFT framework is the Time-Dependent Density Functional Theory (TDDFT),[135] which is an extension of DFT that only includes monoexcitations. The TDDFT approach replaces the many-body time-dependent Schrödinger equation by a set of coupled, single-particle, time-dependent equations. TDDFT is rooted in the generalization of the first Hohenberg–Khon theorem carried out by Runge and Gross establishing that *in a single component system the presence of a scalar field can be accounted as a time dependence on the external potential* (the nucleus–electron potential energy). The Runge–Gross theorem implies that at any time, the electronic density uniquely determines the external potential.

Similar to ground-state DFT, TDDFT also requires a mathematical form for the exchange–correlation functional. In practice, the adiabatic exchange–correlation approximation is assumed, allowing to use the same functional as that for the ground state, although the excited states are not usually taken into account during the functional parameterization process.

Within TDDFT, linear-response TDDFT is the most popular version of TDDFT. The linear-response approach consists in taking only the first perturbation term, which is valid for small perturbations.[136,137] Therefore, the

time variation of the system depends only on the ground-state electron density, which allows the use of the DFT properties. In practice, most of the quantum chemistry codes employs the linear-response TDDFT formalism with the non-Hermitian Casida's equation (Eq. 37), where elements of the **A** and **B** matrices are defined in Eqs. 38 and 39, respectively. ω is the excitation energy, and **X** and **Y** are the excitation and deexcitation vectors, respectively, that correspond to the eigenvectors of the Casida's equation.

$$\begin{pmatrix} \mathbf{A} & \mathbf{B} \\ \mathbf{B}^* & \mathbf{A}^* \end{pmatrix} \begin{pmatrix} \mathbf{X} \\ \mathbf{Y} \end{pmatrix} = \omega \begin{pmatrix} 1 & 0 \\ 0 & -1 \end{pmatrix} \begin{pmatrix} \mathbf{X} \\ \mathbf{Y} \end{pmatrix} \tag{37}$$

$$\begin{aligned} A_{ab,ij} = (\varepsilon_a - \varepsilon_i)\delta_{ab}\delta_{ij} + \int \psi_a^*(r_1)\psi_b^*(r_2)\frac{1}{r_{12}}\psi_i(r_1)\psi_j(r_2)dr_1dr_2 \\ + \int \psi_a^*(r_1)\psi_b^*(r_2)E_{XC}\psi_i(r_1)\psi_j(r_2)dr_1dr_2 \end{aligned} \tag{38}$$

$$\begin{aligned} B_{ab,ij} = \int \psi_a^*(r_1)\psi_j^*(r_2)\frac{1}{r_{12}}\psi_i(r_1)\psi_b(r_2)dr_1dr_2 + \\ \int \psi_a^*(r_1)\psi_j^*(r_2)E_{XC}\psi_i(r_1)\psi_b(r_2)dr_1dr_2 \end{aligned} \tag{39}$$

If the **B** matrix is neglected, Eq. 37 simplifies to a hermitian problem with just the **X** vectors as the solution. This approximation is called the Tamm–Dancoff approximation (TDA). This time-dependent formalism can be also applied to the HF theory leading to the less-common time-dependent Hartree–Fock (TDHF) approach, within which the TDA variant would coincide with the CIS method. Finally, it should be noted that TDDFT presents a problem with the description of charge-transfer (CT) excited states. In particular, TDDFT is not able to provide the correct long-range behavior, according to the Mulliken's rule ($E_{CT} = IP - EA - 1/r$).[138] This wrong behavior is due to the self-

interaction error inherent to DFT, which is minimized by using optimally-tuned long-range functionals.[115–119]

3.1.5 Basis sets

The computed molecular orbitals obtained from either the HF or the KS method are described as a linear combination of atomic orbitals (Eq. 17). The atomic orbitals used are just mathematical functions that reproduce the physical magnitudes of the electrons in the potential created by the isolated nucleus, such as atomic orbitals energies, angular momenta and density distribution functions. Computationally, atomic orbitals are usually described by two type of mathematical expressions: Slater-type orbitals (STOs) (Eq. 40) or Gaussian-type orbitals (GTOs) (Eq. 41)

$$\varphi_{n,l,m_l}^{STO} = N\xi r^{n-1} e^{-\xi r} Y_{l,m_l} \tag{40}$$

$$\varphi_{n,l,m_l}^{GTO} = N\xi r^{n-1} e^{-\xi r^2} Y_{l,m_l} \tag{41}$$

where N is the normalization constant, Y_{l,m_l} are the spherical harmonics and ξ is a variational parameter related to the radial compression of the function. Although there is only a single difference between both type of functions in the exponential part, they present a quite different performance for intergration. On one hand, STOs reproduce accurately the electronic behavior around the nuclear region because they are obtained from solving exactly the Schrödinger equation for hydrogen-like atoms. However, the use of STO functions is computationally inefficient since analytical expressions are not available for the two-electron integrals involving multiple centers. On the other

hand, GTOs exhibit a less steeped behavior at the nuclear region compared to STOs and decay quickly to zero. Nevertheless, the great advantage of GTOs is that there are available analytical expressions for the two-electron integrals allowing an incredible speed up of the calculations in comparison with STOs. To mitigate the GTOs inherent deficiency, each atomic orbital ϕ_i is described as an expansion of several GTO functions (Eq. 42), without compromising the computational cost. This is the reason why GTO functions are more popular to build most of the basis sets.

$$\phi_i = \sum_j c_{ij}\varphi_j \tag{42}$$

Currently, a wide variety of basis set (atomic orbitals sets) are available in the quantum-chemistry codes; for example, the well-known Pople's basis sets,[139,140] the Dunning's correlation-consistent basis sets[141] or the Aldrich's basis sets.[142]

3.1.6 Solvation models

Quantum chemistry methods only take into account the nuclei and electrons in vacuum, which is a reasonable approach to address gas-phase chemistry. However, many phenomena in chemistry take place mainly in solution, where the solvent molecules play an important role in many processes. A first approach to account for solvent effects is to include explicit solvent molecules in the system. However, this is usually an unpractical approach owing to the large number of solvent molecules (and computational cost) necessary to reproduce the solvent macroscopic properties. Alternatively, implicit models

have been developed with the aim of capturing the most important solvent effects over the solute molecules with a small increase in computational cost.[143] The main idea of implicit models is to describe the solvent by a continuum characterized by some macroscopic properties, such as the dielectric constant and the molecular size. Thus, in most implicit models, the solvation energy (ΔE_{sol}), defined as the energy difference between the system in a solvent and in gas phase, takes into account three energetic terms (Eq. 43). The first term is the energetic cost of creating a cavity for the solute in the solvent (ΔE_{cav}). The second term is the non-electrostatic interactions between the solute and the solvent, mainly van-der-Waals interactions (ΔE_{vdW}). These two energetic components are usually computed through parametric formulas where the parameters are solvent-dependent. The last solvation energy term is the electrostatic interaction between the solute and the solvent (ΔE_{elec}). This term is computed by a reaction field, where the continuum polarizes the solute and the solute the continuum. Therefore, ΔE_{elec} is solved by using an iterative procedure.

$$\Delta E_{sol} = \Delta E_{cav} + \Delta E_{VdW} + \Delta E_{elec} \quad (43).$$

The different reaction fields used to calculate ΔE_{elec} give rise to the different continuum solvent models. Among them, the most popular are the Polarizable Continuum Model (PCM)[144] and the Solvation Model Based on Density (SMD).[145]

Another relevant application of the continuum models is the simulation of optical properties in solution, such as the absorption and emission spectra, in which the solvent plays a direct role giving rise to solvatochromism.[146] The most popular implementation is the linear-response PCM coupled to TDDFT calculations. The linear-response PCM approach is a suitable approximation for electronic transitions that imply a small change in the electron density but is not appropriate for states where there is a large electronic rearrangement (*i.e.*, for CT excited states). This occurs because the dynamical response taken into account through the transition density is almost null in this kind of CT excitations.[147] To solve the specific problems associated to CT excited states, state-specific formulations have been developed as efficient alternatives. For instance, the corrected linear response[148] computes the solvent dynamical response from the density difference between the ground and the excited state. A further improvement is the iterative state–specific (SS) approach,[149] in which the iterations are performed for the total excited-state density and, therefore, the ground state contribution is also recalculated by iterating the KS orbitals. The SS approach is recommended to simulate those properties that occur in a timescale where the solvent is totally relaxed (e.g., emission spectra). It should be emphasized that the SS approach can be used in the *non-equilibrium* or *equilibrium* forms, the difference between them being to take into account just the fast polarization (*non-equilibrium*) or both the fast and slow polarization (*equilibrium*). This is a key difference in describing the solvent role in the simulation of different optical processes as absorption spectra (only fast polarization) or emission spectra (fast and slow polarization).[147]

3.1.7 Semiempirical methods

The high computational cost of first-principles methods is due to the large number of integrals that must be calculated, especially two-electron integrals. Thus, semiempirical methods acquire relevance since they allow to compute large systems in a simplified first-principles-like way. Semiempirical methods are generally based on HF or DFT approaches in which simplifications are introduced to alleviate the computational cost.

The oldest HF-based semiempirical methods are those incorporating the Zero-Differential Overlap (ZDO) approach based on neglecting all the two-center two-electron integrals. Models like the CNDO (Complete Neglect of Differential Overlap) or the INDO (Intermediate Neglect of Differential Overlap) methods[150] belong to the ZDO scheme. A more recent approach is the Neglect of Diatomic Differential Overlap (NDDO) integral approximation that adds all two-center integrals. The widely used MNDO (Modified Neglect of Differential Overlap),[151] AM1 (Austin Model 1)[152] and PM3 (Parametric Model number 3)[153] methods belong to the NDDO family. More recently, new semiempirical methods that do not neglect the overlap like the PM7 method have emerged.[154] PM7 is an improvement of the PM6 method but using a modified NDDO.[155] Importantly, and unlike its predecessors, PM7 incorporate energy terms that implicitly account for intermolecular forces (H-bonds and dispersion interactions).

In the last years, semiempirical methods based on DFT have emerged. Two representative models are the Tight-Binding DFT (DFTB) method[156–159] and the Grimme's GFN-xTB method.[160,161] Both methods originate from the DFT philosophy but including simplifications (*e.g.*, they use a minimal basis set and

parameterized two-electron potentials). DFTB relies in a Taylor expansion of the energy with the electronic density and several truncation schemes of the expansion are considered, leading to the approximations known as DFTB, DFTB2 or DFTB-SCC and DFTB3. The main difference between these three approximations is the number of energy operator terms taken into account. Therefore, the most basic DFTB approach leads to a robust method that implies solving a Hückel-like secular equation system. In DFTB2, a dependence of the energy with the atomic charges is introduced, and the energy and atomic charges have to be obtained iteratively since the atomic charges depend on the orbitals vectors. The inclusion of the iterative procedure on the charges is known as self-consistent charges (SCC). Finally, the DFTB3 is quite similar to DFTB-SCC but including also a dependence of the energy with its derivative with respect to the atomic charges. It should be stressed that DFTB presents, in general, the same weaknesses of standard DFT, such as the incorrect treatment of dispersion interactions. Therefore, dispersion corrections available for DFT (*e.g.*, Grimme's D3 correction) have been also adapted for the DFTB variants.

GFN-xTB is the semiempirical approach most used in this Thesis. The GFN-xTB Hamiltonian matrix elements are computed in a similar way to the self-consistent DFTB-based approximations (DFTB-SCC and DFTB3). Therefore, the GFN-xTB method requires an iterative process to obtain the energy of the system. The main difference between the standard DFTB and GFN-xTB methods is the mathematical expression of the energy terms in the Hamiltonian. These energy terms are parameterized in order to be more general and more accurate corrections for hydrogen bonding and dispersion forces have been included in the Hamiltonian.

3.1.8 Molecular mechanics

Molecular mechanics is an approach based on classical mechanics to model molecular systems. It is a computationally-attractive methodology that allow to study large systems composed of thousands of atoms (*e.g.*, large molecular assemblies or biological systems like proteins). In molecular mechanics, the potential energy is calculated using a force field, where the energy is computed as a sum of individual terms (Eq. 44) either accounting for intramolecular degrees of freedom (bond lengths, bond angles and dihedral angles) or non-covalent interactions such as electrostatic or van-der-Waals interactions (vdW).

$$E = E_{\text{bond}} + E_{\text{angle}} + E_{\text{dihedral}} + E_{\text{electrostatic}} + E_{\text{vdW}} \tag{44}$$

The bond and angle energy terms are usually computed from harmonic-oscillator-type quadratic functions (Eq. 45 and 46), where K_i corresponds to the harmonic oscillator force constants and $r_{i,eq}$ and $\varphi_{i,eq}$ are the equilibrium bond lengths and angles, respectively.

$$E_{\text{bond}} = \sum_{i}^{N_{\text{bonds}}} K_i (r_i - r_{\text{i,eq}})^2 \tag{45}$$

$$E_{\text{angle}} = \sum_{i}^{N_{\text{angles}}} K_i (\varphi_i - \varphi_{\text{i,eq}})^2 \tag{46}$$

The dihedral energy term is usually computed by using trigonometric functions taking into account implicitly the periodicity of the degree of freedom. Although each force field may vary in the dihedral energy expression, a

common expression is written in Eq. 47, where n is the multiplicity of the function and δ_i is a phase shift of the dihedral angle ϕ_i.

$$E_{\text{dihedral}} = \sum_{i}^{N_{\text{Dihedral}}} K_i[1+\cos(n\phi_i - \delta_i)] \tag{47}$$

The most sophisticated force fields include additional terms regarding internal degrees of freedom such as improper torsional terms, which are important for the correct description of aromatic rings, or cross-terms, which account for the coupling between the degrees of freedom as bond lengths and bond angles.

The electrostatic term is usually computed using a classical electrostatic potential (Eq. 48), where ε is the dielectric constant of the medium, q_A and q_B are the atomic charges of atoms A and B, and r_{AB} is the distance between the atom pair. The vdW term is usually calculated by using a Lennard–Jones potential (Eq. 49), where r_0 is the distance corresponding to the potential minimum and σ is the energy depth of the potential.

$$E_{\text{electrostatic}} = \sum_{A,B} \frac{q_A q_B}{\varepsilon r_{AB}} \tag{48}$$

$$E_{\text{vdW}} = \sum \sigma \left[\left(\frac{r_0}{r} \right)^{12} - 2 \left(\frac{r_0}{r} \right)^{6} \right] \tag{49}$$

3.1.9 Molecular dynamics

Molecular dynamics consists on the time-dependent simulation of the movement of atoms and molecules using the classical Newton's equations of motion, where the energies and, therefore, the forces are usually calculated by

molecular mechanics. From a practical point of view, the Verlet algorithm (Eq. 50) is the most popular implementation to solve the equations of motion.

$$\mathbf{r}_i(t+\Delta t) = 2\mathbf{r}_i(t) - \mathbf{r}_i(t-\Delta t) + \frac{\mathbf{F}_i(t)}{m_i}\Delta t^2 \tag{50}$$

In this equation, $\mathbf{r}_i$ is the position vector, m_i is the particle mass and **F** the force vector. In the last years, it is common to use molecular dynamics by computing the electronic energy and the forces using DFT or semiempirical (DFTB or GFN–xTB) methods. This approximation is known as semi-classical Born–Oppenheimer molecular dynamics (BOMD). BOMD generally focuses on the nuclear motion in the electronic ground state with no dependence on excited states. Other semi-classical approximations such as surface-hopping or Ehrenfest molecular dynamics take into account the electronic excited states and allow the transition between different electronic states being suitable for photophysics and photochemistry problems. Nevertheless, it should be stressed that, although the electronic energy is computed by means of electronic structure methods, the nuclear motion is completely classical and quantum effects as tunneling are neglected.

3.1.10 Quantum dynamics: Multi-configurational time-dependent Hartree

The Multi-Configurational Time-Dependent Hartree (MCTDH)[162,163] approximation is a method to solve the time-dependent Schrödinger equation for multidimensional systems. Therefore, the wavefunction in MCTDH includes both electron and nuclear parts quantum mechanically, and their time-

evolution is computed according to the time-dependent Schrödinger equation. The counterpart of using this methodology is that standard MCTDH methods are only suitable for problems with a low dimensionality (up to 30 degrees of freedom) due to the huge memory scaling. Nevertheless, it is possible to run quantum dynamics with a larger dimensionality (up to hundreds of degrees of freedom) by using the multi-layer MCTDH (ML-MCTDH) variant.[164] Actually, the ML-MCTDH approach is very useful using model Hamiltonians, such as the vibronic-coupling Hamiltonians, which are very helpful to get insight into the properties of real systems.

In the context of exciton transport, MCTDH is one of the best options to simulate exciton dynamics. The good performance is because exciton transport can be simulated using model Hamiltonians as the Holstein-Pierls Hamiltonian and, in this context, quantum phenomena (*e.g.*, coherences) can be relevant. Semiclassical approximations, such as surface hopping, have been used for exciton dynamics but they present serious problems dealing with coherences (over-coherences). In contrast, MCTDH does not present these kind of problems due to the quantum treatment of the nuclei.

3.2 Charge and energy transport

3.2.1 General Background

Charge and energy transport may be visualized as a redistribution of the charge and exciton density, respectively. In the literature, two limiting transport regimes to study the charge/exciton transport in organic semiconductors are generally invoked, the coherent or incoherent regime (Figure 10). To

distinguish the two regimes, two magnitudes (t_{tr} and t_{rel}) are introduced.[165] t_{tr} (Eq. 51) measures the timescale of the electronic movement, where *V* is the coupling matrix element, whereas t_{rel} (Eq. 52) denotes the timescale of the nuclear relaxation. ω_{rel} in Eq. 52 corresponds to the frequency of the effective normal mode that drives the electronic charge/energy transfer process.

$$t_{tr} = \frac{\hbar}{V} \tag{51}$$

$$t_{rel} = \frac{2\pi}{\omega_{rel}} \tag{52}$$

If $t_{tr} \ll t_{rel}$, the electronic redistribution is much faster than any nuclear configuration change.[166,167] Indeed, this condition is the basis of the adiabatic approximation. In this case, the delocalized adiabatic description (often ascribed to the coherent regime) is appropriate (Figure 10a). When the energy profile of the adiabatic potential energy surface (PES) along the effective vibrational coordinate takes a double-well potential shape due to a weak coupling interaction (Figure 11b), the transition probability can be computed using a non-adiabatic electron/exciton rate constant. However, in strongly coupled systems the PES takes a wide parabolic shape (Figure 11a) and the Arrhenius-like rate approximation is not suitable any more.

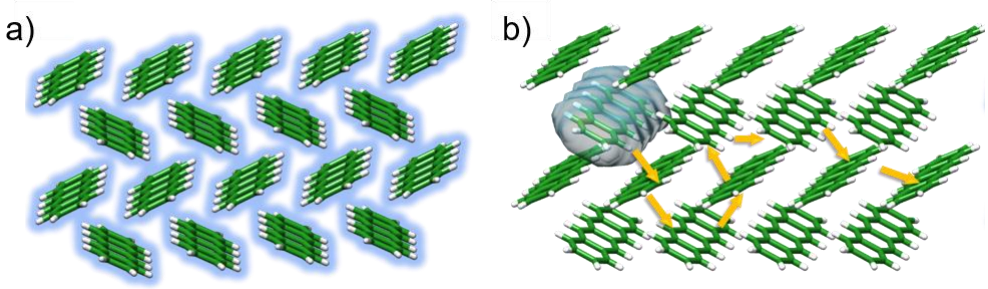

Figure 10. Scheme of the coherent (a) and incoherent (b) transport regimes.

If $t_{tr} \gg t_{rel}$, the nuclear relaxation is then faster than the electronic motion. In this context, the charge/exciton is generally localized and the charge/exciton migration can be seen as a sequence of random hopes from one molecular site to another (incoherent regime, Figure 10b). The incoherent regime is likely to be the most common transport regime for organic semiconductors. In this regime, the coupling matrix element *V* is usually rather small and, therefore, crossing between the potential energy surfaces (diabatic-like) might occur (Figure 11c).

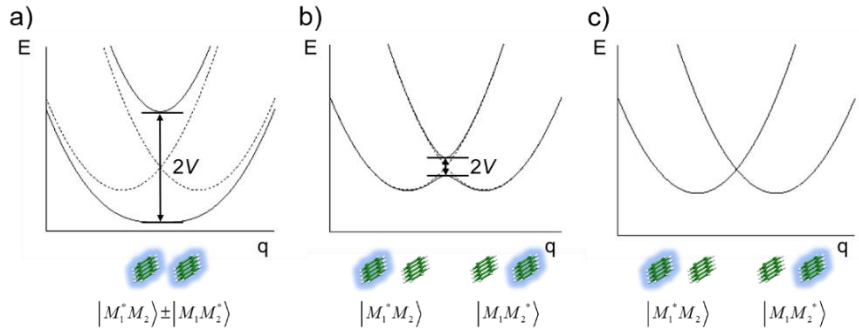

Figure 11. Representation of strongly coupled (a), weakly coupled adiabatic (b) and diabatic (c) potential energy surfaces. At the bottom, the delocalization of the charge/exciton in the minima of the PES is schematized.

Irrespective of the transport regime, the use of a diabatic representation of the electronic states involved in the transport process is generally convenient. However, electronic structure methods only provide an adiabatic representation since they work within the Born–Oppenheimer approximation. Adiabatic states are obtained from the diagonalization of the electronic Hamiltonian. However, a diagonal Hamiltonian implies null potential energy coupling (or static coupling) elements. Nevertheless, the dynamic couplings are not zero. These dynamic couplings are called non-adiabatic couplings since they are associated to the nuclear kinetic energy term and therefore are matrix elements that emerge beyond the Born–Oppenheimer approximation. The non-adiabatic couplings (V_{nad}) indicate the variation of the wavefunction with the nuclear motion (Eq. 53), and they are of great interest to describe non-radiative processes in photochemistry and photophysics because they modulate the non-radiative decay between electronic states along the PESs.

$$V_{\text{nad}} \propto \left\langle \psi_i \middle| \frac{\partial}{\partial R_A} \middle| \psi_j \right\rangle \tag{53}$$

In contrast to the adiabatic representation, the diabatic states are states with no change in its nature or wavefunction (*i.e.*, states with $V_{\text{nad}} = 0$). However, there is no a straightforward way to obtain a correct diabatic representation. In general, diabatic states (ψ_i^{DI}) are built as a linear combination of adiabatic states (ψ_j^{AD}) (Eq. 54).

$$\psi_i^{\text{DI}} = \sum_j C_{ij} \psi_j^{\text{AD}} \tag{54}$$

The most common strategy to find the coefficients C_{ij} is the use of diabatization schemes. Once the adiabatic-to-diabatic orthogonal transformation matrix **C** is determined, the diabatic and adiabatic Hamiltonians are easily connected by $\mathbf{H}^{\mathbf{DI}} = \mathbf{C}\mathbf{H}^{\mathbf{AD}}\mathbf{C}^{T}$ (diabatization), where the diagonal elements of $\mathbf{H}^{\mathbf{DI}}$ correspond to the diabatic energies and the off-diagonal elements to the electronic couplings (V_{ij}). Although there is not a unique adiabatic-to-diabatic transformation,[168] most diabatization schemes, particularly in the context of charge/energy transfer, aim to find the best unitary transformation matrix **C** (Eq. 54) that generates the closest diabatic states with respect to a set of reference states with a well-defined molecular property. Usually, the molecular property employed (transition dipole moment, charge population or exciton population) is localized in the diabatic representation.

3.2.2 Charge and energy transport in the coherent regime

As mentioned previously, when the electronic transition takes place in the same or shorter timescale than the nuclear motion, the charge/energy transport occurs beyond the incoherent regime. To simulate the transport in this regime, the computational modelling must take into account both the nuclear and electronic motions. Therefore, the most suitable approximations are those able to simultaneously account for the nuclear and electronic dynamics. For instance, the semiclassical quantum dynamics techniques (surface hopping or Ehrenfest) have been used to study the charge/exciton transport in organic semiconductors. However, when the size and dimensionality of the system allow it, full quantum dynamics simulations (*e.g.*, the MCTDH technique) are

recommended to avoid the deficiencies related to the classical description of the nuclei.

In the context of charge/exciton dynamics, nuclear motions are responsible for modulating the energy and electronic couplings of the electronic states. These electronic-vibration coupling effects (commonly known as Holstein and Peierls couplings, respectively) should be introduced in the model Hamiltonian for a proper description of the transport.[169] Nevertheless, all the relevant theoretical magnitudes to assess the efficiency of the charge/exciton transport are only estimated from the time evolution of the electronic wavefunction. For instance, exciton diffusion coefficients (D) are computed from the spread of the exciton wavefunction (the variance) over the molecular sites, and the exciton diffusion length (L) is calculated from the exciton diffusion coefficient and the exciton lifetime. D and L are the most important parameters to estimate the exciton transport efficiency because they are the observables that can be experimentally measured.

3.2.3 Charge and energy transport in the incoherent regime: rate constant expressions

As stated above, charge and energy transport processes in organic materials mostly occur in the incoherent regime. In this regime, the nuclear relaxation is faster than the electronic transitions and, therefore, the nuclei reach the thermal equilibrium before any electronic transfer event. Additionally, the electronic/excitonic coupling V_{ij} between the involved electronic states is small and can be accounted for as a perturbation. Under these conditions, the popular Fermi Golden rule (Eq. 55) would be a suitable approach to compute the

transition probability between the electronic states for the transfer (charge or energy) event. .[170,171] In this approach, the transition or rate constant k_{ij} depends exclusively on the square of the electronic/excitonic coupling V_{ij} and the density of states $\delta(E_j - E_i)$ in resonance between the initial (E_i) and final (E_j) states. However, computing the density of states is not always feasible and the Fermi Golden rule is not in general a practical expression to compute the transition rates. Nevertheless, it is the starting point to derive almost all the rates expressions available in the physical-chemistry literature.

$$k_{ij} = \frac{2\pi}{\hbar}\left|V_{ij}\right|^2 \delta(E_j - E_i) \tag{55}$$

In the high-temperature limit, *i.e.*, when the thermal energy exceeds the vibrational energy, vibrations can be treated classically. This classical approach is assumed to obtain the popular Marcus rate expression (Eq. 56), which was initially derived for the outer-sphere electron transfer between ions in solution.[172,173] The great achievement of the rate expression proposed by Marcus is that the density of states can be readily obtained because it depends on the adiabatic difference of Gibbs free energy (ΔG), the reorganization energy (λ) and the temperature (T). As explained below, ΔG and λ can be easily computed and T is a parameter. Another important feature of the Marcus expression is that the resulting rate takes the form of an Arrhenius-like expression where the activation energy is substituted by a function of ΔG and λ, which are much easier to compute.

$$k_{ij} = \frac{2\pi}{\hbar}\left|V_{ij}\right|^2 \frac{1}{\sqrt{4\pi\lambda k_B T}} \exp\left(-\frac{(\lambda + \Delta G)^2}{4\lambda k_B T}\right) \tag{56}$$

An alternative approach but quite similar to the Marcus rate expression is that developed by Bixon and Jortner (Eq. 57), known as the Marcus–Levitch–Jortner (MLJ) rate constant expression.[174] In this expression, the nuclear relaxation motion is split into classical and quantum contributions. This splitting relies on the fact that the normal modes coupling with the electronic processes in organic materials are usually high-frequency modes and the high-temperature limit is no longer valid. The low frequency modes and the environment modes continue to be treated classically. Expression 57 is similar to the Marcus expression with a few but important differences: 1) λ_c denotes the part of the reorganization energy treated classically and 2) S is the Huang-Rhys factor of the effective vibration with frecuency ω_{eff} used to compute the Franck–Condon integrals, $FCI_{\mathrm{nm}}(S)$, thus tunneling through the quantum mode is taken into account. Furthermore, the thermal Boltzmann distribution, denoted as $P_T(n)$, of the initial population of the different vibrational states is included.

$$k_{ij} = \frac{2\pi}{\hbar}\left|V_{ij}\right|^2 \frac{1}{\sqrt{4\pi\lambda_c k_B T}} \sum_n P_T(n) \sum_m \left|FCI_{nm}(S)\right|^2 \mathrm{e}^{-\frac{(\lambda+(m-n)\hbar\omega_{eff}+\Delta G)^2}{4\lambda_c k_B T}} \qquad (57)$$

In the following sections, the parameters required to evaluate k_{ij} for both Marcus and Marcus–Levitch–Jortner expressions are explained in detail.

3.2.4 Energy difference

As stated above, the Gibbs free energy difference (ΔG) is an important parameter required for the non-adiabatic electron/exciton transfer rate

constants. ΔG is usually substituted by the electronic energy difference (ΔE) because entropic effects are commonly negligible.[175,176] Concerning ΔE, there are two different scenarios: 1) the initial and final states involved in the transfer event are energetically degenerate ($\Delta G \sim \Delta E = 0$) or 2) an energy gap appears (Figure 12). The first scenario corresponds to transfer events between identical molecular systems ($M^+ + M \rightarrow M + M^+$), whereas the second situation occurs when the transfer process takes place between nonequivalent molecular systems (*e.g.*, in a donor–acceptor complex, $D + A \rightarrow D^+ + A^-$).

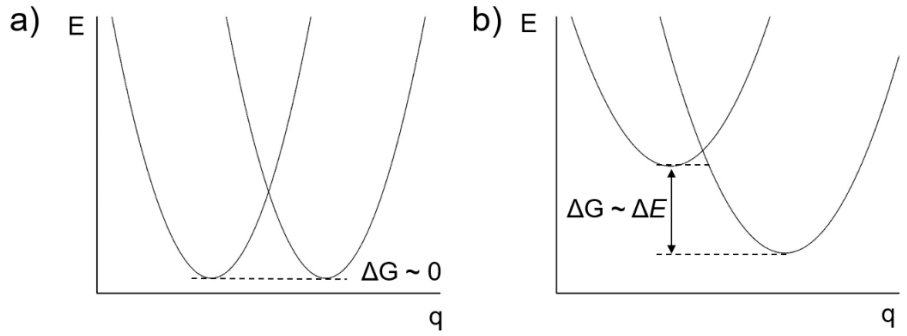

Figure 12. Schematic representation of the diabatic potential energy surfaces between identical molecules (a) and nonequivalent molecular systems (b).

The first scenario usually leads to a huge difference between the diabatic and adiabatic descriptions, and the computation of ΔE in the diabatic representation by standard quantum-chemical methods becomes rather difficult. Nevertheless, despite this difficulty, the energetic equivalence of both states makes easier to estimate ΔE (approximated to zero). Further corrections can be incorporated to improve ΔE; for instance, including static disorder or the effect of an electric field that polarizes the system. On the other hand, in the situation

where the donor and the acceptor are different molecular entities or moieties, the adiabatic states can be seen often as quasi-diabatic states, and, therefore, the energy difference between the minima of the corresponding adiabatic PES can be a good estimation of ΔE.

3.2.5 Reorganization energy

The reorganization energy (λ) is a parameter that accounts for the energy change associated to the nuclear rearrangement that takes place after the electronic redistribution resulting from an electronic transition (charge/energy transfer). In practice, the total reorganization energy is separated in two components: 1) the internal reorganization energy (λ_{int}), that accounts for the structural reorganization of the molecules involved in the transfer process, and 2) the external reorganization energy (λ_{ext}), that takes into account the reorganization of the environment (either solvent molecules when the process occurs in solution or the neighboring molecules in a molecular crystal or aggregate).

3.2.5.1 Internal reorganization energy

The internal reorganization energy is usually split into the contribution of the molecular moieties involved in the transfer process. Therefore, it is computed as the sum of the individual relaxation energies of both fragments upon the charge/exciton transfer. Figure 13a displays a scheme of the four-points approach for the case where both fragments are identical, and Figure 13b

depicts the same scheme for non-identical fragments acting as donor and acceptor. Independently of the situation, the reorganization energy is estimated in a similar way. The reorganization energy is computed as sum of the relaxation energy of both fragments. The relaxation energies are computed as the energy difference, in the corresponding PES after the electronic transition (final state), between the minimum energy geometry of the initial and the final state (Figure 13). Eq. 58 shows the expression of λ_{int} for the charge separation process between a donor (D) and an acceptor (A) molecule. The upperscripts (0/#) denote the geometry of the final/initial state.

$$\lambda_{\text{int}} = \lambda_{\text{int}}^{\text{D}} + \lambda_{\text{int}}^{\text{A}} = (E_{\text{D}^+}^{\#} - E_{\text{D}^+}^{0}) + (E_{\text{A}^-}^{\#} - E_{\text{A}^-}^{0}) \tag{58}$$

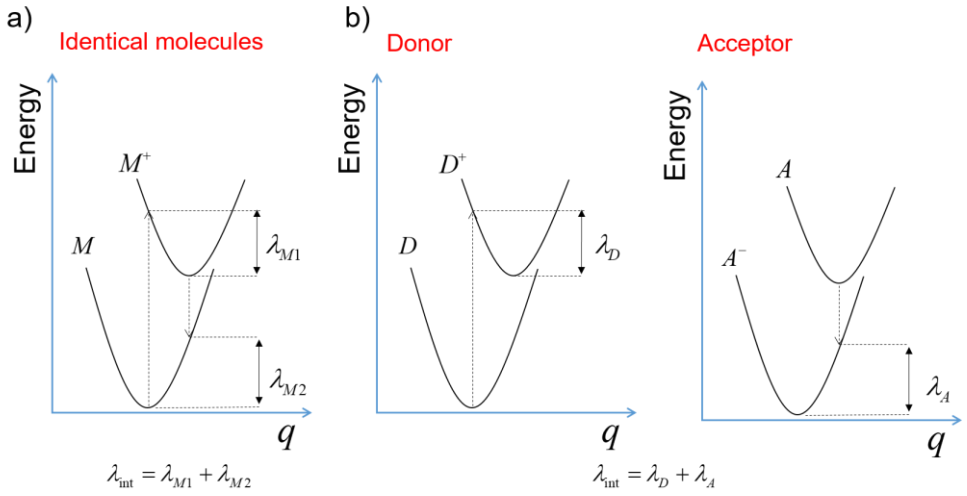

Figure 13. Scheme of the internal reorganization energy for identical molecules (a) and for the case of a donor–acceptor D−A system (b).

The internal reorganization energy can also be decomposed into the contribution of each vibrational normal mode. This is especially relevant when

the nuclear rearrangement is treated in a quantum way as it is the case of the Marcus–Levitch–Jortner rate constant. The internal reorganization energy is computed according to Eq. 59, where S_i is the Huang–Rhys (HR) factor and ω_i the frequency of the respective normal mode.

$$\lambda_{\text{int}} = \sum_i S_i \hbar\omega_i \tag{59}$$

The HR factors are computed according to Malagoli and coworkers.[177,178] Briefly, the HR factors are estimated using Eq. 60, where Δ is the dimensionless displacement for each normal mode. Δ is computed by projecting the nuclear displacement vector (Eq. 61), obtained by comparing the final ($\mathbf{C_f}$) and the initial ($\mathbf{C_0}$) geometry, into the mass-weighted normal mode vectors ($\mathbf{L}$) as expressed in Eq. 62.

$$S_i = \frac{\Delta_i^2}{2} \tag{60}$$

$$\mathbf{C} = \mathbf{C_f} - \mathbf{C_0} \tag{61}$$

$$\Delta_i = \sqrt{\frac{k_i}{\hbar\omega_i}} \sum_{j=1}^{3N} L_{ji} C_j \tag{62}$$

3.2.5.2 External reorganization energy

The external reorganization energy (λ_{ext}) takes into account the environmental rearrangement due to reorientation and polarization effects. In molecular crystals, λ_{ext} is a small contribution to the total reorganization energy with

values generally smaller than 0.1 eV[179] and can be set as a fixed parameter or even neglected.[179]

In contrast to molecular crystals, λ_{ext} can achieve quite large values, even up to 1 eV, in solution. Among the different ways to estimate the external reorganization energy in solution, three approaches are quite popular:

1. Two-sphere Marcus model (Eq. 63),[172,180] where ε_0 and Δe are the vacuum permittivity and the amount of transferred charge, respectively. a_1, a_2 and R are the donor and acceptor sphere radii and the distance between the sphere centers, respectively. Finally, ε_{OP} and ε_s are the optical and zero-frequency dielectric constants of the surrounding media, respectively. These magnitudes are generally obtained from the literature.

$$\lambda_{ext} = \frac{\Delta e^2}{4\pi\varepsilon_0}\left(\frac{1}{2a_1}+\frac{1}{2a_2}-\frac{1}{R}\right)\left(\frac{1}{\varepsilon_{OP}}-\frac{1}{\varepsilon_s}\right) \quad (63)$$

2. Dynamic polarization response. This approach is rooted in the difference between the fast electronic polarization of the solvent and the much slower nuclear motion (solvent reorientation). To take into account these solvent effects, a standard solvent continuum model is employed but using two different dielectrical constants (ε). If $\varepsilon = \varepsilon_{OP}$, only the electronic polarization is taken into account, whereas if $\varepsilon = \varepsilon_s$

both effects are accounted. Thus, λ_{ext} can be computed as the energy difference between both situations.

3. Non-equilibrium versus equilibrium solvation. This approximation is based on the use of the state-specific PCM formalism developed by Improta and coworkers.[149] The SS variant of PCM allows to use the solvent configuration of a previous calculation taking only into account the faster electronic polarization of the solvent (*non-equilibrium*). λ_{ext} is calculated as the difference between this non-equilibrium situation and the fully relaxed solvent configuration obtained through an iterative process (*equilibrium*).

In this Thesis, λ_{ext} in solution has been evaluated as the difference between the total reorganization energy and the internal reorganization energy. It was estimated following the same procedure used for λ_{int}, but in solution, employing the non-equilibrium state-specific PCM approach in the vertical calculation and the equilibrium approach in the calculation of the local minima of the state (Eq. 64, see Figure 13 for notation).

$$\lambda_{ext} = \lambda - \lambda_{int} = (E^{\#}_{D^+}(Eq) - E^{0}_{D^+}(NonEq)) + (E^{\#}_{A^-}(Eq) - E^{0}_{A^-}(NonEq)) - \lambda_{int} \quad (64)$$

3.2.6 Electronic and excitonic coupling

The electronic/excitonic coupling *V* is the interaction between two diabatic states and corresponds, as previously discussed, to the off-diagonal elements of the diabatic Hamiltonian matrix. In Figure 14, the energy of the adiabatic

states is represented as a function of the diabatic energies and the couplings in the two-state model.

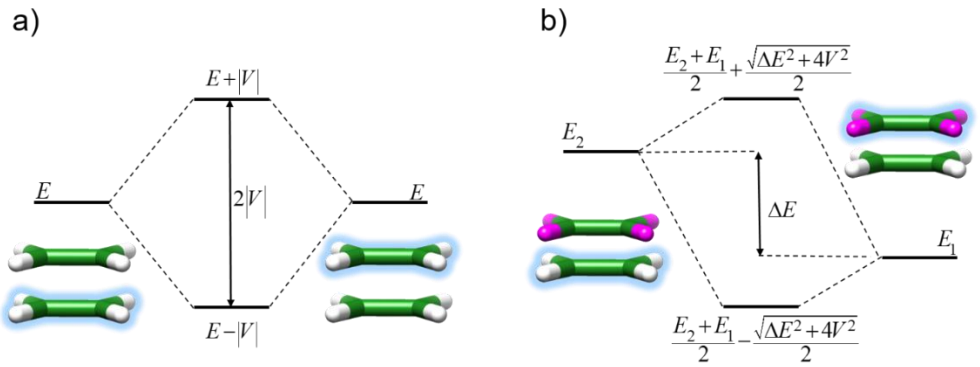

Figure 14. Scheme of the energy splitting for energetically degenerate diabatic states (a) and non-degenerate diabatic states (b). Blue shadow indicates where the charge/exciton is localized.

Note that only the absolute value of the coupling determines the energy levels. Nevertheless, the sign of *V* determines which energy level belong to each eigenfunction, either the symmetric or anti-symmetric combination of the diabatic wavefunctions. A good example of the relevance of the *V* sign is the Kasha's model, which has been successfully employed to understand the optical properties of molecular aggregates (Figure 15).[181–183] This model shows that the adiabatic state resulting from the symmetric combination of the diabatic states is blue-shifted (H aggregate) or red-shifted (J aggregate) depending on the coupling sign (positive or negative). The assignment of the adiabatic state corresponding to the symmetric combination is extremely relevant because only this state holds a non-null transition dipole moment and, thus, optical activity (Figure 15).

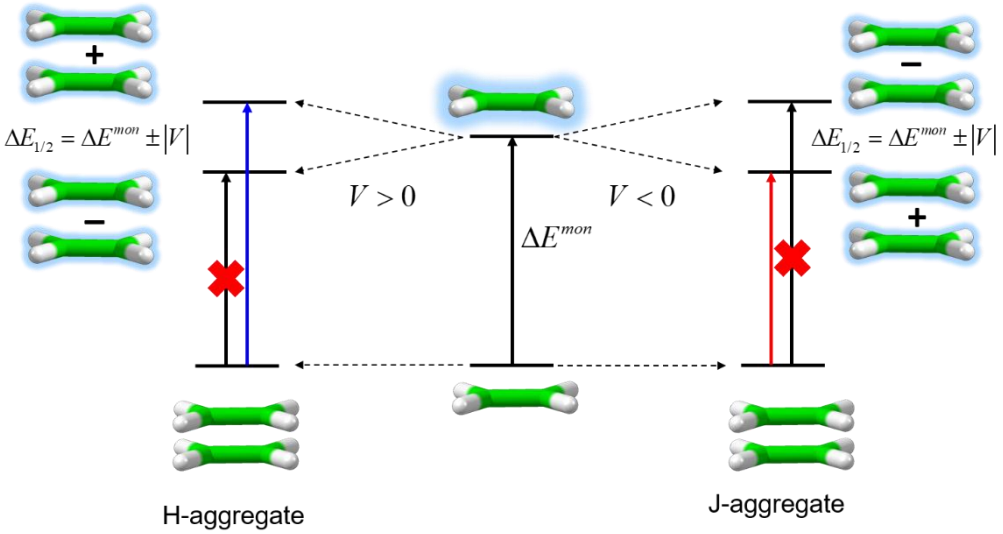

Figure 15. Schematic diagram illustrating the Kasha´s Model. Arrows indicate bright or dark (marked with a red cross) transitions.

Below, the different approaches used to estimate the coupling elements in the context of charge or energy transport along this Thesis are briefly explained.

3.2.6.1 Dimer projection method

The dimer projection method (DIPRO)[184] is an approximation to compute electronic couplings in the charge transfer context. DIPRO works well when the coupling matrix element can be mainly described by a monoelectronic contribution because it is estimated from the Fock matrix in the basis of localized orbitals. In general, the diabatic states can be expressed as single configuration state functions, or single Slater determinants if the spin is neglected, and the coupling matrix element between the diabatic states is just the exchange of an electron from one orbital localized on molecule A to

another orbital localized on molecule B (Figure 16). The DIPRO method is therefore suitable for evaluating electronic couplings in the context of charge transport since the diabatic states can be described as cation or anion states localized in each molecule.

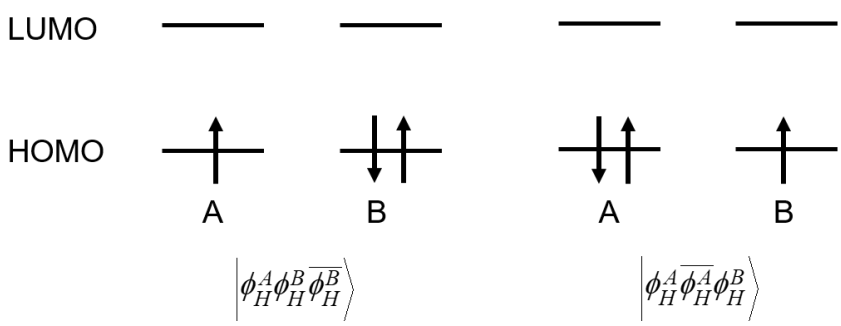

Figure 16. Scheme showing the frontier molecular orbitals for the diabatic states involved in a hole transfer event.

The basic idea behind the DIPRO method is to express the adiabatic molecular orbitals of an AB dimer as a linear combination of the molecular orbitals of isolated monomers (*A* and *B*). The linear expansion coefficients (**C**) are obtained by solving the secular equation

$$\left(\mathbf{H} - E\mathbf{S}\right)\mathbf{C} = 0 \tag{65}$$

where **H** and **S** are the Hamiltonian and overlap matrices, respectively, defined as

$$\mathbf{H} = \begin{pmatrix} E_A & V_{AB} \\ V_{AB} & E_B \end{pmatrix}$$
$$\mathbf{S} = \begin{pmatrix} 1 & S_{AB} \\ S_{AB} & 1 \end{pmatrix} \tag{66}$$

In Eq. 66, E_A and E_B are the diabatic energies, V_{AB} the electronic coupling and S_{AB} the overlap between the diabatic molecular orbitals involved in the charge transfer. The E_A, E_B, V_{AB} and S_{AB} matrix elements are defined as follows:

$$\begin{aligned} E_A &= \left\langle \phi^A \middle| \hat{H} \middle| \phi^A \right\rangle \\ E_B &= \left\langle \phi^B \middle| \hat{H} \middle| \phi^B \right\rangle \\ V_{AB} &= \left\langle \phi^A \middle| \hat{H} \middle| \phi^B \right\rangle \\ S_{AB} &= \left\langle \phi^A \middle| \phi^B \right\rangle \end{aligned} \tag{67}$$

The above integrals are not strictly computed since thay are estimated by projecting the monomer orbital coefficients vector ($\boldsymbol{\gamma}^{A(B)}$) into the dimer orbitals (ψ):

$$\begin{aligned} E_{A(B)} &= \sum_{i,j} \left\langle \phi^{A(B)} \middle| \psi_i \right\rangle \left\langle \psi_i \middle| \hat{H} \middle| \psi_j \right\rangle \left\langle \psi_j \middle| \phi^{A(B)} \right\rangle = \boldsymbol{\gamma}^{\mathbf{A(B)}} \boldsymbol{\varepsilon} \boldsymbol{\gamma}^{\mathbf{A(B)}} \\ V_{AB} &= \sum_{i,j} \left\langle \phi^{A} \middle| \psi_i \right\rangle \left\langle \psi_i \middle| \hat{H} \middle| \psi_j \right\rangle \left\langle \psi_j \middle| \phi^{B} \right\rangle = \boldsymbol{\gamma}^{\mathbf{A}} \boldsymbol{\varepsilon} \boldsymbol{\gamma}^{\mathbf{B}} \end{aligned} \tag{68}$$

where $\boldsymbol{\varepsilon}$ is the diagonal eigenvalue matrix of the dimer molecular orbitals. Finally, to take into account the non-orthogonality of the diabatic molecular orbitals, the overlap is introduced by estimating an effective Hamiltonian ($\mathbf{H}^{\mathbf{eff}}$) computed as a Löwdin transformation[185] of the Hamiltonian (Eq. 69).

$$\mathbf{H}^{\mathbf{eff}} = \mathbf{S}^{-\frac{1}{2}} \mathbf{H} \mathbf{S}^{-\frac{1}{2}} = \begin{pmatrix} E_A^{eff} & V_{AB}^{eff} \\ V_{AB}^{eff} & E_B^{eff} \end{pmatrix} \tag{69}$$

3.2.6.2 Fragment charge difference diabatization scheme

As stated previously, the use of diabatization schemes is a popular approach to obtain the electronic couplings. The aim of the diabatization schemes is to find the adiabatic-to-diabatic rotation matrix (**C**) that relates the adiabatic Hamiltonian matrix to the diabatic one by $\mathbf{H^{DI}} = \mathbf{C}\mathbf{H^{AD}}\mathbf{C}^{\mathbf{t}}$ (Table 1). As there is no a unique definition to build the diabatic states, a molecular property is commonly used for the diabatization process. In the Mulliken–Hush method,[186] the molecular property used to diabatize is the dipole moment whereas, in the fragment charge difference (FCD) method,[187] the charge difference between the donor and acceptor moieties is employed. A similar method for excitonic couplings (known as the fragment exciton difference method[188]) makes use of exciton population difference between the two involved molecular moieties. In the diabatic basis, the Hamiltonian is non-diagonal but the nature of the states does not change along the transfer process. For the FCD method, the diabatic Hamiltonian is non-diagonal whereas the property matrix is diagonal and their elements take integer values between –2 and 2. In contrast, in the adiabatic picture, the Hamiltonian is diagonal but the property matrix not (Table 1).

Table 1. Schematic representation of the matrices involved in the FCD diabatization method.

Matrix	**Adiabatic**	**Diabatic**
Hamiltonian, **H**	$\begin{pmatrix} E_i & 0 \\ 0 & E_j \end{pmatrix}$	$\begin{pmatrix} \varepsilon_i & V_{ij} \\ V_{ji} & \varepsilon_j \end{pmatrix}$
Charge difference, $\Delta\mathbf{q}$	$\begin{pmatrix} \Delta q_{ii} & \Delta q_{ij} \\ \Delta q_{ji} & \Delta q_{jj} \end{pmatrix}$	$\begin{pmatrix} \Delta q_i & 0 \\ 0 & \Delta q_j \end{pmatrix}$

The Δq_{ij} elements that appear in the adiabatic charge difference matrix shown in Table 1 are calculated using Eq. 70, where ρ_{ij} is the one-particle density ($i = j$), or the transition density between the initial i and final j electronic states for the donor–acceptor (D−A) system.

$$\Delta q_{ij} = \int_{\mathbf{r}\in \mathrm{D}} \rho_{ij}(\mathbf{r})\mathrm{d}\mathbf{r} - \int_{\mathbf{r}\in \mathrm{A}} \rho_{ij}(\mathbf{r})\mathrm{d}\mathbf{r} \tag{70}$$

The two–state approach (widely used in the literature) is reasonable when both adiabatic states can be considered as quasi-diabatic states and there is no interference from other states close in energy. When those conditions are not fulfilled, the multi–state FCD variant is a more convenient approach.[189] In the multi–state variant, $N \times N$ adiabatic matrices $\mathbf{H}$ and $\Delta\mathbf{q}$ are initially built. Then the adiabatic $\Delta\mathbf{q}$ matrix is diagonalized to find the adiabatic-to-diabatic transformation matrix $\mathbf{C}$. Once the $\mathbf{C}$ matrix is obtained, the diabatic Hamiltonian can be calculated. After obtaining the diabatic Hamiltonian, a block diagonalization, according to the state nature, is performed to ensure zero couplings between the electronic states of similar nature. Figure 17 schematizes the multi-state FCD diabatization scheme.

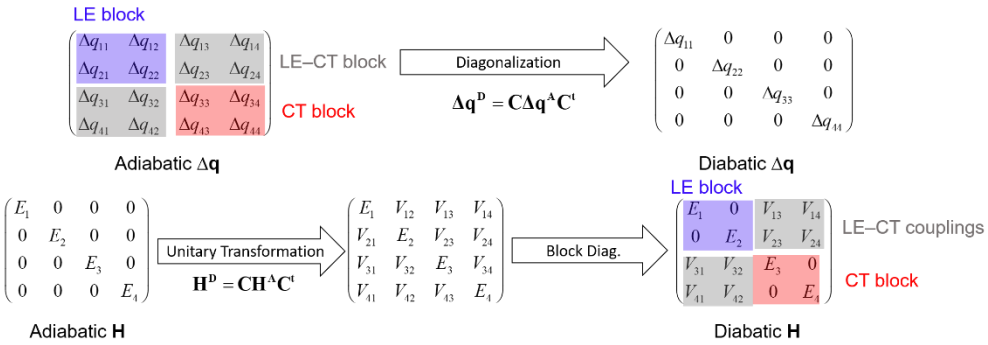

Figure 17. Scheme of the multi-state FCD procedure illustrating a general 4×4 case with two local (LE) and two charge-transfer (CT) states.

3.2.6.3 The Coulombic component of the excitonic coupling

The coupling between local excited states (Figure 18), usually denoted as J_{AB}, comes from bielectronic terms (Eq. 71) according to the Slater–Condon rules for the interaction between Slater determinants that differ in two spin-orbitals (Figure 18).

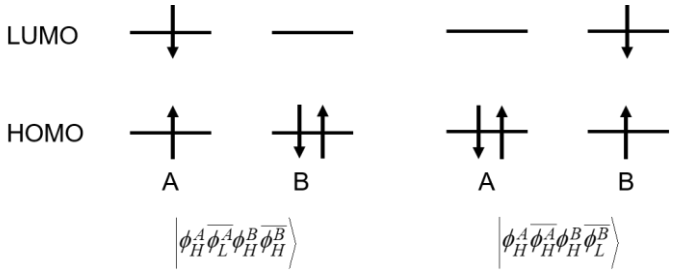

Figure 18. Schematic diagram showing the frontier molecular orbitals for the diabatic states involved in an exciton transfer process.

$$J_{AB} = \left\langle \phi_H^A \overline{\phi_L^A} \phi_H^B \overline{\phi_H^B} \middle| H \middle| \phi_H^A \overline{\phi_H^A} \phi_H^B \overline{\phi_L^B} \right\rangle = \left[\overline{\phi_L^A} \overline{\phi_H^B} \middle| \frac{1}{r_{12}} \middle| \overline{\phi_H^A} \overline{\phi_L^B} \right] - \left[\overline{\phi_H^A} \overline{\phi_H^B} \middle| \frac{1}{r_{12}} \middle| \overline{\phi_L^A} \overline{\phi_L^B} \right] \quad (71)$$

When the molecular moieties are relatively far, the exchange component becomes zero and the excitonic coupling is quite similar to the interaction between the transition dipole moments ($\mu_{A(B)}$)[190] localized on each molecular unit. Eq. 72 represents the point–dipole approximation (PD), which is presumably the approximation most used in the excitonic transport context.

$$J_{AB} \approx \frac{\boldsymbol{\mu}_{\mathbf{A}}\boldsymbol{\mu}_{\mathbf{B}} - 3(\boldsymbol{\mu}_{\mathbf{A}}\mathbf{R})(\boldsymbol{\mu}_{\mathbf{B}}\mathbf{R})}{|R|^5} \tag{72}$$

However, the assumption that a molecule sees the other molecule just as a dipole is not valid at short distances. To solve this problem, a common approach is to evaluate the Coulombic coupling J_{AB} from a set of atomic transition charges (ATC) localized at the atomic positions (Eq. 73).[191]

$$J_{AB} \approx \sum_{i}^{N_A}\sum_{j}^{N_B}\frac{q_i^{tr}q_j^{tr}}{R_{ij}} \tag{73}$$

An additional approximation but with the same philosophy is the Transition Density Cube method (TDC).[192] In the TDC approach, the space is partitioned in a grid of small cubes and the interaction between the transition densities of the cubes belonging to different molecular moieties is performed as indicated in Eq. 74.

$$J_{AB} \approx \sum_{i,j}\frac{M_i^A M_j^B}{R_{ij}} \tag{74}$$

In expressions 73 and 74, q_i^{tr} is the atomic transition charge located on atom *i*, R_{ij} is the distance between the atoms or the grid volume elements in the TDC,

and $M_{i(j)}^{A(B)}$ is the transition density inside the grid volume element cubes. $M_{i(j)}^{A(B)}$ is defined as

$$M_i^A = V_\delta \int_z^{z+\delta z} \int_y^{y+\delta y} \int_x^{x+\delta x} \Psi_0 \Psi_{exc}^* dxdydz \tag{75}$$

where V_δ is the element volume $\left(V_\delta = \delta_x \delta_y \delta_z\right)$. In the two last approximations, the elements used to represent the transition density (charges or small cubes) must sum zero (Eq. 76) and also must recover the transition dipole moment as indicated in Eq. 77.

$$\begin{aligned} \sum_i q_i^A &= 0 \\ \sum_i M_i^A &= 0 \end{aligned} \tag{76}$$

$$\begin{aligned} \sum_i q_i^A R_i &= \mu_A \\ \sum_i M_i^A R_i &= \mu_A \end{aligned} \tag{77}$$

3.2.6.4 Procrustes Diabatization

Although the Coulombic excitonic component is a good estimation of the total excitonic coupling for weakly coupled molecular systems, it may be not good enough for molecular dimers at close intermolecular distances. In molecular crystals or aggregates, short intermolecular contacts can be found and short-range excitonic effects can become relevant. The problem is that, in contrast to the Coulombic potential, the exchange component involved in the description

of short-range effects has no classical expression that facilitates its computation. In this sense, diabatization is a powerful tool that allows to obtain total excitonic couplings including all the long- and short-range effects.

Among the variety of diabatization schemes used for excitonic processes available in the literature, the diabatization based on the atomic transition charges (ATC) developed by Troisi and Aragó is used in this Thesis.[193] In this scheme, the adiabatic atomic transition charges ($\mathbf{q}^{\mathbf{AD}}$) are related to the diabatic charges ($\mathbf{q}^{\mathbf{DI}}$) by a rotation matrix **C** (Eq. 78). The adiabatic set of ATCs is easily obtained from the calculation of the excited states of the dimer. In contrast, a diabatic reference ($\mathbf{q}^{\mathbf{ref}}$) is built, using the ATCs obtained from the calculation of the excited states of a single molecule, to represent one molecule in the excited state whereas the other remains in the ground state.

$$\mathbf{q}^{\mathbf{DI}} = \mathbf{q}^{\mathbf{AD}}\mathbf{C}^{T} \tag{78}$$

Therefore, the best rotation matrix **C** is the one that minimizes the difference between both sets of diabatic charges ($\mathbf{q}^{\mathbf{DI}}$ and $\mathbf{q}^{\mathbf{ref}}$).

$$\mathbf{C}^{T} = \arg\min_{\mathbf{C}} \| \mathbf{q}^{\mathbf{AD}}\mathbf{C}^{T} - \mathbf{q}^{\mathbf{ref}} \| \tag{79}$$

Where the ||·|| symbol denotes the Frobenius norm. Note that $\mathbf{q}^{\mathbf{ref}}$, $\mathbf{q}^{\mathbf{DI}}$ and $\mathbf{q}^{\mathbf{AD}}$ are rectangular matrices with a number of rows equal to the number of atoms and a number of columns equal to the number of states to diabatize, whereas $\mathbf{C}^{T}$ is a square matrix with a dimension equal to the number of states. The use of rectangular matrices is quite unusual; however, it presents the

advantage of providing a better mapping of the property since a full set of charges is obtained instead of a single value for each state.

The problem raised in Eq. 79 is a well-known problem of linear algebra known as Procrustes problem,[194] which has a unique solution:

$$\mathbf{C}^T = \mathbf{U}\mathbf{V}^T \tag{80}$$

where the $\mathbf{U}$ and $\mathbf{V}^T$ matrices are obtained using the singular value decomposition (SVD) as follows:

$$\mathrm{SVD}(\mathbf{q}^{\mathbf{AD}^T}\mathbf{q}^{\mathbf{D}}) = \mathbf{U}\boldsymbol{\Sigma}\mathbf{V}^T \tag{81}$$

Once $\mathbf{C}^T$ is known, the diabatic Hamiltonian is obtained through a unitary transformation of the adiabatic Hamiltonian:

$$\mathbf{H}^{\mathbf{DI}} = \mathbf{C}\mathbf{H}^{\mathbf{AD}}\mathbf{C}^T \tag{82}$$

The main advantage of this diabatization scheme, compared with other diabatization schemes focused in dealing with excitons, is the better mapping of the adiabatic states in the diabatization process since it requires a large number of elements to set a more accurate reference. However, the diabatization scheme proposed also presents a shortcoming: the good behavior of the method requires clean adiabatic states that can be expressed as linear combination of the diabatic reference. Unfortunately, it is common to find charge-transfer states close in energy to the local excited states, and it is not possible to establish an accurate reference for the charge-transfer states because their atomic transition charges are usually zero.

3.2.6.5 Diabatization based on the fragment particle–hole densities (FPHD)

The fragment density matrix diabatization scheme[195] is a scheme developed to include simultaneously local excited states (Frenkel states) and charge-transfer states, which is a non-trivial task. For instance, in the simple case of a dimer, four type of diabatic states can be found: two Frenkel states and two charge-transfer-states (Figure 19).

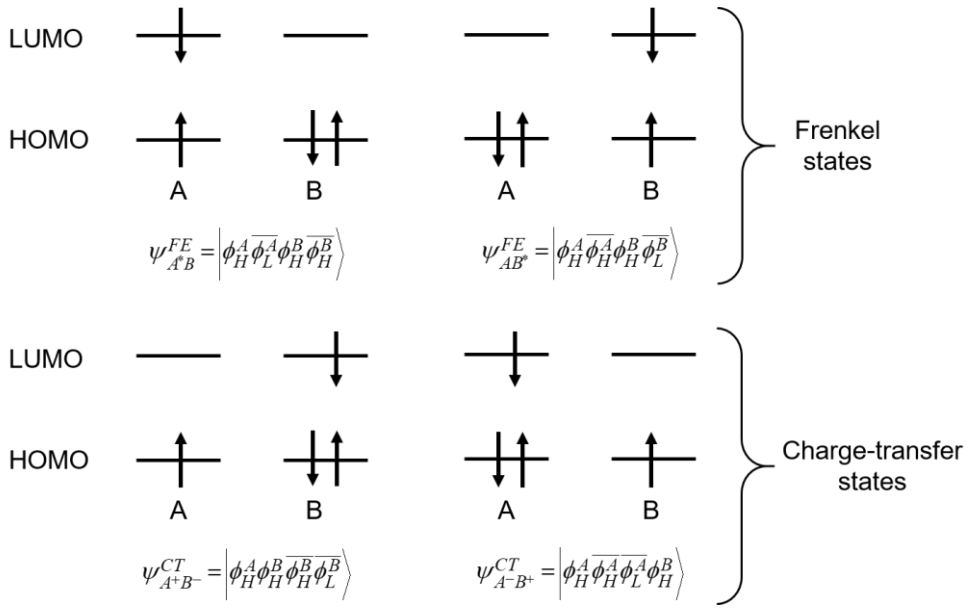

Figure 19. Scheme showing the frontier molecular orbitals diagrams for the all the four diabatic states of a dimer AB in a minimum basis set representation.

By using the hole and electron population of each fragment, the fragment density matrix diabatization allows to set a property that univocally describes both the local and the charge-transfer states. That means that *2N* property matrices are simultaneously used, where *N* is the number of fragments. Figure 20 displays the 4 diabatic property matrices associated to the diabatic states

illustrated in Figure 19. As in the adiabatic representation the four matrices collecting the hole and electron transition density populations are non-diagonal, the FPHD method requires of a unique **C** unitary transformation matrix that performs the adiabatic-to-diabatic transformation to the 2*N* property matrices simultaneously.

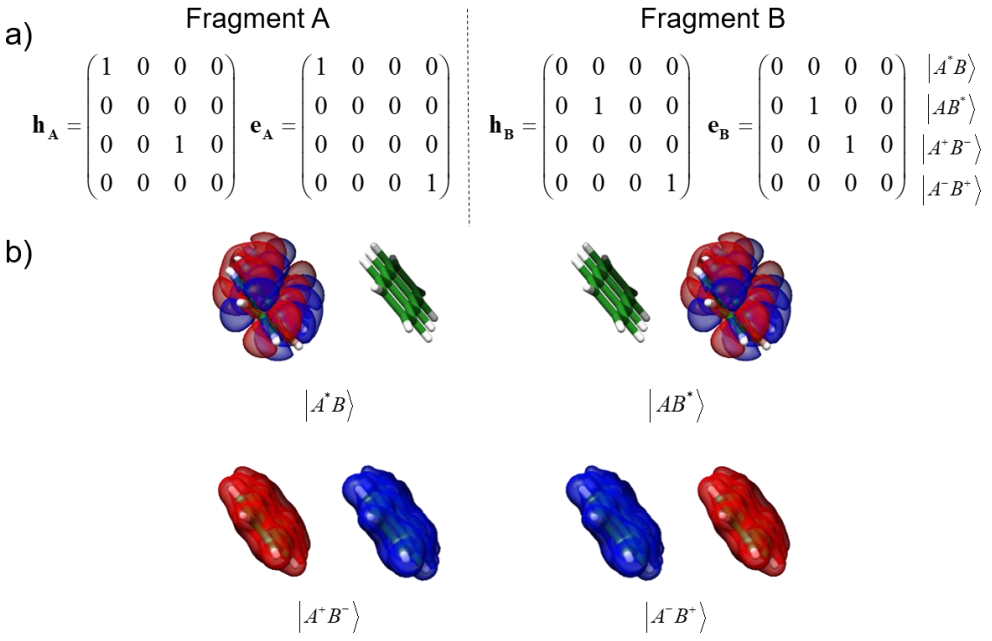

Figure 20. a) Diabatic matrix representation of the hole (**h**) and electron (**e**) transition density populations of each fragment (A or B) for the four states of the model introduced in Figure 19. Labels indicating the diabatic states are provided at the right side. b) Hole (red) and particle (blue) transition densities are represented for each state.

The diabatic states are those that have a maximum localization of the hole and electron populations. This maximum localization is achieved through simultaneous diagonalization of the 2*N* matrices, what is accomplished by the

Jacobi sweep algorithm.[196] Once the adiabatic matrices are diagonalized, the diabatic states can be classified according to their nature, and each subspace of a specific nature must be diagonalized to ensure that the couplings between states of the same nature are zero. This procedure thus implies the diabatization between local excited states or charge-transfer states of equivalent nature, and therefore provides simultaneously electronic and excitonic couplings. Additionally, the adiabatic-to-diabatic rotation matrix allows the decomposition of the adiabatic states into the diabatic, which is a powerful tool for the analysis of the excited states.

3.2.6.6 *Ab-initio* Frenkel–Davydov model Hamiltonian (AIFD)

An alternative approach to diabatization schemes is the use of a Frenkel–Davydov model. The original idea of this model was to build the Hamiltonian in the basis of single-molecule excitations and the wavefunction as a product of single excitations localized on each molecule (Eq. 83).

$$\Psi_i = \psi_i^* \prod_{j \neq i} \psi_j^0 \tag{83}$$

In Eq. 83, ψ_i^* represents the wavefunction of an excited state of molecule *i* and ψ_j^0 represents the wavefunction of molecule *j* in its ground state.

The Frenkel–Davydov model leads to a Hamiltonian that takes the following expression:

$$\hat{H} = \sum_i E_i |i\rangle\langle i| + \sum_{i,j} V_{ij} |i\rangle\langle j| \tag{84}$$

where *i* and *j* run over the molecular sites, E_i is the excitation energies of site *i* and V_{ij} corresponds to the excitonic couplings between different molecular sites. Note that the Frenkel–Davydov model is a tight-binding Hamiltonian and, thus, only excitonic couplings between neighboring sites are accounted for. Although the Frenkel–Davydov model is generally parameterized, *ab-initio* versions that include not only Frenkel states but also charge-transfer states have been proposed in recent years, stressing those developed by Herbert,[197,198] Martinez,[199,200] Fujita[201] and Fujimoto.[202]

The idea of an *ab*-initio Frenkel–Davydov model is to define *a priori* the diabatic wavefunctions and, then, compute the Hamiltonian matrix elements. In particular, the model Hamiltonian used in the studies carried out in this Thesis is quite similar to that developed by Martinez and coworkers,[199,200] the main difference being that in our model Hamiltonian more than a single charge-transfer state can be included.

The steps followed to build up the *ab-initio* Frenkel–Davydov model Hamiltonian for a molecular dimer AB are:

1. The excited states of both monomers are calculated through standard quantum chemical methods. In this Thesis, the CIS method was selected. From those calculations, the fragment molecular orbitals and the CI vectors of the excited states are used to build the diabatic wavefunctions as indicated in the next step.
2. The diabatic wavefunctions are built as products of the wavefunctions of the non-interacting molecules (Eq. 85). The local or Frenkel state wavefunction is characterized by a Slater determinant corresponding to the ground state of one molecule multiplied by the CI expansion of the

excited state of the other molecule. The diabatic charge-transfer wavefunctions cannot be expressed as CI expansions, and are therefore introduced as a single excited determinant where the hole and the electron are generated in molecular orbitals that belong to different molecular fragments.

$$\begin{aligned}
\left|A^{*}B\right\rangle &= \psi_{B}^{0}\sum_{i\in A}^{N_{occ}}\sum_{a\in A}^{N_{virt}} c_{i}^{a}\psi_{A}^{i_{A}\to a_{A}} \\
\left|AB^{*}\right\rangle &= \psi_{A}^{0}\sum_{i\in B}^{N_{occ}}\sum_{a\in B}^{N_{virt}} c_{i}^{a}\psi_{B}^{i_{B}\to a_{B}} \\
\left|A^{+}B^{-}\right\rangle &= \psi_{AB}^{i_{A}\to a_{B}} \\
\left|A^{-}B^{+}\right\rangle &= \psi_{AB}^{i_{B}\to a_{A}}
\end{aligned} \qquad (85).$$

3. An SCF calculation of the full supermolecule is performed to obtain the one- and two-electron integrals in the atomic basis functions, which are then transformed to the molecular orbital basis.
4. The excitation energies and the electronic/excitonic couplings of the Hamiltonian (diagonal and off-diagonal elements) are computed according to the Slater–Condon rules (Eq. 86) assuming that the fragment orbitals are orthogonal.

$$
\begin{aligned}
\Delta E_A^{FE} &= \left\langle A^* B \middle| \hat{H} \middle| A^* B \right\rangle = \sum_{i_A a_A} \sum_{j_A b_A} c_{i_A}^{a_A} c_{j_A}^{b_A} \begin{bmatrix} \delta_{i_A j_A} f_{a_A b_A} - \delta_{a_A b_A} f_{i_A j_A} \\ +2\left(\phi_i^A \phi_a^A \middle| \phi_j^A \phi_b^A\right) - \left(\phi_i^A \phi_j^A \middle| \phi_a^A \phi_b^A\right) \end{bmatrix} \\
\Delta E_{AB}^{CT} &= \left\langle A^+ B^- \middle| \hat{H} \middle| A^+ B^- \right\rangle = f_{a_B a_B} - f_{i_A i_A} + 2\left(\phi_i^A \phi_a^B \middle| \phi_i^A \phi_a^B\right) - \left(\phi_i^A \phi_i^A \middle| \phi_a^B \phi_a^B\right) \\
V_{A-B}^{FE-FE} &= \left\langle A^* B \middle| \hat{H} \middle| A B^* \right\rangle = \sum_{i_A a_A} \sum_{j_A b_A} c_{i_A}^{a_A} c_{j_B}^{b_B} \left[2\left(\phi_i^A \phi_a^A \middle| \phi_j^J \phi_b^B\right) - \left(\phi_i^A \phi_j^B \middle| \phi_a^A \phi_b^B\right) \right] \\
V_{A-AB}^{FE-CT} &= \left\langle A^* B \middle| \hat{H} \middle| A^+ B^- \right\rangle = \sum_{i_A a_A} c_{i_A}^{a_A} \left[\delta_{i_A j_A} f_{a_A b_B} + 2\left(\phi_i^A \phi_a^A \middle| \phi_b^B \phi_j^A\right) - \left(\phi_i^A \phi_j^A \middle| \phi_b^B \phi_a^A\right) \right] \\
V_{A-BA}^{FE-CT} &= \left\langle A^* B \middle| \hat{H} \middle| A^- B^+ \right\rangle = \sum_{i_A a_A} c_{i_A}^{a_A} \left[-\delta_{a_A b_A} f_{i_A j_B} + 2\left(\phi_i^A \phi_a^A \middle| \phi_b^A \phi_j^B\right) - \left(\phi_i^A \phi_j^B \middle| \phi_b^A \phi_a^A\right) \right] \\
V_{AB-BA}^{CT-CT} &= \left\langle \psi_{AB}^{CT} \middle| \hat{H} \middle| \psi_{BA}^{CT} \right\rangle = \left[2\left(\phi_i^A \phi_a^A \middle| \phi_j^B \phi_b^B\right) - \left(\phi_i^A \phi_j^B \middle| \phi_a^A \phi_b^B\right) \right]
\end{aligned}
\tag{86}
$$

3.2.7 Estimation of the charge-carrier mobility: The master equation

In the previous sections, the rate constant expression for charge/energy transport and the different strategies to compute the magnitudes appearing in the expression have been explained. These rate constants measure the average frequency of the transfer process between dimers. However, in molecular aggregates or crystals, each molecule is surrounded by more than a single neighboring molecule. In this context, all the rate constants for the different transfer pathways (at least those between the closest molecular pairs) should be taken into account for a reasonable description of the transport process. In general, the efficiency of the charge transport is evaluated by the charge-carrier mobility (μ), which measures the distance that the charge carrier travels per unit of time and unit of electric bias. μ is a macroscopic property of the material and highly depends on the morphology. Interestingly, μ can be theoretically estimated and experimentally measured facilitating a theoretical-experimental comparison.

Several approaches to compute the charge-carrier mobility are available in the literature, such as kinetic Monte Carlo simulations[203,204] or several master equation approaches.[205,206] The approach used in this Thesis is based on a master equation rooted in the steady-state hypothesis and on charge diluted conditions.[207] In this hypothesis, the charge-carrier density (ρ) remains constant, and therefore:

$$\frac{d\rho_i}{dt} = \sum_j \left(k_{ji}\rho_j - k_{ij}\rho_i \right) = 0 \tag{87}$$

In Eq. 87, k_{ij} is the rate constant for the transfer process from site *i* to *j*, and only the rates between neighboring sites are usually taken into account. Note that $k_{ij} \neq k_{ji}$ because the energy difference ($\Delta G \sim \Delta E$) is different due to the polarization of the molecules as consequence of the electric field (**F**) applied in the device. Thus, ΔE is computed as follows:

$$\Delta E_{ij} = E_j - E_i - q\mathbf{F}\mathbf{r} \approx -q\mathbf{F}\mathbf{r}_{ij} \tag{88}$$

where *q* is the charge of the charge carrier and $\mathbf{r}_{ij}$ the distance vector between the sites. Once the charge-carrier density of all the sites (ρ_i), in the steady-state, are obtained by solving Eq. 87 and using the normalization condition $\sum_i \rho_i = 1$, the charge-carrier mobility in the direction of the electric field is computed as

$$\mu = \frac{1}{|F|^2} \sum_{i,j} \rho_i k_{ij} \mathbf{r}_{ij} \cdot \mathbf{F} \tag{89}$$

Finally, by computing the mobility for different directions of the electric field, the anisotropy maps of the mobility are obtained.

Chapter 4. Supramolecular Polymers

4.1 Introduction

Supramolecular polymers are defined as assemblies constituted by molecular monomers hold together by non-covalent interactions such as hydrogen bonds, π–π interactions and hydrophobic interactions. The rational design of molecular systems that can be used as repeating building blocks to self-assemble through non-covalent interactions sets the basis of the so-called supramolecular polymers science.[208] The search for supramolecular polymers with attractive functionalities, such as semiconducting and chirality properties, self-healing or biomedical materials,[209] has motivated the rise of this interdisciplinary research field.

Biological systems are a great example of how non-covalent interactions determine the structure and functionality of molecular systems. For instance, the stability of DNA is driven by the H-bonding interactions between nucleic bases of the two DNA strands.[5] Other examples are proteins as hemoglobin, where the quaternary structure is due to the assembly of polypeptide chains by non-covalent interactions,[210] or the lipid bilayer of the cell membranes, which assembles mainly by hydrophobic interactions.[211] As a consequence, supramolecular scientists took biological systems as a source of inspiration for the synthesis of artificial supramolecular systems.

The first supramolecular polymer synthesized was reported by Lehn and coworkers in 1990.[212] The polymer results from a triple H-bond array between diamidopyridines and uracil derivatives (Figure 21) and shows a high degree of polymerization due to the large binding constant.[213,214] In addition to H-

bonding interactions, other non-covalent interactions as aromatic, hydrophobic or metal-coordination interactions have been used as driving forces to obtain supramolecular polymers with different functionalities as metal-containing polymers,[215] host-guest assemblies[216] and donor-acceptor polymers.[217] The improvement on the design of molecules that can be self-assembled has opened the door to a new avenue of unconventional materials, such as "molecular motors" or "molecular machines", a breakthrough for which Profs. F. Stoddart, B. Feringa and J. P. Sauvage were awarded the Nobel prize in Chemistry in 2016.

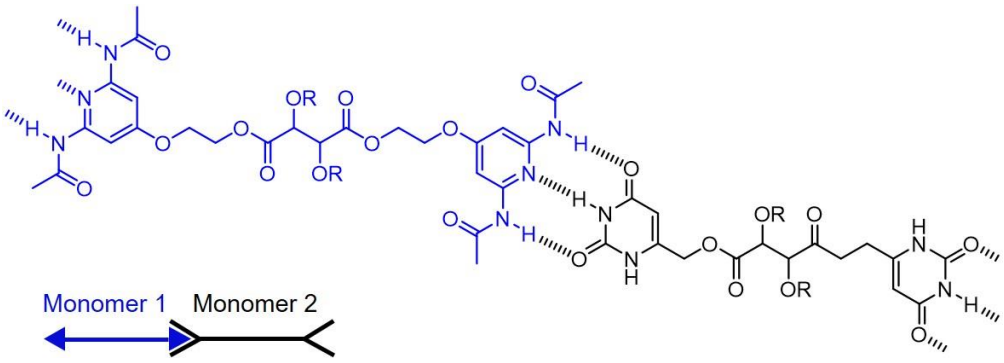

Figure 21. Chemical structure of the first synthetic supramolecular polymer reported.[212] Monomer 1 (blue) interacts with monomer 2 (black) through a triple H-bond array marked as dashed bonds.

A particular family of π-conjugated systems, which easily grows as supramolecular polymers, is that formed by discotic molecules.[218,219] These molecular systems present a planar, disc-shape core structure decorated with peripheral chains that interact between them through hydrophobic interactions. At high concentrations (or at low temperatures), the intermolecular interactions between discotic molecules are relevant, giving rise to highly ordered

columns.[220] In this sense, discotic-based supramolecular aggregates have been successfully used in the field of liquid crystals, being ideal candidates for columnar or nematic liquid crystal structures.[221] Figure 22a displays one of the simplest discotic structures: the benzene-1,3,5-tricarboxamide (BTA) molecule. This system has been widely studied by Meijer and coworkers,[25,222–226] and is usually decorated with side chains of different nature. When forming supramolecular polymers, BTAs present three types of interactions (Figure 22b): the benzene cores interact *via* π–π interactions, the amide groups interact through H-bonds, and the peripheral chains interact *via* dispersion interactions.

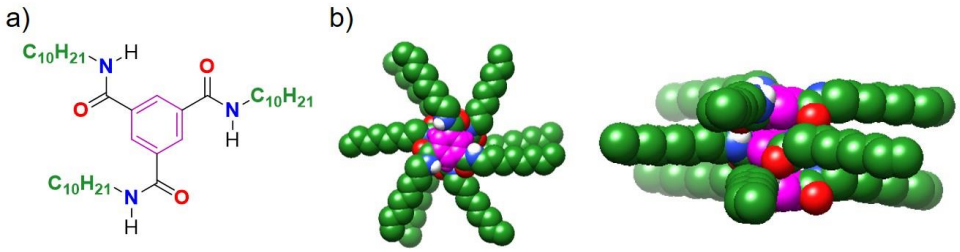

Figure 22. a) Chemical structure of a BTA. b) Top and side views of an ideal BTA trimer. Central benzene rings are represented in magenta, amide groups by the respective atom coloring code (oxygen in red, nitrogen in blue and hydrogen in white) and the aliphatic peripheral chains in green. Hydrogen atoms are omitted for clarity.

Supramolecular polymers, especially columnar and helical aggregates, are perfect candidates to study the phenomenon of chirality.[227] In the context of supramolecular chemistry, chirality emerges from the arrangement of the non-covalent assemblies in a non-symmetric disposition. For instance, helical supramolecular polymers are inherently chiral since a helix implies a right-handed or left-handed growing direction. This topic has been extensively

studied for BTA derivatives by the addition of side chains incorporating stereogenic centers of specific chirality. These *S* or *R* (point chirality) centers induce a preferred helical direction (axial chirality) in the resulting supramolecular polymer, and the process is known as chirality transfer.[25,224,228] The study of the chirality transfer process has motivated new experiments to understand how the chiral character is transferred to achiral homologues (sergeants and soldiers (SaS) experiments), or how enantiomeric mixtures behave in different proportions (majority rules (MRs) experiments). From these experiments, interesting magnitudes that allow to quantify the effectivity of the *transfer and amplification of chirality* are obtained. The helical-reversal penalty (HRP), which measures the energetic cost of forming a domain with an inverse helix, and the mismatch penalty (MMP), which estimates the energetic cost of introducing a molecule of different chirality in the helix, are of special interest. The self-assembling mechanism (especially cooperativity) and the phenomena of transfer and amplification of chirality are, without doubt, important aspects to be understood at atomic detail within the field of supramolecular polymers. Another interesting issue is the complexity of the self-assembly which can lead to different aggregated structures (*pathway complexity*). For instance, a thermodynamically disfavored metastable structure can be first formed because it is kinetically favored, and the stable thermodynamic aggregate is reached either consecutively (*on-pathway*), with no disassembly, or competitively (*off-pathway*), that implies the disassembly and reassembly in a different structure.[18,229–232]

Another interesting phenomenon that emerges from the molecular assembly *via* non-covalent interactions is the change in the optical properties of the supramolecular system. The absorption spectrum of the aggregate, when

compared with the non-aggregate system, usually presents a red or a blue shift, which are associated to J-type or H-type aggregates, respectively. This behavior was initially studied by Kasha, giving rise to the so-called Kasha's model (Section 3.2.6), which shows that the H or J behavior of the aggregate is determined by the sign of the excitonic coupling between vicinal molecules in the aggregate. The origin of the red and blue shifts upon aggregation has also been studied theoretically by F. Spano,[190,233] who expanded the Kasha's model by including the vibrational structure of the absorption bands and also the effect of charge-transfer states. F. Würthner and coworkers have conducted comprehensive studies on the optical properties of supramolecular polymers by designing perylene-bisimide (PBI) derivatives that promote different aggregation patterns.[234,235] For instance, stacked and slipped aggregates of *N*-annulated perylene-bismides (Figure 23) show blue- and red-shifts, respectively, leading to specific changes in the absorption spectra signatures.

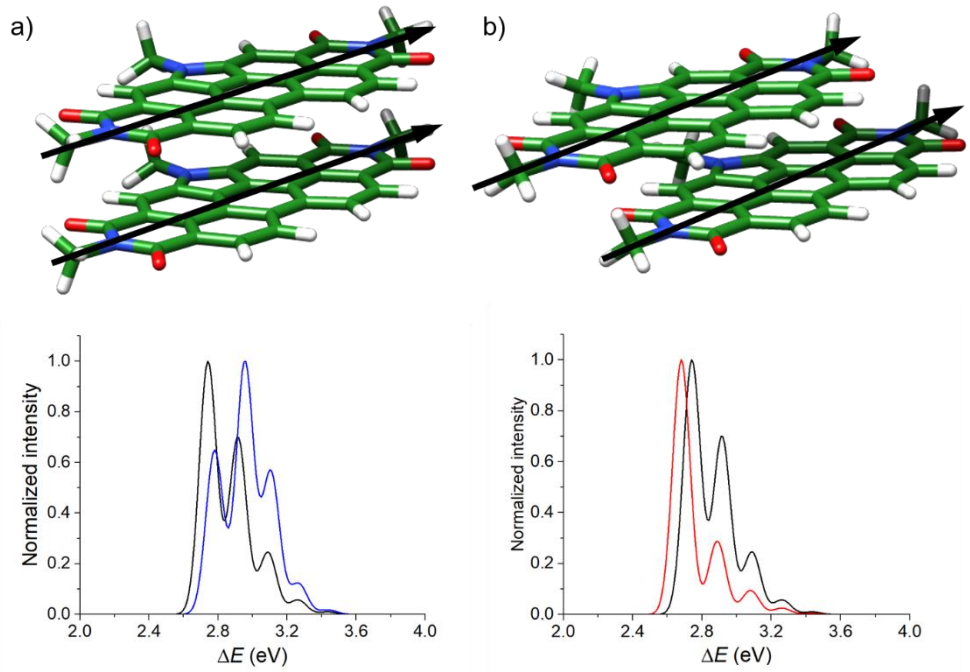

Figure 23. Schematic representation of stacked (a) and slipped (b) dimers of *N*-annulated perylene-bisimides (top) showing H and J behavior in the absorption spectrum (bottom), respectively. Black arrows denote the direction of the transition dipole moment of each PBI. The corresponding absorption spectra of the dimer (blue and red lines), simulated using the Spano's model, are represented and compared with the absorption spectrum predicted for the monomer (black line).

In this chapter, a theoretical study of three different self-assembling systems presenting different behavior is undertaken. First, a study on the preferential helicity (transfer of chirality) of triscarboxamide-based derivatives is performed by using the new cost-effective GFN2-xTB semiempirical methodology. The calculations were carried out to gain insight into the influence that the number of chiral side chains present in the monomer has on

the transfer and amplification of chirality trying to explain the results of MRs experiments. In particular, the theoretical calculations helped to rationalize the evolution of the mismatch penalty with the number of chiral peripheral chains. Second, a star-shaped 2,4,6-tris(triazolyl)-1,3,5-triazine derivative, able to accommodate three gallic acid units between its arms forming a 1:3 host-guest supramolecular complex, is theoretically investigated. The 1:3 host-guest complex is found to self-assemble in an ordered columnar liquid-crystal mesophase that is not observed without the presence of the acid units. A multi-level approach is used to disentangle the origin of the higher stability of the supramolecular aggregate by using a bottom-up approach. The interactions and different structures of the host–guest complex are first analyzed by first-principles calculations, whereas the structure and stability of the aggregates are investigated using semiempirical methods and molecular mechanics calculations. The third and last system discussed in this chapter implies the supramolecular polymerization of squaramide-based macrocycles. Two thermodynamic on-pathway aggregates are proposed based on the different morphology and the changes of the absorption spectra observed experimentally. The proposed supramolecular structures are validated by the study of the optical properties of both aggregates using an extended Kasha's model,[181] which successfully reproduces the uncommon optical features observed in the experimental absorption spectra.

4.2 Results and discussion

4.2.1 Transfer and amplification of chirality in triscarboxamide derivatives

In this section, we present a comparative study of two series of C_3-symmetric 1,3,5-triphenylbenzenetricarboxamides (TPBAs) and oligo(phenylene ethynylene) tricarboxamides (OPE-TAs) (Figure 24). The study was performed in collaboration with the experimental group led by Prof. Luis Sánchez from the *Universidad Complutense de Madrid* and gave rise to Publications 1 and 2 (Section 4.4). A previous study demonstrated that the presence of a stereogenic (*R* or *S*) center in the peripheral chains determined the preferential helical direction of the self-assembly, where left-handed (*M*) helices were found more stable for molecules incorporating *R* chiral groups and right-handed (*P*) helical aggregates were obtained for molecules with *S* groups.[236]

The study was motivated by the previous studies performed on the transfer and amplification of chirality of BTAs by Meijer and collaborators.[209,222,223,225,226] In those studies, BTA is used as an archetypical system to understand the transfer and amplification of chirality in supramolecular polymers. The experiments conducted by Meijer and coworkers indicate that BTAs are a useful molecular model to infer general rules in a research field where the phenomena are analyzed individually for each system, what makes difficult the prediction for new systems. However, the experiments performed by our collaborators on TPBAs and OPE-TAs demonstrated a quite different behavior compared with BTAs. Then, the question to answer was: why do discotic

systems with similar molecular structures such as BTAs, TPBAs and OPE-TAs present different transfer and amplification of chirality properties?

In particular, we analyze the origin of the transfer and amplification of chirality phenomena observed in TPBAs and OPE-TAs bearing a variable number of peripheral chains containing stereogenic centers (Figure 24). These systems are labelled from now as **TN** and **ON**, **T** for TPBAs and **O** for OPE-TAs, **N** denoting the number of chiral side chains. To understand the results obtained from the MRs experiments, we focused on the mismatch penalty enthalpy (ΔH_{MMP}), which represents the energy penalty cost for the insertion of a molecule in its unpreferred helical arrangement. Experimental measurements led to ΔH_{MMP} values of around 1.3 kJ mol^{-1} for TPBAs, independently of the number of chiral centers, and of 2.0 kJ mol^{-1} for **O3**, 2.5 kJ mol^{-1} for **O2** and 5.4 kJ mol^{-1} for **O1**. These values were obtained by fitting the intensity of the circular dichroism (CD) signals recorded for solution mixtures with different enantiomeric excess to the two-component equilibrium (EQ) model developed for cooperative supramolecular copolymerizations.[237]

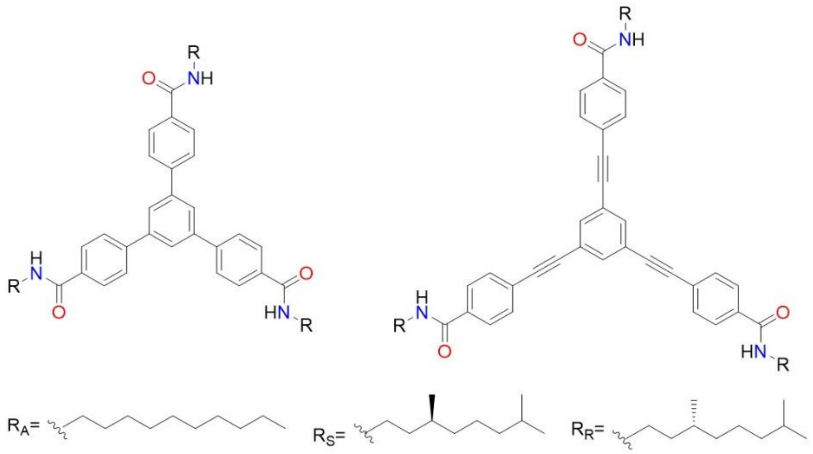

Figure 24. Chemical structure of TPBA (left) and OPE-TA (right). The chemical structures of the $C_{10}H_{21}$ peripheral chains with no chiral center (R_A), a *S*-type stereogenic center (R_S) and an *R*-type stereogenic center (R_R) are shown at the bottom.

Theoretical calculations at the GFN2-xTB semiempirical level were performed to get insight into the relationship between the number of stereocenters and the chirality transfer properties of TPBAs and OPE–TAs, in comparison with BTAs.[25,238,239] These calculations, unless otherwise specified, imply full geometry optimizations of supramolecular oligomers of 20 molecules (20-mers) in gas phase. Subsequently, single-point calculations of the central dodecamers extracted from the previously optimized 20-mers were performed. By using this protocol, a structural model of an infinite supramolecular polymer is tentatively provided, avoiding undesirable terminal effects but keeping the oligomers large enough to be representative of the fibers observed experimentally.

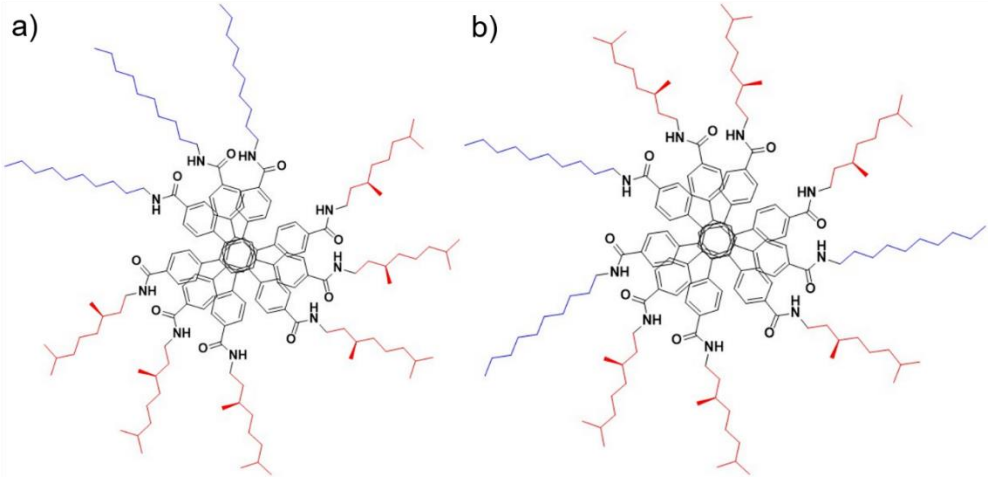

Figure 25. Chemical representation of eclipsed (a) and staggered (b) trimers of **T2**.

Left-handed and right-handed helical aggregates of **TN** and **ON** systems were built up using molecules with **N** = 1, 2 and 3 *R* chiral centers. Note that systems with 1 and 2 chiral side chains do not present C_3 symmetry. This contrasts with previous studies where systems with three chiral or three achiral side chains were only considered.[236,240] Therefore, eclipsed and staggered aggregation patterns, in which achiral and chiral chains are respectively placed in different arms of the helix (eclipsed) or are intercalated along the growing direction of the helix (staggered), are possible (Figure 25). All the optimized structures are stabilized by π–π stacking interactions between the central cores and a triple N−H···O=C H-bond array between the amide groups of consecutive monomers, as illustrated in Figure 26.

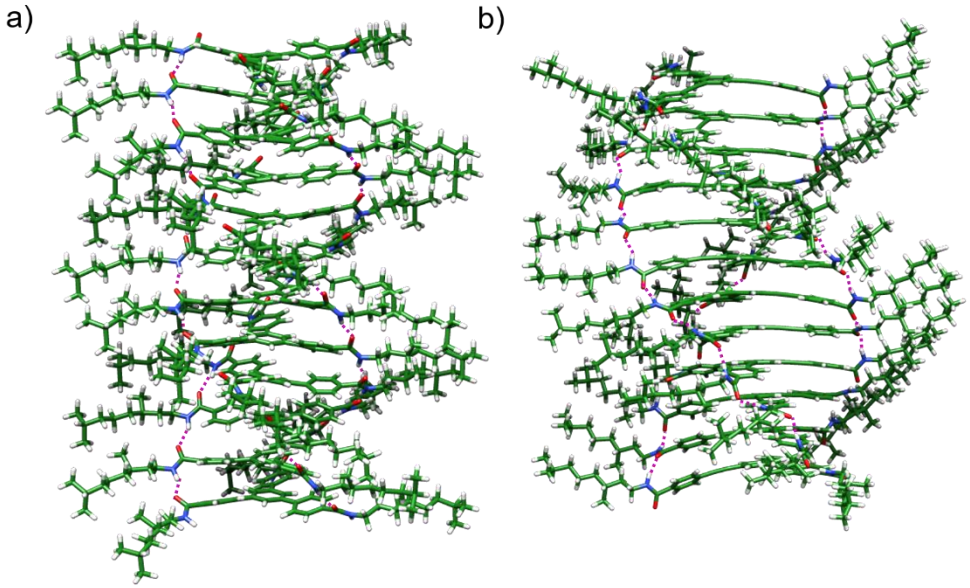

Figure 26. Representation of the central dodecamers extracted from the fully GFN2-xTB-optimized 20-mers of **T3** (a) **O3** (b).

Left-handed (*M*) aggregates in an eclipsed configuration were found to be the most stable for the six systems under study, with the exception of **O1** that was found to be more stable in a staggered disposition (Figure 27). The energy difference between the most stable left- and right-handed aggregates is predicted to increase with the number of chiral chains for TPBAs, with energy differences of 1.0, 5.9 and 16.5 kJ mol^{-1} per monomeric unit for **T1**, **T2** and **T3**, respectively. In OPE–TAs, the energy difference between *P* and *M* helices is calculated with values of 5.0, 2.2 and 6.3 kJ mol^{-1} per monomeric unit for **O1**, **O2** and **O3**, respectively, which are similar to those obtained for TPBAs. OPE–TAs indeed exhibit a different scenario in which the staggered arrangements are found to be more stable for *P*-helices of **O1** and **O2**. Overall, the calculations suggest that the left-handed helices (*M*) are stabilized for the

six molecules under study with *R* chiral centers, independently of the eclipsed or staggered disposition. Thus, the point chirality of the molecule induces a preferential axial chirality on the helix, showing chirality transfer from the molecule to the aggregate.

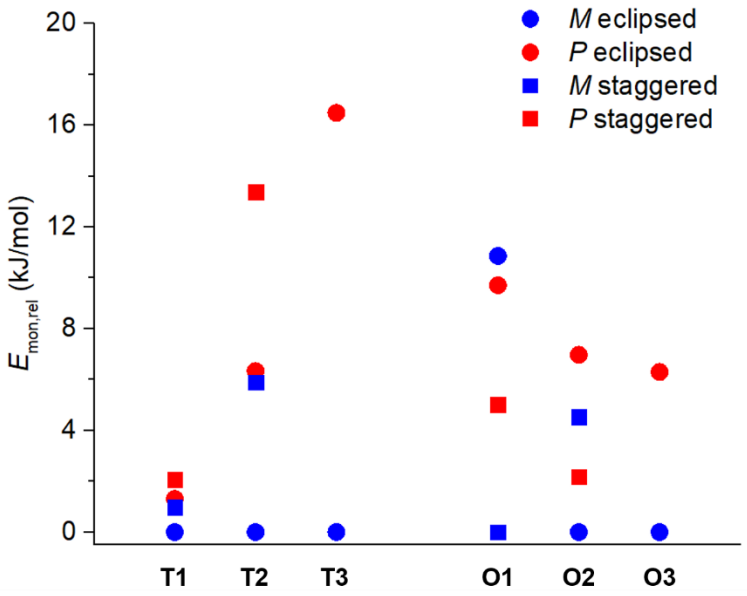

Figure 27. Relative energy per monomeric unit calculated for helical dodecamers of **T1-3** and **O1-3** with right- (*P*) and left-handed (*M*) helicities in eclipsed and staggered dispositions.

The optimized oligomers display slight differences for the most relevant intermolecular parameters (*i.e.*, intermolecular distance, rotation angle and H-bond distances) depending on the number of chiral side chains. TPBA compounds present intermolecular distances (distance between centroids of vicinal benzene cores) of 3.50, 3.44 and 3.49 Å for **T1**, **T2** and **T3**, respectively. The average rotation angles between neighboring molecules

along the stacking axis were computed to be of 26.4, 26.7 and 26.0º, respectively, and the hydrogen-bond distances are also very similar, with average values of 1.85, 1.88 and 1.87 Å, respectively. However, despite the similar values obtained for the intermolecular parameters, the disorder of the peripheral side chains is significantly higher for **T1** (Figure 28). Furthermore, the TPBA core presents a propeller-like nonplanar structure due to the rotation of the phenyl rings attached to the central benzene core to avoid repulsive H···H contacts. The nonplanar geometry of the TPBA core weakens the interaction with vicinal monomers, and produces a deviation from the vertical stacking axis that decreases with the number of chiral side chains. The distance between the centroid of the central benzene ring and the ideal stacking axis lies between 0.56 and 1.76 Å for **T1** and 0.82 and 1.47 Å for **T3**. Therefore, a higher number of chiral chains favor order in the TPBA aggregates because branched chains require a more compact packing, reducing therefore the flexibility and disorder in the aggregate.

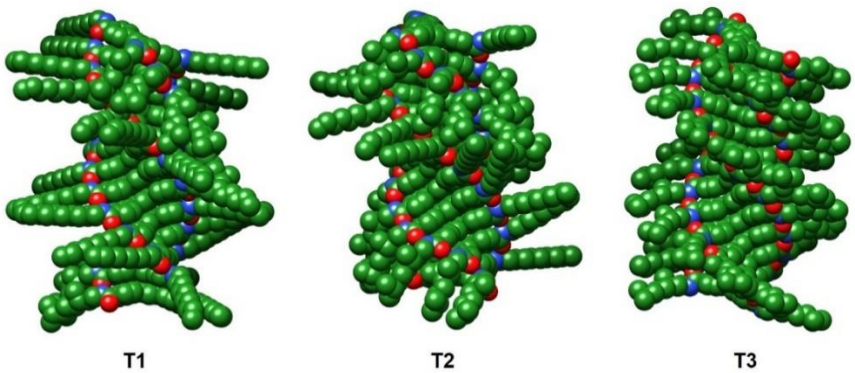

Figure 28. Representation of the most-stable *M*-dodecamers of **T1**, **T2** and **T3**. Hydrogen atoms are omitted for clarity.

The optimized **ON** oligomers constituted by OPE-TA units present a higher order in the supramolecular structure than the **TN** oligomers owing to the planar shape of the monomers. In contrast to TPBAs, the OPE–TA core adopts a fully planar structure in the oligomer because the H···H repulsions mentioned above are completely avoided by the insertion of the acetylenic spacers between the peripheral phenyl groups and the central benzene core. In the **O1**-, **O2**- and **O3**-based oligomers, the molecules are concentrically stacked, with minimal deviations from the stacking axis, and separated by 3.20, 3.26 and 3.25 Å, respectively. The H-bond distances are between 1.73 and 1.95 Å along the *M*-like dodecamers, but the estimated average values are very similar: 1.81 (**O1**), 1.79 (**O2**) and 1.79 Å (**O3**). The average rotation angle between consecutive monomers in the stack slightly increases with the number of chiral chains, with values of 18.3º for **O1**, 18.4º for **O2** and 18.5º for **O3**. The variation of the rotation angle in OPE-TAs is lower than in TPBAs, and it has a lower uncertainty due to the higher order of the OPE-TA oligomers (Figure 29) compared to the TPBA oligomers (Figure 28).

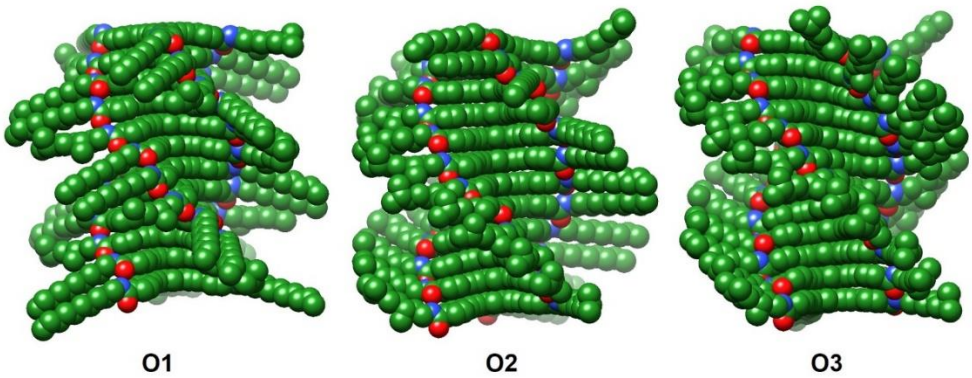

Figure 29. Representation of the most-stable *M*-dodecamers of **O1**, **O2** and **O3**. Hydrogen atoms are omitted for clarity.

The amplification of chirality is a phenomenon by which enantioenriched compounds are generated by the action of a chiral bias. Thus, the systems that show a higher chirality amplification ability require of a smaller amount or excess of the chiral congener. As mentioned above, majority rules (MRs) experiments are used to study the amplification of chirality in enantiomeric mixtures. In MRs experiments, both chiral agents (*R* and *S*) are mixed and the higher chirality amplification is observed when a smaller enantiomeric excess is required to obtain homochiral mixtures. From these experiments, the magnitude obtained to quantify the chirality amplification is the mismatch penalty enthalpy (ΔH_{MMP}). This magnitude measures the energetic cost of introducing a molecule of different chirality in the helix, and thus, lower ΔH_{MMP} means that a smaller enantiomeric excess is needed to obtain homochiral mixtures.

The ΔH_{MMP} values experimentally determined for enantiomeric mixtures of TPBAs at 20 ºC lie around 1.5 kJ mol^{-1} regardless the number of stereogenic centers per monomeric unit. In contrast, the ΔH_{MMP} values for BTAs at 20 ºC decrease from 2.1 to 1.0 kJ mol^{-1}, upon decreasing the number of stereogenic centers per monomeric unit, and those for OPE-TAs increase from 2.0 to 5.4 kJ mol^{-1}.[237,241,242] Therefore, the ΔH_{MMP} values were estimated theoretically to validate the atomistic models proposed and understand how the supramolecular organization determines the chirality amplification properties. The mismatch penalties were theoretically evaluated by inserting a monomer of the wrong enantiomer into the most stable helical conformation computed for the other enantiomer. It should be noted that, to optimize the interactions, the wrong molecule can enter into the aggregate with both an eclipsed or staggered disposition that can be different from that present in the aggregate.

Thus, both dispositions were computed and ΔH_{MMP} was calculated as the energy difference between the lowest-energy oligomer incorporating a molecule of the wrong enantiomer and the completely homochiral aggregate. ΔH_{MMP} values of 1.02, 0.51 and 0.63 kJ mol^{-1} per monomeric unit and per wrong enantiomer were obtained for **T1**, **T2** and **T3**, respectively, and of 3.10, 2.01 and 1.40 kJ mol^{-1} for **O1**, **O2** and **O3**, respectively, in good agreement with those measured experimentally.[241,242] The theoretical ΔH_{MMP} values are slightly smaller but follow the same trends observed experimentally. The values computed for TPBAs are significantly lower than those of OPE–TAs, and are no significantly affected by the number of chiral chains. In contrast, OPE–TAs undergo a notable decrease of ΔH_{MMP} upon increasing the number of chiral chains.

The higher ΔH_{MMP} obtained for OPE–TAs with respect to TPBAs can be rationalized on the basis of the structural parameters computed for the aggregates. In particular, the rotation angle of around 18º estimated for OPE-TAs implies a high steric hindrance between the side chains on vicinal molecules and leads to shorter intermolecular C−H···H−C contacts (*ca.* 3.35 Å) compared with TPBAs (~4.25 Å), for which the larger angle of 26º alleviates the steric hindrance (Figure 30). Although the decrease of ΔH_{MMP} in passing from **O1** to **O3** seems counterintuitive, as a higher steric hindrance would be expected when more branched chains are present, it can be explained by looking to the different contacts between branched chiral chains and achiral chains. Chiral chains display a few strong non-covalent interactions mainly involving the stereogenic groups (Figure 30c). In contrast, the non-covalent contacts between achiral chains are similar all along the carbon-chain because no bulky group forces a special separation of the main chain backbone. This is

in line with the evolution of the rotation angle along the stacking axis that slightly enlarges in passing from **O1** to **O3** to avoid the repulsion of the chiral centers. In contrast, in TPBAs there is no clear trend for ΔH_{MMP} because the contacts imply longer distances (see Figure 30b) and are less affected by the branched chains. Indeed, the rotation angles do not suggest any clear evolution of ΔH_{MMP} with the number of chiral chains and its variation is attributed to the higher disorder observed due to the non-planarity of the monomers. The low ΔH_{MMP} values inferred for TPBAs indicate that the stability of the homochiral mixture is only slightly reduced by the incorporation of the enantiomer to the helical aggregate of its unpreferred helicity.

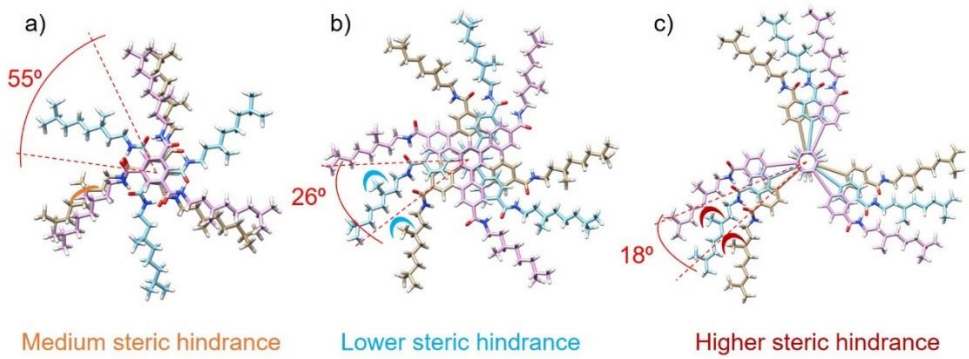

Figure 30. Schematic illustration of the steric hindrance originated by the chiral aliphatic chains in BTAs (a), TPBAs (b) and OPE–TAs (c).

Finally, it is also interesting the comparison between TPBAs and OPE–TAs with the archetypical BTAs studied previously by Meijer.[223,227] To assess this comparison, similar BTA-based aggregates were modeled. BTA aggregates present rotation angles near 55º (Figure 30a), with consistently larger intermolecular contacts between the side chains of neighboring molecules in the range of 5.8–6.5 Å. However, second neighbors in BTAs are quasi-

perfectly stacked, due the rotation angle measured and the C_3-symmetry of the system, and give rise to intermolecular contacts between side chains around 4.0 Å. These contacts are slightly shorter than those between the closer neighbors in TPBAs (~4.25 Å), and longer than the closer intermolecular contacts computed for OPE-TAs (3.35 Å). Therefore, the intermolecular distances between second vicinal molecules in BTAs explain the fact that the values of ΔH_{MMP} in BTAs are between those obtained for TPBAs and OPE-TAs. The atomistic models therefore suggest that the ΔH_{MMP} penalty mainly comes from steric hindrance between the alkyl side chains and help to understand the chirality amplification properties observed experimentally.

Another experiment to study the chirality amplification properties of a supramolecular polymer is the sergeants and soldiers (SaS) experiment, which studies the chiral amplification experienced by the self-assembly of a compound upon the addition of a minute amount of a chiral congener. Unfortunately, this experiment was not possible for TPBAs due to the contamination of linear dichroism observed in the circular dichroism spectra. In a previous work on achiral (**T0**) and fully chiral (**T3**) C_3-symmetric TPBAs, the contamination of the circular dichroism spectra was attributed to the bundling effect favored by van der Waals interactions between the peripheral aliphatic chains of vicinal helical aggregates.[242] To investigate this effect, the bundling of two interdigitated 20-mers was modeled using molecular mechanics simulations. In the previous work, MM calculations predicted a significantly higher interaction energy between **T0** aggregates (–373 kJ mol^{-1}) than for **T3** aggregates (–98 kJ mol^{-1}), and also a shorter separation between the helices of **T0** (29.1 Å) than for **T3** (32.4 Å). This justifies why **T0** assemblies bundle whereas **T3** assemblies do not.[240] Bundles computed for **T1**

and **T2** present, as expected, intermediate interaction energies (–276 and –126 kJ mol^{-1}, respectively) and separation distances (30.0 and 31.5 Å, respectively) between both helices (Figure 31). The larger helix-to-helix interaction energies and the reduction of the helix-to-helix distances found along the series **T3**-**T2**-**T1**-**T0** is justified by the smaller number of branched chains, which hinder an efficient packing. Actually, the high interaction energies predicted for the **T0** and **T1** bundles explain the linear dichroism effects observed experimentally. In contrast, **T2** and **T3** do not present any linear dichroism effect, that may be explained because the much lower interaction energy between the helical oligomers that form the bundle. As conclusion, theoretical calculations indicate that the bundling of the supramolecular polymers based on TPBAs with zero and one chiral chain is responsible for the linear dichroism effects observed experimentally.

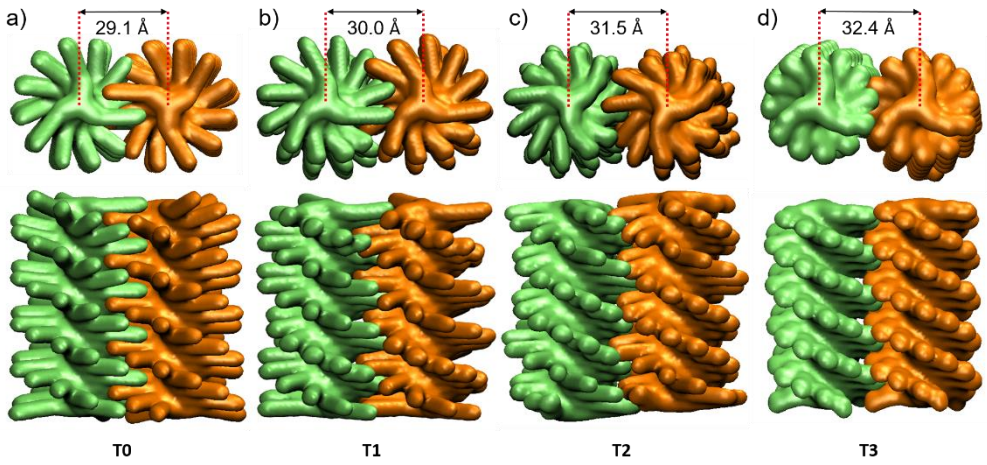

Figure 31. Top and side views of the surface representation of the homochiral helix-to-helix interaction of TPBAs **T0** (a), **T1** (b), **T2** (c) and **T3** (d). The distances between the column centers is indicated in the top view

4.2.2 Liquid crystals based on a T3C$_4$ host–guest complex

Liquid crystals are an intermediate state of matter between the liquid and solid phases. In liquid crystals, molecules may flow as in liquids but preserve a highly ordered structure like in solid crystals.[243] Among others, discotic molecules are perfect candidates for liquid crystals because their molecular structure promotes the self-assembly in ordered columnar or nematic mesophases.[218] Liquid crystals are indeed an appealing alternative for new technological applications due to their interesting optical and electronic functionalities. A representative example of the widely spread use of liquid crystals is the well-known liquid crystal displays (LCD).[244,245]

The star-shaped 2,4,6-tris(triazolyl)-1,3,5-triazine molecule, labelled as **T3C$_4$** (Figure 32a), is a good candidate to form liquid crystals. **T3C$_4$** bears a C_3-symmetric conjugated core that favors an efficient π-stacking thus promoting the columnar self-assembly. Additionally, the voids between the arms of **T3C$_4$** allow the incorporation of complementary units through the H-bonding possibilities offered by the N atoms of the triazine ring and the N and H atoms of the triazole rings (highlighted in red in Figure 32a). However, in contrast to the triscarboxamide systems discussed in Section 4.2.1, where the amide groups can rotate to form hydrogen bonds and reinforce the interaction with vicinal molecules in the direction of the π-stacking, the atoms involved in the H-bonding of **T3C$_4$** will not exhibit that rotation freedom and remain in the **T3C$_4$** plane. Therefore, H-bonds between **T3C$_4$** molecules are not feasible to form columnar aggregates

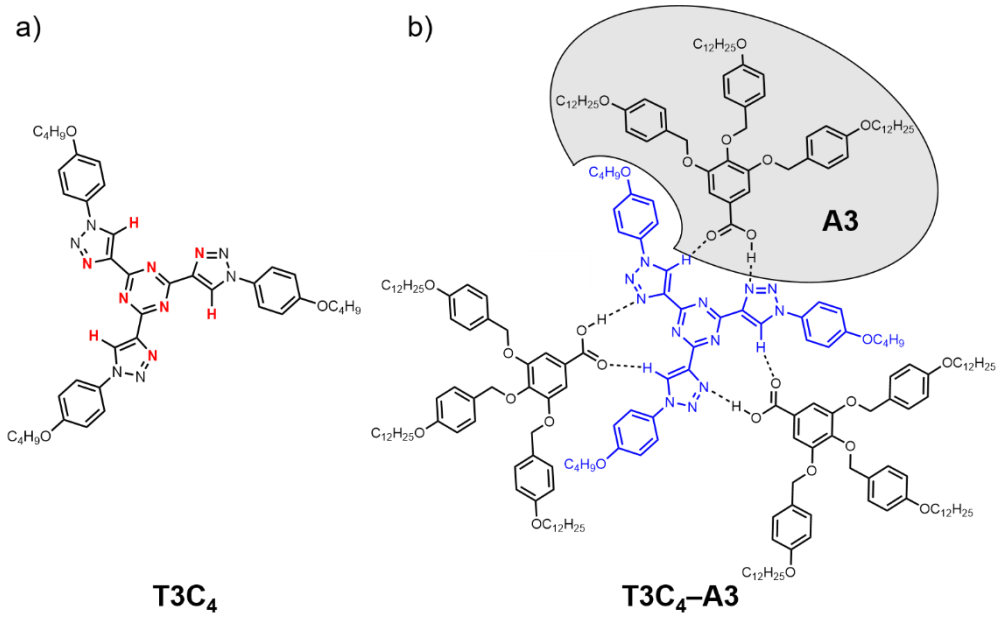

Figure 32. Chemical structure of the **T3C4** unit (a), where the atoms which may promote H-bonds are highlighted in red, and of the 1:3 host–guest **T3C4–A3** complex (b).

The work on the self-assembly of **T3C4**-based systems (Publication 3 in Section 4.4) was done in collaboration with the experimental research group led by Prof. Teresa Sierra from the *Instituto de Ciencias de los Materiales de Aragón*, who synthesized and characterized the **T3C4** unit and its assembled derivatives. They demonstrated that the **T3C4** molecule is able to insert up to three units of 3,4,5-trisubstituted benzoic acids (gallic acid derivatives) through H-bonding interactions leading to 1:3 stoichiometric host–guest supramolecular complexes (Figure 32b) that enhance the formation of hexagonal columnar mesophases.[246] Experiments indeed demonstrate that the **T3C4** molecule by itself does not form ordered liquid-crystal mesophases.[246] In contrast, the **T3C4–A3** supramolecular complex, in which **T3C4** is

combined with the benzoic acid **A3** (Figure 32b), retains the mesomorphic behavior at room temperature being much more stable than the mesophases obtained with other benzoic derivatives bearing alkoxy chains instead of the phenyl rings present in **T3C$_4$–A3**. Therefore, in this section we study, by using different levels of theory, why the insertion of the **A3** acid units provokes such impact on the final liquid-crystal properties. To do that, we focused the study on the interaction of **T3C$_4$** with the **A3** acid and on the self-assembling properties of the resulting **T3C$_4$–A3** host-guest supramolecular complex.

The geometry of the **T3C$_4$** unit was first optimized at the DFT level (B3LYP-D3/6-31G**) assuming two possible conformations: a C_3-symmetric disposition of the triazolyl arms and the non-symmetric disposition observed in the X-ray crystal structure (Figure 33). In gas phase, the C_3-symmetric conformation is computed to be more stable by 2.81 kcal mol^{-1}. Both optimized conformations display a planar core with rotation angles between the central triazine and the attached triazole rings smaller than 1.5º, in good accord with the X-ray structure. In contrast, the rotation angles between the triazole and the vicinal phenyl rings are in the 27–30º range, overestimating the X-ray values. This discrepancy is likely to arise from the packing effects taking place in the crystal.

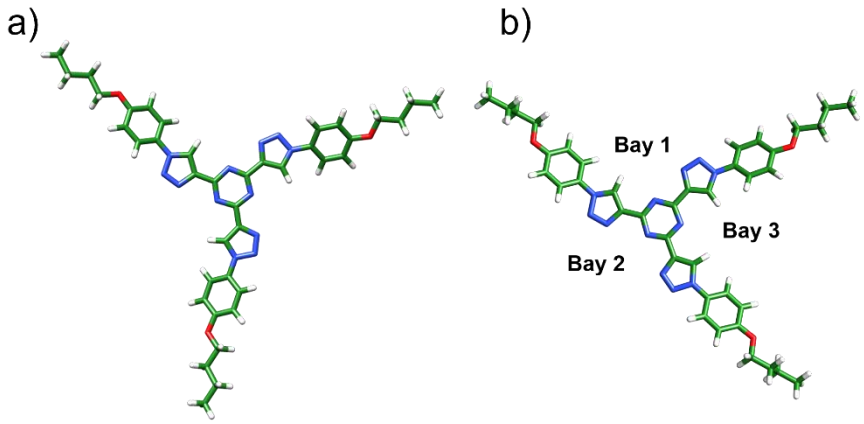

Figure 33. Optimized geometries calculated at the B3LYP-D3/6-31G** level for the C_3-symmetric (a) and asymmetric (b) conformations of **T3C4**.

The host–guest supramolecular assembly between **T3C4** and one benzoic acid molecule was modelled for both the symmetric and non-symmetric conformations of **T3C4** at the B3LYP-D3/6-31G** level. In the C_3-symmetric conformation, the three bays between the arms are equivalent, whereas in the asymmetric conformation three different interaction environments (bays 1–3 in Figure 33b) are possible, bay 1 being equivalent to the bays of the C_3 conformation. Figure 34 displays the interaction of the symmetric **T3C4** with a benzoic acid, with a computed interaction energy of –20.67 kcal mol^{-1}. The H-bond like interactions are labelled as A, B and C. H-bond A is formed between the carbonyl oxygen atom of the carboxylic group and the triazole H atom, with a distance of 2.033 Å. H-bonds B and C are formed between the OH group of the COOH group with the N atoms of the triazole and triazine rings with distances of 1.801 and 3.172 Å, respectively. Therefore, calculations suggest that the host-guest complex between **T3C4** and a benzoic unit is mainly governed by H-bonds with the triazole rings with a weak participation of the

triazine ring. To maximize the interaction, the benzoic acid is out of the **T3C4** plane with a torsional angle of 50º. This gives rise to additional stabilizing C−H···π interactions between the C−H bonds of the terminal phenyl groups and the benzoic acid.

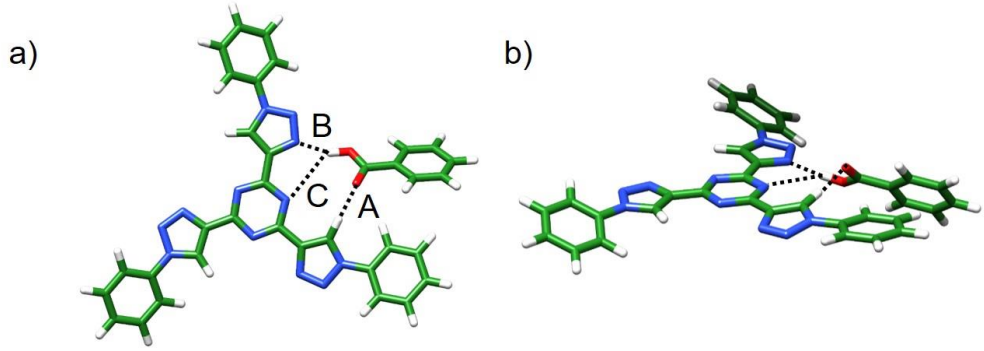

Figure 34. Top (a) and side (b) views of the optimized geometry calculated at the B3LYP-D3/6-31G** level for the host–guest complex formed by a benzoic acid and the C_3-symmetric conformation of **T3C4**.

As stated above, the asymmetric conformer of **T3C4** presents three different positions for the interaction with the benzoic acid (Figure 33b). Figure 35 displays the different host–guest assemblies optimized for this conformer. The structure of the host–guest complex formed through bay 1 (Figure 35a) is equivalent to that found for the symmetric conformation (Figure 34). Two minimum-energy geometries were obtained for the interaction through bay 2 (Figure 35b,c). The first one presents two interactions that stabilize the host–guest complex: a H-bond between the H atom of the COOH group with the N atom of the triazole ring of one arm and the π–π interaction between the benzoic acid and the triazole ring of the other arm. In the second structure, the benzoic acid is set out of the **T3C4** plane in a perpendicular orientation,

allowing the H-bond between the COOH group and the N atom of the triazine. Finally, the interaction through bay 3 leads to a host–guest structure with three H-bond interactions at 1.729, 2.135, and 2.392 Å, respectively (Figure 35d), where the benzoic acid is perpendicular to the **T3C4**. This last structure is the most stable for the complex with asymmetric **T3C4**, but all of them are higher in energy than the complex formed with the C_3 core. This higher stability, together with the disposition of the benzoic acid in the plane of the **T3C4** core and the capability to simultaneously allocate three benzoic molecules, makes the C_3-symmetric structure as the most suitable to form host–guest discotic supramolecular units for further growing in a columnar liquid crystal.

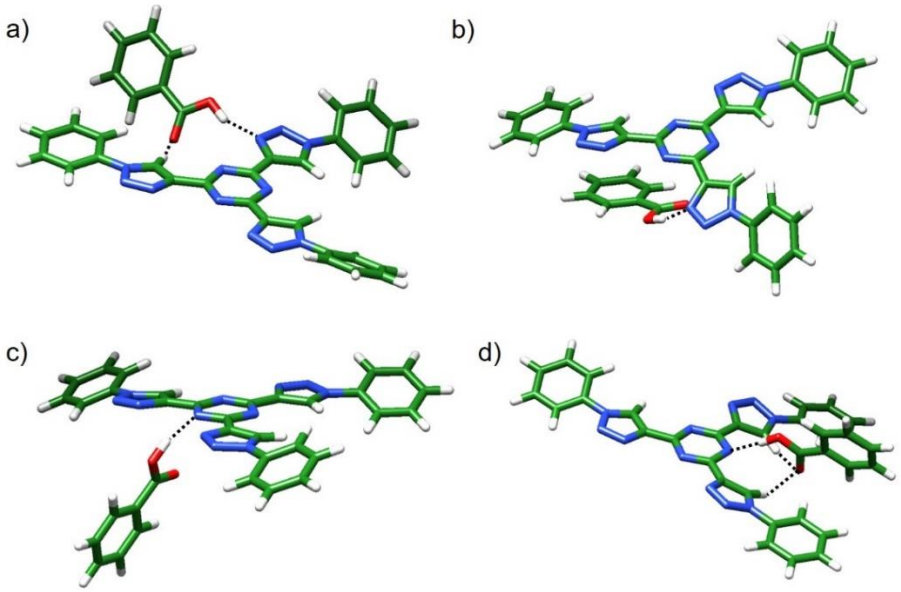

Figure 35. Optimized geometries calculated at the B3LYP-D3/6-31G** level for the host–guest complex formed by a benzoic acid and the non-symmetric **T3C4** molecule. The benzoic acid is interacting through bay 1 (a), bay 2 (b and c) and bay 3 (d).

Once explored the different possible host–guest supramolecular assemblies between **T3C$_4$** and one benzoic molecule, we computed the interaction of the symmetric **T3C$_4$** with two and three benzoic acids to approach the 1:3 supramolecular complex. The binding energy per benzoic unit computed for **T3C$_4$**-benzoic acid complexes with 1:1, 1:2 and 1:3 stoichiometry remains practically constant (~21 kcal mol^{-1}), which suggests that there is no cooperativity between the binding of consecutive acid molecules by **T3C$_4$**.

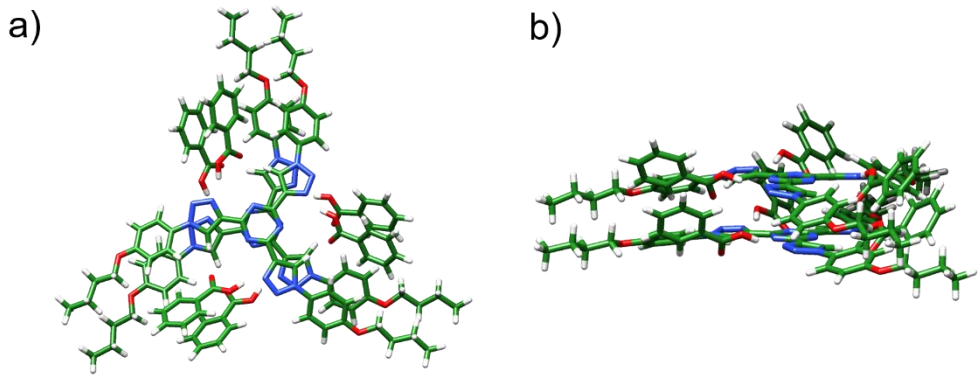

Figure 36. Top (a) and side (b) views of the B3LYP-D3/6-31G**-optimized geometry calculated for a supramolecular dimer of the 1:3 host–guest complex.

In the next step, the self-assembly of the 1:3 host–guest complex was explored by using a multi-level approach. First, a 1:3 **T3C$_4$**-benzoic acid dimer was optimized at the DFT B3LYP-D3/6-31G** level. The dimer shows a helical-like disposition in which the **T3C$_4$** cores are rotated 17° and the centroids of the triazine rings are separated by 3.40 Å (Figure 36). This disposition also favors an efficient π–π stacking between the benzoic acids, which are interacting with the **T3C$_4$** core in the same way as in the 1:1 host–guest complex discussed above (Figure 34). Based on the information extracted from the optimized dimer, a pentamer and an heptamer of a more realistic host–guest

T3C$_4$-A3 complex, in which external O-CH_2-Ph-OC_6H_{13} chains attached to the benzoic acid are included (Figure 37a), were optimized at the semiempirical PM7 level. The optimized aggregates display a helical supramolecular structure similar to the dimer with rotation angles of 16º and a separation between vicinal **T3C$_4$** units of 3.45 Å. This distance is in good agreement with that obtained for the dimer and that estimated for the columnar liquid crystal mesophase based on the X-ray diffraction pattern (3.4 Å).[246] The central molecule of the optimized heptamer was used as the building block of an octamer unit cell that was optimized at the molecular mechanics MM3 level including periodic boundary conditions to avoid terminal effects. Figure 37b,c displays the optimized structure of the unit cell, where the different parts of the 1:3 host-guest **T3C$_4$-A3** complex are highlighted with the colors of the chemical structure shown in Figure 37a. The optimized structure presents a highly ordered helical packing, where both the **T3C$_4$** cores, separated by an average interplanar distance of 3.42 Å, and the benzoic **A3** acids, situated at interplanar distances of 3.75 Å, are interacting by π–π interactions. The presence of the **A3** guests in the interstitial bays of the **T3C$_4$** host induces the helical arrangement of the stack. Furthermore, the outer O-CH_2-Ph-OC_6H_{13} chains of the **A3** acids, colored in red and green in Figure 37b,c, play a crucial role in the high order of the packing. The outer Ph-OC_6H_{13} groups (in red) are perpendicular to the **T3C$_4$** cores and define a parallel-displaced π–π stacking along the rotation of the helix with an average interplanar distance of 3.94 Å. In contrast, the central Ph-OC_6H_{13} groups (in green) lie parallel to the **T3C$_4$** cores forming also a long range parallel-displaced π–π stack and promoting CH⋯ π interactions with the outer groups. A highly-packed helical columnar

self-assembly is therefore obtained for the host–guest supramolecular **T3C$_4$-A3** complex.

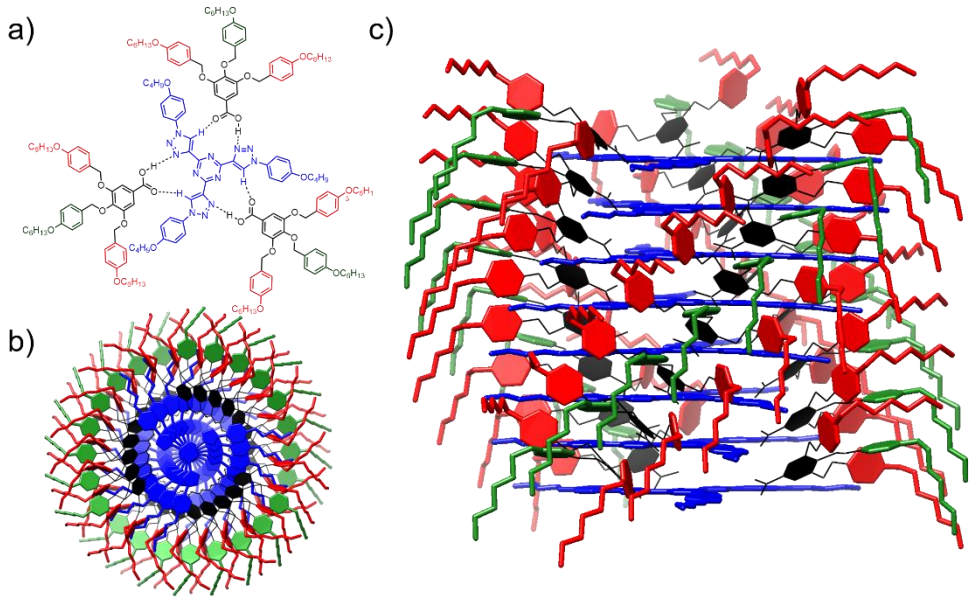

Figure 37. a) Chemical representation and color scheme of the 1:3 **T3C$_4$-A3** host–guest complex used in the PM7 and MM3 calculations. Top (b) and side (c) view of the octamer **T3C$_4$-A3** unit cell minimized at the MM3 level using periodic boundary conditions. Hydrogen atoms are omitted for clarity.

Finally, to analyze the effect of the **A3** acids on the ordering presented by the final supramolecular aggregate, comparative MD simulations using the MM3 force field and periodic boundary conditions were performed for the optimized **T3C$_4$-A3** helical stack and a **T3C$_4$** columnar assembly where the benzoic acids were removed. Figure 38a shows the final snapshots extracted from the two MD simulations. Notably, theoretical calculations reveal that the aggregate of the full 1:3 **T3C$_4$-A3** supramolecular complex maintains a high degree of order along the whole simulation (Figure 38b). The rotation angles and the distances

between the **T3C4** centroids remain constant with small fluctuations with time, and the helical disposition of the **T3C4** cores is preserved along the MD simulation. In contrast, the adjacent molecules in the **T3C4** assembly can easily rotate and displace and the stacking structural parameters suffer large variations with time (Figure 38b). This leads to a loss of regularity in the assembly, which no longer exhibits a helical arrangement although partially preserves the columnar stack (Figure 38a). The higher disorder predicted for the **T3C4** assembly disfavors the formation of liquid-crystal mesophases in accord with the experimental evidence.

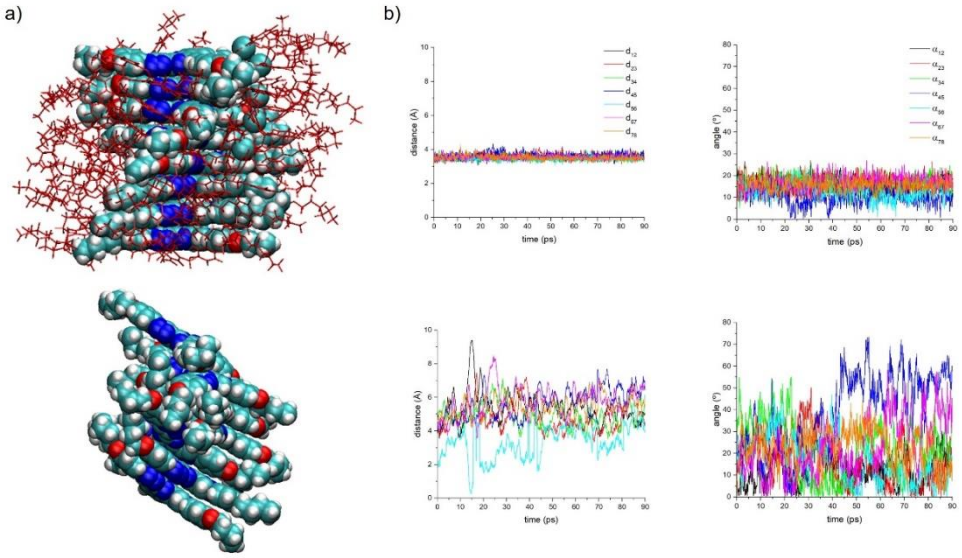

Figure 38. a) Structure of the **T3C4-A3** and **T3C4** octamer unit cells after 90 ps of MD simulations at room temperature. The **A3** moieties are represented by thin red lines. b) Time evolution of the distance between the centroids of the triazine rings (left) and the rotation angles (right) of vicinal molecules for the two MD simulations (top: **T3C4-A3**, bottom: **T3C4**).

To sum up, theoretical calculations indicate that the formation of stable columnar helical aggregates of the 1:3 host-guest **T3C$_4$-A3** complex is largely favored by the interplay between the effective H-bonds, taking place in the supramolecular building block, and the π–π and CH⋯ π interactions between adjacent molecules in the stack. The non-covalent attachment of the **A3** benzoic acids to the **T3C$_4$** moiety generates a template effect in the self-assembly, that favors the compact and highly-ordered helical packing of the **T3C$_4$-A3** supramolecular aggregates able to form columnar liquid crystals in line with the experimental evidence.

4.2.3 Pathway complexity in the aggregation of a squaramide-based macrocycle

Up to now, only helical self-assemblies have been shown and discussed. However, supramolecular chemistry may show more complicated scenarios where the same molecule gives rise to different aggregates under different experimental conditions (concentration, solvent, temperature, etc.). This diversity, that allows achieving supramolecular aggregates with different structural and functional properties (chirality, emission, etc.) from one starting compound, is known as *pathway complexity* and enriches the field of supramolecular chemistry.[209,247,248] Consequently, controlled disassembly and re-assembly in a different functional supramolecular structure by external stimuli as temperature or solvent polarity is highly desired and has become a powerful tool for the development of stimuli responsive nanomaterials.[20,249,250] However, to devise the systems that will give rise to a particular type of aggregates with specific properties and to know the conditions required for

obtaining those aggregates are not an easy task. A common strategy to achieve that goal is to design systems bearing different interaction patterns that can be selectively induced by external stimuli.[18,229,251] On the other hand, computational modelling is a powerful tool that allows to screen the different self-assembling chemical strategies and to provide atomistic models of the structural, energetic and optoelectronic properties of the achievable aggregates.

The work presented in this Section (Publication 4 in Section 4.4) was performed in collaboration with the research group led by Dr. B. Soberats from the *Universitat de les illes Balears* who synthesized and characterized a macrocycle based on two squaramide (SQ) centers labelled **MSq** (Figure 39a). This bissquaramide macrocycle presents pathway complexity giving rise to two aggregation patterns that can be achieved by using the good solvent–bad solvent approach: chloroform ($CHCl_3$) as good solvent and methylcyclohexane (MCH) as bad solvent.

The experimental absorption spectra reveal the existence of two different aggregates depending on the MCH:$CHCl_3$ solvent mixing ratio (Figure 39b).[252] In pure $CHCl_3$ (good solvent), the spectrum corresponds to that of non-aggregated monomeric **MSq** with a broad band centered at 285 nm (black line). Upon MCH addition, a blue shift of the band takes place (blue line), which is attributed to the formation of an H-aggregate labelled as **AggA**. Finally, when the MCH is the major component (red and orange lines), the absorption spectrum drastically changes showing a splitting of the initial band in one blue-shifted band peaking at 268 nm and one red-shifted band at 322 nm, which suggests that a different aggregate is formed (named as **AggB**). The existence

of two different aggregates is furthermore confirmed by the AFM images obtained for spin-coated 1:1 and 3:1 MCH:$CHCl_3$ solutions (Figure 39c). Cyclic-shape aggregates are observed for the 1:1 solution corresponding to the initial H-aggregate, whereas fibrillary aggregates for the 3:1 solution that shows the uncommon splitting of the spectra (see Publication 4 for more details about the experiments). However, experiments do not provide neither any information about the supramolecular structure of the aggregates, nor an explanation of the uncommon changes observed in the absorption spectra. In this section, theoretical calculations are used to unravel the different aggregation patterns by means of structural models and, based on these models, the reasons explaining the changes observed in the absorption spectra. An excitonic Kasha's model has been used to study the electronic spectra of the aggregated species.

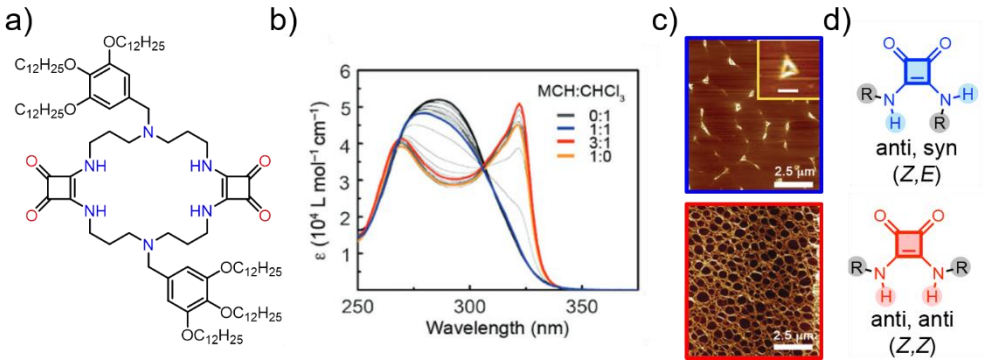

Figure 39. a) Chemical structure of the **MSq** bissquaramide-based macrocycle. b) UV-vis absorption spectra of **MSq** (2.3×10^{-4} M) in different MCH:$CHCl_3$ mixtures. c) AFM height images of spin-coated solutions of **MSq**

in MCH:$CHCl_3$ 1:1 (top) and 3:1 (bottom). d) Chemical representation of the *Z*,*E* and *Z*,*Z* conformations of disecondary squaramides.

A conformational exploration at the GFN2-xTB level using the Grimme's CREST program[253,254] was first performed for the **MSq** macrocycle without the terminal tris(dodecyloxy)benzyl moieties (labelled as **MM** model) and the SQ units in both *Z*,*Z* and *Z*,*E* conformations (Figure 39d). The *Z*,*Z* and *Z*,*E* conformers are usually detected in solution, whereas the *E*,*E* rotamer is highly unfavoured due to steric factors.[255–257] In the case of **MSq**, NMR and FT-IR spectra in different MCH:$CHCl_3$ mixtures suggest that the SQ units are in a *Z*,*E* conformation in the **AggA** aggregate, whereas they may display the more symmetric *Z*,*Z* conformation in **AggB** (see Publication 4). Due to the high flexibility of the **MSq** macrocyle, as many as 626 conformers were obtained from the conformational sampling with *Z*,*Z*-SQ units in an energy window of 6.0 kcal mol^{-1}. In contrast, only 7 conformers were obtained for the *Z*,*E* isomer. Despite the large number of conformers, most of them are quite similar and only the most stable and those that may promote efficient self-assembly were selected for further analysis. The selected conformers were then further reoptimized at the B97-D3/cc-pVTZ level in $CHCl_3$. Figure 40 displays the most relevant structures found for the **MM** model bearing *Z*,*Z*- (conformers **MM1** and **MM2**) and *Z*,*E*-SQ units (conformers **MM3** and **MM4**), and the relative energy differences computed at the GFN2-xTB and B97-D3/cc-pVTZ levels in $CHCl_3$.

Conformer **MM1** (Figure 40a) displays planar SQ units in an almost orthogonal orientation, interacting between them through a short H-bond of 1.95 Å. In contrast, **MM2** shows a zig-zag-like shape with an antiparallel

disposition of the SQ centers, leading to a quasi C_i-symmetric structure stabilized by two intramolecular H-bonds (1.95 Å) between the tertiary amine N atoms and the nearest NH group of the squaramides. Furthermore, it is important to emphasize that in **MM2**, unlike **MM1**, the functional groups of the SQ units that are able to form H-bonds are sterically alleviated, allowing the interaction through H-bonds with other **MM** molecules. Therefore, the **MM2** conformer is expected to promote a more efficient self-assembly than **MM1**.

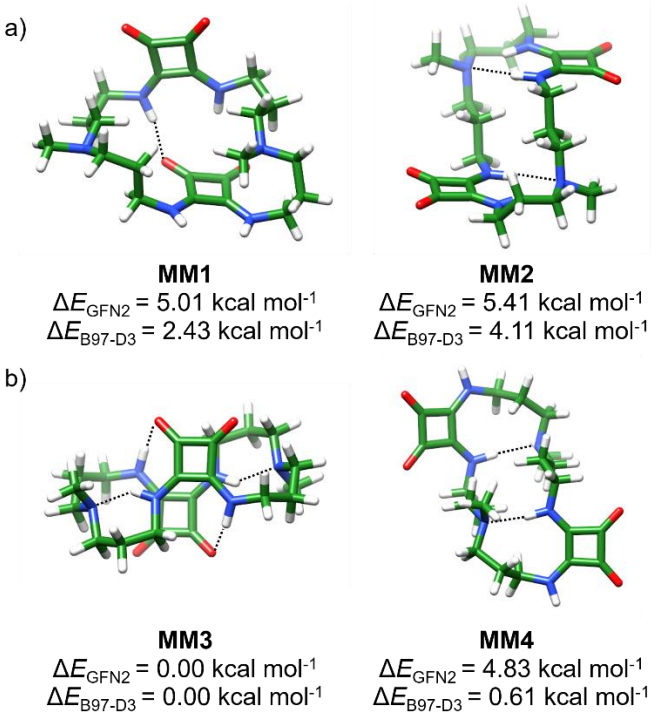

Figure 40. B97-D3/cc-pVTZ minimum-energy geometries computed for **MM** with SQ units in *Z,Z* (a) and *Z,E* (b) conformations. Relative energy differences with respect to the most stable conformer (ΔE) are provided for the optimized structures at both the GFN2-xTB and B97-D3/cc-pVTZ levels.

MM3 and **MM4** (Figure 40b) are the most stable conformers found for the *Z*,*E* isomer. **MM3** presents a C_i-symmetry where the squaramide units are stacked in an antiparallel slightly-shifted disposition, leading to short C−C contacts around 3.15 Å between both squaramides. The **MM3** conformer displays four intramolecular H-bond interactions: two H-bonds between one O atom of a SQ with the NH group in *Z* disposition of the other SQ unit, and two H-bonds between the N atoms of the tertiary amine groups with the NH groups in *E* disposition. Similarly to **MM2**, **MM4** displays a symmetric zig-zag-like structure with two intramolecular H-bond interactions (~2.00 Å) between the tertiary amine N atoms and the NHs in *Z* disposition.

In terms of stability, the *Z*,*E* isomers (**MM3** and **MM4**) are found to be more stable than the *Z*,*Z* isomers (**MM1** and **MM2**), the **MM3** structure being the most stable at both the GFN2-xTB and B97D3/cc-pVTZ levels. At GFN2-xTB, the two *Z*,*Z* conformers are higher in energy by 5.0–5.5 kcal mol^{-1}. The energy differences are reduced at the DFT level, which is indicative that all conformers may coexist in solution. However, **MM1** does not present a conformation that may easily aggregate. Therefore, only the **MM2**, **MM3** and **MM4** conformers are proposed as good candidates to form aggregates.

Aggregates of increasing length based on **MM2**, **MM3** and **MM4** were therefore built up and optimized at the GFN2-xTB level. Figure 41 displays the fully optimized geometry of the supramolecular trimers derived from the three conformers of the **MM** bisquaramide-based macrocycle. Although trimers are small oligomers, they are representative of longer aggregates because they hardly present terminal effects. The **MM2** conformer gives rise to a linear supramolecular arrangement, in which the centers of the **MM**

monomers are separated by 6.1 Å (Figure 41a). In this arrangement, the internal H-bonds are broken, but each **MM** molecule promotes four H-bonds in the 1.88–1.91 Å range with the vicinal molecule, leading to a head-to-tail aggregation pattern. A linear arrangement was also found for the aggregate based on the **MM3** conformer (Figure 41b). In this aggregate, the intramolecular H-bonds between the tertiary amines and the NH groups in *E* disposition are kept. However, the H-bonds between the squaramides found in the isolated conformer are broken to form two intermolecular H-bonds between carbonyl groups and NH groups in *Z* disposition of vicinal monomers. Finally, the supramolecular structure obtained from the **MM4** conformer presents a side-to-side H-bonding pattern, where each SQ forms two intermolecular H-bonds through the CO and NH groups. This aggregation pattern may grow up in a zig-zag stairs-like structure (Figure 41c) or in a more linear way (Figure 41d) with no significant energy difference. The combination of both arrangements may lead to cyclic aggregates.

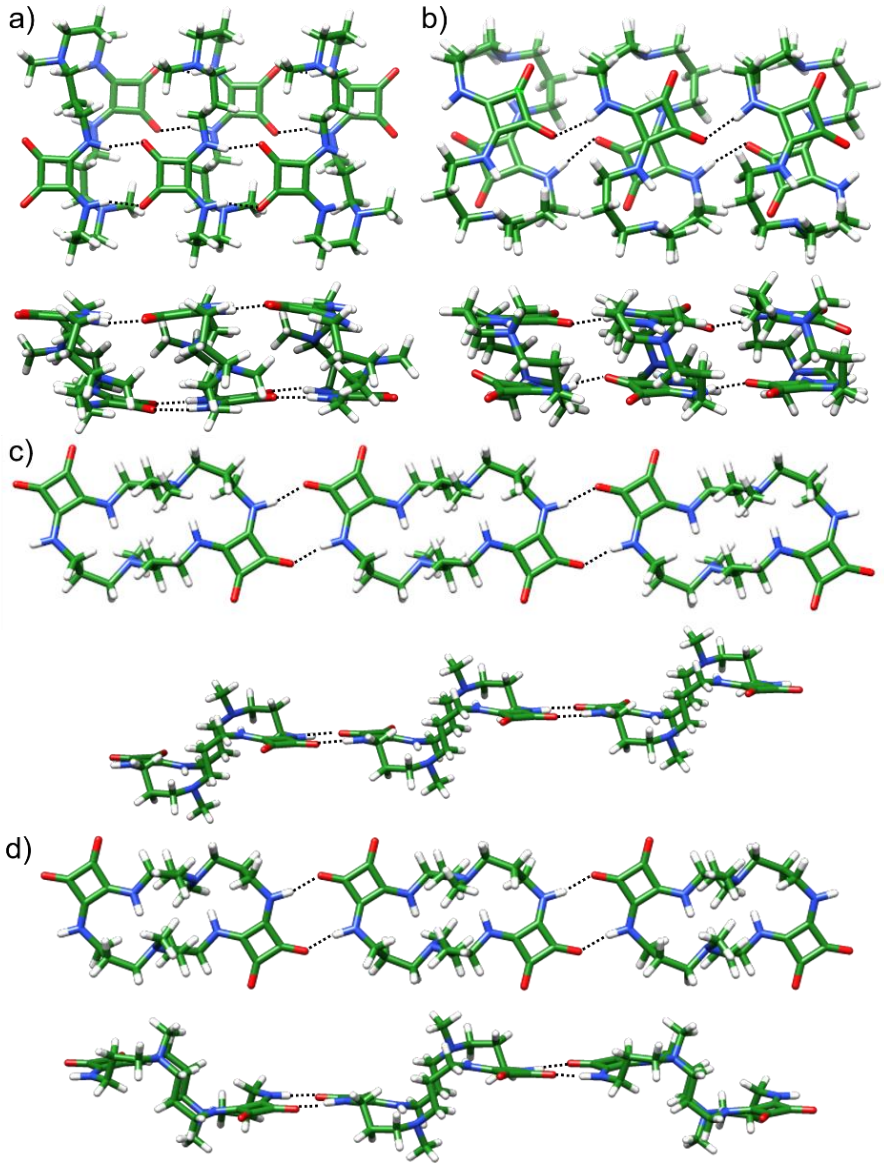

Figure 41. Minimum-energy geometries computed at the GFN2-xTB level in $CHCl_3$ for supramolecular trimers of the **MM2** (a), **MM3** (b) and **MM4** (c and d) conformers.

Figure 42 shows the evolution of the binding energy per monomeric unit (ΔE_{bind}) calculated at GFN2-xTB for **MM2**, **MM3** and **MM4** aggregates upon increasing the size of the aggregate. ΔE_{bind} remains mainly constant for the **MM3** and **MM4** aggregates, the latter being more stable by ~2 kcal mol^{-1} per monomeric unit. In contrast, ΔE_{bind} increases significantly for the **MM2** aggregates until a remarkable size (10–12 monomers) is achieved. This suggests a cooperative nucleation-elongation mechanism for the supramolecular polymerization of the **MM2** (*Z*,*Z*) conformer. Furthermore, it is important to emphasize that the **MM2** (*Z*,*Z*) aggregate becomes significantly more stable than those based on **MM3** and **MM4** upon increasing the size of the oligomer, although the initial monomer was the most energetic. The higher stability of the **MM2** aggregate is likely due to the larger number of intermolecular interactions with each neighbor, four H-bonds instead of two.

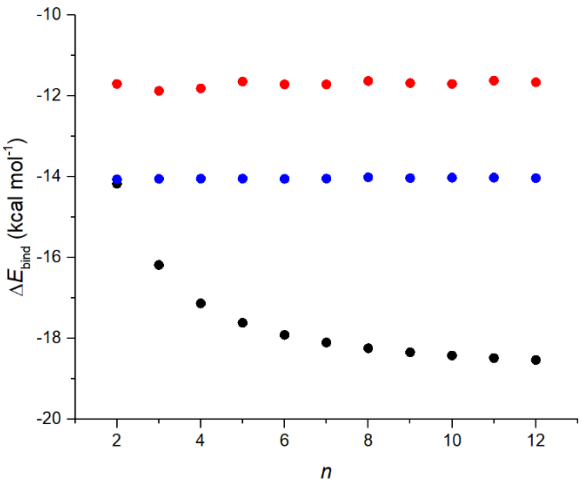

Figure 42. Binding energy per monomer unit (ΔE_{bind}) as the number of monomers (*n*) increases computed for fully optimized (**MM2**)$_n$ (black), (**MM3**)$_n$ (red) and (**MM4**)$_n$ (blue) aggregates at the GFN2-xTB level in $CHCl_3$.

Theoretical calculations therefore indicate that the most stable aggregation pattern is the head-to-tail arrangement obtained from the **MM2** (*Z*,*Z*) conformer, in which each **MM** unit interacts by a total of eight H-bonds which its two neighboring **MM** molecules. The linear shape and higher stability of this aggregate promotes a long-range self-assembling growth and is therefore associated with the **AggB** aggregate observed experimentally, which incorporates *Z*,*Z*-SQ units and forms fibrillar structures (Figure 39c). On the other hand, the **MM3** and **MM4** (*Z*,*E*) conformers self-assemble following a side-to-side pattern, in which each **MM** monomer shares a total of four H-bonds with its two vicinal molecules. The **MM4** aggregate, which is more stable than the **MM3** aggregate, is associated to the **AggA** aggregate detected in 1:1 MCH:$CHCl_3$ solvent mixtures, which includes *Z*,*E*-SQ units and forms cyclic structures (Figure 39c). Additionally, the **MM4** aggregate presents two different growing shapes (zig-zag and linear, Figure 41d) that combined may lead to cyclic arrangements.

After the structural study, the excited states of the aggregates were computed to validate the proposed aggregation models. First, the absorption spectra of the **MM2** and **MM4** conformers were computed by means of TDDFT calculations with the ωB97X-D functional and the cc-pVDZ Dunning's basis set in $CHCl_3$. Both conformers show two bright electronic transitions in the 4.62–4.79 eV energy window (259–269 nm) with similar intensities (Figures 43 and 44), which can be ascribed to the experimental broad absorption band peaking at 285 nm (Figure 39b). For both conformers, the transitions have the same nature and are described as a combination of the π-π* HOMO–1, HOMO → LUMO, LUMO+1 and HOMO–1, HOMO → LUMO+2, LUMO+3 monoexcitations, respectively.

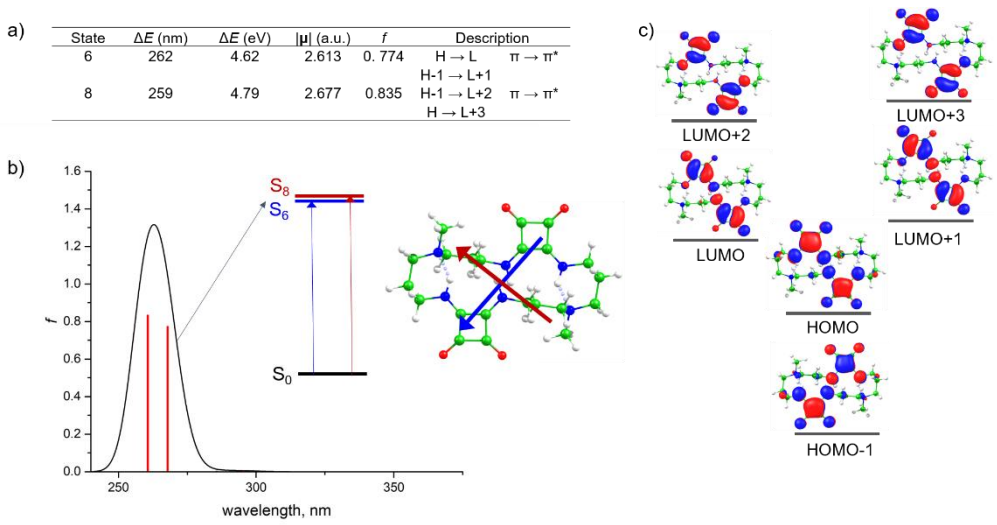

Figure 43. a) Excitation energy (Δ*E*), module of the transition dipole moment (|**μ**|) and oscillator strength (*f*) calculated for the lowest-lying singlet excited states of the **MM2** conformer at the ωB97XD/cc-pVDZ level in $CHCl_3$. H and L denote HOMO and LUMO, respectively. b) TDDFT stick (red lines) and Gaussian-convoluted (black) absorption spectrum of the **MM2** conformer. A diagram of the lowest-energy bright electronic transitions together with the directions of the associated transition dipole moments is provided. c) Isovalue contours (±0.03 a.u.) and relative energy position of the frontier molecular orbitals computed for **MM2** at the ωB97X-D/cc-pVDZ level in $CHCl_3$.

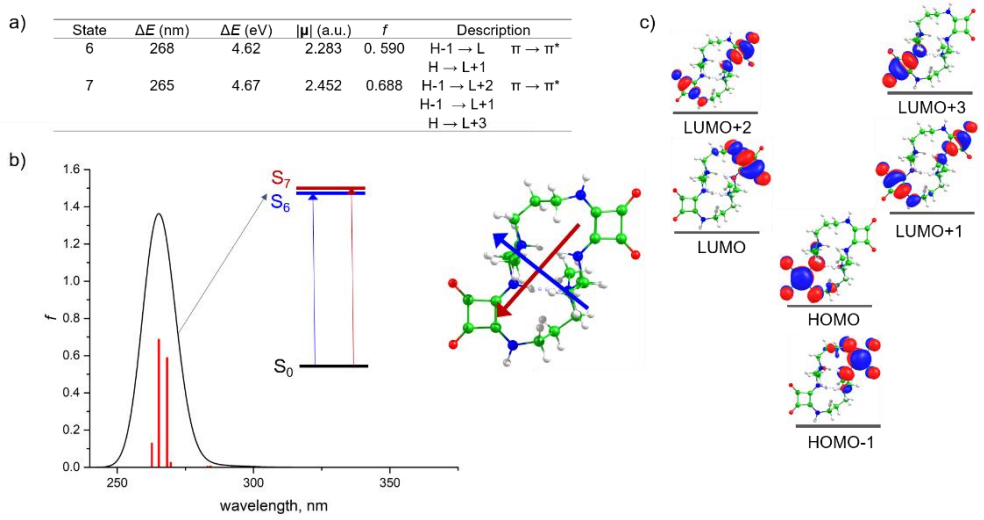

Figure 44. a) Excitation energy (Δ*E*), module of the transition dipole moment (|**μ**|) and oscillator strength (*f*) calculated for the lowest-lying singlet excited states of the **MM4** conformer at the ωB97XD/cc-pVDZ level in $CHCl_3$. H and L denote HOMO and LUMO, respectively. b) TDDFT stick (red lines) and Gaussian-convoluted (black) absorption spectrum of the **MM4** conformer. A diagram of the lowest energy bright electronic transitions together with the directions of the associated transition dipole moments is provided. c) Isovalue contours (±0.03 a.u.) and relative energy position of the frontier molecular orbitals computed for **MM4** at the ωB97X-D/cc-pVDZ level in CHCl3.

Prior to studying the optical properties of the **MM**-based supramolecular aggregates, the singlet excited states of a simple SQ unit in its *Z,Z* (C_{2v}-symmetry) and *Z,E* (C_s-symmetry) conformations were also computed. Similarly to the **MM** conformers, two bright singlet-excited states with energies in the 256–264 nm (4.69–4.84 eV) range are predicted for both SQ isomers. The electronic transitions associated to those states present orthogonal transition dipole moments, as it also predicted for the **MM** conformers (Figures

43 and 44), and are dominated by HOMO → LUMO and HOMO → LUMO+1 monoexcitations, respectively. The bright excited states of the C_{2v}-symmetry *Z,Z* isomer indeed belong to different symmetry irreducible representations (A_1 and B_2), which facilitates the analysis of the aggregates.

The unusual optical properties experimentally observed for the **MSq**-based supramolecular polymers were investigated by using a simplified structural model. For instance, the head-to-tail H-bonding pattern of **MM2**-based aggregates can be visualized as an antiparallel arrangement of two SQ tapes (Figure 41a and Figure 45a-top). Indeed, the optical properties can be explained using a simplified model of the aggregate consisting of a single tape of interacting SQ molecules (Figure 45a-bottom). This simplification is justified because the electronic communication between the two SQ units of the macrocycle appears to be very weak. TDDFT calculates for long SQ oligomers with *Z,Z* conformation, $(SQZZ)_n$ (n = 5, 7, 9 and 11), clearly predict a splitting of the band resulting from the monomer bright states (Figure 45b).

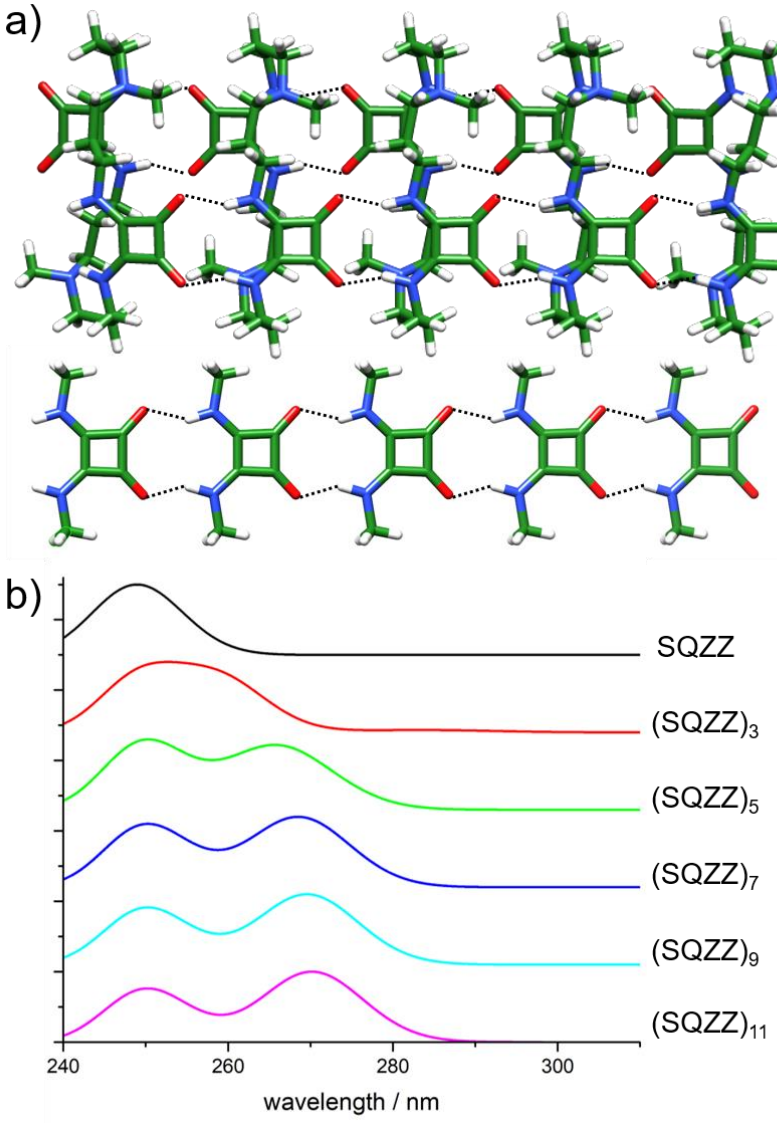

Figure 45. a) Comparison between a full **MM2**-based pentamer (top) and a simplified aggregate model using only a tape of interacting SQ molecules with a head-to-tail H-bonding pattern (bottom). b) Normalized Gaussian-convoluted TDDFT absorption spectra computed for different C_{2v}-symmetry SQZZ oligomers at the ωB97X-D/cc-pVDZ level

To shed light into the spectral changes promoted by the aggregation process, as schematized in Figure 46a, a simple Frenkel-like excitonic Hamiltonian similar to that used in the Kasha's model but including an extra electrostatic term (Eq. 90) was employed.

$$H = \sum_{i}^{N}\sum_{j}^{S}\left(E_j + K_j\right)\left|i_j\right\rangle\left\langle i_j\right| + \sum_{i}^{N}\sum_{j}^{S} J_C\left(\left|i_j\right\rangle\left\langle (i+1)_j\right| + \left|(i+1)_j\right\rangle\left\langle i_j\right|\right) \qquad (90)$$

In Eq. 90, indexes *i* and *j* run over the number of molecules (*N*) and excited states per molecule (*S*), respectively. $\left|i_j\right\rangle$ is therefore the state in which the *i*th molecule is excited to the *j*th state. The parameters used in the Kasha-like model Hamiltonian (Eq. 90) were obtained from quantum chemical calculations, E_j being the monomer excitation energy in gas phase and J_C the excitonic coupling computed using the approximation developed by Curutchet and Menucci.[258] Finally, K_j is an energy shift that takes into account the change of the excitation energy from the gas phase to the aggregated phase, thus including the environmental effects. K_j was computed as $K_j = \left(E_b - 2J_C\right) - E_j$, E_b being the energy of the bright state of the corresponding H-type and J-type excitonic bands in the quantum chemical calculation of the excited states of the larger aggregate computed (11 molecules). The values employed for the parameters and the final simulated spectra are displayed in Figure 46b and c.

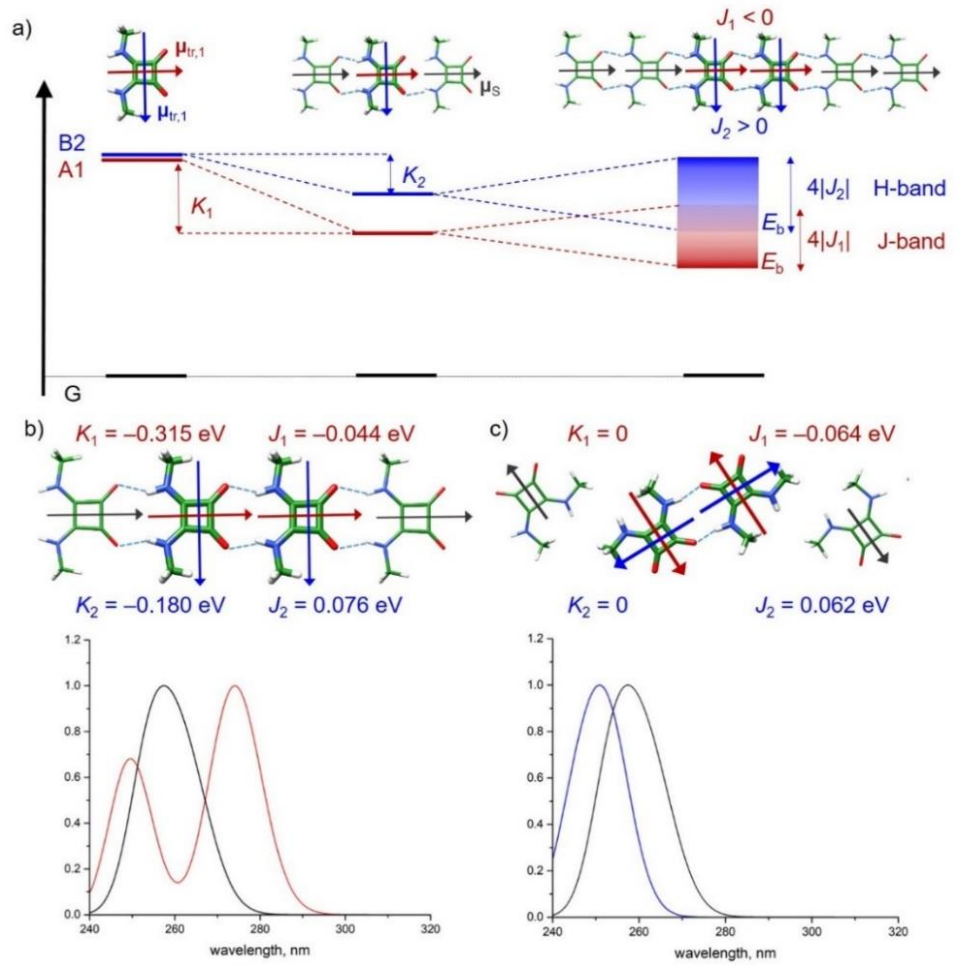

Figure 46. a) Energy diagram to schematically explain the optical properties of SQ-based supramolecular polymers with head-to-tail H-bonding patterns. G denotes the ground state and A_1 and B_2 mean the energetically-close bright excited states of the SQ unit. Linear head-to-tail (b) and side-to-side (c) SQ-based supramolecular polymer models with the parameters used for the Frenkel-type excitonic Hamiltonian, and the theoretical spectra calculated for the monomer (black line) and the respective aggregates (b (red line) and c (blue line)).

Figure 46b shows the simulated absorption spectra obtained from the diagonalization of the model Hamiltonian for both **AggA** and **AggB** aggregates. The simulated spectrum of **AggB** exhibits two absorption bands with maxima at 250 and 274 nm reproducing the experimental absorption band with a double peak at 268 and 322 nm. Therefore, this model confirms that the uncommon splitting of the absorption band is due to two different effects. The first one is the different stabilization that the two bright states of the SQ units experiment in passing from the gas-phase or fully diluted state to the aggregate. The second one is the blue and red shift of each absorption band due to the opposite sign of the couplings, which leads to the appearance of a simultaneous H- (blue-shifted) and J-type (red-shifted) bands. The presence of H- and J-type spectral signatures in the same supramolecular arrangement is an uncommon phenomenon.

The simulated absorption spectrum for **AggA**, which is attributed to a *Z*,*E* SQ-based aggregate with a side-to-side arrangement, only presents a single peak at 251 nm. The parameters computed for this aggregate do not show any stabilization of the SQ excited states when passing from the diluted to the aggregated state, and thus, the stabilization observed in **AggB** is attributed to electrostatic environmental effects due to the permanent dipole moment of the aggregate. Similarly to **AggB**, **AggA** presents H-like and J-like excitonic couplings. However, the effect of the coupling is not enough to split the absorption band, giving rise to a single broad band in the spectrum. The most remarkable feature of the spectrum is the blue-shift of the absorption band compared to the band calculated for a SQ unit in $CHCl_3$. The origin of the blue-shift is due to a hypsochromic solvatochromic effect of the bright states when

varying from $CHCl_3$ to MCH, which is around 0.2 eV, much larger than the excitonic couplings.

4.3 Summary

In this chapter, three different problems related to the structural organization of supramolecular polymers were investigated. In the first one, we delved into the relationship between the supramolecular structure and the transfer and amplification of chirality properties of tricarboxamide-based TPBA and OPE–TA self-assembled supramolecular polymers. These compounds form helical aggregates stabilized by π–π stacking and H-bond interactions that present inherent chirality (axial chirality). Previous experimental evidences proved that right-handed (*M*) or left-handed (*P*) helicities are induced by the presence of *R* or *S* stereogenic centers in the alkyl side chains, respectively; *i.e.*, a transfer of chirality from the molecule to the supramolecular polymer occurs. Additionally, MRs experiments carried out to study the chirality amplification of the tricarboxamide derivatives showed that there was no clear relationship between the number of chiral centers and the evolution of the mismatch penalty enthalpies. In particular, the value of ΔH_{MMP} decreases with the number of chiral chains in OPE-TAs, increases in BTAs and remains constant in TPBAs. Theoretical calculations of large aggregates, which are representative of the bulk of the polymer, reproduce the preferred helicity of the *R* and *S* enantiomers, and reveal that the different behavior in the transfer of chirality arises from the effect of the non-covalent interactions between the side chains. Thus, a correlation between the size and structure of the molecular building

block, that determine the intermolecular arrangement, and the chirality transfer capabilities is found. For OPE-TAs, the ΔH_{MMP} values decrease with the number of chiral centers because of the small rotation angle along the stack (~18º) that gives rise to short H···H contacts (*ca.* 3.35 Å) between the side chains of neighboring molecules that are more extensive for achiral chains. For TPBAs, a larger rotational angle of around 26º is predicted, which leads to longer H···H contacts (longer than 4.25 Å) thus alleviating the steric hindrance. The ΔH_{MMP} values predicted for TPBAs are lower than those of OPE-TAs and remain almost constant upon increasing the number of chiral side chains. Additionally, both systems were compared with BTAs as a reference. BTAs present a slight increase of ΔH_{MMP} values as more chiral side chains are incorporated. Although the distances between side chains on adjacent molecules is quite large (> 6.0 Å), side chains of second neighbors give rise to closer contacts (~4.0 Å) due to the rotational angle of 55º along the stack. These contacts may explain the intermediate values of ΔH_{MMP} obtained for BTAs compared with TPBAs and OPE-TAs. Finally, the bundling of TPBA helices was investigated motivated by the linear dichroism contamination effects observed in the circular dichroism experiments of TPBAs bearing achiral side chains or only one chiral side chain. Calculations reveal that the interaction energy between two interdigitated TPBA helices strongly increases as the number of side chains bearing a stereogenic center decreases, leading to a more effective interdigitation, *i.e.*, to a shorter distance between the helices. Calculations therefore indicate that the bundling of TPBA helices is more likely to occur as the number of chiral side chains is reduced.

The second work addressed enquires into in effect that the H-bonding of **A3** benzoic acids have in the self-assembly of the star-shaped 2,4,6-tris(triazolyl)-

1,3,5-triazine (**T3C$_4$**) moiety. Previous experimental results showed that H-bonded **A3** acids are needed to form stable liquid crystals, since isolated **T3C$_4$** units do not form ordered mesophases. Theoretical calculations show that the C_3-symmetric conformation of the **T3C$_4$** unit is the most stable. This conformation can incorporate three units of the **A3** benzoic acid interacting through H-bonds, and forms a host–guest 1:3 **T3C$_4$-A3** supramolecular complex that can assembly in a columnar way forming helical stacks stabilized by π–π and C−H···π interactions between both the **T3C$_4$** cores and the **A3** acids. The H-bonded **A3** units actually exert a template effect in the self-assembly, that favors the compact and highly-ordered helical packing of the **T3C$_4$-A3** supramolecular aggregates able to form columnar liquid crystals. In contrast, MM/MD simulations showed that **T3C$_4$** assemblies with no acid present a highly disordered structure that precludes the formation of liquid-crystal mesophases.

Lastly, the self-assembly of a bissquaramide-based macrocycle (**MSq**) and the optical properties of the resulting supramolecular aggregates were studied. Experimental data revealed the existence of two aggregates: **AggA** and **AggB**. The **AggA** aggregate presents a cyclic shape, its absorption spectrum is blue-shifted with respect to the isolated macrocycle and the squaramide (SQ) units are suggested to be in a *Z*,*E* disposition. The **AggB** aggregate form fibers, its absorption band splits in two bands, which are red-shifted and blue-shifted with respect to the monomer, and the SQ units bear a *Z*,*Z* disposition. A theoretical conformational screening of the *Z* and *E* isomers of the **MSq** system was initially performed to select the most stable conformations that allow an efficient supramolecular growth. The selected conformer with a *Z*,*E* disposition displays a side-to-side aggregation pattern, which may grow in a

linear or zig-zag isodesmic way. In contrast, the aggregate based on a *Z,Z* conformer presents a linear head-to-tail interaction pattern and grows up in a cooperative way leading to more stable aggregates as the oligomer length increases. The optical properties of both aggregates were studied by using an extended Kasha's model to unravel the origin of the uncommon changes found in the experimental absorption spectra. The blue shift predicted for the side-to-side *Z,E* aggregate nicely correlates with the blue shift experimentally observed for the **AggA** aggregate and is mainly attributed to environmental effects. The simulated absorption spectra of the head-to-tail *Z,Z* aggregate reproduces the splitting of the absorption band found for the **AggB** aggregate. The splitting in red- and blue-shifted bands with respect to the monomer is a quite exotic phenomenon in supramolecular assemblies. Theoretical calculations show that the splitting is associated to different effects: i) an electrostatic stabilization of one of the bright excited states of the SQ units due to the permanent dipole moment of the aggregate, ii) H and J excitonic couplings that produce a blue shift of one absorption band and a red shift of the other band, and iii) the solvatochromic shift due to the change of the solvent composition, responsible for the apparent blue shift of one of the bands. However, the origin of this uncommon phenomenon is still under investigation.

Overall, the main research outcome shared by the three research topics discussed in this chapter is to provide atomistic models that allow to understand the structural, energetic and optical properties, together with the transfer and amplification of chirality properties, of supramolecular polymers resulting from the self-assembly of molecules involving different non-covalent interactions such H-bonding, π–π stacking and C–H···π interactions.

Theoretical calculations proved to be a powerful tool in the field of supramolecular chemistry, where nowadays the systematization of the behavior of the assemblies and the prediction of the properties is a challenging task.

4.4 Publications

Publication 1. E. E. Greciano, J. Calbo, J. Buendía, J. Cerdá, J. Aragó, E. Ortí, L. Sánchez, "Decoding the Consequences of Increasing the Size of Self-Assembling Tricarboxamides on Chiral Amplification", *J. Am. Chem. Soc.*, **2019**, *141*, 7463–7472.

Publication 2. Y. Dorca, R. Sánchez-Naya, J. Cerdá, J. Calbo, J. Aragó, R. Gómez, E. Ortí, L. Sánchez, "Impact of Molecular Size and Shape on the Supramolecular Co-Assembly of Chiral Tricarboxamides: A Comparative Study", *Chem. Eur. J.*, **2020**, *26*, 14700–14707.

Publication 3. B. Feringán, J. Cerdá, B. Diosdado, J. Aragó, E. Ortí, R. Gimenéz, T. Sierra, "On the Structure and Chiral Aggregation of Liquid Crystalline Star-Shaped Triazines H-Bonded to Benzoic Acids", *Chem. Eur. J.*, **2020**, *26*, 15313–15322.

Publication 4. F. Orvay, J. Cerdá, C. Rotger, E. Ortí, J. Aragó, A. Costa, B. Soberats, "Influence of the *Z*/*E* Isomerism on the Pathway Complexity of a Squaramide-Based Macrocyle", *Small*, **2021**, *17*, 2006133

Chapter 5. Charge Transport

5.1 Introduction

Electron transfer is one of the most important processes in the chemistry of electroactive systems, and occurs between an electron-rich donor (D) and an electron-deficient acceptor (A).[259] Whereas electron-donor systems are easily oxidized, showing low ionization potentials, electron-acceptor compounds have large electron affinities and are easily reduced. The electronic and redox properties of π-conjugated organic systems are easily tuned by modifying their chemical structure and attaching electron-donor or electron-acceptor functional groups.[260] This has provided a large variety of organic materials with semiconducting and optical properties suitable for commercial applications in the fields of optoelectronics[261] and photovoltaics.[262,263] Similarly to electrons, holes or electron vacancies, described as positive charges, can be transferred in organic semiconductors but, in contrast to electrons that tend to occupy the lowest-energy unoccupied levels, they reside in the highest-energy occupied levels. We will refer to both processes as charge transfer, which is generally defined as the movement of a charge carrier, either a hole or an electron, from a carrier-rich molecular fragment or molecular moiety to a carrier-deficient one.[259]

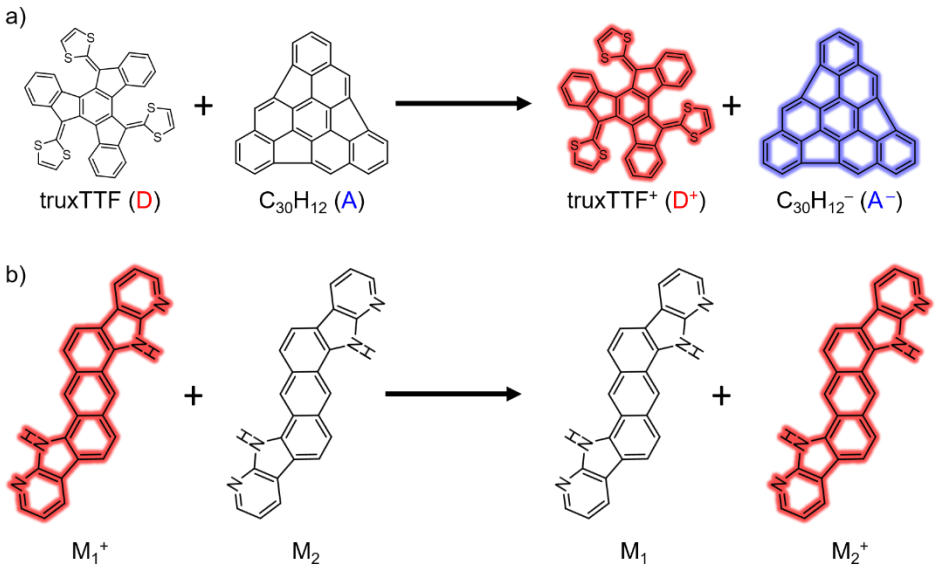

Figure 47. Scheme of the charge transfer reaction in a donor–acceptor (D–A) complex (a) and in a hole transport process (b).

As already mentioned, charge transfer processes have great relevance in organic materials when used as semiconductors in photovoltaic solar cells or in luminescent devices as OLEDs.[264] Efficient charge transfer and charge transport properties are required to obtain high performance devices.[41] A representative example of devices where charge transfer and charge transport play a key role is a bilayer organic solar cell. In these devices, the first process that involves a charge transfer is the charge separation of the exciton at the donor–acceptor (D–A) interface giving rise to the charge carriers.[264] The second process will be the charge migration or transport from the interface to the electrodes through the donor (hole) and acceptor (electron) transporting layers.[41,264]

In the charge transfer process sketched in Figure 47a, charge separation between the donor and the acceptor occurs after the excitation of the donor (photoinduced charge transfer), and later the charges recombine (Figure 48). The D−A pair remains electrically neutral along the photoinduced process but in the charge-separated state the molecular D and A fragments are charged. In contrast, in the hole (or electron) charge transport process sketched in Figure 47b, charge transfer takes place between two identical molecules (one charged and one neutral) and the system (the dimer) has a net electric charge, the initial and final states being equivalent.

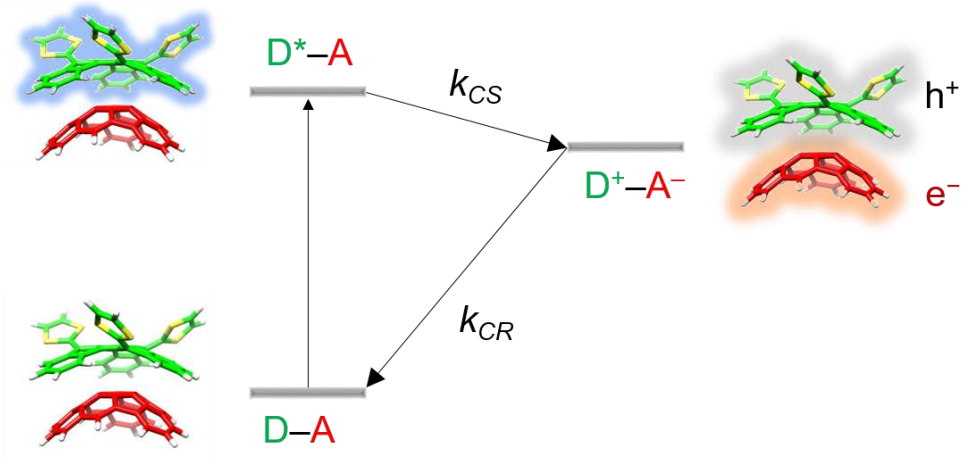

Figure 48. Schematic representation of the photoinduced charge-transfer mechanism in a D−A supramolecular complex.

In this chapter, the theoretical simulation of both types of charge transfer is addressed. Section 5.2.1 is dedicated to the study of a series of hole-transporting materials (HTMs) based on the fusion of the 7-azaindole substructure with π-conjugated polyaromatic systems. The resulting polyheteroaromatic systems (Figure 47b) are prone to self-assemble through

H-bonding. The work presented in this section was done in collaboration with the group of Prof. David Curiel from the *Universidad de Murcia*, who did the experimental synthesis and characterization of the new semiconductors and measured the charge mobilities in organic field-effect transistor (OFET) devices. This collaboration provided a fruitful feedback between experiment and calculations (Publications 5 and 6 in Section 5.4) allowing to understand the effect of the self-assembling ability and the conjugation size of the central polyaromatic spacer on the charge transport properties and, in particular, on the charge mobilities.[265,266] Section 5.2.2 describes the theoretical study of the photoinduced charge transfer undergone in solution by the non-covalent D−A complex formed of truxene-tetrathiafulvene (truxTTF) as donor and the hemifullerene buckybowl ($C_{30}H_{12}$) as acceptor (Figure 47a) (Publication 7 in Section 5.4).[267] The work performed highlights the relevance of considering multi-state effects and accurately treating the effect of the solvent on the excited state energies for a precise theoretical estimation of the charge-separation and charge-recombination rate constants. These rate constants are computed, using the semi-classical Marcus–Levitch–Jortner expression, for all the possible paths mediated by the excited states. All the rates are finally introduced in a kinetic model that allows to simplify the complicated picture due to a manifold of states in a simple three-state picture (ground state, local excited state, and charge transfer state). The global charge-separation and charge-recombination rates estimated from the simplified three-state picture are in good accordance with the experimental values reported in the literature.[268]

5.2 Results and discussion

5.2.1 Hole-transporting materials self-assembled through H-bonds

5.2.1.1 Influence of the hydrogen bonds

Two closely-related systems, 7,15-dihydroanthra[1,2-*b*:5,6-*b′*]diindole (**ADI**) and 7,15-dihydroanthra[1,2-*b*:5,6-*b′*]di(7-azaindole) (**ADAI**), which exhibit similar structure and molecular size (Figure 49a), were studied to assess the relevance of the self-assembly through H-bonds on the charge transport. **ADI** and **ADAI** consist in the fusion of two terminal indole or 7-azaindole units, respectively, with an anthracene central moiety as spacer. They therefore differ in the terminal rings which are either benzene rings in **ADI** or pyridine rings in **ADAI**. The presence of pyridine rings in **ADAI** allows vicinal molecules to interact through $H_{pyrrole}\cdots N_{pyridine}$ H-bonds (Figure 49b), whereas H-bonds in **ADI** are not possible. Therefore, **ADAI** is expected to present a higher-ordered supramolecular structure. Experiments indeed demonstrate that H-bonds are key in the crystal packing found for **ADAI**. Furthermore, organic field-effect transistors were built using both HTM candidates obtaining charge mobilities of 4×10^{-4} and 8×10^{-3} $cm^2\ V^{-1}\ s^{-1}$ for **ADI** and **ADAI**, respectively (see Publication 5 for further details). Our goal was to study theoretically how the self-assembly through H-bonds influences the charge transport properties, and thus, the performance of **ADAI** as HTM.

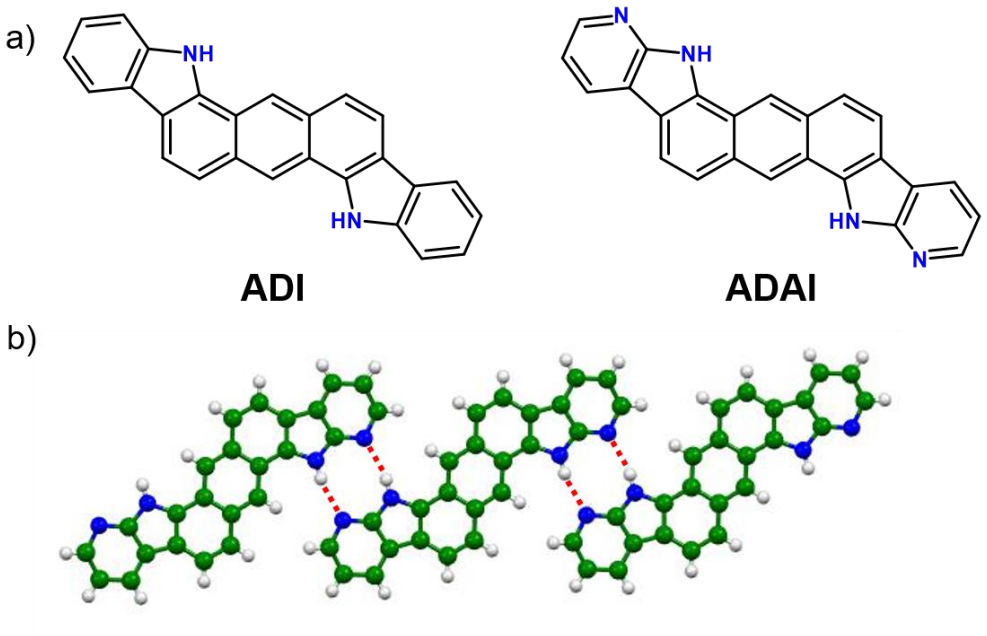

Figure 49. a) Chemical structure of **ADI** and **ADAI**. b) H-bonded structure of **ADAI**.

First, the electronic structure of **ADI** and **ADAI** was studied. Figure 50 displays the topology of the HOMO computed at the B3LYP/6-31G** level in the presence of dimethylformamide (DMF) as solvent using the PCM model. The HOMO presents an identical topology for both systems spreading over the whole conjugated backbone, which should in principle favor the electronic communication between vicinal molecules. Theoretical calculations predict a lower energy HOMO for **ADAI** (–5.12 eV) than for **ADI** (–4.95 eV) in good correlation with the experimental HOMO energies estimated from the oxidation potentials (–5.36 and –5.14 eV, respectively). These values indicate that **ADI** is slightly better donor than **ADAI**.

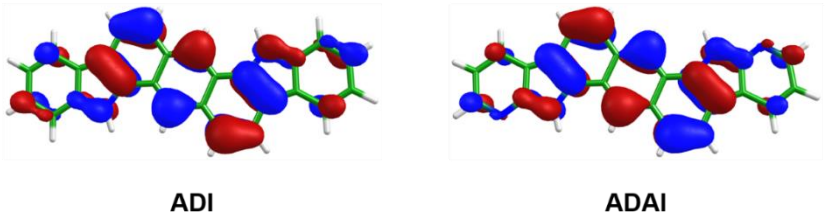

Figure 50. Topology calculated for the HOMO of **ADI** and **ADAI** at the B3LYP/6-31G** level (isocontour surfaces of 0.03 a.u.)

Although the experimental charge mobilities were measured on organic thin films deposited on OFETs, the theoretical simulation of the charge transport properties was performed for the ideal crystal structures. The powder diffraction patterns of the films indeed showed a good correlation with the X-ray patterns obtained for the single crystals thus suggesting a similar ordering of the molecules. Therefore, before going into the study of the transport properties, a brief description of the crystal structures is advisable since the supramolecular organization of the π-conjugated compounds plays a major role in the transport properties. Figure 51 displays the most important features of the herringbone-like crystal packing displayed by **ADI**. As in similar herringbone-packed structures,[269,270] each **ADI** molecule is surrounded by eight neighbor molecules establishing close edge-to-face interactions stabilized by C−H···π and N−H···π and face-to-face π–π contacts (Figure 51a). The slipped disposition of parallel molecules is measured as the shift along the long (1.9 Å) and short (5.4 Å) axis of the molecule (Figure 51b) or by the pitch and roll angles represented in Figure 51c and d, showing values of 39 and 66°, respectively. In summary, the crystal packing of **ADI** can be understood in a simplified way as a body-centered cube packing, where the central molecule

presents an edge-to-face interaction with the eight molecules placed in the corners of the unit cell and a shifted-parallel π–π interaction with the central molecules of the neighboring unit cells.

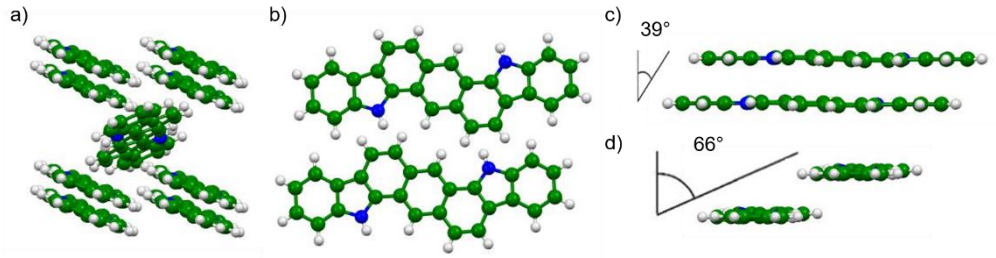

Figure 51. Crystal packing of **ADI**: side (a) and top view (b), and displacement of parallel molecules along the long (c) and short axis (d).

Regarding the crystal structure of **ADAI**, two kind of interactions play a primary role in the final assembly. First, $N{-}H_{pyrrole}\cdots N_{pyridine}$ bonds direct the self-assembly leading to a ribbon-like structure formed by arrays of H-bonded **ADAI** molecules (Figure 52a). The ribbons interact between them through a π-stacking forming a columnar arrangement in which adjacent molecules are shifted by 2.9 and 0.1 Å along the long and short axis with pitch and roll angles of 41 and 2°, respectively (Figure 52b-d). Lastly, the columns of H-bonded ribbons are placed side-to-side in the crystal with a small step of 0.4 Å.

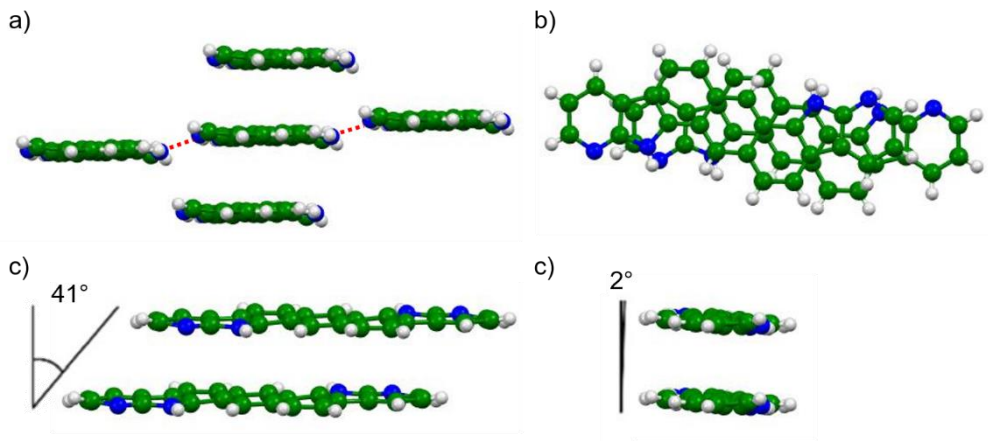

Figure 52. Crystal packing of **ADAI**: side (a) and top view (b), and displacement of parallel molecules along the long (c) and short axis (d).

The charge transport properties of **ADI** and **ADAI** were estimated using a combined protocol that uses DFT calculations, molecular dynamics (MD) simulations and a master equation to finally predict the hole mobilities. Before estimating the hole-transfer rates (k_{ij}) and the respective mobilities (μ), the electronic couplings (hole-transfer integrals t_{ij}) were computed for the most relevant molecular crystal pairs by using the projection method at the B3LYP/6-31G** level. To take into account the fluctuations due to thermal motion, the couplings were calculated for 100 snapshots extracted each 1 ps from a MD simulation of crystal slabs of 91 molecules for **ADI** and 125 molecules for **ADAI**. The sets of t_{ij} values (100 for each system) were fitted to Gaussian distributions with the objective of obtaining the average value ($\langle t_{ij} \rangle$) and the standard deviation (σ_{ij}) that measures the thermal fluctuations (Table 2). Figure 53 shows the crystal supercell representation with the labeling used for each molecular site for both **ADI** and **ADAI**. Note that,

although the **ADI** crystal structure was previously simplified to the edge-to-face and face-to-face interactions, edge-to-face interactions are not all equivalent.

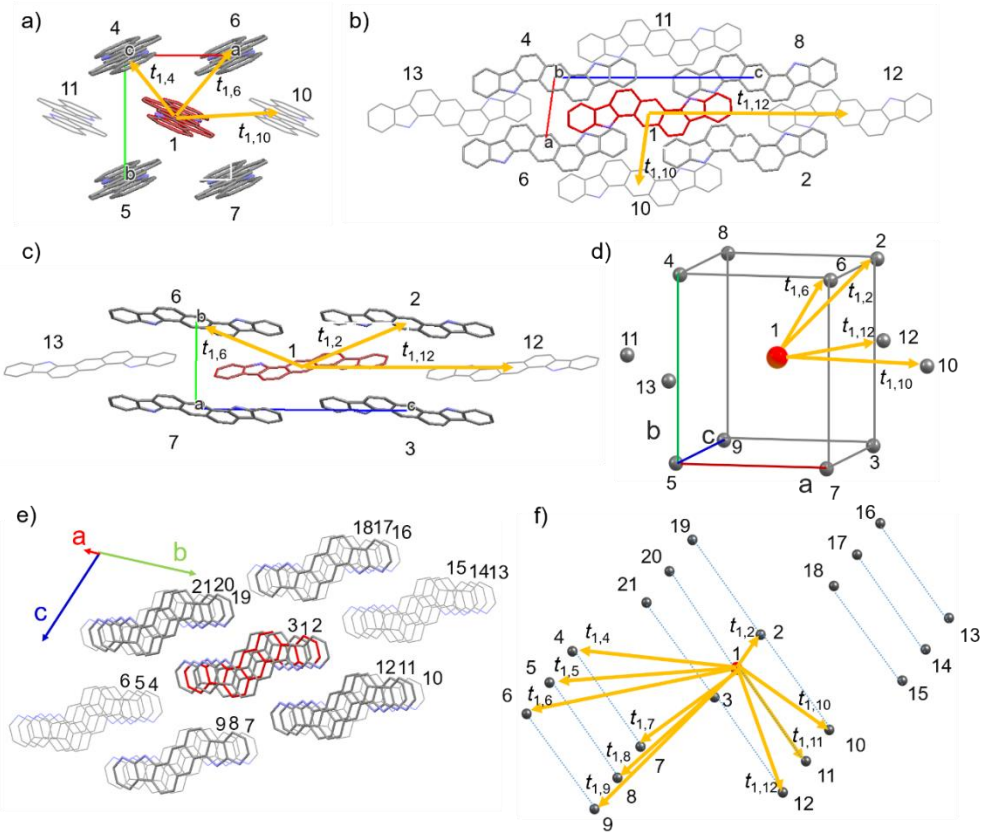

Figure 53. Crystal structure views of the *ab* (a), *ac* (b) and *bc* (c) crystallographic planes of **ADI**. Simplified grid representation of the **ADI** unit cell (d). Crystal structure of **ADAI** (e) and grid representation of that crystal structure (f). Hydrogen atoms have been omitted for clarity. Numbering labels the molecular sites and the t_{ij} transfer integrals

Table 2. Average hole-transfer integral $\left(\left\langle t_{ij}\right\rangle\right)$ and its standard deviations $\left(\sigma_{ij}\right)$ in meV calculated at the B3LYP/6-31G** level for the most relevant molecular crystal pairs of **ADI** and **ADAI**. t_{ij} corresponds to the transfer integrals computed at the experimental crystal structure.

ADI				**ADAI**			
Crystal pairs	t_{ij}	$\left\langle t_{ij}\right\rangle$	σ_{ij}	Crystal pairs	t_{ij}	$\left\langle t_{ij}\right\rangle$	σ_{ij}
$t_{1,2}=t_{1,3}=$ $t_{1,4}=t_{1,5}$	14.4	–6.8	16.9	$t_{1,2}=t_{1,3}$	11.1	0.0	57.8
$t_{1,6}=t_{1,7}=$ $t_{1,8}=t_{1,9}$	6.7	–8.1	10.6	$t_{1,4}=t_{1,15}$	0.7	–	–
$t_{1,10}=t_{1,11}$	40.0	37.7	14.5	$t_{1,5}=t_{1,14}$	0.4	–	–
$t_{1,12}=t_{1,13}$	0.3	–	–	$t_{1,6}=t_{1,16}$	0.0	–	–
				$t_{1,7}=t_{1,18}$	0.2	–	–
				$t_{1,8}=t_{1,17}$	12.1	–12.3	6.5
				$t_{1,9}=t_{1,16}$	0.4	–	–
				$t_{1,10}=t_{1,21}$	0.2	–	–
				$t_{1,11}=t_{1,20}$	8.3	3.0	2.6
				$t_{1,12}=t_{1,19}$	16.8	–13.3	10.0

As expected, the largest values of the effective coupling $\left\langle t_{ij}^{2}\right\rangle^{1/2}$ are obtained for the face-to-face π-stacked dimers with values of 40.4 and 57.8 meV for **ADI** (

$t_{1,10} = t_{1,11}$) and **ADAI** ($t_{1,2} = t_{1,3}$), respectively. **ADI** presents a high average value of the hole-transfer integral (37.7 meV) and a moderate fluctuation (14.5 meV). In contrast, **ADAI** presents a negligible average value of the transfer integral (0.0 meV) but a quite large fluctuation (57.8 meV). This difference arises from the large fluctuations the electronic coupling experiments with small intermolecular movements in **ADAI** compared with **ADI**. The variation of the electronic couplings with the intermolecular disposition is visualized in Figure 54. Finally, it should be emphasized that, although the π–π interacting direction presents the largest coupling and is therefore expected to give rise to the highest charge-transfer rate constant, **ADAI** exhibits a larger number of secondary charge-transfer paths with non-negligible transfer integrals that may help in the charge transport.

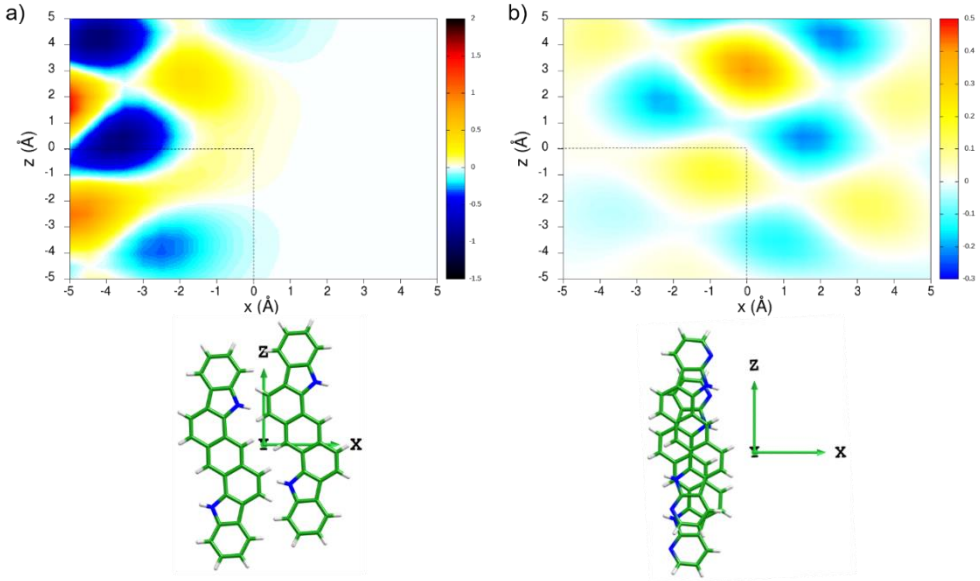

Figure 54. 2D map of t_{ij} (in meV) for face-to-face π-stacked dimers of **ADI** (a) and **ADAI** (b) by moving one molecule along the *x* and *z* axis directions starting from the crystal structure (*x* = 0 Å and *z* = 0 Å, bottom).

Besides transfer integrals and fluctuations between different molecular pairs, the hole mobilities in the crystal planes were computed using a master equation (Section 3.2.7) and an electric field of 10^5 V cm^{-1}, as in similar studies reported in the literature.[205] The estimation of the hole mobilities requires of all the rate constants that were computed according to the MLJ expression (Section 3.2.3, Eq. 57), where the internal reorganization energy was calculated of 159 meV for **ADI** and 183 meV for **ADAI**. The external reorganization energy was set to 50 meV, according to values reported for related molecular crystals,[179,271] and the temperature to 298.15 K.

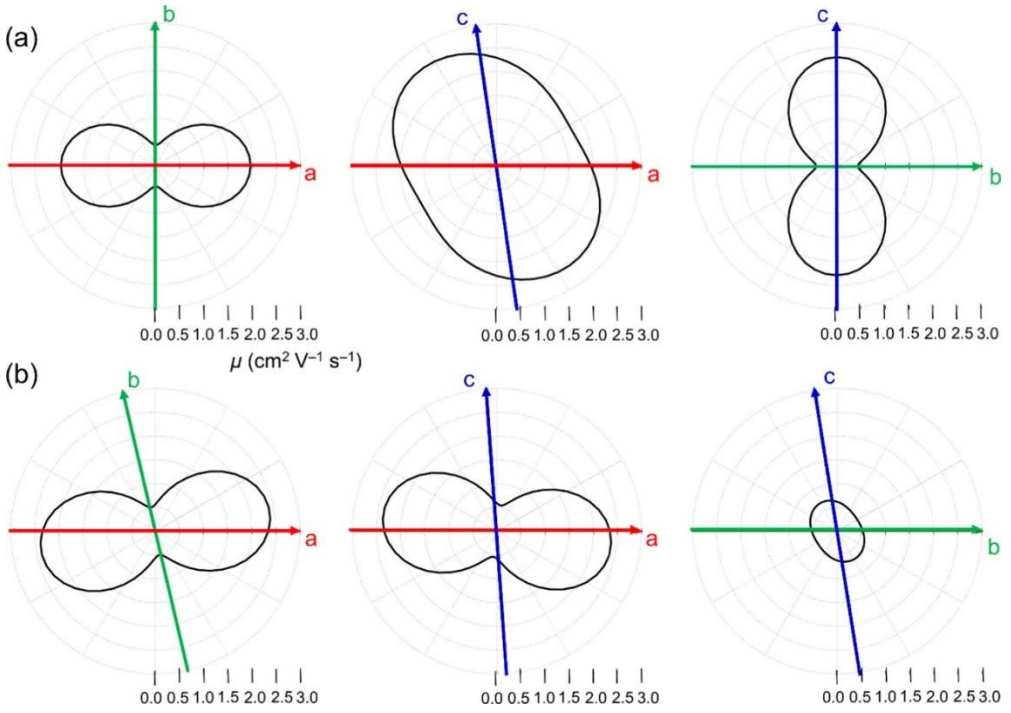

Figure 55. Hole mobilities (μ) calculated for **ADI** (a) and **ADAI** (b) in the *ab* (left), *ac* (middle) and *bc* (right) crystallographic planes.

Figure 55 displays the hole-mobility maps calculated for the crystal lattice planes of **ADI** and **ADAI**. The predicted mobilities, which are obtained in the 0.5–2.5 $cm^2\ V^{-1}\ s^{-1}$ range, are overestimated with respect to the experimental mobilities measured for organic thin films in OFET devices, with values of 4×10^{-4} and 8×10^{-3} $cm^2\ V^{-1}\ s^{-1}$ for **ADI** and **ADAI**, respectively. This overestimation is in line with previous theoretical studies reported in the literature for π–conjugated semiconductors.[271] Nevertheless, the maps shown in Figure 55 offer meaningful information. Even though both molecules present high mobilities in the three crystal planes (*ab*, *ac* and *bc*), there are noticeable differences in the mobility anisotropy. Whereas **ADAI** exhibits better transport properties in the π-stacking direction (*a* crystallographic axis), **ADI** displays a more isotropic transport in the *ac* plane, with a maximum mobility between the *a* and *c* crystallographic axes owing to the simultaneous transport along face-to-face and edge-to-face dimers. It should be emphasized that, as the prediction has been performed for the ideal crystal structures, upper-bound values of the hole mobilities are provided. In contrast, the experimental mobilities are measured for thin films deposited in OFET devices and are quite sensitive to the morphology of the film and to its stability. **ADAI** thin films indeed present a higher degree of crystallinity and a remarkable thermal robustness (see Publication 5 for further details), which may explain the higher mobility measured experimentally. In summary, the better transport properties shown by **ADAI** and their higher thermal stability are a proof of concept that the hydrogen bond-driven self-assembly works as a suitable

strategy to design stable organic semiconductors that, in principle, would provide higher-ordered thin films and, therefore, higher charge mobilities.

5.2.1.2 Effects of the geometry and size of the conjugated system

Once the suitability of the hydrogen bond-driven self-assembly was confirmed, the effect of the size of the conjugated polyaromatic central backbone linking the end-capping H-bonding units on the transport properties was studied. With that purpose in mind, a series of four fused di-7-azaindole systems with an increasing size of the central π-conjugated spacer (benzene (**BDAI**), naphthalene (**NDAI**), anthracene (**ADAI**) and pyrene (**PDAI**)) were investigated (Figure 56).

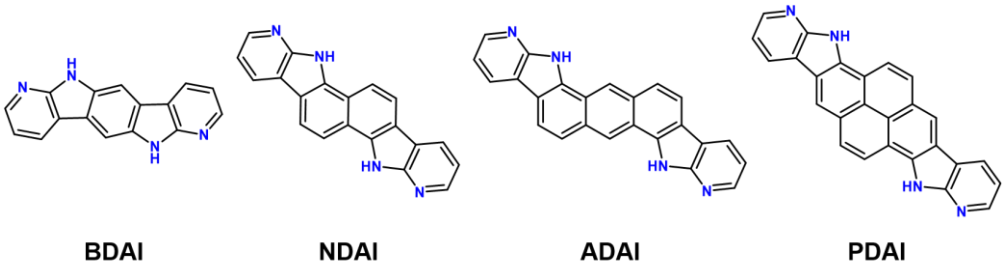

Figure 56. Chemical structure of **BDAI**, **NDAI**, **ADAI** and **PDAI**.

The experimental crystal structures proved that H-bonding is a key factor for the ordering achieved in the crystal packing of **BDAI**, **NDAI**, **ADAI** and **PDAI**, although, interestingly, two differentiated packing patterns were found (see below and Publication 6). OFET devices were built using the four compounds, obtaining hole mobilities of 1.3×10^{-3}, 4.6×10^{-3}, 2.7×10^{-2} and 1.4×10^{-4} $cm^2\ V^{-1}\ s^{-1}$ for **BDAI**, **NDAI**, **ADAI** and **PDAI**, respectively.

The crystal structures, resolved by X-ray diffraction, show that the four molecules present a primary arrangement, similar to that discussed above for **ADAI**, in which vicinal molecules form H-bonded ribbons (Figure 57). The length of the H-bonds increases with the size of the conjugated spacer, with values of 1.9, 2.1, 2.1 and 2.3 Å for **BDAI**, **NDAI**, **ADAI** and **PDAI**, respectively. The H-bonded ribbons are not completely planar, but define small steps in the 0.3–0.7 Å range. As for **ADAI**, H-bonded ribbons form columns by π–π stacking interactions (Figure 57). Adjacent molecules in the stacks are separated by similar distances between 3.4 and 3.6 Å, and are slid in a different degree along the stack depending on the system. The right column of Figure 57 shows the top view of the π–π stacked interacting pairs, the shifts along the short and long molecular axis being: 1.5 and 1.4 Å for **BDAI**, 1.5 and 0.7 Å for **NDAI**, 0.1 and 3.0 Å for **ADAI** and 1.5 and 0.6 Å for **PDAI**. Although the four molecules present H-bonded ribbon-like structures ordered in π-stacked columns, two different interaction patterns between adjacent columns emerge. In **BDAI** and **ADAI**, H-bonded ribbons in adjacent columns are in the same plane forming a layer. In contrast, in **NDAI** and **PDAI**, the adjacent H-bonded ribbons are twisted with respect to each other giving rise to a herringbone-like arrangement (Figure 58).

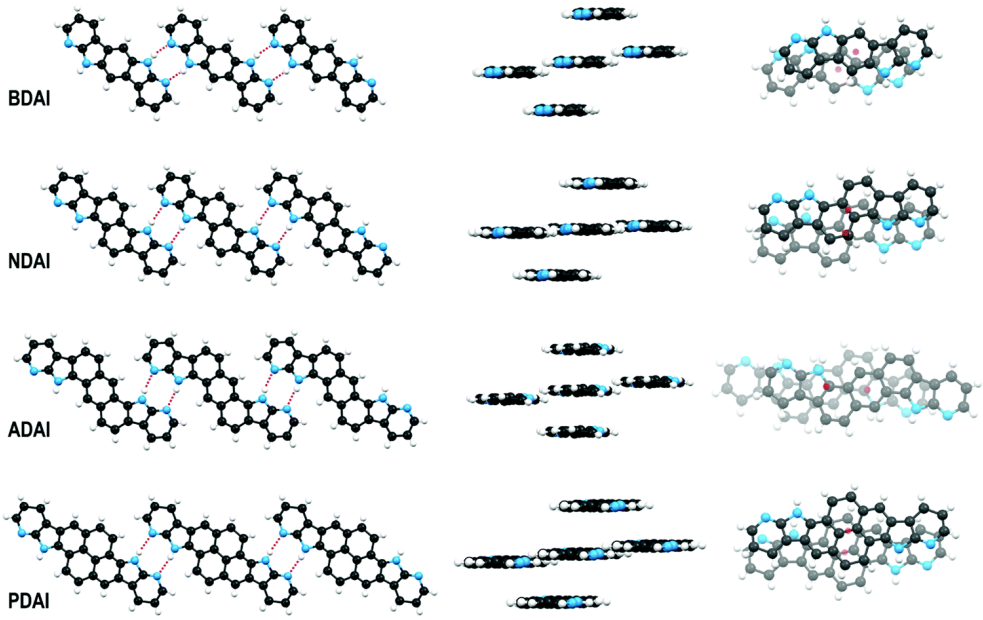

Figure 57. X-ray diffraction crystal packing of **BDAI**, **NDAI**, **ADAI** and **PDAI**. Top view of H-bonded ribbons (left column), side view of the ribbon and the molecules π-stacked over the central molecule (middle column) and top view of the π-stacked dimers (right column).

To screen the most relevant transport paths in the crystal, hole-transfer integrals were computed for all the close molecular pairs of the crystal structure (Figure 58 and Table 3). As already exposed for **ADAI**, the four systems present the largest transfer integral for the π-stacking direction ($t_{1,2} = t_{1,3}$), although the values of this integral do not follow a clear trend with the increasing size of the molecule. This may be explained by the high dependence of the transfer integral on the orbital overlap, which strongly varies with the relative disposition of the two molecules forming the π-stacked dimer, as was discussed above for **ADAI**. In addition to the π-stacking direction, other two

secondary transport paths appear to be relevant. These paths correspond to edge-to-edge interactions along the H-bonded ribbons ($t_{1,4} = t_{1,5}$) and to contacts between molecules in adjacent columns ($t_{1,6} = t_{1,7}$). The $t_{1,4} = t_{1,5}$ couplings show similar values for the four systems because the relative disposition of adjacent molecules in the dimer is fixed to keep the hydrogen bonds.

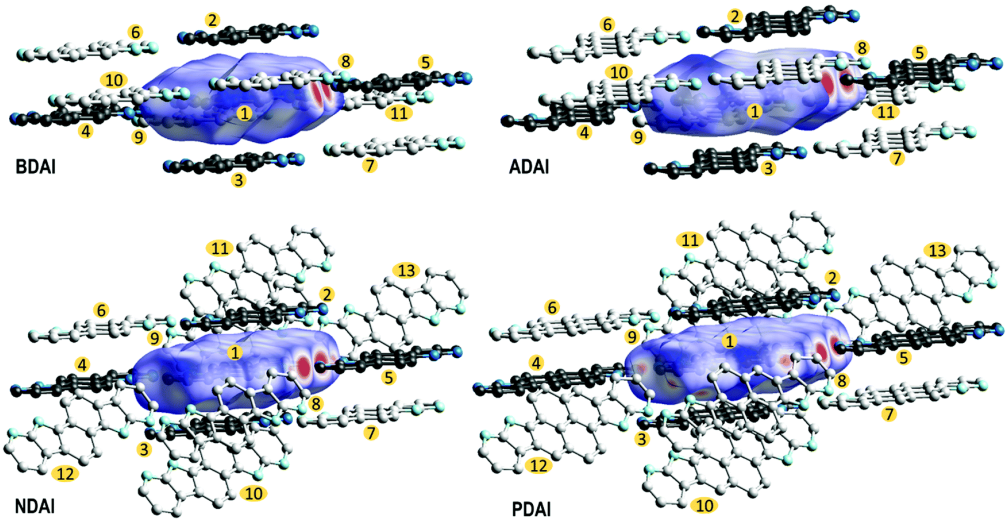

Figure 58. Shortest van der Waals contacts in the crystal. Central molecules are represented by a surface. H-bonded and π-stacked molecules are represented in black and the other molecules in grey. Molecules are labeled with numbers.

Table 3. Hole-transfer integrals ($t_{i,j}$, in meV) computed at the B3LYP/6-31G** level for the short-contact molecular dimers present in the crystal. Molecular pairs are numbered according to Figure 58.

$t_{i,j}$	**BDAI**	**NDAI**	**ADAI**	**PDAI**
$t_{1,2} = t_{1,3}$ (π-stacked)	71.5	71.5	11.1	28.8
$t_{1,4} = t_{1,5}$ (H-bonded)	14.2	14.2	8.3	7.2
$t_{1,6} = t_{1,7}$	6.7	19.1	16.8	23.9
$t_{1,8} = t_{1,9}$	9.3	1.5	12.1	1.9
$t_{1,10} = t_{1,11}$	1.6	1.5	0.4	1.9
$t_{1,12} = t_{1,13}$		0.2		0.0

Average values for the most relevant electronic couplings taking into account the thermal fluctuations of the structure were computed following the same computational protocol used in the previous study. Table 4 displays the average transfer integrals $\left(\left\langle t_{i,j} \right\rangle\right)$, their fluctuations ($\sigma_t$) and the average of the squared transfer integrals estimated as $\left\langle t_{i,j}^2 \right\rangle = \left\langle t_{i,j} \right\rangle^2 + \sigma_t^2$. Table 4 also includes the values estimated for the reorganization energies (λ) and the hole-transfer rate constants (k) computed using the Marcus expression (Eq. 56). The analysis of the fluctuation of the electronic couplings in the different crystal hopping directions reveals that large fluctuations are only obtained for the π-stacked dimers (1,2 = 1,3). This is an expected result since the relative

movement of adjacent molecules in parallel planes is less hindered by the crystal packing than the molecular movement within the H-bonded ribbons that is restricted by the relatively strong H-bonding interactions. Indeed, σ_t is larger than $\langle t_{1,2} \rangle$, indicating that σ_t is the key factor determining the high values of the rate constant. This is especially true for **BDAI** and **ADAI**, which show average electronic couplings close to zero. Therefore, thermal fluctuations are the key factor determining that the largest rate constant is found in the π–π stacking direction, with values close to 10^{13} s^{-1} and at least one order of magnitude higher than the rate constant computed for any other dimer. This result was not at all obvious according to the couplings computed at the crystal geometry (Table 3). The other relevant directions (1,4 = 1,5, 1,6 = 1,7 and 1,8 = 1,9) present lower but non-negligible rate constants (Table 4), indicating the existence of alternative charge-transport paths. It should be remarked that **ADAI** presents, as a whole, the largest rate constants for those alternative paths together with the main transport direction (1,2 = 1,3), thus supporting the best performance of this system. The significant values obtained for the rate constants of the secondary charge-carrier directions suggest that those alternative paths might play an important role when structural defects are present as occurs inherently in thin films.

Table 4. Average hole-transfer integrals $\left(\left\langle t_{ij} \right\rangle\right)$, their standard deviations $\left(\sigma_{ij}\right)$, and average squared transfer integrals $\left(\left\langle t_{ij}^2 \right\rangle\right)$ computed at the B3LYP/6-31G** level for the most relevant dimers of **BDAI**, **NDAI**, **ADAI** and **PDAI**. The hole-transfer rate constants (k) estimated at 298 K for all the dimers and the reorganization energies (λ) used to calculate k are included. Numbering correspond to that used in Figure 58.

Dimer		**BDAI**	**NDAI**	**ADAI**	**PDAI**
	λ (meV)	233	250	182	239
1,2 = 1,3	$\langle t \rangle$ (meV)	–0.7	55.1	0.0	–39.1
	σ_t (meV)	60.1	63.2	57.8	64.6
	$\langle t^2 \rangle$ (meV^2)	3612.5	7030.3	3340.8	5702.0
	k (s^{-1})	1.3×10^{13}	2.1×10^{13}	2.2×10^{13}	1.9×10^{13}
1,4 = 1,5	$\langle t \rangle$ (meV)	–7.4	6.8	3.2	3.9
	σ_t (meV)	5.7	3.1	2.6	2.2
	$\langle t^2 \rangle$ (meV^2)	87.3	55.9	17.0	20.1
	k (s^{-1})	3.1×10^{11}	1.6×10^{11}	1.1×10^{11}	7.6×10^{10}
1,6 = 1,7	$\langle t \rangle$ (meV)	3.8	12.1	17.2	6.7
	σ_t (meV)	4.3	6.7	7.8	4.3
	$\langle t^2 \rangle$ (meV^2)	32.9	191.3	356.7	63.4
	k (s^{-1})	1.2×10^{11}	5.6×10^{11}	2.4×10^{12}	2.1×10^{11}
1,8 = 1,9	$\langle t \rangle$ (meV)	–23.9	2.2	–12.4	–0.5
	σ_t (meV)	13.9	3.7	6.4	4.6
	$\langle t^2 \rangle$ (meV^2)	764.4	18.5	194.7	21.4
	k (s^{-1})	2.7×10^{12}	5.5×10^{10}	1.3×10^{12}	7.2×10^{10}

Disappointingly, the hole-transfer rate constants theoretically estimated do not seem to justify the experimental trend inferred for the hole mobility from measurements in OFET devices (**BDAI**: 1.3×10^{-3}, **NDAI**: 4.6×10^{-3}, **ADAI**: 2.7×10^{-2}, **PDAI**: 1.2×10^{-4} $cm^2\ V^{-1}\ s^{-1}$). The apparent disagreement mainly results from the similar theoretical rates predicted for the stacking direction of all the four systems. However, the better performance observed for **ADAI** can be explained from either experimental and theoretical observations. Experimentally, the AFM images of the thin films demonstrate that **ADAI** presents a granular morphology with larger-size grains and an homogeneous grain-size distribution. This indicates that the thin film built with **ADAI** presents larger crystalline domains, which enhance the hole transport, whereas the other systems present more amorphous or less crystalline morphologies (Publication 6). On the other hand, the theoretical outcomes show that the hole-transport rate constants computed for **ADAI** are, in general, higher for any hopping path considered in the crystal. This suggests that **ADAI** presents a larger number of efficient secondary charge transport channels, which is indicative of a larger tolerance to defects, mitigating the effect of possible traps. The combination of both observations: the high degree crystallinity of the thin film and the existence of efficient secondary transport paths, nicely supports that **ADAI**-based OFETs present the highest hole mobility in this series of molecules.

5.2.2 Photoinduced charge transfer in the truxTTF•$C_{30}H_{12}$ supramolecular complex

The second problem related with charge transfer addressed in this thesis is the study of the photoinduced charge transfer in the supramolecular complex formed by the electron-donor molecule truxene-tetrathiafulvalene (truxTTF) and the half-fullerene buckybowl ($C_{30}H_{12}$) as electron acceptor (Figure 59a). The photoinduced charge transfer in the truxTTF•$C_{30}H_{12}$ heterodimer was previously investigated and the charge-separation (CS) and charge-recombination (CR) rate constants were experimentally determined.[268] The $C_{30}H_{12}$ buckybowl mimics the electron-acceptor behavior of C_{60} when combined supramolecularly with truxTTF, exhibiting an efficient photoinduced CS process and a slower CR event, and may therefore be considered as potential candidate in the context of organic solar cells (OSCs). Nevertheless, there are still open questions: 1) which is the mechanism of the electron transfer? and 2) how the supramolecular organization affects to the electron transfer process? To gain insight into these questions, we have carried out a detailed theoretical study of the processes involved in the photoinduced charge transfer of truxTTF•$C_{30}H_{12}$ with the aim of determining which variables have a stronger impact on the charge transfer (Publication 7 in Section 5.4). The theoretical protocol used and the results obtained are briefly described in this section.

In a previous work, the four minimum-energy revPBE0-D3/cc-pVTZ-optimized geometries shown in Figure 59b were proposed for the truxTTF•$C_{30}H_{12}$ supramolecular heterodimer.[268] Structures **1** and **2** present a bowl–in–bowl interaction pattern where the convex part of the hemifullerene interacts with the concave cavities formed by truxTTF, the cavity formed by

the carbon backbone in **1** and that formed by the central bencene ring and the three dithiole rings in **2**. Structures **3** and **4** are staggered structures implying concave-concave interactions, in which one dithiole ring (**3**) or one benzene ring (**4**) of truxTTF are placed inside the $C_{30}H_{12}$ cavity. Structures **3** and **4** were predicted to be more stable with interaction energies of −25.3 and −28.5 kcal mol^{-1}, respectively, compared with the −21.0 and −19.4 kcal mol^{-1} of structures **1** and **2**, respectively.[268] Therefore, the discussion here focuses on structure **4** since it is expected to be the most abundant in solution.[272]

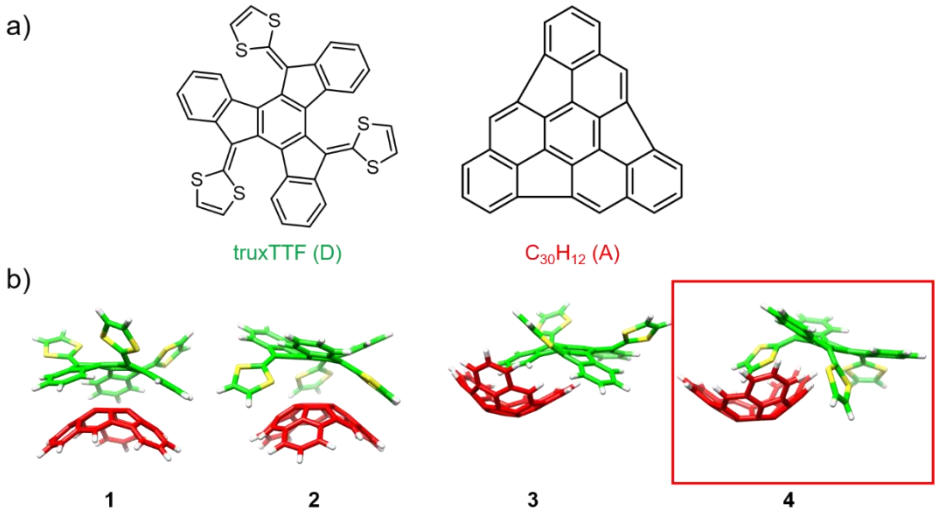

Figure 59. a) Chemical structures of the electron-donor truxTFF and the electron-acceptor buckybowl $C_{30}H_{12}$ (hemifullerene). b) Minimum-energy structures computed at the revPBE0-D3/cc-pVTZ level of theory for the truxTTF•$C_{30}H_{12}$ supramolecular D−A heretodimer.[268] Carbon atoms of truxTTF are represented in green and those of $C_{30}H_{12}$ in red. Hydrogen atoms are represented in white and sulphur in yellow. The most stable structure **4** is highlighted with a red square.

Before calculating the parameters required to evaluate the CS and CR rate constants determining the effectiveness of the photoinduced charge-transfer process, it is needed to determine the energy position of the excited states involved in the process. The excited states were computed within the TDDFT formalism using the TDA approach. Since DFT may fail dealing with charge transfer states due to the self-interaction error,[111,273–275] a large variety of functionals were evaluated and compared including the GGA BLYP, the hybrid B3LYP and its long range version CAM-B3LYP, and the standard and optimally-tuned (OT) long-range corrected functionals LC-BLYP, LC-ωPBE and LC-ωB97X-D. The uncorrected GGA BLYP and hybrid B3LYP functionals provide a complicated and unrealistic picture with many charge-transfer (CT) excited states below the local-excited (LE) bright states. In contrast, the standard version of the long-range corrected functionals CAM-B3LYP, LC-BLYP, LC-ωPBE and LC-ωB97X-D predict a completely opposite picture where the lowest-energy CT states are calculated to be higher in energy than the bright LE states. This picture makes the photoinduced electron transfer observed experimentally unfavourable, and does not match the experimental absorption spectrum, which presents a low-intensity band ascribed to charge transfer transitions.[268] Lastly, the optimally-tuned functionals afford an intermediate picture with few CT states lower in energy than the bright LE states. The OT-LC-BLYP(ω = 0.16 bohr^{-1}) functional was finally adopted because it exhibits the best performance and provides excited states of well-defined nature (see Publication 7 for further details); *i.e.,* the adiabatic excited states can be seen as quasidiabatic states, which is particularly useful when employing non-adiabatic charge-transfer rate expressions.

Figure 60a displays the vertical excitation energies (ΔE), the oscillator strengths (f) and the charge difference between the truxTTF and the $C_{30}H_{12}$ fragments (Δq) computed for the six lowest-energy singlet excited states of truxTTF•$C_{30}H_{12}$. Δq is the parameter employed to define the nature of the excited states. States with $\Delta q < 0.5e$ denote LE states centered on the truxTTF moiety, $0.5e < \Delta q < 1e$ indicate states with mixed LE&CT character and states with $\Delta q > 1e$ are of CT nature. All the electronic transitions to excited states that may be relevant for the charge-separation (CS) and charge-recombination (CR) processes are in the 2.69–3.10 eV range. In this range, there are three CT states that correspond to the S_1, S_3 and S_4 states calculated at 2.69, 2.88 and 2.95 eV and labeled as CT_1, CT_2 and CT_3, respectively. The Δq values for CT_1, CT2 and CT_3 are 1.23, 1.63 and 1.64e, respectively, reflecting the CT nature of the three states, which is visualized for CT_1 in Figure 60b. The LE states correspond to the S_2, S_5 and S_6 states computed at 2.79, 3.04 and 3.07 eV and labeled as LE_1, LE_2 and LE_3, respectively. These states show small Δq values (0.46, 0.11 and 0.13e, respectively), and their local character is supported by the attachment/detachment densities calculated for the LE_2 state as a representative example (Figure 60b). The oscillator strengths shown in Figure 60a put into manifest that all the electronic transitions from the ground state (GS) to the excited CT states have a low but not null intensity, which is in line with the low intensity band observed in the experimental spectrum. They also reveal that the LE_1 state has no relevant intensity (f = 0.035), whereas LE_2 (f = 0.420) and LE_3 (f = 0.558) are quasi-degenerate and very intense, similarly to the picture obtained for isolated truxTTF. Therefore, the photoinduced electron transfer in truxTTF•$C_{30}H_{12}$ presumably will start by excitation to the two bright states LE_2 and LE_3, from which charge separation may follow different

pathways since there are 6 states close in energy, thus leading to a complex scenario.

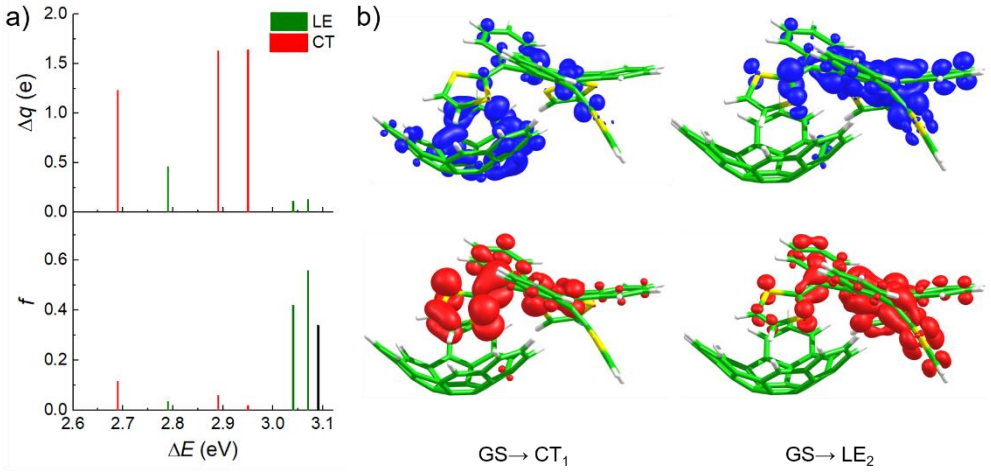

Figure 60. (a) Representation of Δ*q* (top) and oscillator strength (*f*, bottom) *versus* the excitation energy (Δ*E*) calculated for the truxTTF•$C_{30}H_{12}$ heterodimer at the OT-LC-BLYP(ω = 0.16 bohr^{-1}) level in *o*-dichlorobenzene as solvent. The bright lowest-energy excited states (S_2 and S_3) computed for truxTTF at 3.09 eV (bottom, black bar) at the same level of theory are also indicated for comparison purposes. (b) Attachment (top) and detachment (bottom) densities computed for the lowest-energy GS → CT_1 and the bright GS → LE_2 transitions.

As previously anticipated in Section 5.1, the CS and CR rate constants associated to the photoinduced charge transfer in the truxTTF•$C_{30}H_{12}$ supramolecular complex were computed using the Marcus–Levitch–Jortner (MLJ) semi-classical expression (Eq. 57). This expression requires of four parameters: the electronic couplings (V_{ij}), the Gibbs free energy differences (Δ*G*) between the initial and final states, and the reorganization energy (λ)

which is split in the internal and external part. In the following, each parameter is analyzed in detail before estimating the final rate constants.

The electronic couplings V_{ij} between the low-energy LE and CT states (CS process) and between the CT states and the ground state (CR process) were estimated within the TDA-DFT approximation at the OT-LC-BLYP(ω = 0.16 bohr^{-1})/6-31G** + PCM (*o*-dichlorobenzene) level using the ground-state (GS) optimized geometries and the multi-state FCD diabatization method. Table 5 collects all the V_{ij} values computed using both the multi-state approach and a two-state variant (see Section 3.2.6.2 for technical details). The couplings computed for the CS processes with the multi-state approach all are in the 4–44 meV range, similarly to the values reported for other D−A supramolecular heterojunctions.[176,276] The largest values are, in general, those involving the CT_1 state, which is coherent with the Δq value (1.23) that suggests a non-negligible mixing of the CT_1 state with the LE states. The V_{ij} values computed for the CR processes are 10.0, 0.7 and 4.4 meV for the $CT_1 \rightarrow GS$, $CT_2 \rightarrow GS$ and $CT_3 \rightarrow GS$ transitions, respectively, the CR $CT_1 \rightarrow GS$ event then being the most probable recombination path.

Table 5. Absolute electronic couplings (V_{ij}) between the ground state (GS) and charge-transfer (CT) excited states and between local (LE) and CT excited states calculated using the multi-state FCD diabatization scheme. V_{ij} values estimated under the two-state FCD approximation are included within parentheses.

	V_{ij} (meV)		
	CT_1	CT_2	CT_3
GS	10.0 (270.0)	0.7 (67.1)	4.4 (4.3)
LE_1	43.6 (43.9)	20.2 (9.6)	14.8 (7.2)
LE_2	4.1 (10.1)	6.1 (11.2)	9.2 (9.7)
LE_3	32.8 (97.8)	24.0 (25.0)	9.4 (16.1)

It is interesting to compare the values obtained for the electronic couplings from the two-state and the multi-state variants of the FCD diabatization scheme. In general, the two-state approach gives quite reasonable values, compared with the multi-state variant, for the CS processes but for the $V_{LE_3–CT_1}$ value which is largely overestimated. Concerning the CR processes, the two-state values predicted for the $V_{CT_1–GS}$ (270.0 meV) and $V_{CT_2–GS}$ (67.1 meV) couplings significantly overestimate those calculated at the multi-state level (10.0 and 0.7 meV, respectively). This overestimation of the CR couplings is clearly an artifact and is in line with other recent studies.[276] It evidences the crucial role of including multi-state effects for an accurate estimation of the V_{ij} couplings, especially when dealing with systems in which several electron-transfer pathways (either CS or CR) can take place owing to the coexistence of a large number of excited states in a narrow energy window.

The second parameter needed to compute the rate constants is the Gibbs free energy difference (ΔG) between the initial and final states involved in the

electron transfer. In contrast to the hole transport studied in Sections 5, where both states were energetically equivalent, the initial and final states involved in the photoinduced electron transfer in D−A complexes are different (see Figure 48). The ΔG that appears in the MLJ expression relies on the difference between the minima of the two diabatic potential energy surfaces, which include both the internal degrees of freedom and the solvent relaxation. In this study, the ΔG differences are assumed to be similar to the adiabatic energy differences ΔE.

Before computing the ΔE values for the CS (ΔE_{CS}) and CR (ΔE_{CR}) processes, it is interesting to compare how the CT and LE states are stabilized by a polar solvent as o-dichlorobenzene. To do so, vertical excitation energies were computed at the Franck–Condon region with the state-specific (SS) PCM model in an equilibrium configuration. As expected, CT states are largely stabilized, by *ca*. 0.4–0.7 eV, with excitation energies of 2.22, 2.29 and 2.35 eV for the GS → CT_1, GS → CT_2 and GS → CT_3 transitions, respectively, compared with the values obtained using the standard linear-response PCM formalism (2.69, 2.88 and 2.95 eV, respectively). In contrast, the excitation energies to the LE states remain practically unchanged. These outcomes suggest that the SS-PCM approach is more appropriate to capture the solvent relaxation effects in the excited states than the standard linear-response PCM.

The geometry relaxation of the truxTTF•$C_{30}H_{12}$ complex for all the excited states involved in the photoinduced charge transfer is a challenging task because, as already discussed, the states are close in energy in a narrow energy window. Specifically, the CT_1 state of truxTTF•$C_{30}H_{12}$ was fully optimized at the OT-LC-BLYP(ω = 0.16 $bohr^{-1}$)/6-31G** + PCM (*o*-dichlorobenzene)

level and its relaxed geometry was assumed to be the same for the CT_2 and CT_3 states. The energies of the three CT states at the optimized geometry of CT_1 were additionally refined by including the solvent effect at the SS-PCM level. Following this procedure, the adiabatic energy differences between the ground state and the CT_1, CT_2 and CT_3 were 1.75, 2.02 and 2.08 eV, respectively. The optimization of the LE states was not feasible due to convergence problems. However, since the excitation is localized in the donor moiety, only a significant intramolecular relaxation of the truxTTF moiety is expected. Hence, the vertical energies of the LE states of truxTTF•$C_{30}H_{12}$ complex were corrected with the relaxation energies obtained from the optimization of the three first singlet excited states of the isolated truxTTF (0.30, 0.46 and 0.47 eV for LE_1, LE_2 and LE_3, respectively). This led to adiabatic energy differences of 2.45, 2.61 and 2.62 eV between LE_1, LE_2 and LE_3 and the ground state, respectively. Table 6 summarizes all the ΔG_{CS} and ΔG_{CR} values computed for truxTTF•$C_{30}H_{12}$ as the energy differences between the LE and CT states and the GS and CT states, respectively.

Table 6. Gibbs free energy differences (ΔG) between the ground state and the CT states (CR processes) and between the LE and CT excited states (CS processes).

	ΔG (eV)		
	CT_1	CT_2	CT_3
GS	–1.75	–2.02	–2.08
LE_1	–0.70	–0.43	–0.37
LE_2	–0.86	–0.59	–0.53
LE_3	–0.87	–0.60	–0.54

The reorganization energy is the last parameter required to estimate the CS and CR rate constants. To estimate the reorganization energy (λ) associated to the charge transfer processes in solution is convenient to separate the contributions due to the degrees of freedom of the system (internal contribution, λ_{int}) and the solvent degrees of freedom (external contribution, λ_{ext}). The internal reorganization energies for charge-separation (λ_{int}^{CS}) and charge-recombination (λ_{int}^{CR}) were estimated for the isolated donor and acceptor fragments, in gas phase, using the two-points approach explained in Section 3.2.5.1. The internal reorganization energies of the truxTTF and $C_{30}H_{12}$ moieties were estimated to be 0.50 and 0.06 eV, respectively, λ_{int}^{CS} being equal to 0.56 eV. A significantly smaller value of 0.13 eV is predicted for λ_{int}^{CR}, with contributions of 0.07 and 0.06 eV from truxTTF and $C_{30}H_{12}$, respectively. The remarkable difference (0.43 eV) between λ_{int}^{CS} and λ_{int}^{CR} mainly comes from the truxTTF unit, which presents similar equilibrium geometries for the neutral and cation ground states (CR process) but significantly different geometries for the excited and cation states (CS process). In the excited state, a dithiol ring is highly rotated in comparison with the neutral and cation ground states. In contrast, the contribution of the acceptor moiety presents a similar and small value (0.06 eV) for both the CS and CR processes due to the rigidity of the $C_{30}H_{12}$ moiety.

As the semi-classical MLJ expression used to estimate the rate constants include part of the reorganization energy in a quantum way through an effective normal mode, the internal reorganization energy was dissected into

quantum and classical contributions. To do that, the contribution of each normal mode was calculated by computing the Huang–Rhys factors (*S*) according to Malagoli *et al.*[178] (see Section 3.2.5.2). Figure 61 illustrates the contribution of the normal modes to the internal reorganization energy. For the CS processes, the normal modes of truxTTF clearly dominate, showing active vibrations of both high and low frequencies. The former are related to the stretching of the C−C/C=C bonds whereas the later are due to the rotation and bending of the dithiole rings. In contrast, for the CR process, only three high-frequency vibrations associated to the stretching of C−C/C=C bonds of both truxTTF (1478 cm^{-1}) and $C_{30}H_{12}$ (1426 and 1571 cm^{-1}) are relevant. The effective normal mode frequency (ν_{eff}) and Huang–Rhys factors (S_{eff}) were computed by taking into account all the frequencies higher than 250 cm^{-1} as $\nu_{\text{eff}} = \sum_{\nu_k>250} S_k\nu_k \,/\, \sum_{\nu_k>250} S_k$ and $S_{\text{eff}} = \sum_{\nu_k>250} S_k$, and the quantum contribution to the reorganization energy was then computed as $\lambda_{\text{int},q} = \sum_{\nu_k>250} h\nu_k S_k$. The quantum contributions for the CS and CR processes were finally estimated as 0.23 and 0.10 eV with effective frequencies of 683 and 872 cm^{-1} and Huang–Rhys factors of 2.66 and 0.97, respectively. The remaining 0.33 and 0.03 eV for CS and CR processes, respectively, were added to the solvent reorganization energy in the classical contribution to the reorganization energy.

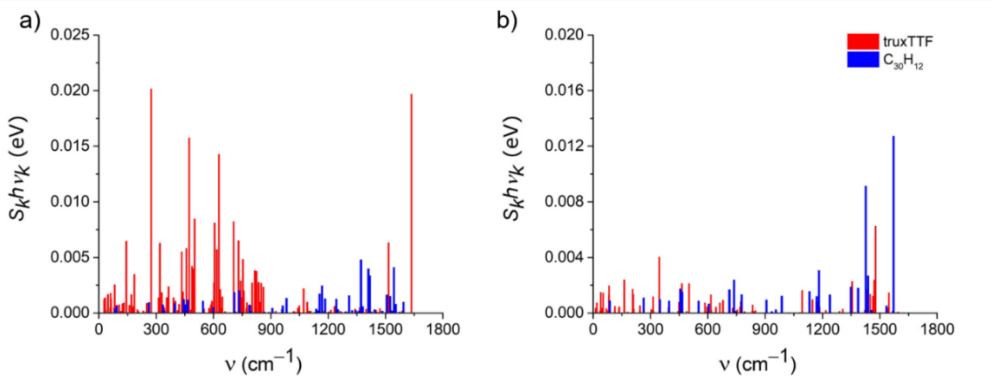

Figure 61. Contribution of each normal mode of the isolated truxTTF and $C_{30}H_{12}$ compounds to the internal reorganization energy of (a) CS and (b) CR processes.

The external reorganization energy (λ_{ext}) was computed by doing the difference between the total reorganization energy and the internal contribution already explained. The total reorganization energy was computed by means of the two-point approach and including the solvent effects within the SS-PCM model (Eqs 91–94). This procedure allows to use two solvent configurations: the equilibrium configuration, where the solvent configuration is fully relaxed for the specific state under study, and the non-equilibrium configuration, that uses the solvent configuration computed for the other state. The final λ_{ext} values computed for the CS processes were 0.38 and 0.51 eV for truxTTF and $C_{30}H_{12}$, respectively, which leads to a total λ_{ext}^{CS} value of 0.89 eV. For the CR processes, λ_{ext}^{CR} was computed to be 0.72 eV with contributions of 0.28 (truxTTF) and 0.44 eV ($C_{30}H_{12}$). Note that the λ_{ext}^{CS} and λ_{ext}^{CR} values are similar between them and significantly larger than λ_{int}^{CS} and λ_{int}^{CR}. Thus, the external

reorganization energies will be the dominant terms in the reorganization associated to the photoinduced charge transfer process, in contrast to what occurs in molecular crystals which usually present a low λ_{ext} value.[179]

$$\lambda_D^{CS} = E_{D^+}^{D^*,NonEq} - E_{D^+}^{D^+,Eq} \quad (91)$$

$$\lambda_D^{CR} = E_D^{D^+,NonEq} - E_D^{D,Eq} \quad (92)$$

$$\lambda_A^{CS} = E_{A^-}^{A,NonEq} - E_{A^-}^{A^-,Eq} \quad (93)$$

$$\lambda_A^{CR} = E_A^{A^-,NonEq} - E_A^{A,Eq} \quad (94)$$

Table 7 collects the k_{CS} and k_{CR} rate constants computed for the different electron-transfer pathways of the truxTTF•$C_{30}H_{12}$ heterodimer together with the parameters employed in their calculation (Eq. 57). Figure 62 presents a schematic diagram showing the kinetic relevance of the different electron-transfer channels. The most likely paths for CS are the $LE_1 \rightarrow CT_1$ and $LE_3 \rightarrow CT_1$ transitions with rate constants of 2.0×10^{12} and 3.0×10^{12} s^{-1}, respectively, which are in good agreement with the reported experimental rate of 6.6×10^{11} s^{-1}.[268] Although the LE_1 state will not be initially populated due to its low oscillator strength, it could be populated *via* internal conversion from LE_2 and LE_3, which is a probable event attending to the small energy difference (~0.2 eV) between LE_1 and LE_2 or LE_3. After the CS event, the CR process is expected to place from the lowest excited state CT_1. The estimated rate constant for the $CT_1 \rightarrow GS$ event is of 2.6×10^9 s^{-1}, which is fairly close to the experimentally estimated constant (1.0×10^{10} s^{-1}).[268]

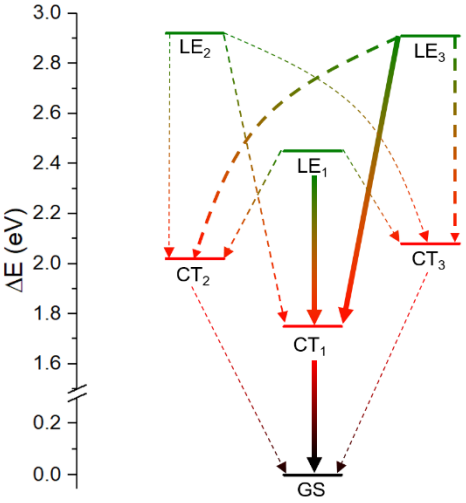

Figure 62. Scheme for all the CS and CR pathways. Thickness of the arrows indicates the relevance of the decay channels according to Table 7.

Table 7. Relevant parameters (V_{ij}, ΔG_{ij}, λ_c, S_{eff}, and ν_{eff}, in eV) and estimated k_{CS} and k_{CR} rate constants (in s^{-1}) for the different electron-transfer pathways of structure **4** of truxTTF•$C_{30}H_{12}$.

Transition	V_{ij}	$-\Delta G_{ij}$	λ_c	S_{eff}	ν_{eff}[a]	k_{ij}
CS process						
$LE_1 \rightarrow CT_1$	0.044	0.74	1.23	2.66	0.085 (683)	2.0×10^{12}
$LE_1 \rightarrow CT_2$	0.020	0.47	1.23	2.66	0.085 (683)	2.2×10^{10}
$LE_1 \rightarrow CT_3$	0.015	0.41	1.23	2.66	0.085 (683)	4.7×10^{9}
$LE_2 \rightarrow CT_1$	0.004	0.83	1.23	2.66	0.085 (683)	3.8×10^{10}
$LE_2 \rightarrow CT_2$	0.006	0.56	1.23	2.66	0.085 (683)	6.0×10^{9}
$LE_2 \rightarrow CT_3$	0.009	0.50	1.23	2.66	0.085 (683)	6.6×10^{9}
$LE_3 \rightarrow CT_1$	0.033	0.84	1.23	2.66	0.085 (683)	3.0×10^{12}
$LE_3 \rightarrow CT_2$	0.024	0.57	1.23	2.66	0.085 (683)	1.3×10^{11}
$LE_3 \rightarrow CT_3$	0.009	0.51	1.23	2.66	0.085 (683)	1.0×10^{10}
CR process						
$CT_1 \rightarrow GS$	0.010	1.75	0.75	0.97	0.108 (872)	2.6×10^{9}
$CT_2 \rightarrow GS$	0.001	2.02	0.75	0.97	0.108 (872)	1.7×10^{5}
$CT_3 \rightarrow GS$	0.004	2.08	0.75	0.97	0.108 (872)	2.3×10^{4}

[a] Values within parentheses are in cm^{-1}.

To gain insight into the effect the structure of the supramolecular complex has on the CS and CR processes, the rate constants were also estimated for structures **2** and **3** of truxTTF•$C_{30}H_{12}$ (Figure 58b). Structure **1** is not discussed because it presents no CT excited state lower in energy with respect to the bright LE states. The highest CS / CR rate constants computed for structures **2** and **3** are estimated to be 1.4×10^{11} / 4.3×10^{9} and 8.6×10^{10} / 1.7×10^{8} s^{-1}, respectively. Therefore, the fastest CS processes are found for structure **4** (2×10^{12} and 3×10^{12} s^{-1}), which presents high electronic couplings and ΔG_{CS} values close to the total reorganization energy, achieving the resonance. It is important to note that structures **2** and **4** showing C···S intermolecular contacts stabilize more the CT states below the LE states compared to structure **3** with no C···S interaction and only one CT state. This opens the door to more CS pathways for **2** and **4**. Regarding the CR process, structure **2** present a k_{CR} similar to that estimated for structure **4** (2.6×10^{9} s^{-1}), and one order of magnitude faster than structure **3**. The k_{CR} value predicted for **3** is lower because the higher-energy CT state is far from compensating the value of the reorganization energy.

Finally, to get a global picture of how the CS and CR processes occur, a simple kinetic model, including all the computed rate constants for the different electron-transfer pathways and tentative rate constants for internal conversion, was formulated. Figure 63 displays the time evolution of the population of the different electronic states according to their nature (LE, CT, and GS) for structures **2**, **3**, and **4**. The fastest CS occurs for structure **4**, the population of the LE states indeed decreasing to a half of its original value in 18.8, 50.0, and 0.5 ps for structures **2**, **3**, and **4**, respectively. The half-life times estimated from the populations of the LE, CT, and GS states were used for estimating global

rate constants thus recovering the more intuitive and simplified three-state picture that considers only one state of LE nature and one of CT nature. The kinetic model leads to global CS (CR) rate constants of 5.3×10^{10}, 2.0×10^{10}, and 2.0×10^{12} s^{-1} (4.3×10^{9}, 2.4×10^{8}, and 3.1×10^{9} s^{-1}) for structures **2**, **3**, and **4**, respectively. Note that the theoretical global rates calculated for structure **4** (the most stable) are in good accord with the global experimental values estimated from spectroscopic measurements (6.6×10^{11} s^{-1} and 1.0×10^{10} s^{-1} for CS and CR events, respectively).

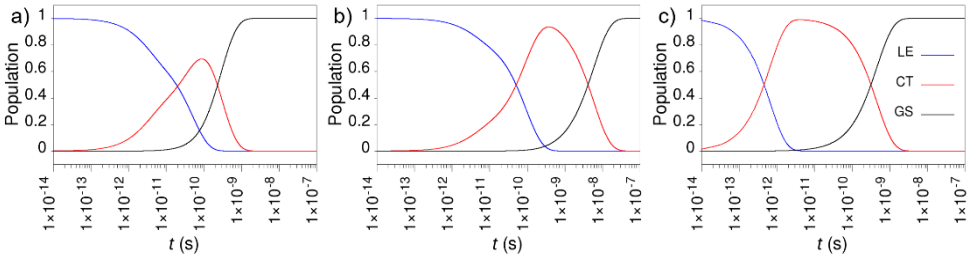

Figure 63. Time evolution of the populations of the electronic states according to their nature (LE, CT, and GS) calculated for structures **2** (a), **3** (b), and **4** (c). Time is represented in logarithmic scale.

5.3 Summary

In this chapter, we have first investigated the hole-transport properties of poly-heteroaromatic systems with capacity to self-assemble through hydrogen bonds. We have mainly focused on the effect the intermolecular H-bonds and the conjugation extension of the central spacer have on the hole-transport properties. In the second part of chapter, we have studied the photoinduced electron-transfer properties of the truxTTF•$C_{30}H_{12}$ supramolecular D−A

heretodimer in solution. In particular, we have developed a theoretical protocol that allow us to rationalize which are the most relevant factors to be taken into account when computing the charge-separation and charge-recombination rate constants.

The effect of intermolecular H-bonding on the hole-transport properties of organic semiconductors was evaluated by studying two closely related π-conjugated systems, labeled **ADI** and **ADAI**. **ADI** and **ADAI** keep the same chemical structure and size but differ in the terminal indole (**ADI**) or 7-azaindole units (**ADAI**) fused to the central anthracene backbone. The 7-azaindole groups allows **ADAI** to form intermolecular $H_{pyrrole}\cdots N_{pyridine}$ H-bonds, whereas H-bonding in **ADI** is not possible. X-ray diffraction structures showed that the use of the 7-azaindole unit is a successful strategy to control the supramolecular organization through H-bonding. The charge transport properties of **ADI** and **ADAI** were estimated using a combined protocol that uses DFT calculations to compute the electronic couplings for all the crystal dimers, molecular dynamics (MD) simulations to take into account the fluctuations in the electronic couplings due to thermal motions, the MLJ expression to estimate the hole-transfer rates and a master equation to finally predict the hole mobilities. As expected, the π–π interacting direction presents the largest coupling for both **ADI** and **ADAI**. Calculations on the ideal crystal structure predict that both molecules present high mobilities in the three crystal planes but **ADAI** exhibits better transport properties in the π-stacking direction and a larger number of secondary charge-transfer paths with non-negligible transfer integrals that may help in the charge transport. These properties together with the higher crystallinity and thermal robustness determined

experimentally for the **ADAI** films explain the higher mobilities found for **ADAI**.

Once proven that the hydrogen bond-driven self-assembly works as a suitable strategy to design higher-ordered organic semiconductors with better transport properties, the effect of the conjugation extension of the central spacer on those properties was studied in a series of compounds similar to **ADAI**, in which the central anthracene spacer was changed by benzene (**BDAI**), naphthalene (**NDAI**) and perylene (**PDAI**). The transport properties were calculated following a protocol similar to that previously used. The π–π stacked dimer is the only that presents a significant dynamic disorder, giving rise to the highest hole-transport rate constants. Unfortunately, it was not possible to establish a direct correlation between the experimental mobilities and the computed mobilities or hole-transport rate constants, because of the high dependence of the experimental mobilities with the degree of crystallinity of the thin film. However, theoretical results clearly suggest that **ADAI** should exhibit better transport properties because it presents a larger number of intermolecular contacts with significant rate constant values. The existence of these efficient secondary transport pathways predicted theoretically together with the high degree of crystallinity experimentally determined for **ADAI** thin films makes **ADAI** the best hole-transporting semiconducting material of the series and more tolerant to structural defects.

The second part of the chapter was focused on the kinetics of the non-radiative photoinduced electron-transfer processes (charge-separation and charge-recombination) experimented by a donor–acceptor (truxTTF•$C_{30}H_{12}$) supramolecular complex in solution. The study reveals a complex decay

mechanism after photoexcitation for truxTTF•$C_{30}H_{12}$ with the contribution of several low-lying excited states of different nature (local and charge-transfer excitations) all close in energy. In this scenario, the absolute rate constants for all the conceivable CS and CR routes were computed by using the Marcus−Levitch−Jorner rate expression, electronic structure calculations, and a multi-state diabatization method. The findings suggest that, for a reasonable estimate of the CS and CR rate constants, it is necessary to include: i) optimally tuned LC corrected density functionals, to predict a correct energy ordering of the low-lying excited states; ii) multi-state effects in the diabatization scheme, to account for the electronic couplings, and iii) environmental solvent effects with SS-PCM, to provide a proper stabilization of the charge-transfer excited states and accurate external reorganization energies. All the calculated rate constants were introduced in a simple but insightful kinetic model that enables estimating global CS and CR rate constants in line with the most generalized three-state model used for CS and CR processes. The global CS and CR rates (2.0×10^{12} and 3.1×10^{9} s^{-1}, respectively) computed for the donor–acceptor truxTTF•$C_{30}H_{12}$ supramolecular complex were found to be in good accord with the experimental estimations (6.6×10^{11} and 1.0×10^{10} s^{-1}).

5.4 Publications

Publication 5. P. Gómez, S. Georgakolopoulos, M. Más-Montoya, J. Cerdá, J. Pérez, E. Ortí, J. Aragó, D. Curiel, "Improving the Robustness of Organic Semiconductors through Hydrogen Bonding", *ACS Appl. Mater. Interfaces*, **2021**, 13, 8620–8630.

Publication 6. P. Gómez, J. Cerdá, M. Más-Montoya, S. Georgakopoulos, I. da Silva, A. García, E. Ortí, J. Aragó, D. Curiel, "Effect of molecular geometry and extended conjugation on the performance of hydrogen-bonded semiconductors in organic thin-film- field-effect transistors" *J. Mater. Chem. C* **2021**, 9, 10819–10829.

Publication 7. J. Cerdá, J. Calbo, E. Ortí, J. Aragó, "Charge-Separation and Charge-Recombination Rate Constants in a Donor-Acceptor Buckybowl-Based Supramolecular Complex: Multistate and Solvent Effects" *J. Phys. Chem. A.* **2021**, 125, 9982–9994.

Chapter 6. Energy transport

6.1 Introduction

As stated in Section 1, the energy or exciton transport is a key process in organic optoelectronic devices. For instance, in organic solar cells (an archetypical optoelectronic device), the exciton, generated after the light absorption, has to diffuse from the bulk of the donor to the donor–acceptor interface for exciton dissociation (charge separation).[277] Therefore, materials able to exhibit efficient exciton diffusion are highly desirable.[278,279] Recently, Headler *et al.* reported that self-assembled fibers based on *N*-heterotriangulenes (Figure 64) are able to transport energy in a very efficient manner achieving exciton diffusion lengths in the 1.6–6.4 μm range, a record for organic semiconductors.[280]

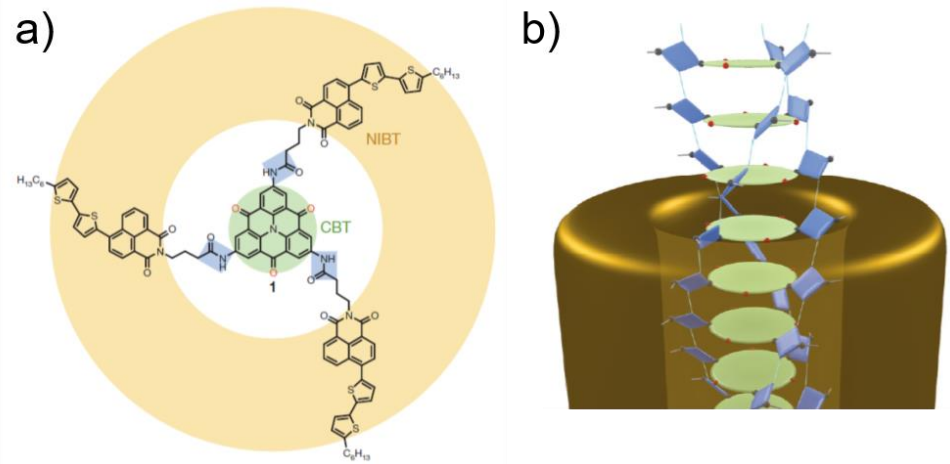

Figure 64. a) Chemical structure of the *N*-heterotriangulene used by Headler and coworkers. b) Scheme of a helical supramolecular column of an *N*-heterotriangulene based compound. Figure extracted from Ref. 280.

An exciton is a Coulombically-bonded hole-electron pair,[281,282] and three types of excitons are distinguished depending on the interaction between the hole and the electron (Figure 65). Mott−Wannier excitons,[283] which are found in inorganic materials, are characterized by low hole-electron binding energies, and long distances between the hole and the electron can be found. In opposition, Frenkel excitons[165,284] are local excitations in the same molecular site giving rise to large binding energies. Other excitations that can be found in organic materials are the charge-transfer excitons,[165] in which the hole and the electron are localized on different molecular sites (typically first or second neighbors).

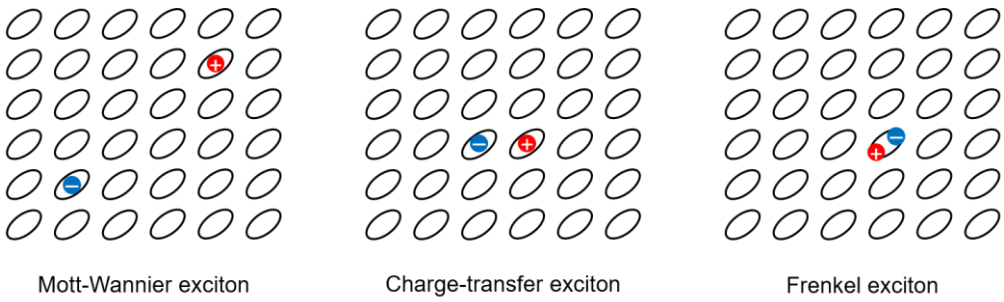

Figure 65. Schematic representation of Mott−Wannier, charge-transfer and Frenkel excitons. Molecular sites are represented by black ellipsoids, holes and electrons by red and blue circles, respectively.

Similarly to charge transfer processes, in the weak-coupling regime, the rate for an energy transfer event can be computed by means of the Fermi's golden rule,[264] in which the Hamiltonian matrix element (the coupling) is a key factor. In the context of energy transfer, the matrix element is the excitonic coupling that measures the interaction between the excited states localized over molecular units. Exciton transport is traditionally understood as the transfer of

a Frenkel exciton from one molecular site to another, and this transfer is known as Förster resonance energy transfer (FRET) mechanism (Figure 66a). The coupling that mediates in the Förster energy transfer mechanism is usually computed as the Coulombic interaction between the transition densities,[192] which can be condensed in transition dipoles or transition atomic charges. In contrast, at short distances or between triplet states other contributions as the exchange may become relevant,[285,286] which leads to the so-called Dexter energy transfer mechanism (Figure 66b). Finally, the last possible mechanism is caused by the mediation of intermediate charge-transfer states in a stepwise mechanism (Figure 66c). The couplings that mediate in this last mechanism are the hole or electron transfer integrals where the monoelectronic contribution is dominant, in opposition to the Coulomb or exchange that are purely bielectronic. This charge-transfer mediated mechanism, in combination with the traditional Förster energy transfer mechanism, has become one of the strategies under study to get higher efficiencies in the energy transport context.[202,287,288]

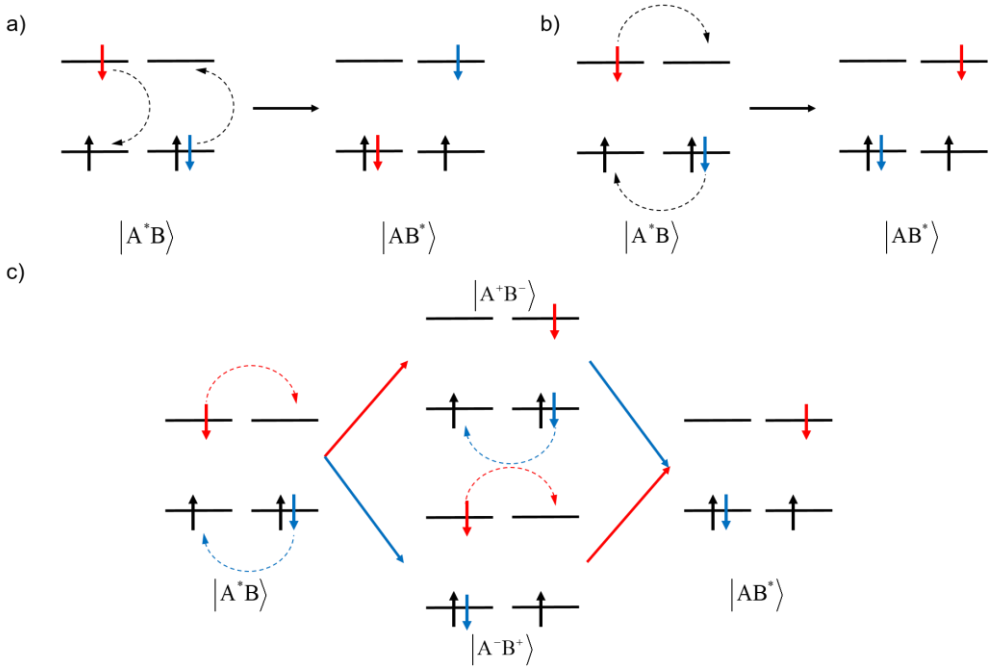

Figure 66. Schemes of Förster (a), Dexter (b) and charge-transfer mediated (c) energy transfer mechanisms.

In this chapter, we present two different sections in the framework of exciton transport in organic systems. First, we focus on the evaluation of the exciton coupling within molecular dimers (Section 6.2.1). In particular, we compare some popular methods to compute excitonic couplings thoroughly analyzing the similarities and discrepancies between the different approximations. Likewise, we pay attention to the impact that the charge-transfer excited states have onto the adiabatic states wavefunctions and energies. This comparison has been performed by using a parallel anthracene dimer as a model emulating the interactions existent in supramolecular aggregates and molecular crystals, where the orbitals are generally delocalized due to the short intermolecular distances. That delocalization always makes hard the analysis of the excited

states in terms of their nature. In the last part of Section 6.2.1 we move from the parallel dimer, which is a toy model, to the two different dimers actually found in the crystal, and the influence of the charge-transfer states in the energy transfer in the crystal is analyzed.

Second, the exciton transport of a supramolecular polymer based on an *N*-heterotriangulene derivative is modelled by means of a combined computational approach that employs electronic structure calculations, model Hamiltonians and a fully quantum dynamics (MCTDH) technique (Section 6.2.2). Namely, we are interested, from the quantum simulations, in estimating exciton diffusion coefficients and the exciton diffusion lengths, which are experimental observables in different situations. The role of the charge-transfer excited states on transport properties is also studied.

6.2 Results and discussion

6.2.1 Comparative analysis of popular methods to estimate excitonic couplings

A comparison of different and common methods to compute the excitonic coupling for the singlet-singlet energy transfer in molecular pairs was first performed. In particular, the dependence of the excitonic couplings with the intermolecular distance for a totally parallel anthracene dimer was analyzed (Figure 67). All the electronic structure calculations to evaluate the excitonic couplings with the different selected approximations were carried out at the CIS/6-31G** level.

The approximations used to evaluate the excitonic couplings can be classified into different categories. The first category groups the approaches that only take into account the Coulombic (long-range) interaction of the excitonic coupling assuming that all the other effects are negligible. Some well-known approximations within this category are the point-dipole (PD) model and the transition density cube (TDC) approach.[192] The former computes the excitonic coupling as an electrostatic interaction between the transition dipole moments localized over each molecular unit, whereas the latter, which is more accurate, computes the coupling as an electrostatic interaction between a large number of point transition densities located on each molecule. Diabatization schemes, which can capture short- and long-range interactions for excitonic couplings, can be collected in another category. In general, these methods make use of a molecular property that can be easily estimated to find the adiabatic-to-diabatic transformation. The off-diagonal terms in the diabatic Hamiltonian correspond to the targeted couplings. Herein, two diabatization schemes, one based on atomic transition charges[193] (ATC) and the other one based on the fragment particle-hole density (FPHD) diabatization scheme,[195] have been used (more details can be found in Section 3.2.6.5). Finally, an *ab initio* Frenkel–Davydov (AIFD) model Hamiltonian, similar to those developed by Herbert,[197,198] Martinez,[199,200] Fujita[201] or Fujimoto,[202] is also discussed (see Section 3.2.6.6 for further details). In this model, the couplings are directly computed by using the Slater-Condon rules between determinants and all interactions (short- and long-range) are included.

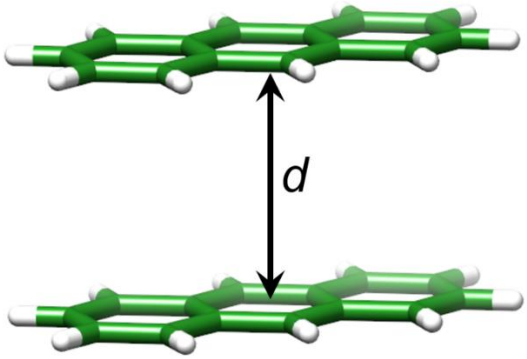

Figure 67. Representation of the anthracene dimer used for the comparative study. The black arrow labeled as "*d*" denotes the relative displacement vector.

Figure 68 shows the excitonic couplings computed for an eclipsed anthracene dimer as a function of the intermolecular distance. At long distances, all the selected methods provide similar excitonic coupling values with no significant difference between them. At distances shorter than 6.0 Å and within the category where only Coulombic interactions are included, the PD approximation starts to deviate from the general trend (Figure 68b). This behavior is well known for those cases where the distance between the molecular sites is smaller than the molecular size since, in that situation, the validity of the PD approximation breaks down.[289] In particular, the PD approach overestimates the excitonic coupling values compared to the TDC method, which can be used as the reference approximation to evaluate the pure Coulombic excitonic coupling as discussed below.

Diabatization schemes show quite different pictures. The diabatization scheme based on atomic transition charges deviates, for instance, from the Coulombic excitonic couplings (TDC method), which may indicate that short-range

effects are becoming important. Nevertheless, the excitonic coupling values computed by using the FPHD diabatization scheme does not present any significant deviation compared to the curve calculated with the TDC method. The origin of the discrepancy between both diabatization methods can be attributed to the interference of other excited states in the adiabatic representation. While the FPHD scheme can be safely used for the diabatization of multiple excited states of different nature (Frenkel-type or CT states), the Procrustes diabatization approach based on ATCs is limited owing to the requirement of defining reference excited states. This is difficult because ATCs for well-defined diabatic CT states are computed to be zero. To investigate this dissimilarity in more detail, the difference between the energies for the Frenkel excited states obtained by the diabatization for the molecular dimer and the isolated monomer is represented in Figure 69. The energies computed with the FPHD scheme for the states where the hole and the particle are in the same fragment (*i.e.*, Frenkel states) are practically equivalent to those excitation energies calculated for the isolated anthracene molecule. A maximum deviation of –0.06 eV for distances shorter than 4.5 Å is found, which is an almost negligible deviation. In contrast, the ATC-based diabatization scheme (Procrustes) presents quite large deviations at short distances, reaching differences up to –0.75 eV at 3.0 Å.

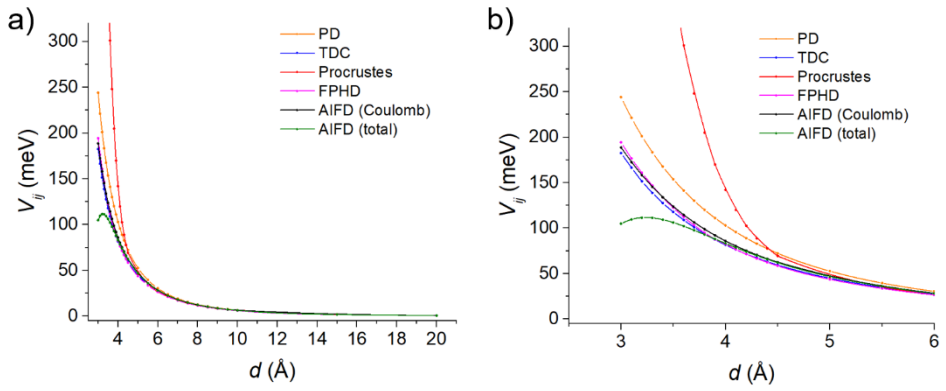

Figure 68. Evolution of the excitonic couplings (V_{ij}) with the intermolecular distance for an eclipsed anthracene dimer (a) computed with the different approximations selected in this Thesis. Magnification of Figure 5a in the 3–6 Å range (b).

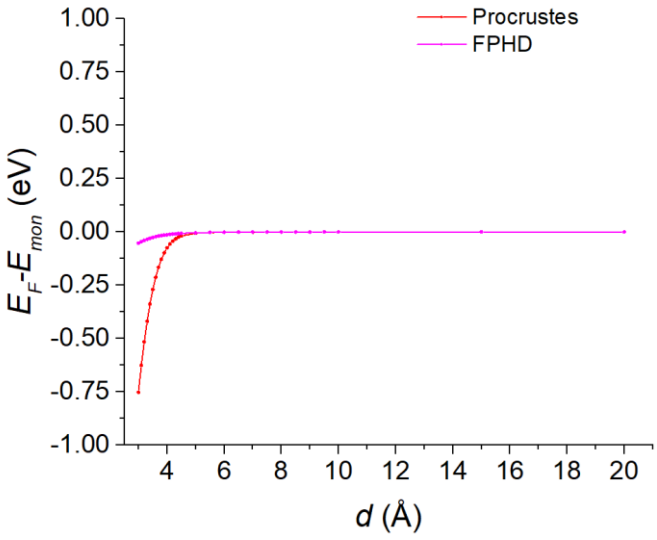

Figure 69. Energy difference between the Frenkel states obtained from the diabatization for the eclipsed anthracene dimer at variable distances and the Frenkel excitation energy of the isolated anthracene molecule.

In the last category of approximations, we have selected an *ab-initio* Frenkel–Davydov model Hamiltonian (see Section 3.2.6.6 for further details). In AIFD models, excitonic couplings are estimated from the direct evaluation of the corresponding matrix elements. Note that, in the AIFD method, the total excitonic coupling can be easily dissected in the long-range (Coulombic) and short-range (overlap and exchange) interaction components by the calculation of the respective one- and two-electron integrals. The Coulombic component of the excitonic couplings computed with the AIFD model (estimated directly from the two-electron Coulomb integral) follows the same trend as the coupling curve obtained with the Coulombic TDC model with differences between both methods below 10 meV in the intermolecular distance range analyzed (Figure 68). This finding clearly suggests that the TDC approach is accurate enough to estimate the Coulombic excitonic coupling component compared to the two-electron integral evaluation. Nevertheless, the evolution of the total excitonic coupling estimated with the AIFD model, especially at short intermolecular distances (<3.5 Å), starts to deviate compared to the rest of approximations selected. That discrepancy might arise from the fact that AIFD uses a localized orbital basis that is not necessarily orthogonal at short distances but it works assuming quasi-orthogonality. This effect could be mitigated by using non-orthogonal CI methodologies.[290–292] Nevertheless, distances lower than 3.5 Å are rarely found in a fully parallel disposition, which is the limiting case where the interaction between the sites is maximized, and thereby the extreme case where the assumptions in which AIFD is rooted are not fulfilled.

Figure 68 clearly reveals a deviation for the three approximations able to incorporate both short- and long-range interactions for the excitonic couplings

(*i.e.*, the FPHD scheme, the Procrustes-based diabatization method and the AIFD model). The significant deviation for the curve calculated with the Procrustes-based diabatization model is ascribed to short-range effects (in particular, mixing of Frenkel and charge-transfer excited states). Note that the Procrustes-based diabatization scheme is a two-state model and, consequently, an increasing error is expected when multi-state interferences in the adiabatic states are present and not properly taken into account in the scheme. This multi-state effect easily originates from a non-negligible coupling between Frenkel-type and CT-type excited states in the adiabatic picture as it has been commonly found in other and similar molecular arrangements.[183,190,293]

In summary, the FHPD diabatization and the AIFD model, both including ionic configurations or charge-transfer states, are the best options to estimate excitonic couplings even in the short-distance (or highly perturbated) limit. These methods provide the best results because they share two essential characteristics: 1) both use the full wavefunction expansion or density, as well as the TDC approach, and 2) both are based in a multi-state model in opposition to other methods that employ the full density of the adiabatic state as the diabatization based on ATCs.

To explore further this idea, the couplings between the Frenkel and CT states, as well as the diabatic energies for all the states, were computed with the FPHD and AIFD methods for the eclipsed anthracene dimer as a function of the intermolecular distance (Figures 70 and 71). Note that the Frenkel−CT (FE−CT) couplings can be accurately approximated to the hole (t_h) and electron (t_e) transfer integrals. Both methods provide a similar picture with similar values for t_h and t_e but with opposite sign, which is consistent with the

symmetry of the model selected. However, discrepancies in the magnitude of the couplings arise when comparing both methods at short distances, what is attributed to the loose of validity of the quasi-orthogonality assumption that roots the AIFD model Hamiltonian. Both methods predict the same behavior where the FE–CT couplings start to have non-negligible values at distances shorter than 6.0 Å. They increase very quickly, becoming of the same magnitude than the FE–FE couplings near 5.0 Å and even higher at shorter distances. Therefore, at short distances, methodologies that include CT states and are able to estimate simultaneously FE–FE and FE–CT couplings are absolutely needed.

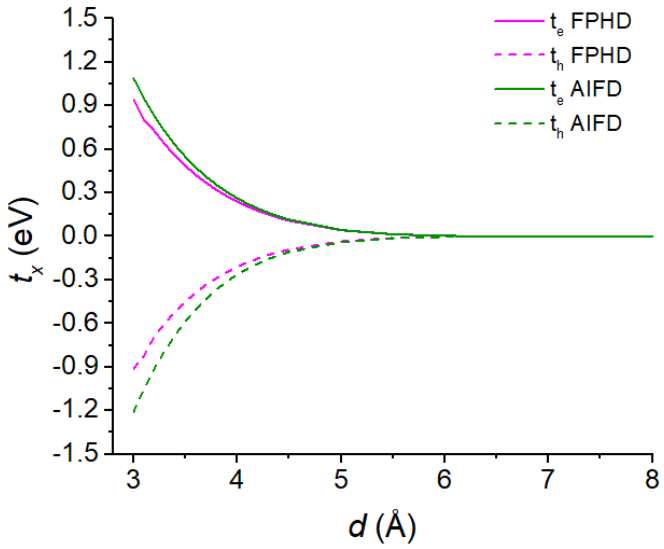

Figure 70. Hole (t_h) and electron (t_e) transfer integrals for the eclipsed anthracene dimer obtained through the FHPD diabatization and the AIFD method.

Apart from the excitonic and electronic couplings, the diabatic energies of the Frenkel (E_{FE}) and the charge-transfer (E_{CT}) excited states were determined with FPHD and AIFD methods as displayed in Figure 71a. Both methods provide similar pictures; *i.e.*, E_{FE} does not present any dependence on the intermolecular distance whereas E_{CT} undergoes a decrease in energy when shortening the intermolecular distance in line with Mulliken's rule.[294] Although both methods give similar diabatic energies at large distances, small differences emerge at short distances (< 6.0 Å), which originate from the diabatic wavefunction definition. In the AIFD method, the diabatic wavefunctions are initially defined and, after the definition, all the matrix elements are computed. In contrast, the diabatic wavefunctions, in the FPHD diabatization, can be only obtained after determining the adiabatic-to-diabatic matrix transformation from the adiabatic wavefunctions. The small decrease of E_{FE} at very short intermolecular contacts for the FPHD diabatization scheme arises from a residual mixing with CT states in the diabatic state. Actually, the difference in the way the state-functions are defined is the reason why E_{FE} is completely constant in the AIFD method and identical to the isolated molecule excitation energy, whereas small deviations are present at short distances in the FHPD diabatization. In summary, the states obtained through the FHPD approach are highly localized but still present a residual mixing that deviates the energy. This residual but non-negligible mixing can be identified by representing the transition dipole moment (TDM) of the diabatic states (Figure 71b). The not null component of the TDM of the Frenkel states decreases due to the residual mixing at short distances, whereas the TDM of the CT states in the direction that would be ideally zero slightly rises when decreasing the intermolecular distance.

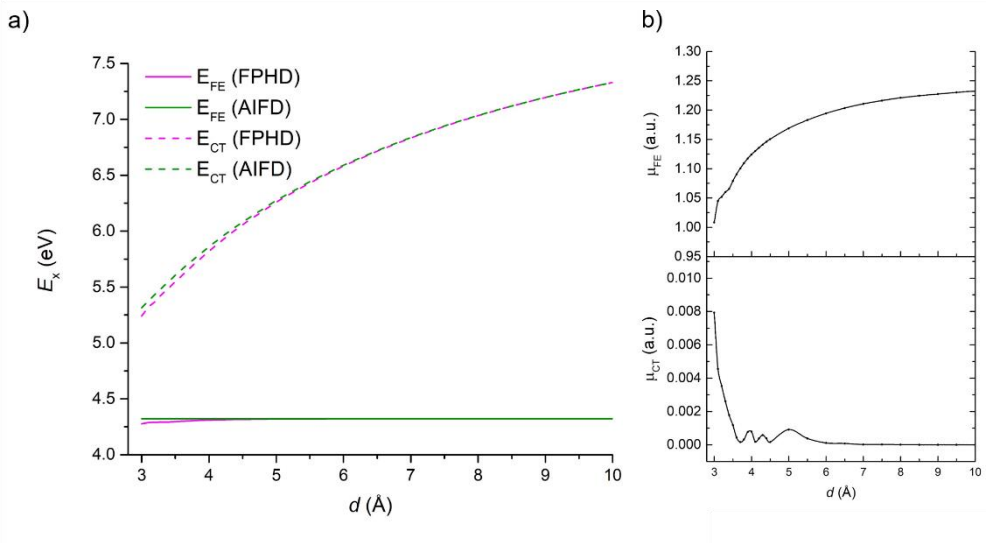

Figure 71. a) Diabatic energies of the Frenkel (E_{FE}) and charge-transfer (E_{CT}) excited states calculated with the FHPD and AIFD methods as a function of the intermolecular distance for an eclipsed anthracene dimer. b) Transition dipole moments (in atomic units) calculated for Frenkel (μ_{FE}) and charge-transfer (μ_{CT}) diabatic states obtained from the FHPD diabatization scheme.

In addition to the diabatic couplings and excited state energies, the adiabatic wavefunctions and energies obtained from both AIFD and FPHD methods were analyzed. Figure 72 displays the energy evolution of the low-lying Frenkel and CT adiabatic states, corresponding to the symmetric and antisymmetric combination of the localized or diabatic states (denoted by the "+" and "–" superscripts, respectively). In general, both methods provide similar adiabatic energies with deviations at short distances that are always smaller than 0.2 eV. It should be noted that the adiabatic energies obtained with the FPHD diabatization scheme are exactly the same as those found from a full supermolecule electronic structure calculation.

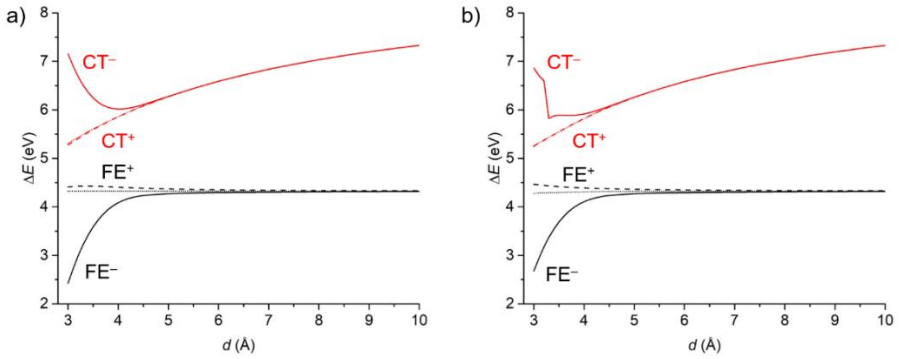

Figure 72. Adiabatic energies calculated by the AIFD (a) and FPHD (b) models calculated for Frenkel (in black) and charge-transfer (in red) states. Symmetric (+) adiabatic states are represented with dashed lines and antisymmetric (–) states with solid lines. Diabatic Frenkel and charge-transfer energies (pointed lines) are represented for comparison purposes.

As inferred from the low values of the FE–FE couplings, the Frenkel adiabatic energies slightly split from the diabatic energy reference at larger distances, because of the long-range nature of the excitonic coupling, whereas in the charge-transfer states the splitting appears at distances lower than 5.0 Å where the FE–CT couplings start to be significant. It should also be mentioned that the symmetric adiabatic states present small energy differences with respect to the diabatic energies, with an energy difference similar to the excitonic coupling for the FE^+ state and practically no difference for the CT^+ in agreement with the negligible CT–CT coupling. This is supported by the wavefunction analysis (Figure 73). The symmetric adiabatic states present a well-defined FE or CT nature and, thereby, the splitting from the diabatic reference is expected to be equal to the couplings as would be obtained from a two-state Kasha model (see Section 3.2.6).

In contrast to the small energy difference found between the symmetric adiabatic states and the diabatic states, the anti-symmetric adiabatic FE^- and CT^- states undergo a significant energy difference at short distances compared to the diabatic energies. This difference comes from an important FE−CT mixing in the anti-symmetric adiabatic FE^- and CT^- states, as supported by the wavefunction analysis presented in Figure 73. Consequently, the large splitting observed for the antisymmetric states arises from the FE–CT couplings that are quite large at short distances.

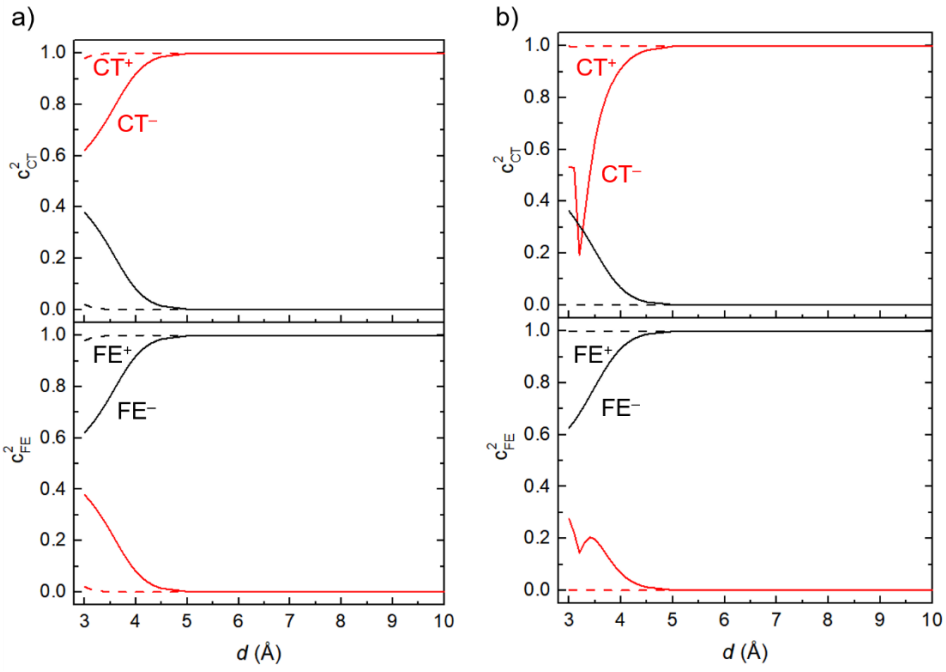

Figure 73. Adiabatic wavefunction description of the Frenkel (bottom) and charge-transfer (top) states in terms of diabatic contributions obtained through the AIFD model (a) or the FHPD diabatization (b). Symmetric (+) and antisymmetric (–) combinations are represented by dashed and solid lines, respectively.

In summary, the comparison between the different methods selected to compute excitonic couplings between excited states provides a good agreement for all the methods at large distances showing that the only parameter that has a clear long-range component is the FE−FE excitonic coupling.[191] However, as recently reported, at short distances the role of the charge-transfer states becomes important.[190,293] Therefore, the use of a diabatization scheme that could separate the states of different electronic nature or a direct method as the AIFD approach have to be employed. However, even both methods provide good description and comparable and meaningful information, they have different advantages and shortcomings. The bottom-up AIFD approach presents a clear well-differentiated definition of all the states included, since they are defined without any information obtained from the full dimer calculation, and allows to generate small models including a few number of states to understand the basic physics of the system. However, AIFD should be always tested with the full calculation to ensure that the state basis used is enough to obtain quantitative results. In contrast, the FHPD method allow to analyze the wavefunctions obtained from the full dimer calculation and identify the most important states. However, the definition of the states is based on a molecular property providing a clear nature of the diabatic states. However, the matching between the diabatic states obtained with the FHPD method with the isolated molecule states is not trivial.

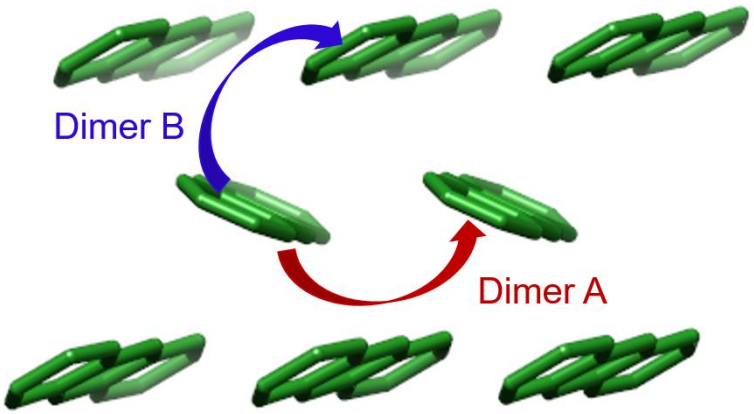

Figure 74. Representation of the herringbone crystal structure of anthracene in the *ab* plane. The most relevant slipped π-stacked and tilted dimers (dimers A and B, respectively) for the transport are labeled. Hydrogen atoms are omitted.

Apart from the eclipsed parallel anthracene dimer, used as an archetype model, the most relevant dimers for the exciton transport in the anthracene crystal along the *ab* plane were also studied using the AIFD model. In particular, the excited states and the diabatic couplings of the slipped π-stacked (A) and tilted (B) dimers were computed (Figure 74). The excitation energies and excitonic couplings computed for the low-lying FE and CT diabatic states are summarized in Table 8. Dimer A presents a significant excitonic coupling J of –78.8 meV between the lowest-energy diabatic FE states predicted at 4.32 eV. The diabatic CT excited states are found to be higher in energy by 2.14 eV compared to the FE excited states. The FE–CT couplings between an FE (A^*B) and the CT excited states (A^-B^+ and A^+B^-), which can be associated to t_h and t_e transfer integrals, are computed to be 54.3 and 70.5 meV, respectively. These

values are in the same order of magnitude as the excitonic coupling *J* between FE states. Note that the FE–CT couplings between an FE (A^*B or AB^*) and the CT excited states (A^+B^- and A^-B^+) are equivalent due to the symmetry of dimer A. The picture for the tilted dimer (B) is quite different owing to the lack of symmetry in dimer B. The lowest-energy diabatic CT states are not energetically equivalent due to the different polarization of both molecules.[295] This is in contrast to dimer A where both molecules are polarized in the same way. The excitonic coupling *J* in dimer B is quite small (–4.5 meV) compared to dimer A (–78.8 meV), and the FE–CT couplings are of the same order of those predicted for dimer A.

Table 8. Excitation energies and excitonic/electronic couplings computed with the AIFD method for the lowest-energy FE and CT diabatic states of the crystalline anthracene dimers (dimers A and B).

	Dimer A	Dimer B
E_{A^*B} (eV)	4.32	4.31
E_{AB^*} (eV)	4.32	4.31
$E_{A^+B^-}$ (eV)	6.46	5.94
$E_{A^-B^+}$ (eV)	6.46	6.45
J (meV)	–78.8	–4.5
t_h (meV)	54.3	38.5 (36.0)[a]
t_e (meV)	70.5	–89.1 (–93.3) [a]

[a] Values within parentheses indicate the second t_h and t_e values due to the asymmetry of the CT states

In a further step, the fluctuation of the excitonic/electronic couplings for the anthracene crystal as a consequence of the thermal motions was studied by molecular dynamics (MD) simulations and electronic structure calculations with the AIFD model. A 3 × 3 × 3 supercell of the anthracene crystal along the crystallographic axes *a*, *b* and *c* was built and a MD simulation was subsequently carried out using the MM3 force field. To evaluated the couplings, structures for dimers A and B taken from MD snapshots each 0.1 ps along 50 ps were used for the AIFD calculations.

Figure 75 displays the distribution of the excitonic coupling *J* and the transfer integrals (t_h and t_e) computed for the crystalline anthracene dimers A and B. Both dimers present average values for all couplings similar to those given in Table 8 for ideal anthracene crystalline dimers. Nevertheless, the analysis of the fluctuation measured as the standard deviation turns out to be highly interesting. Dimers A and B exhibit a narrow distribution for the excitonic couplings *J* with similar standard deviations (21 and 22 meV, respectively). The fluctuation in these dimers comes mainly from Coulombic interactions (long-range) with almost negligible exchange contributions (short-range). These outcomes seem to be in contrast to the previous results reported in the literature for the excitonic couplings *J* in anthracene crystal,[296] where a large fluctuation (especially for dimer B) was found and associated to short-range interactions. This discrepancy comes from methodological aspects as briefly explained below.

Regarding the FE–CT couplings, significant broader distributions, compared to *J* couplings, were found for both dimers. Dimer B holds standard deviation values (60 and 44 meV for t_h and t_e, respectively) higher than those calculated

for dimer A (40 and 38 meV). The broad distributions found for the FE–CT couplings are expected owing to the short-range nature of this coupling (overlap and exchange effects). In fact, the overlap effect is the most relevant because the molecular orbital overlap is very sensitive to small intermolecular structural variations. An interesting point to be stressed is the differences in sign for the t_h and t_e transfer integrals between dimer A and B. t_h and t_e show the same sign for dimer A, whereas they have an opposite sign for dimer B. This change of sign in the transfer integrals has significant consequences for the nature of the adiabatic excited states in both dimers. Whereas the S_1 and S_2 adiabatic excited states of dimer A do not present any significant CT character (99.0 and 99.9% of FE character, respectively), the S_1 excited state of dimer B presents a small but non-negligible CT character (7%). Actually, this small FE–CT mixing was responsible for the significant thermal fluctuation of the excitonic couplings previously reported for anthracene.[296] As a two-level diabatization scheme was used to evaluate the excitonic couplings in the previous study, the two lowest-energy adiabatic excited states for dimer B were likely mixed with CT excited states and that FE–CT interference was unavoidably transferred to the evaluation of the excitonic couplings. As a consequence, the significant thermal fluctuation of excitonic couplings between pure FE excited states was wrongly associated to short-range interactions. Those short-range interactions are important for couplings between FE and CT excited states.

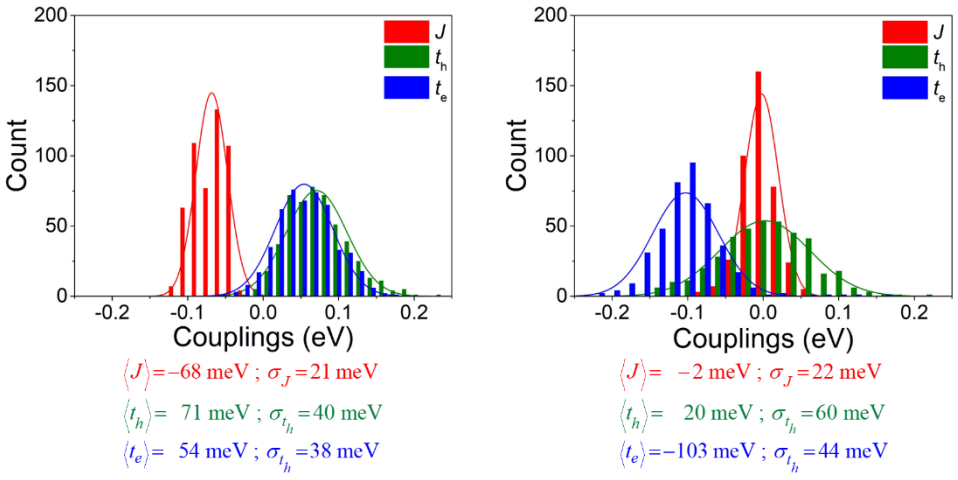

Figure 75. Distribution of the values computed along the MD simulation for the excitonic coupling (J) and the hole (t_h) and electron (t_e) transfer integrals for dimer A (left) and dimer B (right). Average values and standard deviations obtained from the distributions are given (bottom).

The analysis reported here for the anthracene crystal dimers with the AIFD model allows to enhance the knowledge about the role of the short-range interactions for excitonic processes in semiconducting organic crystals with a herringbone disposition. This has been possible since the AIFD method is able to individually dissect all the interactions (short- and long-range) for the evaluation of the excitonic couplings in molecular pairs. In particular, the study allows to conclude that the short-range interactions are essential for significant thermal fluctuations of the excitonic couplings although they are more important for FE–CT couplings than for couplings between pure FE excited states.

6.2.2 Energy transport in ordered *N*-heterotriangulene supramolecular polymers

Based on the already mentioned evidences reported by Headler and coworkers of the unusual and efficient long-range exciton transport in a single-fiber of a supramolecular polymer based on *N*-heterotriangulene,[280] we study the energy transport process to disentangle the reasons behind this exceptional exciton transport.

Initially, the electronic structure and the excited states of a simplified *N*-centered *N*-heterotriangulene (NHT), where the side alkyl chains were substituted by methyl groups (Figure 76a), were studied at the B3LYP/6–31G** level after its previous optimization using a C_3 symmetry. Figure 76b displays the computed frontier molecular orbitals leading to a single HOMO energy level and a double-degenerated LUMO belonging to the irreducible *E* symmetry representation. TDA-DFT calculations predict the two lowest-energy singlet electronic transitions ($S_0 \rightarrow S_1$ and $S_0 \rightarrow S_2$) degenerate in energy at 2.99 eV, which are mainly described by single HOMO $\rightarrow$ $LUMO_1$/$LUMO_2$ monoexcitations. The energy predicted for the $S_0 \rightarrow S_1$ and $S_0 \rightarrow S_2$ transitions is in good agreement with the experimental absorption band observed at 2.70 eV.[280] The picture obtained for the isolated molecule is used as a reference for subsequent calculations on the supramolecular aggregate.

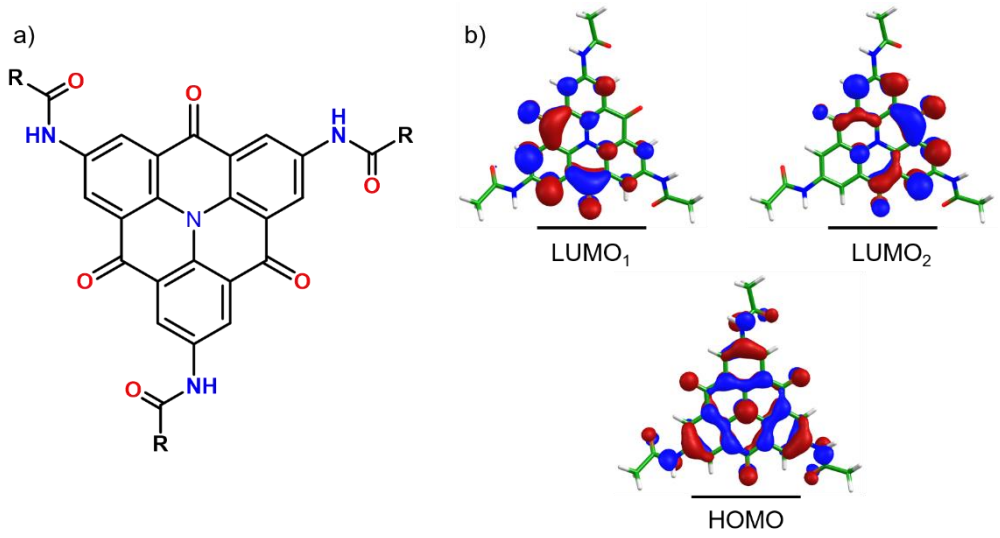

Figure 76. a) Chemical structure of a *N*-Heterotriangulene derivative bearing alkyl-amide peripheral groups. b) Representation of the HOMO and LUMO of the NHT derivative.

An atomistic structural model of the supramolecular polymer of the *N*-heterotriangulene derivative is required to obtain the structural parameters needed for the study of the exciton transport. A supramolecular pentamer of NHT was initially built and fully optimized at the DFT level using the B3LYP functional including the Grimme's D3 dispersion correction (Figure 77a,b). Although the optimized helical oligomer presents noticeable terminal effects affecting the peripheral molecules, the central trimer is good enough to obtain the relevant structural parameters —the intermolecular distance (3.25 Å) and the peach torsion angle (34.5°)— for the representation of an ideal supramolecular polymer.

An ideal NHT dimer, using the central molecule of the previously optimized pentamer and the optimal intermolecular structural parameters, was built as a

model to investigate the electronic and excitonic properties. Surprisingly, despite the short distance between the molecular moieties, the analysis of the excited states of the dimer was relatively easy (see below) due to the localized shape of the molecular orbitals (Figure 77c). This localization comes from the different electronic environment each molecule in the dimer feels as a consequence of the growing dipole moment in the π-stack direction originated by the amide groups.[295] The different environment is evidenced by the significant energy difference between the HOMO and HOMO–3 of the dimer, which correspond to the HOMO of each individual molecule (Figure 77c).

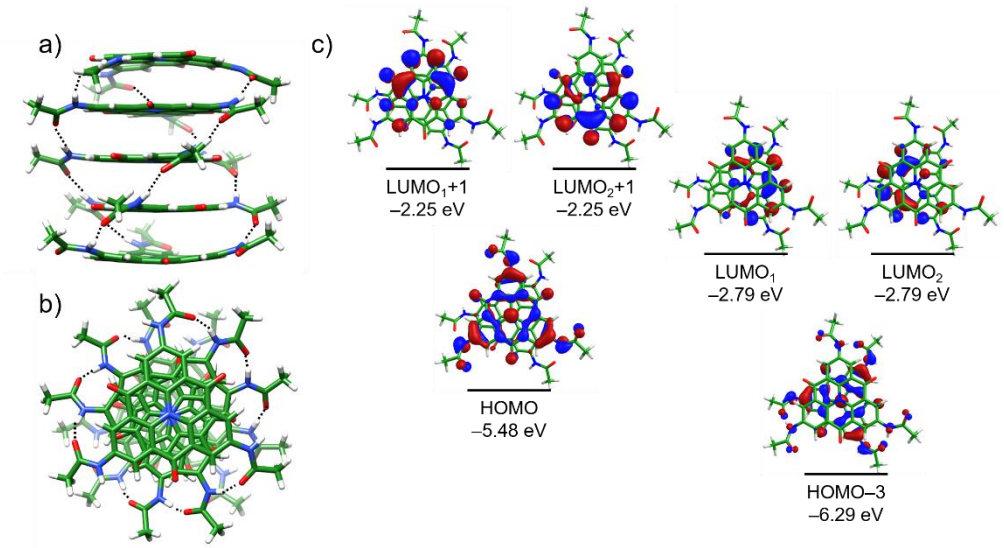

Figure 77. Top (a) and side (b) view of the NHT pentamer optimized at the B3LYP/6-31G** level. (c) Energy diagram and representation of the molecular orbitals of an ideal *N*-heterotriangulene dimer. The displayed molecular orbitals correspond to those resulting from the interaction of the HOMOs and LUMOs localized on each NHT molecular unit.

Table 9 collects the energy of the low-energy singlet excited states that are mainly described by the HOMO → LUMOs monoexcitations computed within the TDA-DFT formalism using the B3LYP functional and the OT-ωB97XD functional with an optimal ω value of 0.15 bohr^{-1}. The use of the optimally-tuned OT-ωB97XD long-range functional is highly recommended due to the relevance of obtaining a relatively accurate estimation of the energy of the lowest-energy CT excited states. The excited states gathered in Table 9 are labeled according to their main nature. Both functionals provide a similar picture where the two lowest-energy adiabatic states correspond to A^+B^- charge-transfer states (S_1 and S_2) described as HOMO → $LUMO_1$/$LUMO_2$ monoexcitations, followed by two FE states (S_3 and S_4). It should be mentioned that the lowest-energy CT states of each nature (i.e., the A^+B^- and A^-B^+ states) are no longer energetically degenerate due to the stabilization or destabilization induced by the electrostatic interaction between the dipole moment generated by the twisted amides with the corresponding CT excited states. A supramolecular dimer model, where both NHT molecules are totally planar (no intermolecular H-bonds), was calculated to confirm if the permanent dipole moment along the π-stacking direction is responsible for the difference in energy of the CT states. Unfortunately, a direct assignment of the low-lying excited states for the planar NHT dimer was not possible due to the delocalized nature of the molecular orbitals involved in the excitations. Nevertheless, this analysis was performed after diabatization in terms of diabatic CT states (see below) and it can be anticipated that, in a planar NHT dimer, the four lowest-energy CT singlet excited states are almost degenerate in energy. Finally, the OT-ωB97XD functional was selected for the next studies because it is expected to provide better energy differences between the excited states.

Table 9. Vertical excitation energy (ΔE) calculated for selected adiabatic singlet excited states (S_i) of the ideal NHT dimer at the DFT level using the B3LYP and OT-ωB97XD ($\omega = 0.15$ bohr^{-1}) functionals. The selected adiabatic excited states are those that can be easily associated with quasi-diabatic states of FE-type (A^*B and AB^*) and CT-type (A^+B^- and A^-B^+) nature.

B3LYP/6-31G**			OT-ωB97XD/6-31G**		
S_i	ΔE (eV)	Nature	S_i	ΔE (eV)	Nature
S_1, S_2	2.162	A^-B^+	S_1, S_2	2.916	A^-B^+
S_3, S_4	2.831	A^*B	S_3, S_4	3.345	A^*B
S_9, S_{10}	3.108	AB^*	S_9, S_{10}	3.647	AB^*
S_{28}, S_{29}	3.495	A^+B^-	S_{18}, S_{19}	4.239	A^+B^-

Table 10 collects the diabatic energies (ΔE), excitonic couplings (J) and holes and electron transfer integrals (t_h and t_e) computed with the FPHD diabatization method for an ideal NHT supramolecular dimer with intermolecular H-bonds defining a permanent dipole moment along the π-stacking. The results obtained for the planar NHT dimer are also included in Table 10 to unveil the effect that the lack of permanent dipole moment has on the energy of the low-lying CT states and, thereby, the effect of the energy splitting of the CT states. Table 10 clearly reveals, irrespective of the density functional, that the dipole moment along the π-stacking direction caused by the twisted amide groups is responsible for the significant energy difference between the CT excited states (A^+B^- and A^-B^+). For the planar NHT dimer, the A^+B^- and A^-B^+ CT states only differ by ca. 0.1 eV whereas this difference significantly rises (> 1 eV) for the NHT dimer with intermolecular H-bonds (twisted amides).

Table 10. Diabatic energies and couplings obtained at the B3LYP and OT-ωB97XD level by using the FPHD diabatization scheme for NHT dimer models with twisted and planar amides. *x* and *y* subscripts makes reference to the main orientation of the transition dipole moment to distinguish between degenerate states.

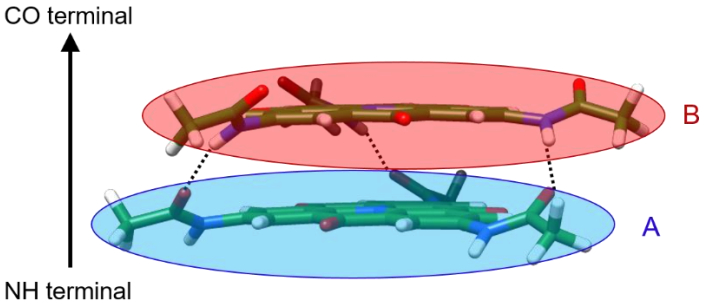

	B3LYP		OT-ωB97XD	
	twisted	planar	twisted	planar
E_{A^*B} (eV)	3.066	2.990	3.527	3.460
E_{AB^*} (eV)	2.927	2.920	3.423	3.400
$E_{A^+B^-}$ (eV)	3.386	2.817	4.168	3.613
$E_{A^-B^+}$ (eV)	2.235	2.699	3.052	3.502
$J^{xx} = J^{yy}$ (meV)	27.9	26.0	49.3	38.8
$J^{xy} = -J^{yx}$ (meV)	27.0	29.2	15.2	40.9
$t_e^{xx} = t_e^{yy}$ (meV)	72.3	91.9	78.0	63.6
$t_e^{xy} = -t_e^{yx}$ (meV)	59.8	23.6	7.9	60.5
$t_h^{xx} = t_h^{yy}$ (meV)	–201.4	–218.7	–238.7	–251.7
$t_h^{xy} = -t_h^{yx}$ (meV)	97.9	26.3	31.4	33.3
J^{eff} (meV)	38.8	39.1	51.6	56.4
t_e^{eff} (meV)	102.3	94.9	78.4	87.7
t_h^{eff} (meV)	–223.9	–220.2	–240.7	–253.9

Table 10 also allows to compare the results obtained at the two DFT levels (B3LYP and OT-ωB97XD). As expected, OT-ωB97XD predicts the low-lying diabatic excited states (both FE and CT) higher in energy compared to the energies found with the hybrid B3LYP functional. Nevertheless, for the further study of the exciton dynamics, what is relevant is the energy difference between the charge-transfer and the Frenkel states (Δ_{CT}). In this respect, OT-ωB97XD should provide more accurate energy differences than B3LYP because it mitigates the severe underestimation of the CT states presented at the B3LYP level. On the other side, all the coupling magnitudes are in general similar regardless the functional employed and the NHT dimer model selected (*i.e.*, the model with the twisted or planar amides). Although the direct couplings (J^{xx}, t_h^{xx} or t_e^{xx}) can differ depending on the functional, they are compensated by the cross-couplings (J^{xy}, t_h^{xy} or t_e^{xy}), and the effective coupling values ($J^{eff} = sign\left(J^{XX}\right)\sqrt{\left(J^{XX}\right)^2 + \left(J^{XY}\right)^2}$, Table 10), which are the most appropriate for the comparison, provide similar values for both functionals and models.

In addition to the diabatic energies and excitonic couplings discussed above, the relaxation energies for the different electronic states (exciton, cation and anion species) of the NHT molecule are necessary to study the final energy transport process. The relaxation energy is related to the electronic-vibrational coupling constant that will be used for the model Hamiltonian (see below). The relaxation energies for the NHT molecule in its first S_1 excited state and its charged states (cation and anion) were computed to be 53.4, 93.2 and 145.1

meV, respectively, at the OT-ωB97XD/6-31G** level. It should be stressed that the relaxation energy obtained for the S_1 state is quite small. Actually, the NHT molecule is likely to be one of the systems with the smallest relaxation energy for excitons. The 53.4 meV value is indeed comparable to the relaxation energies found for C_{60} fullerene (~0.06 eV)[297,298] or for pentacene (~0.05 eV) in their charged anion and cation states, respectively.[299,300] Also note that the relaxation energies for excitons are, in general, notably higher than those for the charged species.

The energy transport properties for the ideal NHT supramolecular polymer are studied by a Holstein-like model Hamiltonian (Eq. 95) including CT states and the ML-MCTDH quantum dynamics technique. The initial wavefunction was constructed by setting all the nuclear degrees of freedom in the Franck–Condon region and only the electronic state that corresponds to the excitation localized in the central molecule of the array was initially populated. The model Hamiltonian incorporates 201 molecular sites (electronic states) modulated each one by a single nuclear degree of freedom, that should be good enough to model the transport properties of the supramolecular polymer. Note that this model Hamiltonian is similar to that employed by F. Spano to successfully predict the optical properties of molecular aggregates.[293,301]

$$
\begin{aligned}
H &= H_{\text{vib}} + H_{\text{FE}} + H_{\text{CT}} + H_{\text{FE-CT}} \\
H_{vib} &= \sum_i \frac{\omega_i}{2}\left(-\frac{\partial}{\partial Q_i} + Q_i^2\right)\mathbf{I} \\
H_{FE} &= \sum_i \left(E_{\text{FE}} + \lambda_{\text{FE}} Q_i\right)\left|i\right\rangle\left\langle i\right| + \sum_i \sum_{j\neq i} J\left|i\right\rangle\left\langle j\right| \\
H_{CT} &= \sum_i \begin{bmatrix} \left(E_{\text{A}^+\text{B}^-} + \lambda_{\text{Cat}} Q_i + \lambda_{\text{An}} Q_{i+1}\right)\left|i^+;(i+1)^-\right\rangle\left\langle i^+;(i+1)^-\right| + \\ \left(E_{\text{A}^-\text{B}^+} + \lambda_{\text{An}} Q_i + \lambda_{\text{Cat}} Q_{i+1}\right)\left|i^-;(i+1)^+\right\rangle\left\langle i^-;(i+1)^+\right| \end{bmatrix} \\
H_{FE-CT} &= \sum_i t_{\text{e}}\left|i\right\rangle\left\langle i^+;(i+1)^-\right| + t_{\text{h}}\left|i\right\rangle\left\langle i^-;(i+1)^+\right| + h.c.
\end{aligned}
\tag{95}
$$

The vibronic Holstein-like Hamiltonian is divided into four terms including the vibrations, the FE excited states (A^*B and AB^*), the CT states (A^+B^- and A^-B^+) and the FE-CT interaction. In this Hamiltonian, the complicated picture due to the double energy degeneracy of the excited states has been simplified in effective non-degenerate FE and CT states; *i.e.*, in a dimer we are only considering 4 electronic states (the diabatic A^*B, AB^*, A^+B^- and A^-B^+ states). The couplings. J, t_h and t_e used correspond to the root mean squared values of the excitonic coupling, hole transfer integral and electron transfer integral, respectively (Table 10). ω_i is the frequency of a normal model that couples the nuclear motion with the electronic levels for each molecular site (denoted as i). ω_i is set to 1400 cm^{-1}, which is a typical value of the normal mode describing the stretching of the conjugated backbone in π-conjugated compounds.[176,302,303] λ_{FE}, λ_{Cat} and λ_{An} are the vibronic coupling constants that shift the Frenkel, cationic and anionic potential energy curves of mode i with respect to the ground state. The vibronic coupling constants are computed as

$\lambda_j = \sqrt{2S}$, where *S* is the corresponding Huang–Rhys factor that reproduces the relaxation energy ($S_j = \lambda_j / \omega_i$). Q_i is the dimensionless coordinate of the normal mode, and E_{FE}, $E_{A^+B^-}$ and $E_{A^-B^+}$ are the diabatic energies of the FE (averaged of E_{A^*B} and E_{AB^*}) and CT states collected in Table 10.

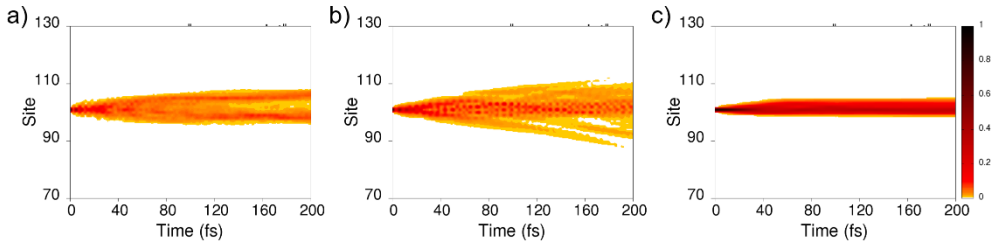

Figure 78. Time evolution of the population of the diabatic Frenkel states for a NHT-based supramolecular polymer model in three different situations: a) all the NHT molecules are totally planar (no permanent dipole moment), b) a more realistic arrangement with intermolecular H-bonds and a dipole moment along the π-stacking direction and c) a model similar to the previous one but without including CT states (right). Yellow color corresponds to a population of 0.001, orange to 0.01, red to 0.1 and black to 1.0

Figure 78 displays the time-evolution of the population of Frenkel states in an NHT-based supramolecular polymer in three different scenarios. The first model includes FE and CT excited states estimated for an arrangement where all the NHT monomers are totally planar, which determines that the CT states are almost degenerate (Table 10). The second model also includes FE and CT states but these states have been computed for a more realistic supramolecular dimer with intermolecular H-bonds and a permanent dipole moment along the

π-stacking direction. The third scenario is similar to the previous one but without CT states. Figure 78 clearly reveals that the simulations taking into account CT states (Figure 78a,b) present significant population (> 0.001) far from the initial populated site (the central one, site number 101), compared to the simulation where only the Frenkel states were included (Figure 78c). For instance, at 200 fs, the simulations that include CT states exhibit 25 (Figure 78a) and 34 molecular sites (Figure 78b) with significant population, whereas only 8 molecular sites are populated when CT states are not included in the simulation (Figure 78c). Note that in the simulations that include CT states the same population threshold is more meaningful since the total state population is divided between FE and CT states (Figure 79).

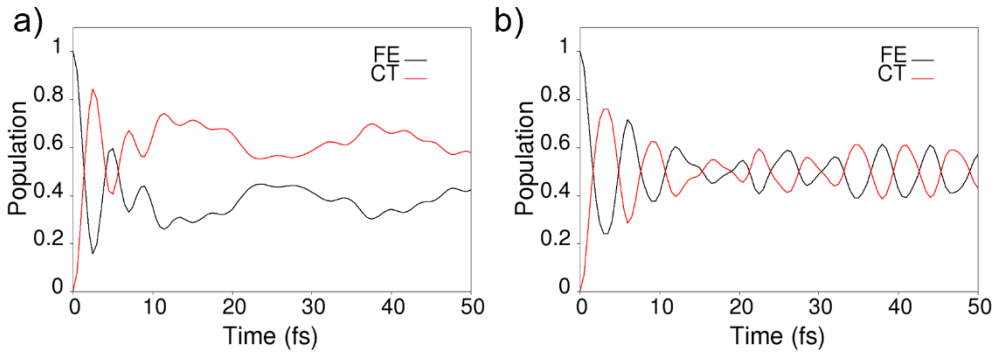

Figure 79. Time evolution of the FE and CT populations along the first 50 fs for a NHT-based supramolecular polymer where all the NHT molecules are: a) planar or b) forming intermolecular H-bonds (twisted amides).

Finally, the exciton diffusion coefficient (*D*) was computed according to:

$$D = \lim_{t\to\infty} \frac{\sigma^2(t) - \sigma^2(0)}{2t} \qquad (96)$$

Where σ^2 is the variance of the population, computed as the slope of a linear fitting of $\sigma^2(t)$ in the diffusive regime, estimated to be beyond 100 fs. The estimated exciton diffusion coefficients from the simulations including CT states were 0.254 (polymer with planar amides) and 0.167 $cm^2\ s^{-1}$ (polymer with twisted amides), whereas a value three orders of magnitude smaller (D = 0.0013 $cm^2\ s^{-1}$) was obtained from the simulation where only FE states were accounted for.

The exciton diffusion length (L) was computed as $L = \sqrt{2D\tau}$, where τ is the excited state lifetime and was fixed 2.3 ns, a value obtained from Ref 280. The estimated exciton diffusion lengths were found to be 341.7 and 277.6 nm for the polymer model with all NHT molecules planar and the model where the NHT molecules exhibit H-bonds, respectively. As expected, a much smaller L (7.3 nm) was predicted from the simulation without CT states. The outcomes therefore indicate that an exciton travels in average over 102 (planar amides) and 83 (twisted amides) NHT molecules (sites) before its decay to the ground state when CT states are included in the energy transport treatment, whereas it only travels through 7 molecules when CT states are omitted.

Our findings therefore support that the charge-transfer mediated energy transfer is an important mechanism that enhances the energy transport in *N*-heterotriangulene-based supramolecular polymers. Although the exciton diffusion lengths estimated in this work are smaller than those experimentally measured (~1.6–6.4 μm), this study clearly highlights the relevance of the CT excited states to enhance the energy transport in *N*-heterotriangulene-based supramolecular polymers. For the near future, other effects such as including non-local disorder by a Holstein–Peierls model Hamiltonian or model beyond

the tight-binding approximation should be tested to disentangle if they affect the efficiency of the exciton transport.

6.3 Summary

This chapter is framed in the context of energy transport in organic semiconductors. The chapter is divided in two well-separated sections. In the first subsection (Section 6.2.1), a thorough comparison of different but representative methodologies available in the literature to estimate excitonic couplings between molecular pairs has been performed. Several types of anthracene dimers (a totally eclipsed face-to-face dimer and the typical herringbone crystal molecular pair) have been employed for the analysis. The second part of the chapter (Section 6.2.2) tackles the energy transport in an *N*-heterotriagulene-based supramolecular polymer from a theoretical perspective by using a bottom-up multi-level approximation.

The evolution of the excitonic couplings computed as a function of the intermolecular distance in a totally eclipsed anthracene dimer and with different approximations (Coulombic potentials, diabatization schemes and direct *ab initio* integrals) reveals that, as expected, all the approaches provide an identical picture at long intermolecular distances since, at these distances, only the Coulombic excitonic interactions persist. In contrast, short-range effects (CT states mixing) become relevant at short intermolecular distances and differences between the different methodologies are evidenced. Among the selected approaches, it is necessary to stress the FPHD diabatization scheme and the AIFD model. Both approximations can deal with the excitonic

couplings between excited states of different nature (*e.g.*, the more challenging FE–CT couplings) including long-range and short-range effects. The second part of Section 6.2.1 provides a deep understanding, by using the AIFD method, of the origin of the thermal fluctuation of the excitonic couplings for anthracene crystal dimers. The outcomes suggest that the excitonic coupling fluctuations are more important for the tilted dimer (dimer B) than for the parallel dimer (dimer A), due to the FE–CT couplings and the FE-CT mixing in dimer B.

The study of the energy transport in an *N*-heterotriagulene-based supramolecular polymer (Section 6.2.2) was carried out in different steps. Initially, a well-ordered supramolecular pentamer of the *N*-heterotriagulene derivative, governed by π–π and H-bond interactions, was obtained at the DFT level. From this supramolecular oligomer, an ideal *N*-heterotriagulene dimer, by using the central molecule and the structural information of the optimized pentamer, was built to compute the adiabatic low-lying excited states by TDA-DFT. These calculations revealed the importance of the CT excited states, which were significantly mixed with the FE-type excited states. From these adiabatic states, the diabatic excited-state energies and excitonic couplings between all relevant (FE- and CT-type) states were computed within the FPHD scheme. This excitonic information was used to parameterize an extended Holstein Hamiltonian model and study the exciton dynamics of the supramolecular polymer with the ML-MCTDH formalism. The ML-MCTDH quantum simulations revealed that the inclusion of the CT states significantly improves the exciton transport in ordered *N*-heterotriangulene-based supramolecular polymers by a significant increase of the exciton diffusion

length (278 nm) with respect to the simulation without including CT states (7 nm).

Chapter 7. Conclusions

The present Thesis aims, from a theoretical perspective, to rationalize the structural, electronic, optical and transport properties of a series of different electro-active non-covalent assemblies of special relevance in the field of organic electronics. The ultimate goal is to establish valuable supramolecular structure-property relationships. In particular, this Thesis focuses on three types of chemical systems: hole-transporting materials (HTMs), donor–acceptor supramolecular complexes and supramolecular polymers. For each system, the spotlight has been put on different relevant electronic processes. The main conclusions obtained from the discussion (Chapters 4-6) are summarized here following.

Supramolecular polymers (Chapter 4)

In this chapter, the structural organization of several supramolecular polymers has been computationally investigated at atomistic resolution to establish the intimate relationship between the supramolecular organization and the (chiro)optical properties. In Section 4.2.1, the self-assembly and, in particular, the effect of chiral substituents in the pendant alkyl chains of tricarboxamide TPBA and OPE–TA compounds, which are derivatives of the simpler BTA system, were studied. Theoretical calculations of large aggregates, which are representative of polymeric systems, reproduce the preferred helicity (*M*- and *P*-type) of the *R* and *S* enantiomers, and reveal that the different amplification of chirality behavior arises from the effect of the non-covalent interactions between the side chains. Thus, a correlation between the size and structure of

the molecular building block, which determines the intermolecular arrangement and the chirality transfer capabilities, is found. In particular, OPE–TAs present the nearest intermolecular contacts, whereas the longer distances were estimated for TPBAs. BTAs are in an intermediate situation. The evolution of the intermolecular distances changes the supramolecular arrangement and explains the experimental trends observed for the mismatch penalty enthalpy ΔH_{MMP}, which estimates the energy penalty cost for the insertion of a molecule in its unpreferred helical arrangement. Finally, the bundling of TPBA helices was investigated motivated by the linear dichroism contamination effects observed in the circular dichroism experiments of TPBAs with none and one chiral side chain. Calculations reveal that the interaction energy between two interdigitated TPBA helices strongly increases as the number of side chains bearing a stereogenic center decreases leading to a more effective interdigitation (bundling).

In Section 4.2.2, a hierarchical self-assembly is theoretically studied. In particular, the effect that the H-bonding of **A3** benzoic acids has on the self-assembly of the star-shaped 2,4,6-tris(triazolyl)-1,3,5-triazine (**T3C$_4$**) moiety was explored. Previous experimental outcomes evidenced that **A3** acids are necessary to form stable liquid crystals, since isolated **T3C$_4$** units were not able to supramolecularly grow in ordered mesophases. A combined computational protocol, involving DFT, semiempirical and molecular mechanics simulations, predicted that the C_3-symmetric **T3C$_4$** conformation was able to accommodate three **A3** benzoic acids by H-bonding generating a host–guest 1:3 **T3C$_4$-A3** supramolecular complex, which further grows in a columnar helical stack stabilized by π–π and C−H···π interactions. MD simulations clearly highlight that H-bonded **A3** units are key (template effect) to generate compact and

highly-ordered helical arrangements rationalizing why the host–guest 1:3 **T3C$_4$-A3** supramolecular system, unlike **T3C$_4$** supramolecular aggregates, form columnar liquid crystals.

Finally, in Section 4.2.3, the self-assembly of a bissquaramide-based macrocycle and the optical properties of the resulting supramolecular aggregates were studied. Experimental data revealed the existence of two aggregates: **AggA** and **AggB**. The former, where the squaramide (SQ) units were supposed to be in a *Z*,*E* disposition, presented a blue-shifted absorption spectrum compared with that registered for the isolated macrocycle . The later aggregate (**AggB**), assumed to have all the SQ moieties in a *Z*,*Z* disposition, exhibited an unusual absorption spectrum with a splitting of the absorption band into a red-shifted and a blue-shifted band. The theoretical conformational screening initially performed for the *Z* and *E* isomers of a bissquaramide-based macrocycle **(MSq)** model allowed to select the most stable conformations leading to an efficient supramolecular growth. The selected conformer with a *Z*,*E* disposition displayed a side-to-side aggregation pattern, capable of growing in a linear or zig-zag isodesmic way. Unlike, the aggregate based on a *Z*,*Z* conformer showed a linear head-to-tail interaction pattern and grew up in a cooperative way leading to more stable aggregates. The optical properties of both aggregates were studied by using an extended Kasha's model to unravel the origin of the uncommon changes found in the experimental absorption spectra. Theoretical calculations revealed that the splitting was associated to different effects: i) an electrostatic stabilization of one of the bright excited states of the SQ units due to the permanent dipole moment of the aggregate, ii) H and J excitonic couplings that produce the blue- and red-shifted components of the absorption band, and iii) the solvatochromic shift due to the change of

the solvent composition, responsible for the apparent blue shift of one of the bands.

Charge transport (Chapter 5)

In this chapter, the hole-transport properties of a series of poly-heteroaromatic compounds, capable of self-assembling by H-bonds, were first investigated. Emphasis was put in the effect the intermolecular H-bonds and the conjugation extension of the central spacer have on the hole-transport properties. In the second part, the photoinduced electron transfer of a truxTTF•$C_{30}H_{12}$ supramolecular D−A heretodimer in solution was computationally studied highlighting the most relevant factors for the prediction of the charge-separation and charge-recombination rate constants.

Initially, the hole-transport properties of two closely related π-conjugated organic semiconductors, that consist in the fusion of a central anthracene core with two terminal indole (**ADI**) and 7-azaindole (**ADAI**) units, were investigated by using a combined multi-level computational protocol. The 7-azaindole groups enables **ADAI** to form intermolecular $H_{pyrrole}\cdots N_{pyridine}$ H-bonds that are not feasible in **ADI**. Therefore, the comparative study of **ADI** and **ADAI** allowed to get insights into the effect of intermolecular H-bonding on the hole-transport properties. As expected, the π–π interacting direction presented the largest transfer integrals for both systems. Calculations on the ideal crystal structure predicted that both molecules presented high mobilities in the three crystal planes but **ADAI** exhibited better transport properties in the π-stacking direction and a larger number of secondary charge-transfer paths with non-negligible transfer integrals owing to the intermolecular H-bonding.

Besides the role of H-bonding on the charge transport, the effect of the conjugation extension of the central spacer was also studied in a series of compounds similar to **ADAI** in which the central anthracene spacer was extended from benzene to perylene. The theoretical comparison revealed that the π–π stacked dimer was the only one presenting a significant dynamic disorder, thus giving rise to the highest hole-transport rate constants. Nevertheless, efficient secondary transport channels with significant rate constant values were identified for **ADAI**. In fact, these secondary transport pathways explain why, among the systems analyzed, **ADAI** exhibited the better transport properties with certain tolerance to structural defects.

The last part of the chapter was focused on the kinetics of the non-radiative photoinduced electron-transfer processes (charge-separation and charge-recombination) experimented by the truxTTF•$C_{30}H_{12}$ donor–acceptor supramolecular complex in solution. The study revealed a complex scenario for the decay mechanism after photoexcitation for truxTTF•$C_{30}H_{12}$ with the participation of six low-lying excited states of different nature (local and charge-transfer excitations) all close in energy. The absolute rate constants for all the conceivable CS and CR pathways were computed by using the Marcus−Levitch−Jorner rate expression, electronic structure calculations, and a multi-state diabatization method. The outcomes suggested that, for a reasonable estimate of the CS and CR rate constants, it is necessary to include: i) optimally tuned LC corrected density functionals, to predict a correct energy ordering of the low-lying excited states; ii) multi-state effects in the diabatization scheme, to account for the electronic couplings, and iii) environmental solvent effects, treated by a SS-PCM model, to provide a proper stabilization of the charge-transfer excited states and accurate external

reorganization energies. All the calculated rate constants were incorporated in a simple but insightful kinetic model that enabled estimating global CS and CR rate constants (2.0×10^{12} and 3.1×10^{9} s^{-1}, respectively) in good agreement with the experimental values (6.6×10^{11} and 1.0×10^{10} s^{-1}).

Energy transport (Chapter 6)

This chapter, framed in the context of energy transport in organic semiconductors, is divided in two sections. In the first part, a systematic comparison of different approaches (Coulombic potentials, diabatization schemes and a direct *ab initio* method) to compute the excitonic couplings between two molecules in a dimer was thoroughly performed by using several types of anthracene dimers. For the totally eclipsed anthracene dimer, all the approaches provided a similar behavior at long intermolecular distances, whereas discrepancies became important at short intermolecular distances due to short-range excitonic interactions (CT states mixing). Among the analyzed approaches, only the FPHD diabatization and the AIFD model are widely recommended since they can estimate the excitonic couplings including long-range and short-range effects. For the relevant herringbone-type dimers present in the anthracene crystal, the AIFD method provided a deep understanding of the origin of the thermal fluctuation of the excitonic couplings. The excitonic coupling fluctuations were shown to be more important for the tilted dimer than for the parallel dimer, present in the anthracene crystal, especially for the short-range FE–CT couplings.

In the second part of the chapter, the energy transport in an *N*-heterotriagulene-based supramolecular polymer was carried out from a bottom-up

computational approach combining electronic structure calculations, Holstein–Peierls model Hamiltonians and quantum dynamics techniques (ML-MCTDH). The fully-quantum exciton diffusion simulations revealed that the inclusion of the CT states significantly improves the energy transport in ordered *N*-heterotriangulene-based supramolecular polymers and determines a significant increase of the exciton diffusion length (278 *vs* 7 nm).

Capítulo 8. Resumen

8.1 Introducción

Las interacciones no covalentes se pueden definir, de forma muy genérica, como las interacciones que tienen lugar entre átomos situados a distancias mayores que las de los enlaces covalentes. Estas interacciones son de gran interés ya que son responsables de muchas de las propiedades macroscópicas de la materia, como por ejemplo el estado en el que las sustancias químicas se presentan a una determinada temperatura. Además, las interacciones no covalentes son responsables de la conformación que adoptan macromoleculas como las proteínas o el ADN, lo cual es fundamental para su actividad biológica.

Los químicos y en especial los químicos de materiales han utilizado los sistemas biológicos como fuente de inspiración para el diseño de nuevos sistemas moleculares que puedan presentar las propiedades deseadas. Para ello el uso y control de las interacciones no covalentes se ha convertido en una herramienta indispensable. De hecho, hoy en día existen distintos materiales, como por ejemplo los cristales líquidos o los semiconductores orgánicos, donde el papel de estas interacciones es indispensable ya que la organización de las moléculas en el cristal o en el dispositivo determinan la eficiencia del material y del dispositivo. Otro tipo de material que ha despertado un interés creciente en los últimos años son los polímeros supramoleculares, en los cuales el proceso de autoensamblado tiene lugar mediante interacciones no covalentes en disolución.

Esta tesis trata sobre el estudio teórico de la propiedades estructurales y electrónicas de materiales ensamblados no covalentes. En primer lugar, en el capítulo 4, se estudia la organización estructural de polímeros supramoleculares con el objetivo de entender cómo las interacciones no covalentes determinan la estabilidad y las propiedades ópticas de estos polímeros. En segundo lugar, en los capítulos 5 y 6, se estudian las propiedades de transporte de carga y energía de semiconductores orgánicos ensamblados no covalentemente, bien sean cristales moleculares, dímeros dador-aceptor o polímeros supramoleculares.

8.1.1 Polímeros supramoleculares

Los polímeros son macromoléculas de alta masa molecular constituidas por unidades repetidas de menor masa molecular llamados monómeros. En la sociedad actual disponemos de una gran variedad de polímeros que ofrecen una gran diversidad de propiedades, en los cuales los monómeros están unidos mediante enlaces covalentes. Sin embargo, el auge de la química supramolecular ha dado lugar a los polímeros supramoleculares, los cuales están constituidos de unidades moleculares (monómeros) unidas mediante interacciones no covalentes.

Los polímeros supramoleculares presentan claras diferencias respecto a los polímeros tradicionales o covalentes. Una de las más importantes es el carácter dinámico de la polimerización, permitiendo el crecimiento y destrucción del polímero mediante estímulos externos como la temperatura o la variación de la composición del disolvente. Este carácter dinámico es una consecuencia

directa del hecho de que estos polímeros se estabilizan mediante interacciones no covalentes las cuales son fácilmente reversibles.

Uno de los aspectos más importantes en el campo de los polímeros supramoleculares es el mecanismo de polimerización, es decir, cómo tiene lugar la formación del polímero partiendo de los monómeros completamente disueltos. El mecanismo más aceptado actualmente es conocido como mecanismo de nucleación-elongación, donde hay dos fases claramente diferenciadas. La etapa de nucleación consiste en la formación de un primer núcleo de agregación, que puede ser un simple dímero o un oligómero de mayor tamaño. A continuación, la elongación conlleva el crecimiento del núcleo ya formado por la adición de nuevas moléculas. Cada una de estas fases está gobernada por una constante de equilibrio, de forma que cuando son iguales para ambas fases se habla de una polimerización isodésmica, mientras que cuando el cociente entre la constante de elongación y la de nucleación es mayor que la unidad se dice que la polimerización es cooperativa.

Por último, la función de muchas biomoléculas depende de la morfología de su estructuras terciaria y cuaternaria, donde las proteínas se pliegan y ensamblan supramolecularmente, y esta morfología viene determinada por la quiralidad del sistema químico. Los sistemas biológicos son una prueba de que existe una relación entre la quiralidad puntual de la molécula y la quiralidad de la estructura final del complejo supramolecular. Un ejemplo es la quiralidad que emerge espontáneamente en los sistemas que forman ensamblados supramoleculares helicoidales. Se ha demostrado que se puede inducir una dirección preferente en la helicidad del polímero supramolecular mediante la adición de grupos quirales en los monómeros. Esto ha dado lugar en los últimos

años a los experimentos que tratan de explicar la transferencia de quiralidad de la molécula al agregado, y aquellos que estudian la amplificación de quiralidad al mezclar compuestos quirales y aquirales o con distinta quiralidad (experimentos de sargentos y soldados o de reglas de mayoría).

8.1.2 Semiconductores orgánicos

Los dispositivos electrónicos juegan un papel fundamental en el día a día de la sociedad moderna, cubriendo un amplio rango de necesidades desde la iluminación o comunicaciones hasta el mundo del entretenimiento. Entre los materiales empleados para la construcción de los dispositivos electrónicos destacan los semiconductores con los que se construyen partes fundamentales de éstos como procesadores, transistores o memorias. Tradicionalmente, los semiconductores empleados son de naturaleza inorgánica y están basados habitualmente en elemento químicos como el silicio o el germanio o sustancias como el arseniuro de galio. Sin embargo, los semiconductores inorgánicos presentan un elevado coste debido a las condiciones requeridas para su procesamiento.

En las últimas décadas ha aparecido una nueva clase de semiconductores derivados de sistemas moleculares basados en el carbono, los semiconductores orgánicos. Estos materiales poseen propiedades difíciles de obtener en los semiconductores inorgánicos, tales como la flexibilidad, que permite crear dispositivos flexibles, o su fácil procesamiento, ya que pueden depositarse desde disolución o vapor. No obstante, estos materiales orgánicos no deben tomarse como sustitutos de los semiconductores inorgánicos sino como una

alternativa que ofrece nuevas posibilidades debido a sus propiedades mecánicas.

Entre los compuestos químicos con potencial para su uso como semiconductores orgánicos destacan los compuestos π-conjugados, los cuales presentan las propiedades requeridas para dicha finalidad. Entre otras, absorción de luz visible y energía de los orbitales moleculares frontera (HOMO y LUMO) apropiada, lo cual permite la inyección o extracción de las cargas con un aporte mínimo de energía. Además, estos materiales tienen la ventaja de que se pueden obtener mediante síntesis química y un diseño racional, que permite modular las propiedades electrónicas y ópticas mediante cambios químicos.

Entre las aplicaciones de los semiconductores orgánicos destacan los dispositivos electroluminiscentes (OLEDs), transistores de efecto de campo (OFETs) o celdas fotovoltaicas (OPVs). Por ejemplo, el funcionamiento de este último dispositivo se puede entender fácilmente mediante cinco procesos:

1. La absorción de luz dando lugar a un excitón.
2. La difusión del excitón desde hasta la interfaz entre el dador y el aceptor de electrones.
3. La separación de cargas (hueco y electrón) del excitón en la interfaz entre el dador y el aceptor.
4. La migración de los huecos y electrones a través de los materiales hacia los electrodos-
5. Finalmente, la extracción de las cargas generando corriente eléctrica.

En tres de estas cinco etapas, en concreto en las etapas 2, 3 y 4 existe un proceso de transferencia de carga o transporte de energía, los cuales son puntos clave a tratar en esta tesis. Un factor determinante en los procesos de transferencia de carga o energía es la disposición relativa, es decir, la organización intermolecular de las moléculas constituyentes del material, la cual determina, junto con las propiedades electrónicas de las propias moléculas, la funcionalidad y propiedades optoelectrónicas de estos sistemas.

8.2 Objetivos

El objetivo de la presente Tesis es racionalizar, desde un punto de vista teórico, las propiedades estructurales, electrónicas, ópticas y de transporte de carga y energía de sistemas de especial relevancia en el campo de los materiales orgánicos semiconductores. El fin último de esta tesis es establecer una relación entre la estructura química y la propiedad estudiada.

Los objetivos específicos de esta Tesis se detallan a continuación:

1) Polímeros supramoleculares. Este capítulo está dividido en tres subsecciones en función de los diferentes polímeros y propiedades que se estudian.
   i. *Sistemas discóticos derivados de benceno-tricarboxamidas:* Establecer relaciones estructura-propiedad entre los cambios estructurales que se dan en derivados de benceno-1,3,5-tricarboxamida, como son el tamaño molecular y el número de centros quirales, con los parámetros termodinámicos que miden la transferencia y la amplificación de la quiralidad.

ii. *Autoensamblado del complejo supramolecular del T3C$_4$ y ácidos benzoicos:* El objetivo de esta subsección es el proporcionar información a nivel atomístico del proceso de autoensamblado y la formación de cristales líquidos para el complejo supramolecular formado por un núcleo de tris(triazolil)triazina y el ácido 3,4,5-(4-alcoxubenciloxi) benzoico.

iii. *Polimerización de un macrociclo de escuaramidas:* Estudiar la polimerización supramolecular de un macrociclo con dos unidades de escuaramidas en función de las posibles conformaciones de estas unidades, con el objetivo de comprender las alternativas de polimerización (*pathway complexity*) y las inusuales propiedades ópticas de los agregados finales.

2) Transporte de carga. Esta sección se centra en los procesos de transporte de carga en dos sistemas distintos:

i. *Semiconductores orgánicos unidos por enlace de hidrógeno:* Identificar los efectos que la capacidad de formar puentes de hidrogeno intermoleculares tienen sobre las propiedades de transporte carga en comparación con sistemas análogos sin posibilidad de formarlos.

ii. *Complejo supramolecular dador-aceptor:* Proporcional una descripción teórica de la cinética de la transferencia electrónica fotoinducida (separación y recombinación de cargas) que tiene lugar en disoluciónentre las unidades dadora y aceptora del complejo supramolecular truxTTF• $C_{30}H_{12}$.

3) Transporte de energía. Este capítulo trata sobre la descripción teórica de los procesos de transferencia de energía (excitones) en agregados

moleculares, de gran relevancia en dispositivos optoelectronicos, y persigue dos objetivos.

i. Analizar el comportamiento de las diferentes aproximaciones utilizadas para la estimación de los acoplamientos excitonicos, especialmente, cuando se tienen en cuenta los estados de transferencia de carga y los efectos de deslocalización electrónica.
ii. Identificar el mecanismo que determina un transporte de energía eficiente en polímeros supramoleculares basados en *N*-heterotriangulenos, y, en particular, el rol de los estados de transferencia de carga.

8.3 Metodología

Para llevar a cabo esta tesis, se ha empleado una amplia gama de calculos químico-cuánticos y de mecánica molecular, además de una serie de estrategias computacionales para abordar los estudios de transporte de carga y energía.

El marco general empleado para la realización de la investigación teórica expuesta en la tesis es la teoría del funcional de la densidad, más conocida por sus siglas en inglés, DFT. Las especificaciones de los cálculos teóricos de los estudios llevados a cabo están completamente detalladas en las correspondientes secciones y publicaciones de la tesis. En líneas generales, el funcional más empleado ha sido el funcional hibrido B3LYP, el cual ha demostrado proporcionar resultados satisfactorios en sistemas orgánicos. En los casos en los que es común que los funcionales híbridos fallen, como es el caso de los sistemas y procesos en los que los estados excitados de

transferencia de carga son relevantes, se ha recurrido al uso de funcionales con la corrección de largo alcance óptimamente parametrizados. Los cálculos de propiedades ópticas se han llevado a cabo con métodos basados en la expansión de la función de onda como combinación de monoexcitaciones del estado fundamental basados en la teoría *Time-Dependent* DFT (TDDFT) o en su variante *Tam-Dancoff* (TDA).

En los casos en los que el tamaño del sistema implicaba un elevado coste y por tanto impedía el uso de métodos *ab initio* o de primeros principios, se ha hecho uso de métodos semiempíricos como el PM7 y, en especial, el GFN2-xTB, el cual ha sido desarrollado en los últimos años. Cuando el tamaño de la simulación era demasiado elevado, incluso para los métodos semiempírico, se realizaron simulaciones de mecánica molecular y dinámica molecular.

Las condiciones de entorno del disolvente en los cálculos DFT se han introducido empleando un modelo de continuo. Estos modelos consisten en la simulación del disolvente como un medio dieléctrico continuo que reproduce las propiedades macroscópicas del disolvente. En ellos, la interacción soluto–disolvente se calcula a través de una perturbación que tiene en cuenta la polarización inducida por el solvente en el soluto y viceversa. En concreto, se ha empleado el modelo continuo polarizable (PCM) y, en los casos que era conveniente obtener la relajación completa del solvente en función de la densidad electrónica del estado excitado, se ha utilizado su variante *state-specific*.

Las propiedades de transporte de carga se han simulado mediante el cálculo de las constantes de velocidad de transferencia de carga, de acuerdo a las expresiones de transferencia electrónica de Marcus, o la variante semiclásica

conocida como ecuación de Marcus-Levitch-Jortner. Ambas expresiones requieren de la energía de reorganización, la cual se separa habitualmente en la componente interna, que da cuenta de los grados de libertad del sistema, y la externa, que incluye los grados de libertad del entorno. La componente interna se ha estimado mediante el cálculo de las diferencias de energía verticales y adiabáticas, mientras que la externa se ha obtenido teniendo en cuenta el efecto del solvente, en las situaciones de polarización rápida o de polarización total. El cálculo de los acoplamientos electrónicos se ha llevado a cabo mediante el uso de una aproximación basada en la proyección de los orbitales moleculares de los monómeros en el dímero (DIPRO), o mediante esquemas de diabatización basados en propiedades moleculares cuando la utilización de esquemas más simples basados en la descripción orbital era insuficiente.

En el capítulo 6, centrado en el transporte de energía, el acoplamiento excitonico se ha evaluado usando diferentes estrategias: i) cálculo de la componente Coulómbica como interacción entre las densidades de transición, ii) esquemas de diabatización basados en propiedades moleculares, e iii) cálculo de los elementos matriciales una vez se han definido las funciones de onda diabaticas *a priori*. La simulación del transporte de energía para el cálculo de coeficientes de difusión del exciton se ha realizado mediante el uso de dinámicas cuánticas, en particular del formalismo *Multi-Layer Multi-Configurational Time Dependent Hartree*, y de Hamiltonianos modelo tipo Holstein.

8.4 Polímeros supramoleculares

En este capítulo se ha investigado la relación entre la estructura supramolecular y las diferentes propiedades de interés de tres tipos de polímeros supramoleculares.

8.4.1 Transferencia y amplificación de quiralidad en derivados de tricarboxamidas.

En el primer estudio ahondamos en la relación existente entre la estructura supramolecular y las propiedades de transferencia y amplificación de quirales de polímeros supramoleculares autoensamblados de diferentes tricarboxamidas (TPBAs, OPE-TAs y BTAs). Estos compuestos forman agregados helicoidales estabilizados por apilamiento π–π e interacciones de enlaces de hidrógeno que presentan quiralidad intrínseca (quiralidad axial). Experimentos previos demostraron que la helicidad dextrógira (*M*) o levógira (*P*) de los agregados es inducida por la presencia de centros estereogénicos *R* o *S*, respectivamente, en las cadenas laterales alquílicas; es decir, se produce una transferencia de quiralidad de la molécula al polímero supramolecular. Además, los experimentos de reglas de mayoría realizados para estudiar la amplificación de la quiralidad mostraron que no había una relación clara entre el número de cadenas perfiféricas quirales y la evolución de las mismatch penalty enthapies (ΔH_{MMP}), las cuales proporcionan una estimación del coste energético que conlleva la incorporación de una molécula con grupos estereorgénicos de una determinada quiralidad en agregados de helicidad no preferida.. En particular, el valor de ΔH_{MMP} disminuye con el número de cadenas quirales en OPE-TAs, aumenta en BTAs y permanece constante en

TPBAs. Cálculos teóricos de agregados grandes reproducen la helicidad preferente de los enantiómeros *R* y *S*, y revelan que el diferente comportamiento en la transferencia de quiralidad es consecuencia de las interacciones no covalentes entre las cadenas laterales. En concreto, se encuentra una correlación entre el tamaño y la estructura del mónomero, los cuales determinan el ordenamiento supramolecular, y las capacidades de transferencia de quiralidad. Para las OPE-TAs, los valores de ΔH_{MMP} disminuyen con el número de centros quirales debido al pequeño ángulo de rotación a lo largo del eje de apilamiento (~18º) que da lugar a contactos cercanos (aprox. 3.35 Å) entre las cadenas laterales de moléculas vecinas, siendo estas interacciones más generales para las cadenas aquirales. Las TPBAs muestran un ángulo de rotación mayor de alrededor de 26º, lo que conduce a contactos H···H más largos (más de 4,25 Å) aliviando el impedimento estérico. De este modo, los valores de ΔH_{MMP} estimados para las TPBAs son menores que los de las OPE-TAs y permanecen casi constantes al aumentar el número de cadenas laterales quirales. Utilizando las BTAs como referencia, estas presentan un ligero aumento de los valores de ΔH_{MMP} a medida que se incorporan más cadenas laterales quirales. Aunque la distancia entre las cadenas laterales de las moléculas vecinas es bastante grande (> 6,0 Å), las cadenas laterales de los segundos vecinos en el apilamiento dan lugar a contactos más estrechos (~4,0 Å) debido al ángulo de rotación de 55º entre moléculas vecinas. Estos contactos pueden explicar los valores intermedios de ΔH_{MMP} obtenidos para las BTAs en comparación con las TPBAs y OPE-TAs. Finalmente, se investigó la posible interdigitación de hélices de TPBA con objeto de explicar los efectos de contaminación por dicroísmo lineal observados en los experimentos de dicroísmo circular de TPBAs. Los cálculos

teóricos revelan que la energía de interacción entre dos hélices de TPBA interdigitadas aumenta considerablemente a medida que disminuye el número de cadenas laterales que llevan un centro estereogénico, lo que conduce a una interdigitación más eficaz. Por lo tanto, los cálculos indican que es más probable que ocurra la interdigitación de hélices de TPBA a medida que se reduce el número de cadenas laterales quirales, explicando de este modo los fenómenos de dicroísmo lineal que se observen para TPBAs con ninguna y una cadena quiral lateral debido a la formación de fibras por agrupación de varias hélices.

8.4.2 Cristales líquidos basados en complejos supramoleculares derivados del T3C$_4$

En esta sección se investiga el efecto que tiene la unión mediante enlaces de hidrógeno de unidades de ácido benzoico (A3) en el autoensamblaje del compuesto π-conjugado de 2,4,6-tris(triazolil)-1,3,5-triazina (T3C$_4$). Los resultados experimentales anteriores mostraron que los ácidos A3 son necesarios para formar cristales líquidos estables, ya que las unidades T3C$_4$ no son capaces, por sí mismas, de formar mesofases ordenadas. Los cálculos teóricos muestran que la conformación simétrica C_3 de la unidad T3C$_4$ es la más estable y es capaz de incorporar tres unidades del ácido benzoico A3 a través de enlaces de hidrógeno, dando lugar a un complejo supramolecular 1:3 (T3C$_4$-A3). Este complejo puede ensamblarse en forma de columna formando pilas helicoidales estabilizadas por interacciones π–π y C−H ···π entre los núcleos T3C4 y los ácidos A3. Las unidades de A3 ejercen, de hecho, un efecto de plantilla en el autoensamblaje, el cual favorece el empaquetamiento

helicoidal compacto y altamente ordenado de los complejos supramoleculares de T3C_4-A3 y la formación de cristales líquidos columnares. Por el contrario, las simulaciones MM/MD demostraron que los agregados a que dan lugar las unidades de T3C_4 sin unidades de A3 presentan una estructura altamente desordenada que dificulta la formación de mesofases de cristal líquido.

8.4.3 Agregación (pathway complexity) de macrociclos basados en esquaramidas.

Por último, se estudió el autoensamblaje de un macrociclo que contiene dos unidades de escuaramida (MSq) y las propiedades ópticas de los agregados supramoleculares resultantes. Los datos experimentales revelaron la existencia de dos agregados: AggA y AggB. El agregado AggA da lugar a estructuras cíclicas, su espectro de absorción está desplazado hacia el azul con respecto al monómero aislado y las unidades de escuaramida (SQ) presentan una conformación *Z,E*. Por el contrario, el agregado AggB forma fibras, su banda de absorción se divide en dos bandas, desplazadas respectivamente al rojo y al azul respecto al monómero, y las unidades SQ tienen una disposición *Z,Z*. Inicialmente se realizó un cribado conformacional de los isómeros del sistema MSq en función de la disposición *Z*/*E* de las SQs con objeto de seleccionar las conformaciones más estables que permitieran un crecimiento supramolecular eficiente. El confórmero seleccionado con una disposición *Z,E* muestra un patrón de agregación de tipo "*side-to-side*", el cual crece de forma lineal o en zig-zag por un mecanismo isodésmico. Por el contrario, el agregado basado en el confórmero *Z,Z* más estable presenta un patrón de interacción lineal "*head-to-tail*" y crece de manera cooperativa, lo que conduce a agregados más

estables a medida que aumenta la longitud del oligómero. Las propiedades ópticas de ambos agregados se estudiaron utilizando un modelo de Kasha extendido para desentrañar el origen de los cambios poco comunes encontrados en los espectros de absorción experimental. El desplazamiento hacia el azul predicho para el agregado *Z,E* "*side-to-side*" se correlaciona muy bien con el desplazamiento hacia el azul observado experimentalmente para el agregado AggA y se atribuye principalmente a un desplazamiento solvatocrómico. El espectro de absorción simulado del agregado *Z,Z* "*head-to-tail*" reproduce el desdoblamiento de la banda de absorción encontrada para el agregado AggB. La división en dos bandas desplazadas hacia el rojo y el azul con respecto al monómero es un fenómeno bastante exótico en los ensamblajes supramoleculares. Los cálculos teóricos muestran que el desdoblamiento está asociado a una suma de efectos: i) la estabilización electrostática de uno de los estados excitados brillantes de las unidades SQ, la cual es debida a la presencia del momento dipolar permanente del agregado, ii) los acoplamientos excitónicos H y J que producen un desplazamiento hacia el azul de una banda de absorción y un desplazamiento hacia el rojo de la otra banda, e iii) el desplazamiento solvatocrómico debido al cambio en la composición del solvente, el cual provoca el aparente desplazamiento hacia el azul de una de las bandas.

8.5 Transporte de Carga

En este capítulo se ha llevado a cabo la caracterización teórica de las propiedades de transporte de carga entre unidades unidas por interacciones no

covalentes. En particular, se han estudiado las propiedades como transportadores de huecos de sistemas aromáticos auto-ensamblados por puentes de hidrogeno. Por otro lado, se ha estudiado la separación y recombinación de cargas asociadas a la transferencia de carga fotoinducida que tiene lugar en disolución par el complejo supramolecular compuesto por el truxTTF como dador y el hemifullereno ($C_{30}H_{12}$) como aceptor. A continuación, se detallan los aspectos más relevantes de los estudios llevados a cabo en este capítulo.

8.5.1 Materiales transportadores de huecos auto-ensamblados mediante enlaces de hidrógeno

Se ha evaluado el efecto del autoensamblaje mediante enlaces de hidrógeno en las propiedades de transporte de huecos de semiconductores orgánicos. En concreto, se han estudiado dos sistemas π-conjugados estrechamente relacionados, denominados ADI y ADAI, los cuales mantienen la misma estructura policíclica y tamaño, pero difieren en las unidades terminales de indol (ADI) o 7-azaindol (ADAI) fusionadas con el esqueleto central de antraceno. Los grupos 7-azaindol permiten que ADAI forme enlaces de hidrógeno $H_{pirrol}\cdots N_{piridina}$ intermoleculares, los cuales no son posibles en ADI. Las estructuras de difracción de rayos X mostraron que la incorporación de la unidad de 7-azaindol es una estrategia exitosa para controlar la organización supramolecular a través de enlaces de hidrógeno. Las propiedades de transporte de carga de ADI y ADAI se estimaron utilizando un protocolo teórico que combina cálculos DFT para calcular los acoplamientos electrónicos para todos los dímeros de cristal y simulaciones de dinámica molecular (MD)

para tener en cuenta las fluctuaciones en los acoplamientos electrónicos debido a movimientos térmicos, junto con el modelo MLJ para estimar las constantes de velocidad de transferencia de huecos y una ecuación maestra para finalmente predecir las movilidades de los huecos. Como era de esperar, la dirección de interacción π–π presenta el acoplamiento más grande tanto para ADI como para ADAI. Los cálculos sobre la estructura cristalina ideal predicen que ambas moléculas presentan altas movilidades en los tres planos cristalinos, pero ADAI muestra mejores propiedades de transporte en la dirección de apilamiento π y una mayor cantidad de canales secundarios de transferencia de carga con acoplamientos significativos que pueden ayudar en el transporte de carga. Estas propiedades, junto con la mayor cristalinidad y robustez térmica determinadas experimentalmente para las películas ADAI, explican las mayores movilidades encontradas para ADAI.

Una vez comprobado que el autoensamblaje mediante enlaces de hidrógeno funciona como una estrategia adecuada para diseñar semiconductores orgánicos con un ordenamiento supramolecular superior y mejores propiedades de transporte, se estudió el efecto de la extensión de la conjugación π del espaciador central sobre dichas propiedades en una serie de compuestos similares a ADAI, en los que el espaciador central de antraceno se cambió por benceno (BDAI), naftaleno (NDAI) y perileno (PDAI). Las propiedades de transporte se calcularon siguiendo un protocolo similar al utilizado anteriormente. El dímero apilado π–π es el único que presenta un desorden dinámico significativo, dando lugar a las constantes de velocidad de transporte de huecos más altas. Desafortunadamente, no fue posible establecer una correlación directa entre las movilidades experimentales y las movilidades y constantes de velocidad de transporte de huecos estimadas teóricamente,

debido a la alta dependencia de los valores experimentales con el grado de cristalinidad de la película orgánica sobre el que se realizan las medidas. Sin embargo, los resultados teóricos indican claramente que ADAI debe exhibir mejores propiedades de transporte porque presenta un mayor número de contactos intermoleculares con valores significativos de constante de velocidad. La existencia de estas rutas de transporte secundarias eficientes predichas teóricamente junto con el alto grado de cristalinidad determinado experimentalmente para las películas delgadas de ADAI hacen de ADAI el mejor material semiconductor transportador de huecos de la serie y más tolerante a los defectos estructurales.

8.5.2 Transferencia de carga fotoinducida en el complejo supramolecular truxTTF•$C_{30}H_{12}$

La segunda parte del capítulo se centró en el estudio de la cinética de los procesos no radiativos de separación de carga (CS) y recombinación de carga (CR) asociados a la transferencia de electrones fotoinducida () experimentada por el complejo supramolecular dador-aceptor (truxTTF•$C_{30}H_{12}$) en disolución. El estudio revela que el sistema truxTTF•$C_{30}H_{12}$ experimenta un complejo mecanismo de decaimiento después de la fotoexcitación, en el que intervienen varios estados excitados de diferente naturaleza (excitaciones locales y de transferencia de carga) muy cercanos en energía. En este escenario, las constantes de velocidad para todas las rutas CS y CR concebibles se calcularon utilizando la expresión de velocidad de Marcus-Levitch-Jorner, cálculos de estructura electrónica y un método de diabatización incluyendo “efectos multiestado”. Los resultados obtenidos sugieren que, para una

estimación razonable de las constantes de velocidad de CS y CR, es necesario incluir: i) funcionales con corrección de largo alcance optimizados, para predecir el orden de energía correcto de los estados excitados bajos, ii) efectos multiestado en el esquema de diabatización, para dar cuenta de los acoplamientos electrónicos, e iii) efectos del solvente estimados con la aproximación SS-PCM, para describir adecuadamente la estabilización de los estados excitados de transferencia de carga y la estimación precisa de la energía de reorganización externa. Todas las constantes de velocidad calculadas se introdujeron en un modelo cinético que permitió estimar las constantes de velocidad globales de CS y CR, de forma conceptualmente comparable al modelo de tres estados más generalizado utilizado para describir los procesos de CS y CR. Se encontró que las constantes globales de CS y RC ($2{,}0 \times 10^{12}$ y $3{,}1 \times 10^{9}$ s^{-1}, respectivamente) calculadas para el complejo supramolecular dador-aceptor truxTTF•$C_{30}H_{12}$ estaban en buen acuerdo con las estimaciones experimentales ($6{,}6 \times 10^{11}$ y $1{,}0 \times 10^{10}$ s^{-1}).

8.6 Transporte de energía

Este capítulo se enmarca en el contexto del transporte de energía, también denominado transporte excitónico, en semiconductores orgánicos. En la primera parte, se ha realizado una comparación exhaustiva de diferentes metodologías disponibles en la bibliografía para estimar acoplamientos excitónicos en dímeros moleculares. Para realizar el análisis, se ha empleado como sistema modelo un dímero de antraceno totalmente eclipsado a distancias variables y los dímeros que se encuentran en el cristal. La segunda parte del

capítulo aborda el transporte de energía en un polímero supramolecular modelo basado en el *N*-heterotriaguleno.

8.6.1 Comparación de los diferentes métodos para el cálculo de acoplamientos excitónicos.

Se ha realizado un estudio comparativo de la evolución de los acoplamientos excitónicos en función de la distancia intermolecular en un dímero de antraceno totalmente eclipsado utilizando diferentes aproximaciones (potencial Coulómbico, esquemas de diabatización e integrales directas *ab initio*). El estudio muestra que, como era de esperar, todas las aproximaciones proporcionan una imagen idéntica para distancias intermoleculares largas, ya que a estas distancias sólo persisten las interacciones excitónicas de tipo Coulómbico. En cambio, los efectos de corto alcance (mezcla de estados de transferencia de carga o CT) cobran relevancia a distancias intermoleculares cortas y evidencian diferencias entre las distintas metodologías. Entre los enfoques seleccionados, es necesario destacar el esquema de diabatización FPHD y el modelo AIFD. Ambas aproximaciones permiten estimar los acoplamientos excitónicos entre estados excitados de diferente naturaleza (por ejemplo, los acoplamientos FE-CT), incluyendo por tanto los efectos de largo y corto alcance. La segunda parte del estudio proporciona una comprensión en profundidad, utilizando el método AIFD, del origen de la fluctuación térmica de los acoplamientos excitónicos para los dímeros de cristal de antraceno. Los resultados sugieren que las fluctuaciones del acoplamiento excitónico son más importantes para los dímeros “inclinados” que para los dímeros con una disposición paralela-desplazada de los antracenos, debido a la mayor

fluctuación los acoplamientos FE-CT y a la mezcla de estados FE y estados CT en los primeros.

8.6.2 Transporte de energía en polimeros supramoleculares basados en N-heterotriangulenos

El estudio de la capacidad de transporte de energía de un polímero supramolecular modelo basado en una estructura polcíclica π-conjugada de *N*-heterotriaguleno se llevó a cabo en diferentes pasos. Inicialmente, se obtuvo la estructura de un pentámero supramolecular bien ordenado del derivado de *N*-heterotriaguleno, gobernado por interacciones π–π y enlaces de hidrógeno, a nivel DFT. A partir de este oligómero supramolecular, se construyó un dímero de *N*-heterotriaguleno ideal, mediante el uso de la molécula central y la información estructural del pentámero optimizado, con el objetivo de calcular los estados excitados adiabáticos más bajos en energía a nivel TDA-DFT. Estos cálculos mostraron la importancia de los estados excitados CT, los cuales se mezclan significativamente con los estados excitados locales de tipo FE. A partir de estos estados adiabáticos, se calcularon las energías de los estados excitados diabáticos y los acoplamientos excitónicos entre todos los estados relevantes (tipo FE y CT) usando el esquema FPHD. La información obtenida se utilizó para parametrizar un Hamiltoniano modelo del tipo Holstein y estudiar la dinámica excitónica del polímero supramolecular con el formalismo ML-MCTDH. Las simulaciones cuánticas ML-MCTDH revelan que la inclusión de los estados CT mejora significativamente el transporte de excitones del polímero supramolecular dando lugar a un aumento muy

importante de la longitud de difusión del excitón (278 nm) cuando se compara con la simulación que no incluye estados CT (7 nm).

Bibliography

(1) Hatada, K.; Fox, R. B.; Kahovec, J.; Maréchal, E.; Mita, I.; Shibaev, V. P. Definitions of Terms Relating to Degradation, Aging, and Related Chemical Transformations of Polymers (IUPAC Recommendations 1996). *Pure Appl. Chem.* **1996**, *68*, 2313–2323.

(2) Ciferri, A. *Supramolecular Polymers*; CRC Press, 2005.

(3) Sangeetha, N. M.; Maitra, U. Supramolecular Gels: Functions and Uses. *Chem. Soc. Rev.* **2005**, *34*, 821–836.

(4) Ajayaghosh, A.; Praveen, V. K.; Vijayakumar, C. Organogels as Scaffolds for Excitation Energy Transfer and Light Harvesting. *Chem. Soc. Rev.* **2007**, *37*, 109–122.

(5) Watson, J. D.; Crick, F. H. C. Molecular Structure of Nucleic Acids: A Structure for Deoxyribose Nucleic Acid. *Nature* **1953**, *171*, 737–738.

(6) Savyasachi, A. J.; Kotova, O.; Shanmugaraju, S.; Bradberry, S. J.; Ó'Máille, G. M.; Gunnlaugsson, T. Supramolecular Chemistry: A Toolkit for Soft Functional Materials and Organic Particles. *Chem* **2017**, *3*, 764–811.

(7) Menger, F. M. Supramolecular Chemistry and Self-Assembly. *Proc. Natl. Acad. Sci.* **2002**, *99*, 4818–4822.

(8) Huang, F.; Anslyn, E. V. Introduction: Supramolecular Chemistry. *Chem. Rev.* **2015**, *115*, 6999.

(9) Cordier, P.; Tournilhac, F.; Soulié-Ziakovic, C.; Leibler, L. Self-Healing and Thermoreversible Rubber from Supramolecular Assembly. *Nat. 2008 4517181* **2008**, *451*, 977–980.

(10) Mukhopadhyay, P.; Fujita, N.; Takada, A.; Kishida, T.; Shirakawa, M.; Shinkai, S. Regulation of a Real-Time Self-Healing Process in Organogel Tissues by Molecular Adhesives. *Angew. Chem. Int. Ed.* **2010**, *49*, 6338–6342.

(11) Soberats, B.; Uchida, E.; Yoshio, M.; Kagimoto, J.; Ohno, H.; Kato, T. Macroscopic Photocontrol of Ion-Transporting Pathways of a Nanostructured Imidazolium-Based Photoresponsive Liquid Crystal. *J. Am. Chem. Soc.* **2014**, *136*, 9552–9555.

(12) Feringán, B.; Romero, P.; Serrano, J. L.; Folcia, C. L.; Etxebarria, J.; Ortega, J.; Termine, R.; Golemme, A.; Giménez, R.; Sierra, T. H-Bonded Donor–Acceptor Units Segregated in Coaxial Columnar Assemblies: Toward High Mobility Ambipolar Organic Semiconductors. *J. Am. Chem. Soc.* **2016**, *138*, 12511–12518.

(13) Lugger, J.; Mulder, D. J.; Sijbesma, R.; Schenning, A. Nanoporous Polymers Based on Liquid Crystals. *Materials (Basel).* **2018**, *11*, 104.

(14) Lugger, J. A. M.; Mulder, D. J.; Bhattacharjee, S.; Sijbesma, R. P. Homeotropic Self-Alignment of Discotic Liquid Crystals for Nanoporous Polymer Films. *ACS Nano*

2018, *12*, 6714–6724.

(15) Yan, X.; Wang, F.; Zheng, B.; Huang, F. Stimuli-Responsive Supramolecular Polymeric Materials. *Chem. Soc. Rev.* **2012**, *41*, 6042–6065.

(16) Appel, E. A.; Barrio, J. del; Loh, X. J.; Scherman, O. A. Supramolecular Polymeric Hydrogels. *Chem. Soc. Rev.* **2012**, *41*, 6195–6214.

(17) Whitesides, G. M.; Boncheva, M. Beyond Molecules: Self-Assembly of Mesoscopic and Macroscopic Components. *Proc. Natl. Acad. Sci.* **2002**, *99*, 4769–4774.

(18) Matern, J.; Dorca, Y.; Sánchez, L.; Fernández, G. Revising Complex Supramolecular Polymerization under Kinetic and Thermodynamic Control. *Angew. Chem. Int. Ed.* **2019**, *58*, 16730–16740.

(19) L. Brunsveld; B. J. B. Folmer; Meijer, E. W.; Sijbesma, R. P. Supramolecular Polymers. *Chem. Rev.* **2001**, *101*, 4071–4097.

(20) De Greef, T. F. A.; Smulders, M. M. J.; Wolffs, M.; Schenning, A. P. H. J.; Sijbesma, R. P.; Meijer, E. W.; Greef, T. F. A. De; Smulders, M. M. J.; Wolffs, M.; Schenning, A. P. H. J.; Sijbesma, R. P.; Meijer, E. W. Supramolecular Polymerization. *Chem. Rev* **2009**, *109*, 5687–5754.

(21) Chen, Z.; Lohr, A.; Saha-Möller, C. R.; Würthner, F. Self-Assembled π-Stacks of Functional Dyes in Solution: Structural and Thermodynamic Features. *Chem. Soc. Rev.* **2009**, *38*, 564–584.

(22) Zhao, D.; Moore, J. S. Nucleation-Elongation: A Mechanism for Cooperative Supramolecular Polymerization. *Org. Biomol. Chem.* **2003**, *1*, 3471–3491.

(23) Herkert, L.; Droste, J.; Kartha, K. K.; Korevaar, P. A.; de Greef, T. F. A.; Hansen, M. R.; Fernández, G. Pathway Control in Cooperative vs. Anti-Cooperative Supramolecular Polymers. *Angew. Chem. Int. Ed.* **2019**, *58*, 11344–11349.

(24) Gershberg, J.; Fennel, F.; Rehm, T. H.; Lochbrunner, S.; Würthner, F. Anti-Cooperative Supramolecular Polymerization: A New K2–K Model Applied to the Self-Assembly of Perylene Bisimide Dye Proceeding via Well-Defined Hydrogen-Bonded Dimers. *Chem. Sci.* **2016**, *7*, 1729–1737.

(25) Palmans, A. R. A.; Meijer, E. W. Amplification of Chirality in Dynamic Supramolecular Aggregates. *Angew. Chem. Int. Ed.* **2007**, *46*, 8948–8968.

(26) Dimitrakopoulos, C. D.; Malenfant, P. R. L. Organic Thin Film Transistors for Large Area Electronics. *Adv. Mater.* **2002**, *14*, 99–117.

(27) Forrest, S. R. The Path to Ubiquitous and Low-Cost Organic Electronic Appliances on Plastic. *Nat. 2004 4286986* **2004**, *428*, 911–918.

(28) Muccini, M. A Bright Future for Organic Field-Effect Transistors. *Nat. Mater. 2006 58* **2006**, *5*, 605–613.

(29) Usta, H.; Facchetti, A.; Marks, T. J. N-Channel Semiconductor Materials Design for Organic Complementary Circuits. *Acc. Chem. Res.* **2011**, *44*, 501–510.

(30) Wang, C.; Dong, H.; Hu, W.; Liu, Y.; Zhu, D. Semiconducting π-Conjugated Systems in Field-Effect Transistors: A Material Odyssey of Organic Electronics. *Chem. Rev.* **2011**, *112*, 2208–2267.

(31) Gelinck, G. H.; Huitema, H. E. A.; van Veenendaal, E.; Cantatore, E.; Schrijnemakers, L.; van der Putten, J. B. P. H.; Geuns, T. C. T.; Beenhakkers, M.; Giesbers, J. B.; Huisman, B.-H.; Meijer, E. J.; Benito, E. M.; Touwslager, F. J.; Marsman, A. W.; van Rens, B. J. E.; de Leeuw, D. M. Flexible Active-Matrix Displays and Shift Registers Based on Solution-Processed Organic Transistors. *Nat. Mater. 2004 32* **2004**, *3*, 106–110.

(32) Gundlach, D. J.; Royer, J. E.; Park, S. K.; Subramanian, S.; Jurchescu, O. D.; Hamadani, B. H.; Moad, A. J.; Kline, R. J.; Teague, L. C.; Kirillov, O.; Richter, C. A.; Kushmerick, J. G.; Richter, L. J.; Parkin, S. R.; Jackson, T. N.; Anthony, J. E. Contact-Induced Crystallinity for High-Performance Soluble Acene-Based Transistors and Circuits. *Nat. Mater. 2008 73* **2008**, *7*, 216–221.

(33) Sirringhaus, H. Device Physics of Solution-Processed Organic Field-Effect Transistors. *Adv. Mater.* **2005**, *17*, 2411–2425.

(34) Na, S.-I.; Kim, S.-S.; Jo, J.; Kim, D.-Y. Efficient and Flexible ITO-Free Organic Solar Cells Using Highly Conductive Polymer Anodes. *Adv. Mater.* **2008**, *20*, 4061–4067.

(35) Sekitani, T.; Zschieschang, U.; Klauk, H.; Someya, T. Flexible Organic Transistors and Circuits with Extreme Bending Stability. *Nat. Mater. 2010 912* **2010**, *9*, 1015–1022.

(36) Rogers, J. A.; Someya, T.; Huang, Y. Materials and Mechanics for Stretchable Electronics. *Science* **2010**, *327*, 1603–1607.

(37) White, M. S.; Kaltenbrunner, M.; Głowacki, E. D.; Gutnichenko, K.; Kettlgruber, G.; Graz, I.; Aazou, S.; Ulbricht, C.; Egbe, D. A. M.; Miron, M. C.; Major, Z.; Scharber, M. C.; Sekitani, T.; Someya, T.; Bauer, S.; Sariciftci, N. S. Ultrathin, Highly Flexible and Stretchable PLEDs. *Nat. Photonics 2013 710* **2013**, *7*, 811–816.

(38) Kaltenbrunner, M.; White, M. S.; Głowacki, E. D.; Sekitani, T.; Someya, T.; Sariciftci, N. S.; Bauer, S. Ultrathin and Lightweight Organic Solar Cells with High Flexibility. *Nat. Commun. 2012 31* **2012**, *3*, 1–7.

(39) Kippelen, B.; Brédas, J.-L. Organic Photovoltaics. *Energy Environ. Sci.* **2009**, *2*, 251–261.

(40) Meerheim, R.; Lüssem, B.; Leo, K. Efficiency and Stability of P-i-n Type Organic Light Emitting Diodes for Display and Lighting Applications. *Proc. IEEE* **2009**, *97*, 1606–1626.

(41) Kulkarni, A. P.; Tonzola, C. J.; Babel, A.; Jenekhe, S. A. Electron Transport Materials

for Organic Light-Emitting Diodes. *Chem. Mater.* **2004**, *16*, 4556–4573.

(42) Yang, X.; Zhou, G.; Wong, W.-Y. Recent Design Tactics for High Performance White Polymer Light-Emitting Diodes. *J. Mater. Chem. C* **2014**, *2*, 1760–1778.

(43) R. Newman, C.; Frisbie, C. D.; da Silva Filho, D. A.; Bredas, J.-L.; Ewbank, P. C.; Mann, K. R. Introduction to Organic Thin Film Transistors and Design of N-Channel Organic Semiconductors. *Chem. Mater.* **2004**, *16*, 4436–4451.

(44) Facchetti, A. Semiconductors for Organic Transistors. *Mater. Today* **2007**, *10*, 28–37.

(45) Xu, Y.; Liu, C.; Khim, D.; Noh, Y.-Y. Development of High-Performance Printed Organic Field-Effect Transistors and Integrated Circuits. *Phys. Chem. Chem. Phys.* **2015**, *17*, 26553–26574.

(46) Sirringhaus, H. Organic Field-Effect Transistors: The Path Beyond Amorphous Silicon. *Adv. Mater.* **2014**, *26*, 1319–1335.

(47) Kearns, D.; Calvin, M. Photovoltaic Effect and Photoconductivity in Laminated Organic Systems. *J. Chem. Phys.* **2004**, *29*, 950–951.

(48) Tang, C. W. Two-layer Organic Photovoltaic Cell. *Appl. Phys. Lett.* **1998**, *48*, 183–185.

(49) Riede, M.; Mueller, T.; Tress, W.; Schueppel, R.; Leo, K. Small-Molecule Solar Cells—Status and Perspectives. *Nanotechnology* **2008**, *19*, 424001.

(50) Dennler, G.; Scharber, M. C.; Brabec, C. J. Polymer-Fullerene Bulk-Heterojunction Solar Cells. *Adv. Mater.* **2009**, *21*, 1323–1338.

(51) Chidichimo, G.; Filippelli, L. Organic Solar Cells: Problems and Perspectives. *Int. J. Photoenergy* **2010**, *2010*, 123534.

(52) Deibel, C.; Dyakonov, V. Polymer–Fullerene Bulk Heterojunction Solar Cells. *Reports Prog. Phys.* **2010**, *73*, 096401.

(53) Service, R. F. Outlook Brightens for Plastic Solar Cells. *Science* **2011**, *332*, 293–293.

(54) Cao, W.; Xue, J. Recent Progress in Organic Photovoltaics: Device Architecture and Optical Design. *Energy Environ. Sci.* **2014**, *7*, 2123–2144.

(55) Ismail, Y. A. M.; Soga, T.; Jimbo, T. Improvement in Light Harvesting and Performance of P3HT:PCBM Solar Cell by Using 9,10-Diphenylanthracene. *Sol. Energy Mater. Sol. Cells* **2009**, *93*, 1582–1586.

(56) Wang, Y.; Zheng, B.; Tamai, Y.; Ohkita, H.; Benten, H.; Ito, S. Dye Sensitization in the Visible Region for Low-Bandgap Polymer Solar Cells. *J. Electrochem. Soc.* **2014**, *161*, D3093.

(57) Rand, B. P.; Peumans, P.; Forrest, S. R. Long-Range Absorption Enhancement in Organic Tandem Thin-Film Solar Cells Containing Silver Nanoclusters. *J. Appl. Phys.* **2004**, *96*, 7519–7526.

(58) Xue, J.; Uchida, S.; Rand, B. P.; Forrest, S. R. Asymmetric Tandem Organic Photovoltaic Cells with Hybrid Planar-Mixed Molecular Heterojunctions. *Appl. Phys. Lett.* **2004**, *85*, 5757–5759.

(59) Gilot, J.; Wienk, M. M.; Janssen, R. A. J. Double and Triple Junction Polymer Solar Cells Processed from Solution. *Appl. Phys. Lett.* **2007**, *90*, 143512.

(60) Kim, J. Y.; Lee, K.; Coates, N. E.; Moses, D.; Nguyen, T.-Q.; Dante, M.; Heeger, A. J. Efficient Tandem Polymer Solar Cells Fabricated by All-Solution Processing. *Science* **2007**, *317*, 222–225.

(61) Tvingstedt, K.; Andersson, V.; Zhang, F.; Inganäs, O. Folded Reflective Tandem Polymer Solar Cell Doubles Efficiency. *Appl. Phys. Lett.* **2007**, *91*, 123514.

(62) Bi, P.; Hao, X. Versatile Ternary Approach for Novel Organic Solar Cells: A Review. *Sol. RRL* **2019**, *3*, 1800263.

(63) Ameri, T.; Khoram, P.; Min, J.; Brabec, C. J. Organic Ternary Solar Cells: A Review. *Adv. Mater.* **2013**, *25*, 4245–4266.

(64) Liu, T.; Luo, Z.; Fan, Q.; Zhang, G.; Zhang, L.; Gao, W.; Guo, X.; Ma, W.; Zhang, M.; Yang, C.; Li, Y.; Yan, H. Use of Two Structurally Similar Small Molecular Acceptors Enabling Ternary Organic Solar Cells with High Efficiencies and Fill Factors. *Energy Environ. Sci.* **2018**, *11*, 3275–3282.

(65) Fu, H.; Wang, Z.; Sun, Y. Advances in Non-Fullerene Acceptor Based Ternary Organic Solar Cells. *Sol. RRL* **2018**, *2*, 1700158.

(66) Yin, P.; Zheng, T.; Wu, Y.; Liu, G.; Zhang, Z.-G.; Cui, C.; Li, Y.; Shen, P. Achieving Efficient Thick Active Layer and Large Area Ternary Polymer Solar Cells by Incorporating a New Fused Heptacyclic Non-Fullerene Acceptor. *J. Mater. Chem. A* **2018**, *6*, 20313–20326.

(67) Tang, Y.; Sun, H.; Wu, Z.; Zhang, Y.; Zhang, G.; Su, M.; Zhou, X.; Wu, X.; Sun, W.; Zhang, X.; Liu, B.; Chen, W.; Liao, Q.; Woo, H. Y.; Guo, X. A New Wide Bandgap Donor Polymer for Efficient Nonfullerene Organic Solar Cells with a Large Open-Circuit Voltage. *Adv. Sci.* **2019**, *6*, 1901773.

(68) Privado, M.; Malhotra, P.; Cruz, P. de la; Singhal, R.; Cerdá, J.; Aragó, J.; Ortí, E.; Sharma, G. D.; Langa, F. Ternary Organic Solar Cell with a Near-Infrared Absorbing Selenophene–Diketopyrrolopyrrole-Based Nonfullerene Acceptor and an Efficiency above 10%. *Sol. RRL* **2020**, *4*, 1900471.

(69) Akselrod, G. M.; Deotare, P. B.; Thompson, N. J.; Lee, J.; Tisdale, W. A.; Baldo, M. A.; Menon, V. M.; Bulović, V. Visualization of Exciton Transport in Ordered and Disordered Molecular Solids. *Nat. Commun. 2014 51* **2014**, *5*, 1–8.

(70) Kietzke, T. Recent Advances in Organic Solar Cells. *Adv. Optoelectron.* **2007**, *2007*, 040285.

(71) Peumans, P.; Uchida, S.; Forrest, S. R. Efficient Bulk Heterojunction Photovoltaic

Cells Using Small-Molecular-Weight Organic Thin Films. *Nat. 2003 4256954* **2003**, *425*, 158–162.

(72) Yu, G.; Gao, J.; Hummelen, J. C.; Wudl, F.; Heeger, A. J. Polymer Photovoltaic Cells: Enhanced Efficiencies via a Network of Internal Donor-Acceptor Heterojunctions. *Science* **1995**, *270*, 1789–1791.

(73) Shaheen, S. E.; Brabec, C. J.; Sariciftci, N. S.; Padinger, F.; Fromherz, T.; Hummelen, J. C. 2.5% Efficient Organic Plastic Solar Cells. *Appl. Phys. Lett.* **2001**, *78*, 841–843.

(74) Padinger, F.; Rittberger, R. S.; Sariciftci, N. S. Effects of Postproduction Treatment on Plastic Solar Cells. *Adv. Funct. Mater.* **2003**, *13*, 85–88.

(75) Ma, W.; Yang, C.; Gong, X.; Lee, K.; Heeger, A. J. Thermally Stable, Efficient Polymer Solar Cells with Nanoscale Control of the Interpenetrating Network Morphology. *Adv. Funct. Mater.* **2005**, *15*, 1617–1622.

(76) Peet, J.; Kim, J. Y.; Coates, N. E.; Ma, W. L.; Moses, D.; Heeger, A. J.; Bazan, G. C. Efficiency Enhancement in Low-Bandgap Polymer Solar Cells by Processing with Alkane Dithiols. *Nat. Mater. 2007 67* **2007**, *6*, 497–500.

(77) Park, S. H.; Roy, A.; Beaupré, S.; Cho, S.; Coates, N.; Moon, J. S.; Moses, D.; Leclerc, M.; Lee, K.; Heeger, A. J. Bulk Heterojunction Solar Cells with Internal Quantum Efficiency Approaching 100%. *Nat. Photonics 2009 35* **2009**, *3*, 297–302.

(78) Coropceanu, V.; Cornil, J.; da Silva Filho, D. A.; Olivier, Y.; Silbey, R.; Brédas, J. L. Charge Transport in Organic Semiconductors. *Chem. Rev.* **2007**, *107*, 926–952.

(79) Brédas, J.-L.; Norton, J. E.; Cornil, J.; Coropceanu, V. Molecular Understanding of Organic Solar Cells: The Challenges. *Acc. Chem. Res.* **2009**, *42*, 1691–1699.

(80) Fratini, S.; Ciuchi, S.; Mayou, D.; de Laissardière, G. T.; Troisi, A. A Map of High-Mobility Molecular Semiconductors. *Nat. Mater. 2017 1610* **2017**, *16*, 998–1002.

(81) Troisi, A.; Orlandi, G. Charge-Transport Regime of Crystalline Organic Semiconductors: Diffusion Limited by Thermal Off-Diagonal Electronic Disorder. **2006**.

(82) Troisi, A. Prediction of the Absolute Charge Mobility of Molecular Semiconductors: The Case of Rubrene. *Adv. Mater.* **2007**, *19*, 2000–2004.

(83) Stafström, S. Electron Localization and the Transition from Adiabatic to Nonadiabatic Charge Transport in Organic Conductors. *Chem. Soc. Rev.* **2010**, *39*, 2484–2499.

(84) Ciuchi, S.; Fratini, S. Electronic Transport and Quantum Localization Effects in Organic Semiconductors. *Phys. Rev. B* **2012**, *86*, 245201.

(85) Ciuchi, S.; Fratini, S.; Mayou, D. Transient Localization in Crystalline Organic Semiconductors. *Phys. Rev. B* **2011**, *83*, 081202.

(86) Butler, K. T.; Frost, J. M.; Skelton, J. M.; Svane, K. L.; Walsh, A. Computational

Materials Design of Crystalline Solids. *Chem. Soc. Rev.* **2016**, *45*, 6138–6146.

(87) Frisch, M. J.; Trucks, G. W.; Schlegel, H. B.; Scuseria, G. E.; Robb, M. A.; Cheeseman, J. R.; Scalmani, G.; Barone, V.; Petersson, G. A.; Nakatsuji, H.; Li, X.; Caricato, M.; Marenich, A. V.; Bloino, J.; Janesko, B. G.; Gomperts, R.; Mennucci, B.; Hratchian, H. P.; Ortiz, J. V.; Izmalov, A. F.; Sonnenberg, J. L.; Williams-Young, D.; Ding, F.; Lipparini, F.; Egidi, F.; Goings, J.; Peng, B.; Petrone, A.; Henderson, T.; Ranasinghe, D.; Zakrzewski, V. G.; Gao, J.; Rega, N.; Zheng, G.; Liang, W.; Hada, M.; Ehara, M.; Toyota, K.; Fukuda, R.; Hasegawa, J.; Ishida, M.; Nakajima, T.; Honda, Y.; Kitao, O.; Nakai, H.; Vreven, T.; Throsell, K.; Montgomery, J. A.; Jr.; Peralta, J. E.; Ogliaro, F.; Beapark, M. J.; Heyd, J. J.; Brothers, E. N.; Kudin, K. N.; Staroverov, V. N.; Keith, T. A.; Kobayash, R.; Normand, J.; Raghavachari, K.; Rendell, A. P.; Burant, J. C.; Iyengar, S. S.; Tomasi, J.; Cossi, M.; Millam, J. M.; Klene, M.; Adamo, C.; Cammi, R.; Ochterski, J. W.; Martin, R. L.; Morokuma, K.; Farkas, O.; Foresman, J. B.; Fox, D. J. Gaussian16. Gaussian Inc.: Wallingford CT 2016.

(88) Stewart, J. J. P. MOPAC2016. Stewart Computational Chemistry: Colorado Springs, CO, USA 2016.

(89) Bannwarth, C.; Caldeweyher, E.; Ehlert, S.; Hansen, A.; Pracht, P.; Seibert, J.; Spicher, S.; Grimme, S. Extended Tight-Binding Quantum Chemistry Methods. *WIREs Comput. Mol. Sci.* **2021**, *11*, e1493.

(90) Rackers, J. A.; Wang, Z.; Lu, C.; Laury, M. L.; Lagardère, L.; Schnieders, M. J.; Piquemal, J.-P.; Ren, P.; Ponder, J. W. Tinker 8: Software Tools for Molecular Design. *J. Chem. Theory Comput.* **2018**, *14*, 5273–5289.

(91) Worth, G. A.; Giri, K.; Richings, G. W.; Burghardt, I.; Beck, M. H.; Jäcke, A.; Meyer, H. D. The QUANTICS Package, Version 1.1. University of Birmingham: Birmingham, U.K. 2015.

(92) Hartree, D. R. The Wave Mechanics of an Atom with a Non-Coulomb Central Field. Part I. Theory and Methods. *Math. Proc. Cambridge Philos. Soc.* **1928**, *24*, 89–110.

(93) Szabo, A.; Ostlund, N. S. *Modern Quantum Chemistry. Introduction to Advanced Electronic Structure*; Dover Publications, 1993.

(94) Pople, J. A.; Nesbet, R. K. Self-Consistent Orbitals for Radicals. *J. Chem. Phys.* **1954**, *22*, 571–572.

(95) Thomas, L. H. The Calculation of Atomic Fields. *Math. Proc. Cambridge Philos. Soc.* **1927**, *23*, 542–548.

(96) Burke, K.; Wagner, L. O. DFT in a Nutshell. *Int. J. Quantum Chem.* **2013**, *113*, 96–101.

(97) Teller, E. On the Stability of Molecules in the Thomas-Fermi Theory. *Rev. Mod. Phys.* **1962**, *34*, 627–631.

(98) Perdew, J. P.; Burke, K.; Ernzerhof, M. Generalized Gradient Approximation Made

Simple. *Phys. Rev. Lett.* **1996**, *77*, 3865–3868.

(99) Tao, J.; Perdew, J. P.; Staroverov, V. N.; Scuseria, G. E. Climbing the Density Functional Ladder: Nonempirical Meta–Generalized Gradient Approximation Designed for Molecules and Solids. *Phys. Rev. Lett.* **2003**, *91*, 146401.

(100) Becke, A. D. Density-Functional Exchange-Energy Approximation with Correct Asymptotic Behavior. *Phys. Rev. A* **1988**, *38*, 3098–3100.

(101) Lee, C.; Yang, W.; Parr, R. G. Development of the Colle-Salvetti Correlation-Energy Formula into a Functional of the Electron Density. *Phys. Rev. B* **1988**, *37*, 785–789.

(102) Adamo, C.; Barone, V. Toward Reliable Density Functional Methods without Adjustable Parameters: The PBE0 Model. *J. Chem. Phys.* **1999**, *110*, 6158–6170.

(103) Zhao, Y.; Truhlar, D. G. A New Local Density Functional for Main-Group Thermochemistry, Transition Metal Bonding, Thermochemical Kinetics, and Noncovalent Interactions. *J. Chem. Phys.* **2006**, *125*, 194101.

(104) Zhao, Y.; Truhlar, D. G. The M06 Suite of Density Functionals for Main Group Thermochemistry, Thermochemical Kinetics, Noncovalent Interactions, Excited States, and Transition Elements: Two New Functionals and Systematic Testing of Four M06-Class Functionals and 12 Other Function. *Theor. Chem. Accounts 2007 1201* **2008**, *120*, 215–241.

(105) Yan, Z.; Truhlar, D. G. Comparative DFT Study of van Der Waals Complexes: Rare-Gas Dimers, Alkaline-Earth Dimers, Zinc Dimer, and Zinc-Rare-Gas Dimers. *J. Phys. Chem. A* **2006**, *110*, 5121–5129.

(106) Scuseria, G. E.; Ayala, P. Y. Linear Scaling Coupled Cluster and Perturbation Theories in the Atomic Orbital Basis. *J. Chem. Phys.* **1999**, *111*, 8330–8343.

(107) Ayala, P. Y.; Scuseria, G. E. Linear Scaling Second-Order Moller–Plesset Theory in the Atomic Orbital Basis for Large Molecular Systems. *J. Chem. Phys.* **1999**, *110*, 3660–3671.

(108) Likura, H.; Tsuneda, T.; Yanai, T.; Hirao, K. A Long-Range Correction Scheme for Generalized-Gradient-Approximation Exchange Functionals. *J. Chem. Phys.* **2001**, *115*, 234109–1372.

(109) Tsuneda, T.; Hirao, K. Long-Range Correction for Density Functional Theory. *Wiley Interdiscip. Rev. Comput. Mol. Sci.* **2014**, *4*, 375–390.

(110) Chai, J. Da; Head-Gordon, M. Systematic Optimization of Long-Range Corrected Hybrid Density Functionals. *J. Chem. Phys.* **2008**, *128*, 084106.

(111) Vydrov, O. A.; Scuseria, G. E. Assessment of a Long-Range Corrected Hybrid Functional. *J. Chem. Phys.* **2006**, *125*, 234109.

(112) Baer, R.; Neuhauser, D. Density Functional Theory with Correct Long-Range Asymptotic Behavior. *Phys. Rev. Lett.* **2005**, *94*, 043002.

(113) Livshits, E.; Baer, R. A Well-Tempered Density Functional Theory of Electrons in Molecules. *Phys. Chem. Chem. Phys.* **2007**, *9*, 2932–2941.

(114) Tawada, Y.; Tsuneda, T.; Yanagisawa, S.; Yanai, T.; Hirao, K. A Long-Range-Corrected Time-Dependent Density Functional Theory. *J. Chem. Phys.* **2004**, *120*, 8425.

(115) Yi, Y.; Coropceanu, V.; Brédas, J. L. Exciton-Dissociation and Charge-Recombination Processes in Pentacene/C 60 Solar Cells: Theoretical Insight into the Impact of Interface Geometry. *J. Am. Chem. Soc.* **2009**, *131*, 15777–15783.

(116) Zhang, C. R.; Sears, J. S.; Yang, B.; Aziz, S. G.; Coropceanu, V.; Brédas, J. L. Theoretical Study of the Local and Charge-Transfer Excitations in Model Complexes of Pentacene-C60 Using Tuned Range-Separated Hybrid Functionals. *J. Chem. Theory Comput.* **2014**, *10*, 2379–2388.

(117) Yang, B.; Yi, Y.; Zhang, C. R.; Aziz, S. G.; Coropceanu, V.; Brédas, J. L. Impact of Electron Delocalization on the Nature of the Charge-Transfer States in Model Pentacene/C60 Interfaces: A Density Functional Theory Study. *J. Phys. Chem. C* **2014**, *118*, 27648–27656.

(118) Stein, T.; Kronik, L.; Baer, R. Reliable Prediction of Charge Transfer Excitations in Molecular Complexes Using Time-Dependent Density Functional Theory. *J. Am. Chem. Soc.* **2009**, *131*, 2818–2820.

(119) Körzdörfer, T.; Brédas, J.-L. Organic Electronic Materials: Recent Advances in the DFT Description of the Ground and Excited States Using Tuned Range-Separated Hybrid Functionals. *Acc. Chem. Res.* **2014**, *47*, 3284–3291.

(120) Refaely-Abramson, S.; Sharifzadeh, S.; Govind, N.; Autschbach, J.; Neaton, J. B.; Baer, R.; Kronik, L. Quasiparticle Spectra from a Nonempirical Optimally Tuned Range-Separated Hybrid Density Functional. *Phys. Rev. Lett.* **2012**, *109*, 226405.

(121) Karolewski, A.; Kronik, L.; Kümmel, S. Using Optimally Tuned Range Separated Hybrid Functionals in Ground-State Calculations: Consequences and Caveats. *J. Chem. Phys.* **2013**, *138*, 204115.

(122) Yanai, T.; Tew, D. P.; Handy, N. C. A New Hybrid Exchange-Correlation Functional Using the Coulomb-Attenuating Method (CAM-B3LYP). *Chem. Phys. Lett.* **2004**, *393*, 51–57.

(123) Rohrdanz, M. A.; Herbert, J. M. Simultaneous Benchmarking of Ground- and Excited-State Properties with Long-Range-Corrected Density Functional Theory. *J. Chem. Phys.* **2008**, *129*, 034107.

(124) Perdew, J. P.; Schmidt, K. Jacob's Ladder of Density Functional Approximations for the Exchange-Correlation Energy. *AIP Conf. Proc.* **2001**, *577*, 1–20.

(125) Calbo, J.; Ortí, E.; Sancho-García, J. C.; Aragó, J. The Nonlocal Correlation Density Functional VV10: A Successful Attempt to Accurately Capture Noncovalent

Interactions. *Annu. Rep. Comput. Chem.* **2015**, *11*, 37–102.

(126) Grimme, S. Semiempirical GGA-Type Density Functional Constructed with a Long-Range Dispersion Correction. *J. Comput. Chem.* **2006**, *27*, 1787–1799.

(127) Antony, J.; Grimme, S. Density Functional Theory Including Dispersion Corrections for Intermolecular Interactions in a Large Benchmark Set of Biologically Relevant Molecules. *Phys. Chem. Chem. Phys.* **2006**, *8*, 5287–5293.

(128) Dion, M.; Rydberg, H.; Schröder, E.; Langreth, D. C.; Lundqvist, B. I. Van Der Waals Density Functional for General Geometries. *Phys. Rev. Lett.* **2004**, *92*, 246401.

(129) Vydrov, O. A.; Van Voorhis, T. Nonlocal van Der Waals Density Functional: The Simpler the Better. *J. Chem. Phys.* **2010**, *133*, 244103.

(130) Grimme, S.; Antony, J.; Ehrlich, S.; Krieg, H. A Consistent and Accurate Ab Initio Parametrization of Density Functional Dispersion Correction (DFT-D) for the 94 Elements H-Pu. *J. Chem. Phys.* **2010**, *132*, 154104.

(131) Grimme, S.; Ehrlich, S.; Goerigk, L. Effect of the Damping Function in Dispersion Corrected Density Functional Theory. *J. Comput. Chem.* **2011**, *32*, 1456–1465.

(132) Verbeek, J.; Lenthe, J. H. Van. The Generalized Slater–Condon Rules. *Int. J. Quantum Chem.* **1991**, *40*, 201–210.

(133) Davidson, E. R. The Iterative Calculation of a Few of the Lowest Eigenvalues and Corresponding Eigenvectors of Large Real-Symmetric Matrices. *J. Comput. Phys.* **1975**, *17*, 87–94.

(134) Caricato, M.; Trucks, G. W.; Frisch, M. J. A Comparison of Three Variants of the Generalized Davidson Algorithm for the Partial Diagonalization of Large Non-Hermitian Matrices. *J. Chem. Theory Comput.* **2010**, *6*, 1966–1970.

(135) Elliott, P.; Burke, K.; Furche, F. In *Excited states from time-dependent density functional theory In Reviews in Computational Chemistry*; 2007.

(136) Casida, M. E.; Huix-Rotllant, M. Progress in Time-Dependent Density-Functional Theory. *Annu. Rev. Phys. Chem.* **2012**, *63*, 287–323.

(137) Marques, M. A. L.; Gross, E. K. U. Time-Dependet Density Functional Theory. *Annu. Rev. Phys. Chem.* **2004**, *55*, 427–455.

(138) Mulliken, R. S. Structures of Complexes Formed by Halogen Molecules with Aromatic and with Oxygenated Solvent S1. *J. Am. Chem. Soc.* **1950**, *72*, 600–608.

(139) Ditchfield, R.; Hehre, W. J.; Pople, J. A. Self-Consistent Molecular-Orbital Methods. IX. An Extended Gaussian-Type Basis for Molecular-Orbital Studies of Organic Molecules. *J. Chem. Phys.* **2003**, *54*, 724–728.

(140) Francl, M. M.; Pietro, W. J.; Hehre, W. J.; Binkley, J. S.; Gordon, M. S.; DeFrees, D. J.; Pople, J. A. Self-consistent Molecular Orbital Methods. XXIII. A Polarization-type

Basis Set for Second-row Elements. *J. Chem. Phys.* **1982**, *77*, 3654–3665.

(141) Jr., T. H. D. Gaussian Basis Sets for Use in Correlated Molecular Calculations. I. The Atoms Boron through Neon and Hydrogen. *J. Chem. Phys.* **1998**, *90*, 1007–1023.

(142) Weigend, F.; Ahlrichs, R. Balanced Basis Sets of Split Valence, Triple Zeta Valence and Quadruple Zeta Valence Quality for H to Rn: Design and Assessment of Accuracy. *Phys. Chem. Chem. Phys.* **2005**, *7*, 3297–3305.

(143) Tomasi, J.; And, B. M.; Cammi, R. Quantum Mechanical Continuum Solvation Models. *Chem. Rev* **2005**, *105*, 2999–3093.

(144) Scalmani, G.; Frisch, M. J. Continuous Surface Charge Polarizable Continuum Models of Solvation. I. General Formalism. *J. Chem. Phys.* **2010**, *132*, 114110.

(145) Marenich, A. V.; Cramer, C. J.; Truhlar, D. G. Universal Solvation Model Based on Solute Electron Density and on a Continuum Model of the Solvent Defined by the Bulk Dielectric Constant and Atomic Surface Tensions. *J. Phys. Chem. B* **2009**, *113*, 6378–6396.

(146) Su, Y.; Ren, H.; Li, X. Novel Nonequilibrium Solvation Theory for Calculating the Solvatochromic Stokes Shift by State-Specific TD-DFT. *Chem. Phys. Lett.* **2019**, *732*, 136640.

(147) Guido, C. A.; Jacquemin, D.; Adamo, C.; Mennucci, B. Electronic Excitations in Solution: The Interplay between State Specific Approaches and a Time-Dependent Density Functional Theory Description. *J. Chem. Theory Comput.* **2015**, *11*, 5782–5790.

(148) Caricato, M.; Mennucci, B.; Tomasi, J.; Ingrosso, F.; Cammi, R.; Corni, S.; Scalmani, G. Formation and Relaxation of Excited States in Solution: A New Time Dependent Polarizable Continuum Model Based on Time Dependent Density Functional Theory. *J. Chem. Phys.* **2006**, *124*, 124520.

(149) Improta, R.; Barone, V.; Scalmani, G.; Frisch, M. J. A State-Specific Polarizable Continuum Model Time Dependent Density Functional Theory Method for Excited State Calculations in Solution. *J. Chem. Phys.* **2006**, *125*, 054103.

(150) Jensen, F. *Introduction to Computational Chemistry*; John Wiley & Sons, 1999.

(151) Dewar, M. J. S.; Thiel, W. Ground States of Molecules. 38. The MNDO Method. Approximations and Parameters. *J. Am. Chem. Soc.* **2002**, *99*, 4899–4907.

(152) Dewar, M. J. S.; Zoebisch, E. G.; Healy, E. F.; Stewart, J. J. P. Development and Use of Quantum Mechanical Molecular Models. 76. AM1: A New General Purpose Quantum Mechanical Molecular Model. *J. Am. Chem. Soc.* **2002**, *107*, 3902–3909.

(153) Stewart, J. J. P. Optimization of Parameters for Semiempirical Methods I. Method. *J. Comput. Chem.* **1989**, *10*, 209–220.

(154) Stewart, J. J. P. Optimization of Parameters for Semiempirical Methods VI: More

Modifications to the NDDO Approximations and Re-Optimization of Parameters. *J. Mol. Model. 2012 191* **2012**, *19*, 1–32.

(155) Stewart, J. J. P. Optimization of Parameters for Semiempirical Methods V: Modification of NDDO Approximations and Application to 70 Elements. *J. Mol. Model. 2007 1312* **2007**, *13*, 1173–1213.

(156) Porezag, D.; Frauenheim, T.; Köhler, T.; Seifert, G.; Kaschner, R. Construction of Tight-Binding-like Potentials on the Basis of Density-Functional Theory: Application to Carbon. *Phys. Rev. B* **1995**, *51*, 12947–12957.

(157) Elstner, M.; Porezag, D.; Jungnickel, G.; Elsner, J.; Haugk, M.; Frauenheim, T.; Suhai, S.; Seifert, G. Self-Consistent-Charge Density-Functional Tight-Binding Method for Simulations of Complex Materials Properties. *Phys. Rev. B* **1998**, *58*, 7260–7268.

(158) Elstner, M. The SCC-DFTB Method and Its Application to Biological Systems. *Theor. Chem. Accounts 2005 1161* **2005**, *116*, 316–325.

(159) Christensen, A. S.; Kubař, T.; Cui, Q.; Elstner, M. Semiempirical Quantum Mechanical Methods for Noncovalent Interactions for Chemical and Biochemical Applications. *Chem. Rev.* **2016**, *116*, 5301–5337.

(160) Grimme, S.; Bannwarth, C.; Shushkov, P. A Robust and Accurate Tight-Binding Quantum Chemical Method for Structures, Vibrational Frequencies, and Noncovalent Interactions of Large Molecular Systems Parametrized for All Spd-Block Elements ($Z = 1–86$). *J. Chem. Theory Comput.* **2017**, *13*, 1989–2009.

(161) Bannwarth, C.; Ehlert, S.; Grimme, S. GFN2-XTB—An Accurate and Broadly Parametrized Self-Consistent Tight-Binding Quantum Chemical Method with Multipole Electrostatics and Density-Dependent Dispersion Contributions. *J. Chem. Theory Comput.* **2019**, *15*, 1652–1671.

(162) Meyer, H. D.; Gatti, F.; Worth, G. A. *Multidimensional Quantum Dynamics*; WILEY-VCH Verlag GmbH & Co. KGaA: Weinheim, Germany, 2009.

(163) Meyer, H. D.; Manthe, U.; Cederbaum, L. S. The Multi-Configurational Time-Dependent Hartree Approach. *Chem. Phys. Lett.* **1990**, *165*, 73–78.

(164) Wang, H.; Thoss, M. Multilayer Formulation of the Multiconfiguration Time-Dependent Hartree Theory. *J. Chem. Phys.* **2003**, *119*, 1289–1299.

(165) May, V.; Khün, O. *Charge and Energy Transfer Dynamics in Molecular Systems*, Third Edit.; WILEY-VCH Verlag: Weinheim, Germany, 2011.

(166) Mccutcheon, D. P. S.; Nazir, A. Coherent and Incoherent Dynamics in Excitonic Energy Transfer: Correlated Fluctuations and off-Resonance Effects. *Phys. Rev. B* **2011**, *83*, 165101.

(167) G Bennett, D. I.; Maly, P.; Kreisbeck, C.; van Grondelle, R. Mechanistic Regimes of Vibronic Transport in a Heterodimer and the Design Principle of Incoherent Vibronic Transport in Phycobiliproteins. **2018**.

(168) Mead, C. A.; Truhlar, D. G. Conditions for the Definition of a Strictly Diabatic Electronic Basis for Molecular Systems. *J. Chem. Phys.* **1982**, *77*, 6090–6098.

(169) Girlando, A.; Grisanti, L.; Masino, M.; Bilotti, I.; Brillante, A.; Della Valle, R. G.; Venuti, E. Peierls and Holstein Carrier-Phonon Coupling in Crystalline Rubrene. *Phys. Rev. B - Condens. Matter Mater. Phys.* **2010**, *82*, 035208.

(170) A M D irac, B. P.; John, S. The Quantum Theory of the Emission and Absorption of Radiation. *Proc. R. Soc. London. Ser. A, Contain. Pap. a Math. Phys. Character* **1927**, *114*, 243–265.

(171) Fermi, E. *Nuclear Physics*; University of Chicago Press, 1950.

(172) Marcus, R. A. On the Theory of Oxidation-Reduction Reactions Involving Electron Transfer. I. *J. Chem. Phys.* **1956**, *24*, 966–978.

(173) Marcus, R. A. Electron Transfer Reactions in Chemistry. Theory and Experiment. *Rev. Mod. Phys.* **1993**, *65*, 599–610.

(174) Bixon, M.; Jortner, J. In *Advances in Chemical Physics*; John Wiley & Sons, Inc., 1999; Vol. 106, pp 35–202.

(175) Martínez, J. P.; Solà, M.; Voityuk, A. A. Theoretical Estimation of the Rate of Photoinduced Charge Transfer Reactions in Triphenylamine C 60 Donor-Acceptor Conjugate. *J. Comput. Chem.* **2016**, *37*, 1396–1405.

(176) Liu, T.; Troisi, A. Absolute Rate of Charge Separation and Recombination in a Molecular Model of the P3HT/PCBM Interface. *J. Phys. Chem. C* **2011**, *115*, 2406–2415.

(177) Coropceanu, V.; Malagoli, M.; da Silva Filho, D. A.; Gruhn, N. E.; Bill, T. G.; Brédas, J. L. Hole- and Electron-Vibrational Couplings in Oligoacene Crystals: Intramolecular Contributions. *Phys. Rev. Lett.* **2002**, *89*, 275503.

(178) Malagoli, M.; Coropceanu, V.; da Silva Filho, D. A.; Brédas, J. L. A Multimode Analysis of the Gas-Phase Photoelectron Spectra in Oligoacenes. *J. Chem. Phys.* **2004**, *120*, 7490–7496.

(179) Mcmahon, D. P.; Troisi, A. Evaluation of the External Reorganization Energy of Polyacenes. *J. Phys. Chem. Lett.* **2010**, *1*, 941–946.

(180) Marcus, R. A. Chemical and Electrochemical Electron-Transfer Theory. *Annu. Rev. Phys. Chem.* **1964**, *15*, 155–196.

(181) Kasha, M. Energy Transfer Mechanisms and the Molecular Exciton Model for Molecular Aggregates. *Radiat. Res.* **1963**, *20*, 55–70.

(182) Chuang, C.; Bennett, D. I. G.; Caram, J. R.; Aspuru-Guzik, A.; Bawendi, M. G.; Cao, J. Generalized Kasha's Model: T-Dependent Spectroscopy Reveals Short-Range Structures of 2D Excitonic Systems. *Chem* **2019**, *5*, 3135–3150.

(183) Hestand, N. J.; Spano, F. C. Molecular Aggregate Photophysics beyond the Kasha Model: Novel Design Principles for Organic Materials. *Acc. Chem. Res.* **2017**, *50*, 341–350.

(184) Baumeier, B.; Kirkpatrick, J.; Andrienko, D. Density-Functional Based Determination of Intermolecular Charge Transfer Properties for Large-Scale Morphologies. *Phys. Chem. Chem. Phys* **2010**, *12*, 11103–11113.

(185) Löwdin, P. On the Non-Orthogonality Problem Connected with the Use of Atomic Wave Functions in the Theory of Molecules and Crystals. *J. Chem. Phys.* **2004**, *18*, 365–375.

(186) Cave, R. J.; Newton, M. D. Generalization of the Mulliken-Hush Treatment for the Calculation of Electron Transfer Matrix Elements. *Chem. Phys. Lett.* **1996**, *249*, 15–19.

(187) Voityuk, A. A.; Rösch, N. Fragment Charge Difference Method for Estimating Donor–Acceptor Electronic Coupling: Application to DNA π-Stacks. *J. Chem. Phys.* **2002**, *117*, 5607–5616.

(188) Hsu, C.-P. The Electronic Couplings in Electron Transfer and Excitation Energy Transfer. *Acc. Chem. Res.* **2009**, *42*, 509–518.

(189) Yang, C.-H.; Hsu, C.-P. A Multi-State Fragment Charge Difference Approach for Diabatic States in Electron Transfer: Extension and Automation. *J. Chem. Phys.* **2013**, *139*, 154104.

(190) Hestand, N. J.; Spano, F. C. Expanded Theory of H- and J-Molecular Aggregates: The Effects of Vibronic Coupling and Intermolecular Charge Transfer. *Chem. Rev.* **2018**, *118*, 7069–7163.

(191) Kistler, K. A.; Spano, F. C.; Matsika, S. A Benchmark of Excitonic Couplings Derived from Atomic Transition Charges. *J. Phys. Chem. B* **2013**, *117*, 2032–2044.

(192) Krueger, B. P.; Scholes, G. D.; Fleming, G. R. Calculation of Couplings and Energy-Transfer Pathways between the Pigments of LH2 by the Ab Initio Transition Density Cube Method. *J. Phys. Chem. B* **1998**, *102*, 5378–5386.

(193) Aragó, J.; Troisi, A. Excitonic Couplings between Molecular Crystal Pairs by a Multistate Approximation Vibronic Enhancement of Excitation Energy Transport: Interplay between Local and Non-Local Exciton-Phonon Interactions Quantum Dynamics of a Vibronically Coupled Linear Chai. *J. Chem. Phys.* **2015**, *142*, 164107.

(194) Schönemann, P. H. A Generalized Solution of the Orthogonal Procrustes Problem. *Psychometrika* **1966**, *31*, 1–10.

(195) Wang, Y. C.; Feng, S.; Liang, W.; Zhao, Y. Electronic Couplings for Photoinduced Charge Transfer and Excitation Energy Transfer Based on Fragment Particle-Hole Densities. *J. Phys. Chem. Lett.* **2021**, *12*, 1032–1039.

(196) Cardoso, J. F.; Souloumiac, A. Jacobi Angles for Simultaneous Diagonalization. *SIAM*

J. Matrix Anal. Appl. **1996**, *17*, 161–164.

(197) Morrison, A. F.; You, Z.-Q.; Herbert, J. M. Ab Initio Implementation of the Frenkel−Davydov Exciton Model: A Naturally Parallelizable Approach to Computing Collective Excitations in Crystals and Aggregates. *J. Chem. Theory Comput.* **2014**, *10*, 5366–5376.

(198) Morrison, A. F.; Herbert, J. M. Analytic Derivative Couplings and First-Principles Exciton/Phonon Coupling Constants for an Ab Initio Frenkel-Davydov Exciton Model: Theory, Implementation, and Application to Compute Triplet Exciton Mobility Parameters for Crystalline Tetracene. *J. Chem. Phys.* **2017**, *146*, 224110.

(199) Li, X.; Parrish, R. M.; Liu, F.; Schumacher, S. I. L. K.; Martínez, T. J. An Ab Initio Exciton Model Including Charge-Transfer Excited States. *J. Chem. Theory Comput.* **2017**, *13*, 3493–3504.

(200) Li, X.; Parrish, R. M.; Martínez, T. J. An Ab Initio Exciton Model for Singlet Fission. *J. Chem. Phys.* **2020**, *153*, 184116.

(201) Fujita, T.; Mochizuki, Y. Development of the Fragment Molecular Orbital Method for Calculating Nonlocal Excitations in Large Molecular Systems. *J. Phys. Chem. A* **2018**, *122*, 3886–3898.

(202) Fujimoto, K. J. Transition-Density-Fragment Interaction Combined with Transfer Integral Approach for Excitation-Energy Transfer via Charge-Transfer States. *J. Chem. Phys.* **2012**, *137*, 034101.

(203) Gali, S. M.; Matta, M.; Lessard, B. H.; Castet, F.; Muccioli, L. Ambipolarity and Dimensionality of Charge Transport in Crystalline Group 14 Phthalocyanines: A Computational Study. *J. Phys. Chem. C* **2018**, *122*, 2554–2563.

(204) Sousa, L.; Volpi, R.; da Silva Filho, D. A.; Linares, M. Mobility Field and Mobility Temperature Dependence in PC61BM: A Kinetic Monte-Carlo Study. *Chem. Phys. Lett.* **2017**, *689*, 74–81.

(205) Stehr, V.; Pfister, J.; Fink, R. F.; Engels, B.; Deibel, C. First-Principles Calculations of Anisotropic Charge-Carrier Mobilities in Organic Semiconductor Crystals. *Phys. Rev. B - Condens. Matter Mater. Phys.* **2011**, *83*, 155208.

(206) Wang, D.; Chen, L.; Zheng, R.; Wang, L.; Shi, Q. Communications: A Nonperturbative Quantum Master Equation Approach to Charge Carrier Transport in Organic Molecular Crystals. *J. Chem. Phys.* **2010**, *132*.

(207) Zhang, X.; Li, Z.; Lu, G. First-Principles Simulations of Exciton Diffusion in Organic Semiconductors. *Phys. Rev. B* **2011**, *84*, 235208.

(208) Harada, A. *Supramolecular Polymer Chemistry*; Wiley-VCH Verlag GmbH & Co. KGaA, 2012.

(209) Aida, T.; Meijer, E. W.; Stupp, S. I. Functional Supramolecular Polymers. *Science* **2012**, *335*, 813–817.

(210) Ahmed, M. H.; Ghatge, M. S.; Safo, M. K. In *Subcellular Biochemistry*; Springer, 2020; Vol. 94, pp 345–382.

(211) Alberts, B.; Johnson, A.; Lewis, J.; Raff, M.; Roberts, K.; Walter, P. *Molecular Biology of the Cell*, 4th editio.; Garland Science, 2002.

(212) Fouquey, C.; Lehn, J.-M.; Levelut, A.-M. Molecular Recognition Directed Self-Assembly of Supramolecular Liquid Crystalline Polymers from Complementary Chiral Components. *Adv. Mater.* **1990**, *2*, 254–257.

(213) Sijbesma, R. P.; Beijer, F. H.; Brunsveld, L.; Folmer, B. J. B.; Hirschberg, J. H. K. K.; Lange, R. F. M.; Lowe, J. K. L.; Meijer, E. W. Reversible Polymers Formed from Self-Complementary Monomers Using Quadruple Hydrogen Bonding. *Science* **1997**, *278*, 1601–1604.

(214) Ligthart, G. B. W. L.; Ohkawa, H.; Sijbesma, R. P.; Meijer, E. W. Complementary Quadruple Hydrogen Bonding in Supramolecular Copolymers. *J. Am. Chem. Soc.* **2005**, *127*, 810–811.

(215) Rehahn, M. Organic/Inorganic Hybrid Polymers. *Acta Polym.* **1998**, *49*, 201–224.

(216) Huang, F.; Isaacs, L. Guest Editorial: Responsive Host-Guest Systems. *Acc. Chem. Res.* **2014**, *47*, 1923–1924.

(217) Hoeben, F. J. M.; Jonkheijm, P.; Meijer, E. W.; Schenning, A. P. H. J. About Supramolecular Assemblies of π-Conjugated Systems. *Chem. Rev.* **2005**, *105*, 1491–1546.

(218) Wöhrle, T.; Wurzbach, I.; Kirres, J.; Kostidou, A.; Kapernaum, N.; Litterscheidt, J.; Haenle, J. C.; Staffeld, P.; Baro, A.; Giesselmann, F.; Laschat, S. Discotic Liquid Crystals. *Chem. Rev.* **2016**, *116*, 1139–1241.

(219) Sergeyev, S.; Pisula, W.; Geerts, Y. H. Discotic Liquid Crystals: A New Generation of Organic Semiconductors. *Chem. Soc. Rev.* **2007**, *36*, 1902–1929.

(220) Lee, C. C.; Grenier, C.; Meijer, E. W.; Schenning, A. P. H. J. Preparation and Characterization of Helical Self-Assembled Nanofibers. *Chem. Soc. Rev.* **2009**, *38*, 671–683.

(221) Vera, F.; Barberá, J.; Romero, P.; Serrano, J. L.; Ros, M. B.; Sierra, T. Orthogonal Action of Noncovalent Interactions for Photoresponsive Chiral Columnar Assemblies. *Angew. Chem. Int. Ed.* **2010**, *49*, 4910–4914.

(222) Roosma, J.; Mes, T.; Leclère, P.; Palmans, A. R. A.; Meijer, E. W. Supramolecular Materials from Benzene-1,3,5-Tricarboxamide-Based Nanorods. *J. Am. Chem. Soc.* **2008**, *130*, 1120–1121.

(223) Stals, P. J. M.; Everts, J. C.; de Bruijn, R.; Filot, I. A. W.; Smulders, M. M. J.; Martín-Rapún, R.; Pidko, E. A.; de Greef, T. F. A.; Palmans, A. R. A.; Meijer, E. W. Dynamic Supramolecular Polymers Based on Benzene-1,3,5-Tricarboxamides: The Influence of Amide Connectivity on Aggregate Stability and Amplification of Chirality. *Chem.*

Eur. J. **2010**, *16*, 810–821.

(224) Cantekin, S.; Balkenende, D. W. R.; Smulders, M. M. J.; Palmans, A. R. A.; Meijer, E. W. The Effect of Isotopic Substitution on the Chirality of a Self-Assembled Helix. *Nat. Chem.* **2011**, *3*, 42–46.

(225) Kulkarni, C.; Meijer, E. W.; Palmans, A. R. A. Cooperativity Scale: A Structure–Mechanism Correlation in the Self-Assembly of Benzene-1,3,5-Tricarboxamides. *Acc. Chem. Res.* **2017**, *50*, 1928–1936.

(226) Wang, F.; Gillissen, M. A. J.; Stals, P. J. M.; Palmans, A. R. A.; Meijer, E. W. Hydrogen Bonding Directed Supramolecular Polymerisation of Oligo(Phenylene-Ethynylene)s: Cooperative Mechanism, Core Symmetry Effect and Chiral Amplification. *Chem. Eur. J.* **2012**, *18*, 11761–11770.

(227) Cantekin, S.; de Greef, T. F. A.; Palmans, A. R. A. Benzene-1,3,5-Tricarboxamide: A Versatile Ordering Moiety for Supramolecular Chemistry. *Chem. Soc. Rev.* **2012**, *41*, 6125–6137.

(228) Goor, O. J. G. M.; Hendrikse, S. I. S.; Dankers, P. Y. W.; Meijer, E. W. From Supramolecular Polymers to Multi-Component Biomaterials. *Chem. Soc. Rev* **2017**, *46*, 6621–6637.

(229) Korevaar, P. A.; George, S. J.; Markvoort, A. J.; Smulders, M. M. J.; Hilbers, P. A. J.; Schenning, A. P. H. J.; De Greef, T. F. A.; Meijer, E. W. Pathway Complexity in Supramolecular Polymerization. *Nature* **2012**, *481*, 492–496.

(230) Ogi, S.; Sugiyasu, K.; Manna, S.; Samitsu, S.; Takeuchi, M. Living Supramolecular Polymerization Realized through a Biomimetic Approach. *Nat. Chem. 2014 63* **2014**, *6*, 188–195.

(231) Ma, X.; Zhang, Y.; Zhang, Y.; Liu, Y.; Che, Y.; Zhao, J. Fabrication of Chiral-Selective Nanotubular Heterojunctions through Living Supramolecular Polymerization. *Angew. Chem. Int. Ed.* **2016**, *55*, 9539–9543.

(232) Wagner, W.; Wehner, M.; Stepanenko, V.; Ogi, S.; Würthner, F. Living Supramolecular Polymerization of a Perylene Bisimide Dye into Fluorescent J-Aggregates. *Angew. Chem. Int. Ed.* **2017**, *56*, 16008–16012.

(233) Oleson, A.; Zhu, T.; Dunn, I. S.; Bialas, D.; Bai, Y.; Zhang, W.; Dai, M.; Reichman, D. R.; Tempelaar, R.; Huang, L.; Spano, F. C. Perylene Diimide-Based Hj- And HJ-Aggregates- And Prospect of Exciton Band Shape Engineering in Organic Materials. *J. Phys. Chem. C* **2019**, *123*, 20567–20578.

(234) Würthner, F. Perylene Bisimide Dyes as Versatile Building Blocks for Functional Supramolecular Architectures. *Chem. Commun.* **2004**, *4*, 1564–1579.

(235) Würthner, F.; Saha-Möller, C. R.; Fimmel, B.; Ogi, S.; Leowanawat, P.; Schmidt, D. Perylene Bisimide Dye Assemblies as Archetype Functional Supramolecular Materials. *Chem. Rev.* **2016**, *116*, 962–1052.

(236) Buendía, J.; Calbo, J.; García, F.; Aragó, J.; Viruela, P. M.; Ortí, E.; Sánchez, L. Helical Supramolecular Polymerization of C_3-Symmetric Amides and Retroamides: On the Origin of Cooperativity and Handedness. *Chem. Commun.* **2016**, *52*, 6907–6910.

(237) Markvoort, A. J.; Ten Eikelder, H. M. M.; Hilbers, P. A. J.; De Greef, T. F. A.; Meijer, E. W. Theoretical Models of Nonlinear Effects in Two-Component Cooperative Supramolecular Copolymerizations. *Nat. Commun.* **2011**, *2*, 509.

(238) Vantomme, G.; Huurne, G. M. ter; Kulkarni, C.; Eikelder, H. M. M. ten; Markvoort, A. J.; Palmans, A. R. A.; Meijer, E. W. Tuning the Length of Cooperative Supramolecular Polymers under Thermodynamic Control. *J. Am. Chem. Soc.* **2019**, *141*, 18278–18285.

(239) Smulders, M. M. J.; Stals, P. J. M.; Mes, T.; Paffen, T. F. E.; Schenning, A. P. H. J.; Palmans, A. R. A.; Meijer, E. W. Probing the Limits of the Majority-Rules Principle in a Dynamic Supramolecular Polymer. *J. Am. Chem. Soc.* **2009**, *132*, 620–626.

(240) Díaz-Cabrera, S.; Dorca, Y.; Calbo, J.; Aragó, J.; Gómez, R.; Ortí, E.; Sánchez, L. Hierarchy of Asymmetry at Work: Chain-Dependent Helix-to-Helix Interactions in Supramolecular Polymers. *Chem. Eur. J.* **2018**, *24*, 2826–2831.

(241) Greciano, E. E.; Calbo, J.; Buendía, J.; Cerdá, J.; Aragó, J.; Ortí, E.; Sánchez, L. Decoding the Consequences of Increasing the Size of Self-Assembling Tricarboxamides on Chiral Amplification. *J. Am. Chem. Soc.* **2019**, *141*, 7463–7472.

(242) Dorca, Y.; Sánchez-Naya, R.; Cerdá, J.; Calbo, J.; Aragó, J.; Gómez, R.; Ortí, E.; Sánchez, L. Impact of Molecular Size and Shape on the Supramolecular Co-Assembly of Chiral Tricarboxamides: A Comparative Study. *Chem. Eur. J.* **2020**, *26*, 14700.

(243) Kumar, S.; Kang, S. W. In *Encyclopedia of Condensed Matter Physics*; Elsevier Inc., 2005; pp 111–120.

(244) Bremer, M.; Kirsch, P.; Klasen-Memmer, M.; Tarumi, K. The TV in Your Pocket: Development of Liquid-Crystal Materials for the New Millennium. *Angew. Chem. Int. Ed.* **2013**, *52*, 8880–8896.

(245) Geelhaar, T.; Griesar, K.; Reckmann, B. 125 Years of Liquid Crystals-A Scientific Revolution in the Home. *Angew. Chem. Int. Ed.* **2013**, *52*, 8798–8809.

(246) Feringán, B.; Romero, P.; Serrano, J. L.; Giménez, R.; Sierra, T. Supramolecular Columnar Liquid Crystals Formed by Hydrogen Bonding between a Clicked Star-Shaped s -Triazine and Benzoic Acids. *Chem. Eur. J.* **2015**, *21*, 8859–8866.

(247) Lehn, J.-M. Perspectives in Chemistry-Aspects of Adaptive Chemistry and Materials. *Angew. Chem. Int. Ed.* **2015**, *54*, 3276–3289.

(248) Amabilino, D. B.; Smith, D. K.; Steed, J. W. Supramolecular Materials. *Chemical Society Reviews*. Royal Society of Chemistry May 7, 2017, pp 2404–2420.

(249) Yang, L.; Tan, X.; Wang, Z.; Zhang, X. Supramolecular Polymers: Historical

Development, Preparation, Characterization, and Functions. *Chemical Reviews*. American Chemical Society August 12, 2015, pp 7196–7239.

(250) Görl, D.; Soberats, B.; Herbst, S.; Stepanenko, V.; Würthner, F. Perylene Bisimide Hydrogels and Lyotropic Liquid Crystals with Temperature-Responsive Color Change. *Chem. Sci.* **2016**, *7*, 6786–6790.

(251) Wehner, M.; Würthner, F. Supramolecular Polymerization through Kinetic Pathway Control and Living Chain Growth. *Nature Reviews Chemistry*. Nature Research January 1, 2020, pp 38–53.

(252) Orvay, F.; Cerdá, J.; Rotger, C.; Ortí, E.; Aragó, J.; Costa, A.; Soberats, B.; Orvay, F.; Rotger, C.; Costa, A.; Soberats, B.; Cerdá, J.; Ortí, E.; Aragó, J. Influence of the Z/E Isomerism on the Pathway Complexity of a Squaramide-Based Macrocycle. *Small* **2021**, *17*, 2006133.

(253) Grimme, S. Exploration of Chemical Compound, Conformer, and Reaction Space with Meta-Dynamics Simulations Based on Tight-Binding Quantum Chemical Calculations. *J. Chem. Theory Comput.* **2019**, *15*, 2847–2862.

(254) Pracht, P.; Bohle, F.; Grimme, S. Automated Exploration of the Low-Energy Chemical Space with Fast Quantum Chemical Methods. *Phys. Chem. Chem. Phys.* **2020**, *22*, 7169–7192.

(255) Rotger, M. C.; Piña, M. N.; Frontera, A.; Martorell, G.; Ballester, P.; Deyà, P. M.; Costa, A. Conformational Preferences and Self-Template Macrocyclization of Squaramide-Based Foldable Modules. *J. Org. Chem.* **2004**, *69*, 2302–2308.

(256) Sato, K.; Seio, K.; Sekine, M. Squaryl Group as a New Mimic of Phosphate Group in Modified Oligodeoxynucleotides: Synthesis and Properties of New Oligodeoxynucleotide Analogues Containing an Internucleotidic Squaryldiamide Linkage. *J. Am. Chem. Soc.* **2002**, *124*, 12715–12724.

(257) Thorpe, J. E. 1 H Nuclear Magnetic Resonance Spectra of Some Squaramides. *J. Chem. Soc. B Phys. Org.* **1968**, No. 0, 435–436.

(258) Curutchet, C.; Mennucci, B. Toward a Molecular Scale Interpretation of Excitation Energy Transfer in Solvated Bichromophoric Systems. **2005**.

(259) Jensen, W. B. *The Lewis Acid-Base Concepts: An Overview*; New York Wiley, 1980.

(260) Petty, M. C. *Electroactive Organic Compounds*; John Wiley & Sons, Ltd, 2007.

(261) Forrest, S. R.; Thompson, M. E. Introduction: Organic Electronics and Optoelectronics. *Chem. Rev.* **2007**, *107*, 923–925.

(262) Bredas, J.-L.; Durrant, J. R. Organic Photovoltaics. *Acc. Chem. Res.* **2009**, *42*, 1689–1690.

(263) Nozik, A. J.; Miller, J. Introduction to Solar Photon Conversion. *Chem. Rev.* **2010**, *110*, 6443–6445.

(264) Brédas, J.-L.; Beljonne, D.; And, V. C.; Cornil, J. Charge-Transfer and Energy-Transfer Processes in π-Conjugated Oligomers and Polymers: A Molecular Picture. *Chem. Rev* **2004**, *104*, 4971–5003.

(265) Gómez, P.; Georgakopoulos, S.; Mas-Montoya, M.; Cerda, J.; Pérez, J.; Ortí, E.; Aragó, J.; Curiel, D. Improving the Robustness of Organic Semiconductors through Hydrogen Bonding. *ACS Appl. Mater. Interfaces* **2021**, *13*, 8620–8630.

(266) Gómez, P.; Cerdá, J.; Más-Montoya, M.; Georgakopoulos, S.; Da Silva, I.; García, A.; Ortí, E.; Aragó, J.; Curiel, D. Effect of Molecular Geometry and Extended Conjugation on the Performance of Hydrogen-Bonded Semiconductors in Organic Thin-Film Field-Effect Transistors. *J. Mater. Chem. C* **2021**, *9*, 10819–10829.

(267) Cerdá, J.; Calbo, J.; Ortí, E.; Aragó, J. Charge-Separation and Charge-Recombination Rate Constants in a Donor-Acceptor Buckybowl-Based Supramolecular Complex: Multistate and Solvent Effects. *J. Phys. Chem. A* **2021**, *125*, 9982–9994.

(268) Gallego, M.; Calbo, J.; Aragó, J.; Krick Calderon, R. M.; Liquido, F. H.; Iwamoto, T.; Greene, A. K.; Jackson, E. A.; Pérez, E. M.; Ortí, E.; Guldi, D. M.; Scott, L. T.; Martín, N. Electron Transfer in a Supramolecular Associate of a Fullerene Fragment. *Angew. Chem. Int. Ed.* **2014**, *53*, 2170–2175.

(269) Boudreault, P.-L. T.; Wakim, S.; Blouin, N.; Simard, M.; Tessier, C.; Tao, Y.; Leclerc, M. Synthesis, Characterization, and Application of Indolo[3,2-b]Carbazole Semiconductors. *J. Am. Chem. Soc.* **2007**, *129*, 9125–9136.

(270) Más-Montoya, M.; Georgakopoulos, S.; Cerón-Carrasco, J. P.; Pérez, J.; Tárraga, A.; Curiel, D. Structure–Property Correlation behind the High Mobility of Carbazolocarbazole. *J. Phys. Chem. C* **2018**, *122*, 11736–11746.

(271) Stehr, V.; Fink, R. F.; Tafipolski, M.; Deibel, C.; Engels, B. Comparison of Different Rate Constant Expressions for the Prediction of Charge and Energy Transport in Oligoacenes. *WIREs Comput. Mol. Sci.* **2016**, *6*, 694–720.

(272) Gallego, M.; Calbo, J.; Krick Calderon, R. M.; Pla, P.; Hsieh, Y.-C.; Pérez, E. M.; Wu, Y.-T.; Ortí, E.; Guldi, D. M.; Martín, N. Complexation and Electronic Communication between Corannulene-Based Buckybowls and a Curved Truxene-TTF Donor. *Chem. Eur. J.* **2017**, *23*, 3666–3673.

(273) Dreuw, A.; Head-Gordon, M. Failure of Time-Dependent Density Functional Theory for Long-Range Charge-Transfer Excited States: The Zincbacteriochlorin-Bacteriochlorin and Bacteriochlorophyll-Spheroidene Complexes. *J. Am. Chem. Soc.* **2004**, *126*, 4007–4016.

(274) Lundberg, M.; Siegbahn, P. E. M. Quantifying the Effects of the Self-Interaction Error in DFT: When Do the Delocalized States Appear? *J. Chem. Phys.* **2005**, *122*, 224103.

(275) Tsuneda, T.; Hirao, K. Self-Interaction Corrections in Density Functional Theory. *J. Chem. Phys.* **2014**, *140*, 18A513.

(276) Kastinen, T.; Da Silva Filho, D. A.; Paunonen, L.; Linares, M.; Ribeiro Junior, L. A.; Cramariuc, O.; Hukka, T. I. Electronic Couplings and Rates of Excited State Charge Transfer Processes at Poly(Thiophene-: Co -Quinoxaline)-PC71BM Interfaces: Two- versus Multi-State Treatments. *Phys. Chem. Chem. Phys.* **2019**, *21*, 25606–25625.

(277) Gregg, B. A. Excitonic Solar Cells. *J. Phys. Chem. B* **2003**, *107*, 4688–4698.

(278) Flanders, N.; Kirschner, M.; Kim, P.; Fauvell, T.; Evans, A.; Helweh, W.; Spencer, A.; Schaller, R.; Dichtel, W.; Chen, L. Large Exciton Diffusion Coefficients in Two Dimensional Covalent Or-Ganic Frameworks with Different Domain Sizes Revealed by Ultrafast Exciton Dynamics. *J. Am. Chem. Soc.* **2020**, *142*, 14957–14965.

(279) Wan, Y.; Stradomska, A.; Knoester, J.; Huang, L. Direct Imaging of Exciton Transport in Tubular Porphyrin Aggregates by Ultrafast Microscopy. *J. Am. Chem. Soc.* **2017**, *139*, 7287–7293.

(280) Haedler, A. T.; Kreger, K.; Issac, A.; Wittmann, B.; Kivala, M.; Hammer, N.; Köhler, J.; Schmidt, H.-W.; Hildner, R. Long-Range Energy Transport in Single Supramolecular Nanofibres at Room Temperature. *Nature* **2015**, *523*, 196–199.

(281) Liang, W. Y. Excitons. *Phys. Educ.* **1970**, *5*, 003.

(282) Knox, R. S. In *Collective Excitations in Solids*; Springer US, 1983; pp 183–245.

(283) Wannier, G. H. The Structure of Electronic Excitation Levels in Insulating Crystals. *Phys. Rev.* **1937**, *52*, 191–197.

(284) Frenkel, J. On the Transformation of Light into Heat in Solids. I. *Phys. Rev.* **1931**, *37*, 17–44.

(285) Murphy, C. B.; Zhang, Y.; Troxler, T.; Ferry, V.; Martin, J. J.; Jones, W. E. Probing Förster and Dexter Energy-Transfer Mechanisms in Fluorescent Conjugated Polymer Chemosensors. *J. Phys. Chem. B* **2004**, *108*, 1537–1543.

(286) Skourtis, S. S.; Liu, C.; Antoniou, P.; Virshup, A. M.; Beratan, D. N. Dexter Energy Transfer Pathways. *Proc. Natl. Acad. Sci. U. S. A.* **2016**, *113*, 8115–8120.

(287) Balawi, A. H.; Stappert, S.; Gorenflot, J.; Li, C.; Müllen, K.; Andrienko, D.; Laquai, F. Direct and Energy-Transfer-Mediated Charge-Transfer State Formation and Recombination in Triangulene-Spacer-Perylenediimide Multichromophores: Lessons for Photovoltaic Applications. *J. Phys. Chem. C* **2019**, *123*, 16602–16613.

(288) Tamura, H. Triplet Exciton Transfers and Triplet-Triplet Annihilation in Anthracene Derivatives via Direct versus Superexchange Pathways Governed by Molecular Packing. *J. Phys. Chem. A* **2020**, *124*, 7943–7949.

(289) Czikklely, V.; Forsterling, H. D.; Kuhn, H. Extended Dipole Model for Aggregates of Dye Molecules. *Chem. Phys. Lett.* **1970**, *6*, 207–210.

(290) Oosterbaan, K. J.; White, A. F.; Head-Gordon, M. Non-Orthogonal Configuration Interaction with Single Substitutions for Core-Excited States: An Extension to Doublet

Radicals. *J. Chem. Theory Comput.* **2019**, *15*, 2966–2973.

(291) Sundstrom, E. J.; Head-Gordon, M. Non-Orthogonal Configuration Interaction for the Calculation of Multielectron Excited States. *J. Chem. Phys.* **2014**, *140*, 114103.

(292) Kathir, R. K.; De Graaf, C.; Broer, R.; Havenith, R. W. A. Reduced Common Molecular Orbital Basis for Nonorthogonal Configuration Interaction. *J. Chem. Theory Comput.* **2020**, *16*, 2941–2951.

(293) Hestand, N. J.; Spano, F. C. Interference between Coulombic and CT-Mediated Couplings in Molecular Aggregates: H- to J-Aggregate Transformation in Perylene-Based π-Stacks. *J. Chem. Phys.* **2015**, *143*, 244707.

(294) Mulliken, R. S. Molecular Compounds and Their Spectra Molecular Compounds and Their Spectra. II1. *J. Phys. Chem.* **1952**, *56*, 801–822.

(295) Valeev, E. F.; Coropceanu, V.; Da, D. A.; Filho, S.; Salman, S.; Brédas, J.-L. Effect of Electronic Polarization on Charge-Transport Parameters in Molecular Organic Semiconductors. *J. Am. Chem. Soc.* **2006**, *128*, 9882–9886.

(296) Aragó, J.; Troisi, A. Dynamics of the Excitonic Coupling in Organic Crystals. *Phys. Rev. Lett.* **2015**, *114*, 026402.

(297) Imahori, H.; Tkachenko, N. V; Vehmanen, V.; Tamaki, K.; Lemmetyinen, H.; Sakata, Y.; Fukuzumi, S. An Extremely Small Reorganization Energy of Electron Transfer in Porphyrin-Fullerene Dyad. *J. Phys. Chem. A* **2001**, *105*, 1750–1756.

(298) Larsson, S.; Klimkws, A.; Rodriguez-Monge, L.; Duskesas, G. Reorganization Energies in Organic π Systems. *J. Mol. Struct.* **1998**, *425*, 155–159.

(299) Gruhn, N. E.; Filho, D. A. da S.; Bill, T. G.; Malagoli, M.; Coropceanu, V.; Antoine, K.; Brédas, J.-L. The Vibrational Reorganization Energy in Pentacene: Molecular Influences on Charge Transport. *J. Am. Chem. Soc.* **2002**, *124*, 7918–7919.

(300) Kera, S.; Hosoumi, S.; Sato, K.; Fukagawa, H.; Nagamatsu, S.; Sakamoto, Y.; Suzuki, T.; Huang, H.; Chen, W.; Wee, A. T. S.; Coropceanu, V.; Ueno, N. Experimental Reorganization Energies of Pentacene and Perfluoropentacene: Effects of Perfluorination. *J. Phys. Chem. C* **2013**, *117*, 22428–22437.

(301) Schröter, M.; Ivanov, S. D.; Schulze, J.; Polyutov, S. P.; Yan, Y.; Pullerits, T.; Kühn, O. Exciton-Vibrational Coupling in the Dynamics and Spectroscopy of Frenkel Excitons in Molecular Aggregates. *Phys. Rep.* **2015**, *567*, 1–78.

(302) Fornari, R. P.; Aragó, J.; Troisi, A. Exciton Dynamics in Phthalocyanine Molecular Crystals. *J. Phys. Chem. C* **2016**, *120*, 7987–7996.

(303) Wang, L.; Beljonne, D. Optical Properties of Regioregular Poly(3-Hexylthiophene) Aggregates from Fully Atomistic Investigations. *CrystEngComm* **2016**, *18*, 7297–7304.

List of publications

Articles in the thesis

Supramolecular Polymers

1. E. E. Greciano, J. Calbo, J. Buendía, J. Cerdá, J. Aragó, E. Ortí, L. Sánchez, "Decoding the Consequences of Increasing the Size of Self-Assembling Tricarboxamides on Chiral Amplification", *J. Am. Chem. Soc.*, **2019**, *141*, 7463–7472.

2. Y. Dorca, R. Sánchez-Naya, J. Cerdá, J. Calbo, J. Aragó, R. Gómez, E. Ortí, L. Sánchez, "Impact of Molecular Size and Shape on the Supramolecular Co-Assembly of Chiral Tricarboxamides: A Comparative Study", *Chem. Eur. J.*, **2020**, *26*, 14700–14707.

3. B. Feringán, J. Cerdá, B. Diosdado, J. Aragó, E. Ortí, R. Giménez, T. Sierra, "On the Structure and Chiral Aggregation of Liquid Crystalline Star-Shaped Triazines H-Bonded to Benzoic Acids", *Chem. Eur. J.*, **2020**, *26*, 15313–15322.

4. F. Orvay, J. Cerdá, C. Rotger, E. Ortí, J. Aragó, A. Costa, B. Soberats, "Influence of the *Z*/*E* Isomerism on the Pathway Complexity of a Squaramide-Based Macrocyle", *Small*, **2021**, *17*, 2006133.

Charge Transport

5. P. Gómez, S. Georgakolopoulos, M. Más-Montoya, J. Cerdá, J. Pérez, E. Ortí, J. Aragó, D. Curiel, "Improving the Robustness of Organic

Semiconductors through Hydrogen Bonding", *ACS Appl. Mater. Interfaces*, **2021**, *13*, 8620–8630.

6. P. Gómez, J. Cerdá, M. Más-Montoya, S. Georgakopoulos, I. da Silva, A. García, E. Ortí, J. Aragó, D. Curiel, "Effect of molecular geometry and extended conjugation on the performance of hydrogen-bonded semiconductors in organic thin-film field-effect transistors", *J. Mater. Chem. C.* **2021**, *9*, 10819–10829.

7. J. Cerdá, J. Calbo, E. Ortí, J. Aragó, "Charge-Separation and Charge-Recombination Rate Constants in a Donor-Acceptor Buckybowl-Based Supramolecular Complex: Multistate and Solvent Effects", *J. Phys. Chem. A.* **2021**, *125*, 9982–9994.

Articles related with the thesis

Supramolecular Polymers

8. Y. Dorca, J. S. Valera, J. Cerdá, J. Aragó, R. Gómez. E. Ortí. L. Sánchez, "Synergy of Axial and Point Chirality to Construct Helical N-Heterotriangulene-Based Supramolecular Polymers", *ChemNanoMat*, **2018**, *4*, 781–784.

9. M. Castillo-Vallés, E. Beltrán, J. Cerdá, J. Aragó, P. Romero, J. L. Serrano, E. Ortí, R. Giménez, T. Sierra, "Self-Assembly of Clicked Star-Shaped Triazines into Functional Nanostructures", *ChemNanoMat*, **2018**, *5*, 130–137.

10. Y. Dorca, J. Cerdá, J. Aragó, E. Ortí, L. Sánchez, "Flipping Motion To Bias the Organized Supramolecular Polymerization of N-Heterotriangulenes", *Chem. Mater*. **2019**, *31*, 7024–7032.

11. M. A. Martínez, A. Doncel-Giménez, J. Cerdá, J. Calbo, R. Rodríguez, J. Aragó, J. Crassous, E. Ortí, L. Sánchez, "Distance Matters: Biasing Mechanism, Transfer of Asymmetry, and Stereomutation in N-Annulated Perylene Bisimide Supramolecular Polymers", *J. Am. Chem. Soc.* **2021**, *143*, 13281-13291.

Charge Transport

12. M. Privado, P. Malhotra, P. de la Cruz, R. Singhal, J. Cerdá, J. Aragó, E. Ortí, G. D. Sharma, F. Langa, "Ternary Organic Solar Cell with a Near-Infrared Absorbing Selenophene–Diketopyrrolopyrrole-Based Nonfullerene Acceptor and an Efficiency above 10%", *Solar RRL*, **2019**, *4*, 1900471.

13. R. Caballero, M. Barrejón, J. Cerdá, J. Aragó, S. Seetharaman, P. de la Cruz, E. Ortí, F. D'Souza, F. Langa, "Self-Assembly-Directed Organization of a Fullerene–Bisporphyrin into Supramolecular Giant Donut Structures for Excited-State Charge Stabilization", *J. Am. Chem. Soc.* **2021**, *143*, 11199–11208.

Other Contributions

14. A. Ullah, J. Cerdá, J. J. Baldoví, S. A. Varganov, J. Aragó, A. Gaita-Ariño, "In Silico Molecular Engineering of Dysprosocenium-Based Complexes to Decouple Spin Energy Levels from Molecular Vibrations", *J. Phys. Chem. Lett.* **2019**, *10*, 7678–7683.

15. J. Cuny, J. Cerdá, N. Ansari, Ali A. Hassanali, M. Rapacioli, A. Simon, "Simulation of Liquids with the Tight-Binding Density-Functional Approach and Improved Atomic Charges", *J. Phys. Chem. B* **2020**, *124*, 7421–7432.

List of acronyms

Acronym	Meaning
A	Aceptor
ADAI	7,15-Dihydroanthra[1,2-*b*:5,6-*b′*]di(7-azaindole)
ADI	7,15-Dihydroanthra[1,2-*b*:5,6-*b′*]diindole
AFM	Atomic Force Microscopy
AIFD	Ab-Initio Frenkel-Davydov
ATC	Atomic Transition Charge
BDAI	6,12-Dihydropyrido[2,3-*b*]pyrido[3',2':4,5]pyrrolo[2,3-*f*]indole
BO	Born-Oppenheimer
BTA	Benzene-1,3,5-tricarboxamide
CD	Circular Dichroism
CI	Configuration Interaction
CIS	Configuration Interaction Singles
CR	Charge-Recombination
CS	Charge-Separation
CT	Charge Transfer
D	Donor
DFT	Density Functional Theory
DFTB	Tight-Binding DFT
DIPRO	Dimer Projection Method
DMF	Dimethylformamide
EA	Electron Affinity
Eq	Equilibrium
FCD	Fragment Charge Difference
FE	Frenkel Exciton
FPHD	Fragment Particle Hole Densities
FRET	Förster Resonance Energy Transfer
FT-IR	Fourier Transform Infrared Spectroscopy
GGA	Generalized Gradient Approximation
GS	Ground State

Acronym	Meaning
GTO	Gaussian-Type Orbital
HF	Hartree Fock
HOMO	Highest Occupied Molecular Orbital
HR	Huang–Rhys
HRP	Helical Reversal Penalty
HTM	Hole-Transporting Material
IP	Ionization Potential
KS	Khon-Sham
LC	Long-Range Corrected
LCD	Liquid Crystal Display
LE	Local Excited State
LUMO	Lowest Unoccupied Molecular Orbital
MCH	Methylcyclohexane
MCTDH	Multi-Configurational Time-Dependent Hartree
MD	Molecular Dynamics
MLJ	Marcus–Levitch–Jortner
MM	Molecular Mechanics
MMP	Mismatch Penalty
MR	Majority Rules
NDAI	7,14-Dihydronaphtho[1,2-b:5,6-b']di(7-azaindole)
NHT	N-Heterotriangulenes
NMR	Nuclear Magnetic Resonance
NonEq	Non-Equilibrium
OFET	Organic Field Effect Transistor
OLED	Organic Light-Emitting Diodes
OPE-TA	Oligo(Phenylene Ethynylene) Tricarboxamides
OPV	Organic Photovoltaic
OT	Optimally-Tuned
PCM	Polarizable Continuum Model
PD	Point-Dipole
PDAI	5,13-Dihydropyreno[1,2-b:6,7-b']di(7-azaindole)
PES	Potential Energy Surface
SaS	Sergeants and Soldiers Experiments
SQ	Squaramid

Acronym	Meaning
SS	State Specific
STO	Slater-Type Orbitals
$T3C_4$	2,4,6-Tris(triazolyl)-1,3,5-triazine
TDA	Tamm-Dancoff
TDC	Transition Density Cube
TDDFT	Time-Dependent Density Functional Theory
TDM	Transition Dipole Moment
TPBA	1,3,5-Triphenylbenzenetricarboxamides
truxTTF	Truxene-Tetrathiafulvalene
vdW	van-der-Waals
XC	Exchange-Correlation